

UC Riverside

UC Riverside Electronic Theses and Dissertations

Title

Development and Use of Particle into Liquid Sampling Time-of-Flight Mass Spectrometry (PILS-ToF) for Characterization of Aerosol Particles

Permalink

<https://escholarship.org/uc/item/95c1p0nn>

Author

Clark, Christopher Holmes

Publication Date

2012

Peer reviewed|Thesis/dissertation

UNIVERSITY OF CALIFORNIA
RIVERSIDE

Development and Use of Particle into Liquid Sampling Time-of-Flight Mass
Spectrometry (PILS-ToF) for Characterization of Aerosol Particles

A Dissertation submitted in partial satisfaction
of the requirements for the degree of

Doctor of Philosophy

in

Chemical and Environmental Engineering

by

Christopher Holmes Clark

September 2012

Dissertation Committee:

Dr. David R. Cocker III, Chairperson

Dr. Akua Asa-Awuku

Dr. Joseph M. Norbeck

Copyright by
Christopher Holmes Clark
2012

The Dissertation of Christopher Holmes Clark is approved:

Committee Chairperson

University of California, Riverside

Acknowledgements

No man is an island,
Entire of itself.
Each is a piece of the continent,
A part of the main.

– John Donne, “Meditation 17” Devotions upon Emergent Occasions

First and foremost it is important to acknowledge my family. I would like to acknowledge the sacrifice of my wife, Alexis N. Clark, who has been the emotional underpinning of 12 years of university study. Financial and emotional support has come also from my parents, David Clark, Debra Clark-Todd, and John Todd, and my grandparents Paul Franklin (deceased), Barbara Franklin, Herbert Clark, and Ruth Clark (deceased). It is important that I also acknowledge the emotional and financial assistance of my best friend and fraternal brother David Hosey.

I sincerely appreciate the kindness and patience of my graduate advisor Dr. David Cocker, without whom I would have abandoned my graduate studies. I acknowledge my other committee members, Dr. Joseph Norbeck and Dr. Akua Asa-Awuku, who provided initial direction to this dissertation and the guidance required for completion. Dr. Bill Carter and Dr. Gookyoung Heo of University of California, Riverside College of Engineering Center for Environmental Research and Technology (UCR CE-CERT) provided crucial input into the formation of the experimental plan and chemical mechanistic insight. Additionally, two visiting researchers helped shape the path of this dissertation. Dr. Katie Purvis-Roberts of Claremont McKenna College introduced me to the Particle into Liquid Sampler (PILS) a lynch pin of my dissertation. Dr. Kei Sato of

the Asian Environment Research Group in Tsukuba, Ibaraki, Japan introduced me to the processes of isoprene oligomerization a theme of this dissertation.

In my time at UCR I have had the help of a myriad of graduate students as friends and co-workers, but some have done more than just socialize, these have become valued colleagues and friends. Dr. Quentin Malloy and Dr. Shunsuke Nakao have helped me run experiments and mentored me in countless ways. Mr. Derek Price, Ms. Ping Tang, and Ms. Xiaochen Tang have helped with experiments and have kept equipment running. In the Atmospheric Process Laboratory at UCR CE-CERT all graduate students owe a debt of acknowledgement to Mr. Kurt Bumiller and Mr. Charles Bufalino for their initial construction of the Atmospheric Chambers and their sage-like wisdom regarding its repair and operation.

I must thank my employer, the Naval Surface Warfare Center, Corona (NSWC, Corona), which has paid my tuition for the past 4 years. The specific managers and supervisors who have supported me in this effort are: Mr. Arman Hovakemian, Mr. Robert Fritzsche, Mr. John Griffith, Mr. Jeff Walden, Mr. Laron Scott, Ms. April Fritzsche, Lt. Col. (ret.) Marie Juliano, Mr. Maxie Perdue, and Mr. Mike Bishop. I would like to more specifically acknowledge Mr. Mike Bishop, whose tireless support of my graduate work assured success. I have been blessed at NSWC, Corona to have excellent co-workers who have helped me keep up with work tasking while giving me moral support towards dissertation completion, they are: Ms. Mary Graupmann, Ms. Lindsay Hum, Ms. Christin Schliemann, and Mr. Scott Stanco.

Finally, I would like to acknowledge research funding from University of California Transportation Center, W. M. Keck Foundation, National Science Foundation (ATM-0449778 and ATM-0901282), California Air Resources Board and the University of California, Riverside, Department of Chemical and Environmental Engineering.

Dedicated to my wife and best friend Alexis Nicole Clark

ABSTRACT OF THE DISSERTATION

Development and Use of Particle into Liquid Sampling Time-of-Flight Mass Spectrometry (PILS-ToF) for Characterization of Aerosol Particles

by

Christopher Holmes Clark

Doctor of Philosophy, Graduate Program in Chemical and Environmental Engineering
University of California, Riverside, September 2012
Dr. David R. Cocker III, Chairperson

This dissertation introduces and makes use of the Particle-into-Liquid-Sampler coupled to a Time-of-Flight mass spectrometer (PILS-ToF), a new instrumental method used here to provide new chemical characterization information on secondary organic aerosol (SOA). The PILS-ToF instrument improves upon drawbacks found in current state-of-the-art mass spectral chemical characterization methods to include lack of time resolution and ion fragmentation by electron impact ionization in the Aerodyne Aerosol Mass Spectrometer (AMS). The functionality of the PILS-ToF for collection and response to SOA particle formation is validated against a scanning mobility particle sizer (SMPS), a widely accepted and standardized physical chemical characterization instrument, for a well characterized SOA formation experiment, dark ozonolysis of α -pinene. The PILS-ToF is also used to lend insight into oligomer growth during the NO photo-oxidation of isoprene. It is of atmospheric importance to study SOA formation from isoprene, as it is globally the most abundant non-methane hydrocarbon in the

ambient. SOA from isoprene is further studied using the PILS-ToF as part of the suite instrumentation at the University of California, Riverside, College of Engineering, Center for Environmental Research and Technology (CE-CERT) atmospheric chamber providing a complete chemical and physical characterization of SOA formed by isoprene with various oxidants under a myriad of oxidant concentration conditions. In addition, the PILS-ToF is used, again in tandem with other chemical and physical characterization methods at CE-CERT, to probe temperature effects on SOA formation from isoprene under many different oxidizing conditions. Finally, the PILS-ToF is used to provide new mechanistic information on SOA formation from trimethylamine and tributylamine, two tertiary amines emitted from anthropogenic and animal husbandry processes. For these two tertiary amines, the PILS-ToF provides evidence of oligomerization which gives a potential explanation to the high SOA yields from these parent compounds.

Table of Contents

Chapter 1: Introduction	1
1.1 Introduction of Dissertation	1
1.2 Introduction Reference.....	4
Chapter 2: Real-time study of particle phase products from dark ozonolysis of α -pinene and photo oxidation of isoprene using particle into liquid sampling directly coupled to a time of flight mass spectrometer (PILS-ToF).....	6
2.1 Introduction.....	6
2.2 Materials and Methods.....	8
2.2.1 PILS-ToF	8
2.2.2 chamber experiments	9
2.3 Results and Discussions.....	10
2.3.1 α -pinene ozonolysis	11
2.3.2 isoprene NO photo-oxidation.....	15
2.4 Conclusions.....	22
2.4 Reference	24
2.6 Tables.....	27
2.7 Figures.....	33
Chapter 3: Characterization of secondary organic aerosol (SOA) from isoprene	39
3.1 Introduction.....	39
3.2 Materials and Methods.....	41
3.2.1 environmental chamber.....	41
3.2.2 gas and particle analysis.....	41
3.3 Results and Discussions.....	44

3.3.1 SOA formation.....	44
3.3.1.1 SOA formation from isoprene photo-oxidation.....	44
3.3.1.2 SOA formation from dark reactions of isoprene.....	46
3.3.2 SOA Physical Characterization.....	48
3.3.3 SOA chemical characterization.....	50
3.3.3.1 SOA AMS characterization	50
3.3.3.2 PILS-ToF Characterization.....	52
3.3.3.2.a PILS-ToF Characterization of Isoprene Photo-oxidation	53
3.3.3.2.b PILS-ToF characterization of isoprene dark reactions	58
3.4 Conclusions.....	62
3.5 Reference	65
3.6 Tables.....	69
3.7 Figures.....	85
Chapter 4: Temperature effects on secondary organic aerosol (SOA) from the dark ozonolysis and NO photo-oxidation of Isoprene	94
4.1 Introduction.....	94
4.2 Materials and Methods.....	95
4.2.1 environmental chamber.....	95
4.2.2 gas and particle analysis.....	95
4.3 Results and Discussions	98
4.3.1 SOA formation.....	98
4.3.2 SOA physical characterization.....	99
4.3.3 SOA chemical characterization.....	100
4.4 Conclusions.....	105

4.5 Reference	107
4.6 Tables	110
4.7 Figures.....	121
Chapter 5: Characterization of secondary organic aerosol (SOA) formed during NO _x photo-oxidation and dark nitrate radical reactions of trimethyl amine and tributyl amine by particle into liquid sampling directly coupled to a time of flight mass spectrometry (PILS-ToF).....	
5.1 Introduction.....	130
5.2 Materials and Methods.....	131
5.3 Results and Discussions.....	133
5.3.1 Trimethylamine (TMA)	133
5.3.2 Tributylamine (TBA)	139
5.4 Conclusions.....	145
5.5 Reference	146
5.6 Tables	148
5.7 Figures.....	151
Chapter 6: Summary	
Appendix A: Secondary organic aerosol formation from the photooxidation of isoprene, 1,3-butadiene, and 2,3-dimethyl-1,3-butadiene under high NO _x conditions	
	163
Appendix B: Secondary Organic Aerosol Formation from Phenolic Compounds in the Absence of NO _x	
	214

List of Tables

Table 2.1. PILS instrument flow-rates	27
Table 2.2. Experimental conditions and results	28
Table 2.3. Line Parameters for Van Krevelen Lines shown in Figure 2.6	29
Table 2.4. PILS-ToF Ion Formula Matches for those ions in the mass spectrum shown in Figure 2.5f having an intensity greater than 1000 ion counts.....	30
Table 3.1. Experimental conditions and aerosol mass and yield results.....	69
Table 3.2. Summary of SOA chemical and physical characterization data.....	70
Table 3.3. PILS-ToF mass spectral ion matches with the corresponding correlations experiments in Table 3.1 and literature references	71
Table 4.1. Experimental conditions and results	110
Table 4.2. Summary of SOA chemical and physical characterization data.....	111
Table 4.3. PILS-ToF mass spectral ion matches with the corresponding correlations experiments in Table 4.1 and literature references	112
Table 5.1. Experimental conditions and aerosol mass formation results.....	148
Table 5.2. Ion matches corresponding to Figure 5.5b correlated to the mechanism in Figure 5.1 for experiment MEZ021112	149
Table 5.3. Ion matches corresponding to Figure 5.5c correlated to the mechanism in Figure 5.1 for experiment MEZ021512	150
Table A.1. Experimental conditions and results.....	199
Table A.2. Oligoesters detected by LC-TOFMS and AMS.....	200
Table B.1. Experimental test matrix (low NO _x)	237
Table B.2. Phenolic formation yield from OH reaction with benzene, toluene, and <i>m</i> -xylene	240
Table B.3. Estimated contribution of phenolic route to benzene, toluene, and <i>m</i> -xylene SOA.....	241

List of Figures

Figure 2.1: Flow diagram of Particle into Liquid Sampling coupled to Time-of-Flight Mass Spectrometry (PILS-ToF).....	33
Figure 2.2: a) Plot of the PILS-ToF total measured ion-counts (TIC) and wall-loss corrected aerosol mass formation, as measured by SMPS, during the dark α -pinene ozonolysis, EPA1311A. Inset is the linear correlation of PILS-ToF TIC at maximum to the maximum wall corrected aerosol formation, as measured by SMPS. b) Contour plot of PILS-ToF mass spectrum as a function of reaction time.....	34
Figure 2.3: Individual PILS-ToF extracted mass spectra for α -pinene ozonolysis run EPA1311A. a) Mass spectra 10 min. into reaction (background). b) Mass spectra 50 min. into reaction. c) Mass spectra 380 min. into reaction.	35
Figure 2.4: a) Plot of the PILS-ToF total measured ion-counts (TIC) and wall-loss corrected aerosol mass formation, as measured by SMPS, during the NO photo-oxidation of isoprene, EPA1353A. b) Contour plot of PILS-ToF mass spectrum as a function of reaction time.....	36
Figure 2.5: Individual PILS-ToF extracted mass spectra for NO photo-oxidation of isoprene, EPA1353A. a) Mass spectra 10 min. into reaction (background). b) Mass spectra 35 min. into reaction. c) Mass spectra 60 min. into reaction. d) Mass spectra 75 min. into reaction. e) Mass spectra 100 min. into reaction. f) Mass spectra 300 min. into reaction.....	37
Figure 2.6: Van Krevelen Diagram of the final state (reaction time=300min.) PILS-ToF mass spectra of the NO photo-oxidation of isoprene, EPA1353A. a) represents mass spectral peaks confirmed with the literature compared to this work. b) presents mass spectral peak matches corresponding to new apparent reaction lines observed in this work.	38
Figure 3.1: Final (a) SOA yield and (b) isoprene consumption (Δ HC) shown as a function of experimental initial ozone concentration for isoprene dark ozonolysis experiments	85
Figure 3.2: Final SOA (a) particle density as measured by APM-SMPS and (b) particle volatility fraction remaining (VFR) as measured by VTDMA as a function of initial NO concentration for isoprene photo-oxidation experiments	86

Figure 3.3: Final SOA (a) particle density as measured by APM-SMPS and (b) particle volatility fraction remaining (VFR) as measured by VTDMA as a function of initial ozone concentration for isoprene dark ozonolysis and dark N ₂ O ₅ experiments	87
Figure 3.4: PILS-ToF mass spectra for isoprene photo-oxidation experiments (a) EPA1353A, (b) EPA1392A, (c) EPA1382A, (d) EPA1303A, (e) EPA1467A, (f) EPA1375A, and (g) EPA1397A	88
Figure 3.5: PILS-ToF ion matches presented as Van Krevelen Plots for isoprene photo-oxidation experiments (a) EPA1353A, (b) EPA1382A, (c) EPA1303A, (d) EPA1467A, (e) EPA1375A, and (f) EPA1397A. *Note mass spectral intensity of an individual ion is presented through a gradient gray scale, where white represents no ion intensity, black represents an ion intensity of 5000 counts or above.	89
Figure 3.6: PILS-ToF mass spectra for isoprene dark ozonolysis experiments (a) EPA1425A, (b) EPA1562A, (c) EPA1480A, (d) EPA1428A, (e) EPA1445A, and (f) EPA1473A	90
Figure 3.7: PILS-ToF ion matches presented as Van Krevelen Plots for isoprene dark ozonolysis experiments (a) EPA1425A, (b) EPA1562A, (c) EPA1480A, (d) EPA1428A, (e) EPA1445A, and (f) EPA1473A. *Note mass spectral intensity of an individual ion is presented through a gradient gray scale, where white represents no ion intensity, black represents an ion intensity of 5000 counts or above.	91
Figure 3.8: PILS-ToF mass spectra for isoprene dark reaction of isoprene and N ₂ O ₅ , EPA1562A	92
Figure 3.9: PILS-ToF ion matches presented as Van Krevelen Plots for dark reaction of isoprene and N ₂ O ₅ , EPA1562	93
Figure 4.1: Experimental SOA yield as a function of environmental chamber reaction temperature for a) NO and H ₂ O ₂ photo-oxidation experiments and b) dark ozonolysis experiments	121
Figure 4.2: SOA density, as measured by APM-SMPS, as a function environmental chamber reaction temperature for isoprene H ₂ O ₂ only photo-oxidation, NO + H ₂ O ₂ photo-oxidation, and dark ozonolysis	122
Figure 4.3: Volatile fraction remaining, as measured by VTDMA, as a function environmental chamber reaction temperature for isoprene H ₂ O ₂ only photo-oxidation, NO + H ₂ O ₂ photo-oxidation, and dark ozonolysis	123

Figure 4.4: PILS-ToF mass spectra for isoprene NO photo-oxidation experiments (a) EPA1353A and (b) EPA1559A performed at environmental chamber temperatures of 300 K and 278 K respectively..... 124

Figure 4.5: PILS-ToF mass spectra for isoprene H₂O₂ photo-oxidation experiments (a) EPA1566A, (b) EPA1467A, and (c) EPA1556A performed at environmental chamber temperatures of 313 K, 300 K, and 278 K respectively..... 125

Figure 4.6: PILS-ToF mass spectra for isoprene dark ozonolysis experiments (a) EPA1563A, (b) EPA1445A, and (c) EPA1583A performed at environmental chamber temperatures of 313 K, 300 K, and 278 K respectively..... 126

Figure 4.7: PILS-ToF ion matches presented as Van Krevelen Plots for isoprene NO photo-oxidation experiments (a) EPA1353A and (b) EPA1559A performed at environmental chamber temperatures of 300 K and 278 K respectively. *Note mass spectral intensity of an individual ion is presented through a gradient gray scale, where white represents no ion intensity, black represents an ion intensity of 5000 counts or above. 127

Figure 4.8: PILS-ToF ion matches presented as Van Krevelen for isoprene H₂O₂ photo-oxidation experiments (a) EPA1566A, (b) EPA1467A, and (c) EPA1556A performed at environmental chamber temperatures of 313 K, 300 K, and 278 K respectively. *Note mass spectral intensity of an individual ion is presented through a gradient gray scale, where white represents no ion intensity, black represents an ion intensity of 5000 counts or above..... 128

Figure 4.9: PILS-ToF ion matches presented as Van Krevelen for isoprene dark ozonolysis experiments (a) EPA1563A, (b) EPA1445A, and (c) EPA1583A performed at environmental chamber temperatures of 313 K, 300 K, and 278 K respectively. *Note mass spectral intensity of an individual ion is presented through a gradient gray scale, where white represents no ion intensity, black represents an ion intensity of 5000 counts or above..... 129

Figure 5.1: Proposed mechanism for oligomer formation from hydroxyl reaction with trimethylamine (TMA) reacting with hydroxyl radical (Price, Tang et al. 2012) 151

Figure 5.2: Trimethylamine (TMA) experimental end-state PILS-ToF mass spectra for a) MEZ020312, b) MEZ021012, and c) MEZ021312 152

Figure 5.3: Van Krevelen plots (a-c) and modified-Van Krevelen plots (d-f), where N:C ratio is on the ordinate, for molecular matches of final state PILS-ToF mass spectra in

trimethylamine (TMA)experiments a)MEZ020312, b)MEZ021012, c)MEZ021312, d)MEZ020312, e)MEZ021012, f)MEZ021312	153
Figure 5.4: Proposed mechanism for formation of major PILS-ToF observed SOA species from tributylamine (TBA) (Price, Tang et al. 2012)	154
Figure 5.5: Tributylamine (TBA) experimental end-state PILS-ToF mass spectra for a) MEZ020612, b) MEZ021112, and c) MEZ021512	155
Figure 5.6: Van Krevelen plots (a-c) and modified-Van Krevelen plots (d-f), where N:C ratio is on the ordinate, for molecular matches of final state PILS-ToF mass spectra in tributylamine (TBA) experiments a)MEZ020612, b)MEZ021112, c)MEZ021512, d)MEZ020612, e)MEZ021112, f)MEZ021512	156
Figure A.1: Conjugated dienes used in this study.....	202
Figure A.2: Time profiles of (a) gas concentration, (b) SOA mass concentration, and (c) PTR-MS signals during isoprene/NO _x /H ₂ O ₂ experiment at 300 K (EPA1078W). The NO ₂ photolysis rate for this run was 0.12 min ⁻¹ . The NO _x analyzer used was a chemiluminescence type; NO _x signals of this instrument include not only the signals of NO and NO ₂ but also the signals of NO _y species (e.g., nitric acid).	203
Figure A.3: Time-dependent SOA growth curves measured in diene/NO _x /H ₂ O ₂ experiments with (a) isoprene (EPA1108W, EPA1108E, EPA1115E), (b) 1,3-butadiene (EPA1094W, EPA1094E, EPA1132W, EPA1132E), and (c) DMB (EPA1104W, EPA1104E, EPA1115W). All results plotted were obtained at initial NO _x concentrations of 249–267 ppb and at an NO ₂ photolysis rate of 0.40 min ⁻¹	204
Figure A.4: Flow-injection LC-TOF mass spectra of off-line SOA samples obtained during the photooxidation of (a) isoprene at 300 K (EPA1108W), (b) isoprene at 278 K (EPA1148W), (c) isoprene-1- ¹³ C (EPA1082W), (d) 1,3-butadiene (EPA1094W), and (e) DMB (EPA1104W).	205
Figure A.5: Typical LC-TOFMS base peak chromatograms of SOA formed from the photooxidation of (a) isoprene at 300 K (EPA1058E), (b) isoprene at 278 K (EPA1148W), and (c) 1,3-butadiene (EPA1132W).	206
Figure A.6: Typical TOF-AMS raw mass spectra of SOA formed from the photooxidation of (a) isoprene (EPA1170W), (b) isoprene-1- ¹³ C (EPA1082W), and (c) 1,3-butadiene (EPA1094W).....	207

Figure A.7: Proposed mechanism of particle-phase product formation from the photooxidation of isoprene and 1,3-butadiene in the presence of NO _x . R1 is a methyl group (isoprene) or a hydrogen atom (1,3-butadiene).	208
Figure A.8: Proposed mechanism of (a) isoprene-1-13C and (b) DMB photooxidation in the presence of NO _x	209
Figure A.9: Oligomer distribution measured in experiments with isoprene (EPA1058E, EPA1060E, and EPA1061E). SOA mass loading was changed between 3 and 26 μg m ⁻³ by changing the initial reactant concentrations, maintaining the isoprene/NO _x ratio within the range 0.6–0.9.....	210
Figure A.10: Time profiles of particulate product mass signals measured by (a) ToF-AMS during an experiment with isoprene (EPA1070W) and (b) LC-TOFMS during an experiment with isoprene (EPA1078E).	211
Figure A.11: Time profiles of (a) PTR-MS signals, (b) SOA mass concentration, and (c) LC-TOFMS oligomer mass signals measured in a lights-off experiment with isoprene (EPA1090W).....	212
Figure A.12: Time profiles of (a) isoprene concentration, (b) SOA concentration, and (c) volume fraction remaining (VFR) measured during experiments with isoprene at 278 K (EPA1148W) and 300 K (EPA1078W). The NO ₂ photolysis rate for both experiments was set to 0.12 min ⁻¹	213
Figure B.1: SOA yield of benzene, toluene, m-xylene, and their phenolic compounds in the absence of NO _x (Dotted lines are one product model fit for phenolic compounds). 242	
Figure B.2: Formation of cresols from OH reaction with toluene.	243
Figure B.3: Time series of the O/C ratio of SOA formed from aromatic hydrocarbons and phenolic compounds.....	244
Figure B.4: Time series of the density of SOA formed from aromatic hydrocarbons and phenolic compounds	245
Figure B.5: The relationship between density and elemental compositions of SOA formed from aromatic hydrocarbons and phenolic compounds	246
Figure B.6: ESI/APCI-ToF mass spectrums of SOA formed by OH reaction with phenolic compounds	247

Figure B.7: Possible formation pathway of a bicyclic hydroperoxide (C₆H₈O₆) from OH reaction with phenol in the absence of NO_x inferred from aromatics oxidation mechanisms (e.g., Calvert et al., 2002; Johnson et al., 2005). Catechol formation from phenol is reported to be approximately 80% (Olariu et al., 2002)..... 248

Figure B.8: PILS-ESI-ToF mass spectrums of SOA formed by OH reaction with phenolic compounds 249

Chapter 1: Introduction

1.1 Introduction of Dissertation

Aerosol chemical characterization in environmental chamber studies and atmospheric studies is crucial to our understanding of the ambient environment. Aerosol particles affect global climate (Kanakidou, Seinfeld et al. 2005; IPCC 2007), public health (Davidson, Phalen et al. 2005; Pope and Dockery 2006), visibility (Eldering and Cass 1996), and therefore public policy (EPA 1997). In engineering effective atmospheric environmental solutions, it is important to have a fundamental understanding of the chemical nature of aerosol particles. Currently, the most powerful aerosol chemical characterization techniques are mass spectral techniques. Of these new mass spectral techniques, in-situ aerosol mass spectrometry using a focused particle beam with electron impact ionization (Jimenez, Canagaratna et al. 2009) and filter sampling followed by ex-situ liquid chromatography coupled to a atmospheric pressure ionization mass spectrometer (Surratt, Chan et al. 2010) have emerged as two of the most popular of these mass spectral methods.

Although these two mass spectral tools have served well to chemically characterize aerosol particles, they have two significant downfalls. In the case of in-situ aerosol mass spectrometry using a focused particle beam with electron impact ionization, like the Aerodyne aerosol mass spectrometer (AMS), particle species are provided as complex ion fragments that make for difficult data analysis requiring convoluted software tools. In the case of filter sampling followed by ex-situ liquid chromatography coupled

to an atmospheric pressure ionization mass spectrometer, data analysis is simpler, but only chemical speciation of a discrete final state is available, giving little insight into particle-phase reaction intermediates in chamber studies or transient species in the ambient.

Given these drawbacks a research question was born: “can a new mass spectral technique be developed that observes un-fragmented ions, provides near real-time data, and has an acceptable sensitivity be developed?” This dissertation successfully tests the hypothesis that a particle-into-liquid sampler (PILS), as introduced by Orsini et al. (Orsini, Ma et al. 2003), can be coupled directly to a mass spectrometer to yield new and valuable chemical characterization data on water-soluble organic aerosol. The evidence for this thesis is laid out in four subsequent body chapters, a conclusion and two appendices.

In Chapter 2, the particle-into-liquid-sampler coupled to an accurate mass time-of-flight mass spectrometer, here after referred to as the PILS-ToF, is introduced, validated, and used to characterize two atmospherically pertinent secondary organic aerosol (SOA) systems, α -pinene dark ozonolysis and isoprene NO photo-oxidation. This study finds that the PILS-ToF system can indeed give real-time aerosol chemical characterization of water soluble aerosol with little to no ion fragmentation. Mass spectral ions are seen in the electrospray or atmospheric chemical ionization methods as the parent ion + or – a proton, depending on the desired mass spectral polarity.

It is of atmospheric importance to study SOA formation from isoprene as it is globally the most abundant non-methane hydrocarbon in the ambient (Guenther, Hewitt et al. 1995). With this in mind, Chapter 3 uses the PILS-ToF, among the suite of instrumental tools available at the UCR CE-CERT Environmental Chambers, to give a comprehensive and intercomparable experimental overview of dry nucleating SOA from isoprene. These environmental chamber studies probe a myriad of oxidation conditions to include: low NO_x and high NO_x photo-oxidation, dark nitrate radical attack, and dark ozonolysis. This study finds that the oxidant system used for isoprene oxidation plays a significant role in the yield, physical properties, and chemical nature of the SOA formed. Furthering the study of the nature of SOA formed from isoprene, Chapter 4 evaluates the effect of reaction temperature on SOA formed from isoprene from the various oxidizing conditions previously mentioned. Chapter 4 finds that temperature plays an interesting role in the nature of SOA from isoprene, depending on the oxidant, as aerosol species volatility processes compete with species reaction rates.

Chapter 5 looks at PILS-ToF results from trimethylamine and tributylamine, two atmospherically relevant tertiary amines emitted from industrial and animal husbandry processes (Ge, Wexler et al. 2011). The PILS-ToF lends support to two new mechanisms, proposed by the unpublished work by the unpublished work of Price et al. (Price, Tang et al., in prep., 2012) for SOA formation from trimethylamine and tributylamine. SOA formation from trimethylamine and tributylamine was studied by PILS ToF for low- NO_x photo-oxidation (where H_2O_2 alone was added to the chamber), high- NO_x photo-oxidation (where NO and H_2O_2 were added to the chamber), and dark

nitrate radical reaction (where N_2O_5 was added to the chamber) of both trimethylamine and tributylamine. The PILS-ToF indicates that for trimethylamine, the reaction can proceed through an oligomerization of a repeating subunit monomer. For SOA formation from tributylamine, the most common pathway for SOA formation is sequential oxidation of the butyl carbon chains.

Mass spectral data from filter sampling of SOA from isoprene was used in the manuscript provided in Appendix A to validate the PILS-ToF system (Sato, Nakao et al. 2011). Furthermore, the manuscript in Appendix B uses the PILS-ToF to lend mechanistic insight into SOA formation from phenols, as phenols are an important reaction intermediate in SOA formation from aromatic hydrocarbons (Nakao, Clark et al. 2011). Overall, this dissertation introduces, characterizes and utilizes the PILS-ToF system to provide new chemical insight to SOA formed in the UCR CE-CERT environmental chambers.

1.2 Introduction Reference

- Davidson, C. I., R. F. Phalen, et al. (2005). "Airborne Particulate Matter and Human Health: A Review." *Aerosol Science and Technology* 39(8): 737-749.
- Eldering, A. and G. R. Cass (1996). "Source-oriented model for air pollutant effects on visibility." *Journal of Geophysical Research* 101(D13): 19343-19369.
- EPA, U. S. (1997). 1997 Clean Air Rules for Ozone and Particulate Matter. U. S. E. P. Agency.
- Ge, X., A. S. Wexler, et al. (2011). "Atmospheric amines - Part I. A review." *Atmos. Environ.* 45(3): 524-546.
- Guenther, A., C. N. Hewitt, et al. (1995). "A global model of natural volatile organic compound emissions." *Journal of Geophysical Research* 100: 8873-8892.

- IPCC (2007). Intergovernmental Panel on Climate Change: Climate Change 2007: The Physical Science Basis, IPCC.
- Jimenez, J. L., M. R. Canagaratna, et al. (2009). "Evolution of Organic Aerosols in the Atmosphere." *Science* (Washington, DC, U. S.) 326(5959): 1525-1529.
- Kanakidou, M., J. H. Seinfeld, et al. (2005). "Organic aerosol and global climate modelling: a review." *Atmos. Chem. Phys.* 5(4): 1053-1123.
- Nakao, S., C. Clark, et al. (2011). "Secondary organic aerosol formation from phenolic compounds in the absence of NO_x." *Atmos. Chem. Phys.* 11(20): 10649-10660.
- Orsini, D. A., Y. Ma, et al. (2003). "Refinements to the particle-into-liquid sampler (PILS) for ground and airborne measurements of water soluble aerosol composition." *Atmospheric Environment* 37: 1243-1259.
- Pope, C. A. and D. W. Dockery (2006). "Health Effects of Fine Particulate Air Pollution: Lines that Connect." *Journal of the Air & Waste Management Association* 56(6): 709-742.
- Price, D., X. Tang, et al. (2012). "Mechanism of SOA formation from Amines." In *Preparation*.
- Sato, K., S. Nakao, et al. (2011). "Secondary organic aerosol formation from the photooxidation of isoprene, 1,3-butadiene, and 2,3-dimethyl-1,3-butadiene under high NO_x conditions." *Atmos. Chem. Phys.* 11(14): 7301-7317.
- Surratt, J. D., A. W. H. Chan, et al. (2010). "Reactive intermediates revealed in secondary organic aerosol formation from isoprene." *Proceedings of the National Academy of Sciences*.

Chapter 2: Real-time study of particle phase products from dark ozonolysis of α -pinene and photo oxidation of isoprene using particle into liquid sampling directly coupled to a time of flight mass spectrometer (PILS-ToF)

2.1 Introduction

Chemical characterization of secondary organic aerosols (SOA) formed in environmental chambers is required for complete understanding of SOA reaction mechanisms. Towards this end, work on sampling and instrumentation for the mass spectral chemical characterization of aerosols has been prolific in recent years yielding aerosol mass spectral techniques that have varying aerosol sampling and sample ionization methods (Eygluénent, Le Person et al. 2008; Cross, Onasch et al. 2009; Faulhaber, Thomas et al. 2009). Never the less, two mass spectral based methods appear to dominate the field of aerosol chemical characterization, in-situ aerosol mass spectrometry using a focused particle beam with electron impact ionization (Jimenez, Canagaratna et al. 2009) and filter sampling followed by ex-situ liquid chromatography coupled to a atmospheric pressure ionization mass spectrometer (Surratt, Chan et al. 2010). Although these mass spectral tools have served well toward the chemical characterization of SOA they have significant drawbacks. In the case of in-situ aerosol mass spectrometry using a focused particle beam with electron impact ionization, particle species are provided as complex ion fragments that make for difficult data analysis requiring complex software tools. In the case of filter sampling followed by ex-situ liquid chromatography coupled to an atmospheric pressure ionization mass spectrometer,

data analysis is simpler but only chemical speciation of a discrete final state is practical, giving little insight into particle-phase reaction intermediates.

Here, a new mass spectral technique is proposed that directly couples the particle-into-liquid sampler (PILS), as developed and refined by Orsini et al. (Orsini, Ma et al. 2003), to the atmospheric ionization inlet of an accurate mass time-of-flight mass spectrometer, this system is termed here the PILS-ToF. The goal of the PILS-ToF, as introduced here, is to chemically speciate the particle phase products from the formation of SOA in the University of California, Riverside, College of Engineering, Center for Environmental Research and Technology (CE-CERT) atmospheric chambers using “soft” ionization that leads to fewer ion fragments in real reaction time. The ability to chemically speciate SOA generated in real-time allows the promise of observing particle-phase intermediates in real-time.

To date, the PILS has been directly coupled either to ion chromatographs (IC) or total organic carbon (TOC) analyzers (Orsini, Ma et al. 2003; Peltier, Weber et al. 2007). Offline PILS-ToF measurements were published by Bateman et al (Bateman, Nizkorodov et al. 2010). However, we report here the direct injection of a PILS sample into the ionization source of the mass spectrometer which allows for real-time chemical speciation of aerosol particles. This method is particularly effective for characterizing the chemical mechanisms of particle formation as intermediates can be observed.

Here the PILS-ToF system is validated against other particle measurement methods, both chemical and physical. The PILS-ToF is further applied to the

characterization of particle phase reactions occurring during the dark ozonolysis of α -pinene and the photo-oxidation of isoprene and NO, as performed in the CE-CERT atmospheric chambers. These two hydrocarbon oxidant systems were chosen for study as they are reported to form particle phase oligomers and are atmospherically relevant (Hall and Johnston 2010; Surratt, Chan et al. 2010).

2.2 Materials and Methods

2.2.1 PILS-ToF

The PILS head was manufactured by Brechtel Manufacturing, Inc. and is described in detail by Orsini et al. and is only briefly outlined here (Orsini, Ma et al. 2003). The PILS collects particles from the chamber through a 1/2" sample line, to reduce pressure drop in sample collection, into a Venturi. The Venturi expands from 1/2" at its inlet to 2" at its outlet. Steam is injected at the entrance of the Venturi through a 1/16" stainless steel tube located in the annular region of the Venturi. It should be noted that the steam is produced from in-house purified HPLC grade water with a measured resistivity of greater than 18.2 M Ω and less than 5 ppb total organic carbon. The steam condenses around the aerosol particles in the 2" inner diameter by 5" long finned tube. The water soluble organic material dissolves, or is encapsulated, and the entrained droplets are focused by a second Venturi onto a quartz impaction plate. At the quartz impaction plate, a wash flow of HPLC water flushes the impacted liquid droplets to the high pressure liquid chromatography (HPLC) pump responsible for injecting the sample into the ionization source of the Agilent Accurate Mass 6210 ToF. A flow diagram of

the as-built PILS-ToF is shown in Figure 2.1 with corresponding stream flows provided in Table 2.1.

The ToF has installed a multimode ionization source, allowing for positive and negative atmospheric pressure chemical ionization or electrospray ionization. The Mass spectrometer is tuned weekly and calibrated daily and has an average mass accuracy of +/- 0.001 M/Z units (10 ppm).

2.2.2 chamber experiments

Experiments were conducted in UCR/CE-CERT chambers, described in detail elsewhere (Carter, Cocker et al. 2005). Briefly, the large chamber facility consists of two 90m³ FEP Teflon[®] film reactors located in a temperature controlled room, which is continuously flushed with purified air. The reactors are attached to a rigid collapsible frame to minimize diffusion of contaminants into the reactors by maintaining a positive differential pressure with respect to the chambers surroundings. The chamber has four banks of black lights (272 lights in total). Each light source emits a sufficiently high 360 nm wavelength photon flux to drive NO₂ at a photolysis rate of $k_1=0.51 \text{ min}^{-1}$.

Connected to the large chambers are two in house built scanning mobility particle sizers (SMPS), similar to those described by Cocker et al. (Cocker, Flagan et al. 2001), along with the PILS-ToF described above. Hydrocarbon concentration is tracked by gas valve sampling gas chromatography (GC) using an Agilent 6890N GC equipped with a flame ionization detector (FID). NO and NO_x concentration is measured during reaction by Thermo Environmental Instruments Inc. model 42C trace level NO-NO₂-NO_y analyzer.

O₃ concentration is measured by a Dasibi Environmental Corporation model 1003-AH. CO concentration was measured by a Thermo Environmental Instruments Inc. model 48C trace level CO analyzer. All quantitative gas-phase instrumentation is calibrated to a gas standard prior to each chamber experiment.

Liquid hydrocarbon is introduced to the chamber by placing a known aliquot of hydrocarbon injected into a glass bulb, where a flowing particle-free purified air stream evaporates the hydrocarbon into the chamber. CO injections into the chamber are performed by flowing gas from a UHP CO cylinder at a specific flowrate over a set amount of time. O₃ is injected by flowing particle-free purified air through a laboratory built O₃ generator. NO injection is done using UHP NO, a vacuum rack, and known volume glass bulb. All experiments reported here are performed dry, RH<1%, with no aerosol seed.

2.3 Results and Discussions

PILS-ToF measurements were taken on two reaction systems, the dark ozonolysis of α -pinene and the NO photo-oxidation of isoprene. During SOA formation and aging, both these reaction systems have been reported to form 2nd-generation and higher large molecular weight oligomer products. These oligomers are an optimum test bed for the PILS-ToF system in evaluation of its real-time aerosol chemical characterization capabilities. It has been confirmed by others that these oligomer products are not products of the ionization source, but are indeed formed during the SOA chamber reactions (Camredon, Hamilton et al. 2010; Gao, Hall et al. 2010; Sato, Nakao et al.

2011); the data presented here supports these findings. Table 2.2 gives the experimental parameters for all SOA chamber experiments reported here.

As part of the PILS-ToF characterization, PILS-ToF chamber background characterization experiments were performed. These experiments included: pure-air only runs (with and without black lights), photo-oxidation of 250 ppb NO, photo-oxidation 250 ppb of NO₂, and photo-oxidation of 3 ppm H₂O₂. Background experiments were performed in the absence of any measureable hydrocarbon concentration, as measured by GC-FID. Results from the PILS-ToF during these background experiments showed no significant signal change in the total ion counts throughout these experiments. This absence of a PILS-ToF background signal correlated with no significant particle formation observed by the SMPS during these chamber experimental runs.

2.3.1 α -pinene ozonolysis

α -Pinene dark ozonolysis was conducted under the procedures outlined above. The initial concentration of CO, ozone, and α -pinene, whose PILS-ToF spectra is analyzed in detail here (corresponding to experiment ID in Table 2.2 of EPA1311A), were 30 ppm, 125 ppb, and 150 ppb respectively. PILS-ToF mass spectra taken during SOA formation from α -pinene ozonolysis used positive mode ESI with data recorded from M/Z 60 to 1000.

The SMPS and PILS-ToF total ion count (TIC) traces for SOA formation during EPA1311 are presented in Figure 2.2a. Figure 2.2a shows that particle formation as

observed by the PILS-ToF, is proportional in the α -pinene system to the particle formation measured by the SMPS. The inset to Figure 2.2a shows a plot of the change in ion-counts measured by the PILS-ToF during particle formation plotted against maximum particle mass concentration observed by SMPS for a set of α -pinene experiments corresponding to run ID experiments MEZ102309, MEZ102709, and MEZ110509. This set of experiments which varied the initial α -pinene concentration, thereby varying maximum particle mass concentration, ranged in maximum particle mass concentration from 50-993 $\mu\text{g}/\text{m}^3$. PILS-ToF signal is highly linear when plotted against the maximum the SMPS measured particle mass concentration, giving an observed correlation coefficient R^2 of 0.9995 with a positive bias. It should be noted that the PILS-ToF data reported in the inset to Figure 2.2a, MEZ102309, MEZ102709, and MEZ110509, all used the APCI ionization source in the ToF.

Figure 2.2b expands the PILS-ToF TIC signal into a contour plot where reaction time is on the x-axis, mass-to-charge is on the y-axis, and ion count intensity is plotted using a color gradient. Each mass spectral scan presented on the contour plot in Figure 2.2b is a summation of 5 minutes of mass spectra. In addition to 5 minute spectral averaging, each average mass spectral trace in the contour plot is reduced to unit mass resolution. This two step data reduction method allows for computational efficiency in rendering the contour plot while losing little information in a contour plot presentation.

The PILS-ToF signal in Figure 2.2b shows that a clear and coherent mass spectral pattern emerges at 10 min. into the reaction of α -pinene and ozone as particle nucleation

occurs. The PILS-ToF mass spectrum at 50 minutes provided in Figure 2.3b, a time corresponding to the completion of particle nucleation, can broadly be broken into two mass spectral regimes at M/Z 250.

Those masses below M/Z 250 broadly correspond to the compounds observed by Yu et al. (Yu, Cocker et al. 1999). This mass spectral regime below m/z 250 is dominated by positive ions 139.1224, 141.1136, 155.1331, 157.1293, 169.1484, 171.1294, 173.1104, 185.1466, 199.1278, and 201.1645 corresponding to the parent particle phase compounds norpinone, 2,2-dimethyl-cyclobutyl-1,3-dicarboxaldehyde, norpinonaldehyde, 2,2-dimethyl-3-formyl-cyclobutyl-methanoic acid, pinaldehyde, norpinonic acid isomers, norpinic acid, pinonic acid, C₁₀H₁₄O₃ (which has an unknown structure), and 10-hydroxyl pinonic acid. These ions alone, without their secondary fragments, contribute 44% to the PILS-ToF TIC and are widely reported in the literature. It is hypothesized that 80% of the total PILS-ToF ion counts observed after nucleation can be attributed to the 10 ions corresponding to the 10 molecules listed directly above.

Although it appears that carboxylic acids and aldehydes with pinene-based backbones dominate the mass spectra, there are significant peaks observed with m/z above 300. These high m/z features have been broadly attributed to oligomers (Gao, Keywood et al. 2004; Camredon, Hamilton et al. 2010; Gao, Hall et al. 2010). When looking at Figure 2.2b, the onset of nucleation is observed immediately, corresponding to the initial introduction of ozone. Small oligomer formation seems to occur concurrently

with particle nucleation. The predominant ion observed by the PILS-ToF throughout SOA formation is at m/z 391.3839 (Figure 2.3b and 2.3c).

Camredon et al. (Camredon, Hamilton et al. 2010) assign m/z 391 as a sodium ion adduct of a molecule with molecular weight of 368.4212 AMU. Gao et al. (Gao, Hall et al. 2010) assigns a negative ion of molecular weight M/Z 389.1655, which would have an equivalent positive ion at m/z 391.1655, to $C_{18}H_{30}O_9$. Camredon et al. (Camredon, Hamilton et al. 2010) further support their assignment through use of an MCM v.3.1 model result showing a molecule of molecular weight 368.4212, and molecular formula $C_{19}H_{28}O_7$, as a probable product of the ester formation reaction of pinic acid ($M=186.2060$ AMU) and 10-hydroxy-pinonic acid ($M=200.2327$ AMU) in which a water molecule is lost. The ion mass defect of m/z 391.3839, observed here by the PILS-ToF, supports the findings of Camredon et al. (Camredon, Hamilton et al. 2010).

A molecule of the positive ion at m/z 369.2837 is also observed, at low intensity. The mass difference between this dimer molecule observed here and that of the molecule observed and modeled by Camredon et al. (Camredon, Hamilton et al. 2010) is 0.0271 AMU. Although this mass difference is outside the accuracy of 0.001 of the calibrated mass spectrometer used here, it is an order of magnitude less than the difference between the observation reported here and the work of Gao et al. of 0.2184 (Gao, Hall et al. 2010). The observation here supports the work of Camredon et al. in their dimer assignment, who assign and model this single dimer species of molecular weight 368 (Camredon, Hamilton et al. 2010).

When examining Figure 2.2b further, it is seen that particle products at an m/z above 550 are seen to form. These high mass species begin appearing 20 minutes after the initial addition of ozone. PILS-ToF spectra from SOA formed in α -pinene dark ozonolysis supports the findings in the literature while validating the applicability and performance of the PILS-ToF in the characterization of water-soluble SOA products.

2.3.2 isoprene NO photo-oxidation

Isoprene NO photo oxidation was performed in the presence of H_2O_2 in the UCR/CE-CERT chamber by the procedure outlined in the materials and methods section above. The initial concentration of NO, H_2O_2 , and isoprene, used in the isoprene photo oxidation experiment reported here (corresponding to experiment EPA1353A in Table 2.2) were 500 ppb, 3 ppm, and 250 ppb respectively. PILS-ToF spectra taken during SOA formation from isoprene photo oxidation used negative mode ESI with data recorded from m/z 60 to 1000. Negative mode ESI was chosen to allow for comparison to offline liquid mass spectral data collected by Surratt et al. and Sato et al. (Surratt, Murphy et al. 2006; Sato 2008).

The SMPS and PILS-ToF TIC traces for SOA formation during EPA1353 are presented in Figure 2.4a. Figure 2.4c expands the PILS-ToF TIC signal into a contour plot where reaction time is on the x-axis, mass-to-charge is on the y-axis, and ion count intensity is plotted using a color gradient. The data is processed as described above for the contour plot of α -pinene ozonolysis. Figure 2.5a-f gives detailed PILS-ToF mass spectra at chosen discrete times during the isoprene photo oxidation reaction.

In examining Figure 2.4a, the PILS-ToF TIC trace can be seen to directly correlate to chamber particle formation as observed by the SMPS. This correlation is consistent with the observations for the dark ozonolysis of α -pinene above. The corresponding contour plot in Figure 2.4b contrasts the contour plot shown for α -pinene in Figure 2.2b in that large molecular weight compounds, those above m/z 500, are observed to form over time. High molecular weight products are observed to grow in between 50 and 125 minutes after lights are turned on. The observed mass spectra change very little after 125 minutes, indicating little chemical ageing of the chamber SOA.

Figure 2.5a shows the PILS-ToF background spectra, taken prior to the beginning of photolysis. The spectra in Figure 2.5a is subtracted from all subsequent spectra. Figure 2.5b-d give intermediate spectra taken directly prior, during, and directly after SOA particle nucleation at 35 min., 60 min. and 75 min. into the reaction respectively. The spectra in Figure 2.5e is taken at 100 min., during particle mass growth, and Figure 2.5f is taken at 300 min., the final reaction state PILS-ToF spectra.

In Figure 2.5a, five ions account for greater than 50% of the background spectra. These ions are m/z : 112.9861, 213.1139, 226.9793, 231.1243, and 257.1767. Mass-to-charge 112.9861, the largest intensity peak in the background spectra accounting for 33% of the background spectra and 226.9793 can be attributed to sodium trifluoroacetate, used to tune the ToF prior to PILS-ToF data collection (Moini, Jones et al. 1998). The other

background ions, m/z 213.1139, 231.1243, and 257.1986, can be attributed to hydrocarbon contaminants from a rubber liquid chromatography sample septa.

A close examination of the PILS-ToF TIC trace (Figure 2.4b) reveals a peak of transient ions begins forming at 25 min. into the reaction, which has significantly less intensity by 50 min. into the reaction. Figure 2.5b, the PILS-ToF mass spectra corresponding to reaction time of 35 min., shows the bulk of these transient ions to be between 200 and 300 m/z . The major transient ions present are m/z : 248.8974, 249.8969, 250.8960, 251.8944, 253.8930, and 243.9032 making up 23%, 17%, 10%, 9%, 6%, and 3% of the mass spectrum, respectively. These ions account for 65% of the total mass spectral abundance at 35 minutes into the reaction. These ions could not be identified due to their extraordinary negative mass defect.

Figure 2.5f shows that by the end of the reaction, these transient ions are barely visible in the overall mass spectrum, accounting for less than 1% of the total mass spectrum. Figure 2.5f shows a major oligomerization mass spectral pattern consistent with the formation of nitro-oligoesters, as reported by Surratt et al. and Sato et al. (Surratt, Chan et al. 2010; Sato, Nakao et al. 2011). The dimer nitro-oligoester $C_8H_{13}NO_9$ has a calculated molecular weight of 267.0590, the expected ion weight [M-H] of 266.0512, and an observed ion m/z of 266.0756. The trimer is observed at m/z 368.1165 a difference or 102 AMU. Each further oligomer is observed at the interval of 102 AMU, corresponding to the addition of the monomer. The highest nitro-oligoester observed is the nine-unit oligomer observed above the background is at an m/z 980.3448.

In addition to the nitro-oligoester, many other oligoesters were observed during the NO photooxidation of isoprene. Some of these oligoesters seen in Figure 2.5f have been observed previously, but some others are previously unreported, but given a molecular formula assignment here. Table 2.4 gives the PILS-ToF molecular formula assignments for all mass spectral peaks of the peaks with intensity 1000 ion-counts or greater observed in Figure 2.5f, the final state mass spectra for experiment EPA1353A, and these ions corresponding mass defect. These assigned ions account for 78% of the total ion counts observed in Figure 2.5f.

The final state PILS-ToF mass spectra is further presented and analyzed by use of the Van Krevelen Method which yields a Van Krevelen Diagram (Van Krevelen 1950), shown in Figure 2.6a,b. The Van Krevelen plot is made by simply calculating the H:C and O:C ratios for mass spectral molecular matches of peaks observed in the final state mass spectra shown in Figure 2.5f, whose ion matches are given in detail in Table 2.4. In Figure 2.6a, the molecular formulas are broken up into two categories, those previously observed in the literature and those matched in this work. The molecules previously observed account for only 14% of the total ion counts shown in Figure 2.5f, while the molecules matched in this work make up the remaining 64% of the total ion counts. All PILS-ToF mass spectral ions that have been previously reported in the by Surratt et al. or Sato et al. appear on one of three lines of Figure 2.6a, where these lines are captioned a, b, and c (Surratt, Murphy et al. 2006; Sato 2008).

Figure 2.6b shows six new lines indicating six additional particle phase chemical mechanisms, labeled lines d, e, f, g, h, and i. Those chemical mechanistic lines shown in Figure 2.6b make up 57% of the observed final state PILS-ToF mass spectra shown in Figure 2.5f. Table 2.4 references those ions observed here and observed previously with notations correlating the peak match to the corresponding line on the Van Krevelen plots. The lines in Figure 2.6a and 2.6b are highly correlated, with R^2 correlation coefficients equal to or approaching 1. The linear regressed formulas and correlation coefficients of lines a-i in Figure 2.6a and 2.6b are provided in Table 2.3.

Line a of Figure 2.6a contains oligoesters and nitro oligoesters observed by both Surratt et al. and Sato et al. (Surratt, Chan et al. 2010; Sato, Nakao et al. 2011). The oligoesters on line a begin with the monomer $C_5H_8O_5$ and the monomer unit $[-C_4H_6O_3-]$ up to $C_{29}H_{43}O_{23}$. Line a also contains all the most intense nitro-oligoesters with repeating subunit 102 AMU seen clearly in Figure 2.5f observed by both Surratt et al. and Sato et al. (Surratt, Chan et al. 2010; Sato, Nakao et al. 2011). Line b corresponds to those oligomers having two nitro-ester groups where these molecules are introduced by Sato et al. (Sato, Nakao et al. 2011). Molecules on Line c are also all oligoesters, but begin with monomer $C_4H_8O_4$. It should be noted that common analysis of a Van Krevelen Diagram would assign Line a of Figure 2.6a to oxidation or reduction reactions and Lines b and c of Figure 2.6a to hydration or condensation reactions (Van Krevelen 1950; Kim, Kramer et al. 2003).

In Figure 2.6b, most molecules falling on line d can be attributed to oligoesters with an initial building block of m/z 267.0596 corresponding to an assigned molecular match of $C_{12}H_{12}O_7$. Four additional oligoesters lie on line d each with a 102 AMU spacing, like the oligoesters reported by Surratt et al., the observed m/z for these PILS-ToF mass spectral peaks are 369.0887, 471.1178, 573.1476, and 673.1766. These four observed PILS-ToF mass spectral peaks match the molecular formulas of $C_{16}H_{18}O_{10}$, $C_{20}H_{24}O_{13}$, $C_{24}H_{30}O_{16}$, and $C_{28}H_{36}O_{19}$ respectively. In addition to the 5 oligoesters, separated by a repeating subunit of m/z 102, there is an additional mass spectral molecular match lying on line e having an observed m/z of 407.1186 which is matched to a molecular formula of $C_{16}H_{24}O_{12}$. The ion counts on line d account for only 1% of the total ion counts observed in Figure 2.5f.

Line e of Figure 2.6b again corresponds to a series of oligoesters separated by both a repeating subunit of m/z 102 and 58. The molecular matches on line e of Figure 2.6b having a separation of m/z 102 are 189.0441, 291.0765, 393.1063, 495.1360, and 597.1638 having molecular matches of $C_7H_{10}O_6$, $C_{11}H_{16}O_9$, $C_{15}H_{22}O_{12}$, $C_{19}H_{28}O_{16}$, and $C_{23}H_{34}O_{18}$ respectively. Each of these oligoesters on line f separated by m/z 102, starting at m/z 291.0765, has an intermediate oligoester offset by 58 AMU. These offset esters are found at m/z 349.0812, 451.1133, and 553.1430, corresponding to molecular matches of $C_{13}H_{18}O_{11}$, $C_{17}H_{24}O_{14}$, and $C_{21}H_{30}O_{17}$ respectively. Two other PILS-ToF molecular matches fall on line e having m/z 304.0260 and 335.0973, these have been assigned molecular matches of $C_{10}H_{11}NO_{10}$ and $C_{13}H_{20}O_{10}$ respectively. The molecular matches on line e account for 2% of the PILS-ToF ions observed in Figure 2.5f.

Line f of Figure 2.6b shows two apparent series of oligoesters separated by m/z 102. The first set of ion molecular matches separated by m/z 102 are: 307.0718, 409.1024, 511.1320, and 613.1606; who have molecular matches of: $C_{11}H_{16}O_{10}$, $C_{15}H_{22}O_{13}$, $C_{19}H_{28}O_{16}$, and $C_{23}H_{33}O_{19}$ respectively. The second set of molecular matches lying on line f of Figure 2.6b separated by m/z 102 are: 321.0861, 423.1150, 525.1438, and 627.1725; whose molecular matches are: $C_{12}H_{18}O_{10}$, $C_{16}H_{24}O_{13}$, $C_{20}H_{30}O_{16}$, and $C_{24}H_{36}O_{20}$ respectively. The molecular match for m/z 146.9714 of $C_4H_3O_6$ also lies on line f of Figure 2.6b with no clear correlation to an oligomeric series. The ion molecular matches on line f of Figure 2.6b account for 2% of the PILS-ToF total ion counts observed in Figure 2.5f.

Observed ions that have been matched to lie on line g of Figure 2.6b make up 50% of the total ion counts observed in Figure 2.5f. One ion alone, at m/z 123.9869, makes up 49% of the total ion counts observed. The ion m/z 123.9891 is matched to the molecule $C_5H_2O_4$. The other two ions on Figure 2.6b line g, m/z 126.9938 and 129.0243, match to molecules $C_5H_4O_4$ and $C_5H_6O_4$ respectively. These ions on Figure 2.6b line g appear to be simply highly oxygenated forms of the five carbon backbone of isoprene.

On Figure 2.6b line h a series of apparent nitro-oligoesters is observed. These nitro-oligoesters are again separated by m/z 102, indicative of the addition the monomer observed at m/z 119.0391 matched to $C_4H_8O_4$ as proposed by Surratt et al. (Surratt, Chan et al. 2010). The nitro-oligoesters lying on line h of Figure 2.6b are m/z 366.1338,

468.1635, and 570.2258 which match to the molecules $C_9H_{21}NO_{14}$, $C_{13}H_{27}NO_{17}$, and $C_{17}H_{33}NO_{20}$. In addition to the three nitro-oligoesters, two ions that have no apparent reaction series at 539.2003 and 569.2179 are observed; matched to the molecules $C_{17}H_{32}O_{19}$ and $C_{22}H_{24}O_{17}$ respectively. The ions observed to fall on line h of Figure 2.6b make up 1% of the total ion counts of Figure 2.5f.

In looking at the molecular matches of the ions on line i of Figure 2.6b, four of six ions match to a 17 carbon backbone. These ions are m/z 435.1182, 469.1214, 500.1232, and 531.1283, matched to the molecules $C_{17}H_{24}O_{13}$, $C_{17}H_{26}O_{15}$, $C_{17}H_{27}NO_{16}$, and $C_{17}H_{28}N_2O_{17}$ respectively. The two ions that are not matched to a molecule with 17 carbons are 583.1538 and 614.1557, matched to the molecules with 22 carbons, $C_{22}H_{32}O_{18}$ and $C_{22}H_{33}NO_{19}$ respectively. The ions shown to lie on line i of Figure 2.6b account for 1% of the total ion counts in Figure 2.5f.

2.4 Conclusions

A new time-resolved mass spectral method is presented here by coupling the PILS to a “soft” ionization ToF-MS. Data presented here uses reactions of two different hydrocarbon systems known to form SOA in chamber studies to validate the PILS-ToF. The PILS-ToF total ion counts are validated to the physical measurement of aerosol mass by SMPS, where the correlation is shown to be linear with an offset. The PILS-ToF is then validated chemically by comparing the chemical characterization results to those previously reported for dark α -pinene ozonolysis and the photooxidation of isoprene and NO using other mass spectral methods. Additionally, for NO photo-oxidation of

isoprene, the PILS-ToF elucidated five new potential oligomeric paths while showing that a single ion matching a highly oxygenated five carbon structure, the same number of carbons of isoprene, accounted for 49% of the total ion counts observed by the PILS-ToF.

As for the PILS-ToF chemical characterization capabilities, it is shown here that the PILS-ToF agrees with previously reported filter sampling results “soft-ionization” mass spectral results for both reaction systems.

The PILS-ToF shows utility due to its time-resolution and ionization method, electrospray or chemical ionization opposed to electron impact ionization used by most aerosol mass spectrometers. The time resolution allows for aerosol transients or intermediates to be observed. While the “soft” ionization makes molecular identification much easier as complex software packages are not necessary for data analysis, as is the case for high-resolution AMS data.

2.4 Reference

- Bateman, A. P., S. A. Nizkorodov, et al. (2010). "High-Resolution Electro-spray Ionization Mass Spectrometry Analysis of Water-Soluble Organic Aerosols Collected with a Particle into Liquid Sampler." Analytical Chemistry **82**(19): 8010-8016.
- Camredon, M., J. F. Hamilton, et al. (2010). "Distribution of gaseous and particulate organic composition during dark α -pinene ozonolysis." Atmos. Chem. Phys. **10**(6): 2893-2917.
- Carter, W. P. L., D. R. I. Cocker, et al. (2005). "A new environmental chamber for the evaluation of gas-phase chemical mechanisms and secondary aerosol formation." Atmospheric Environment **39**: 7768-7788.
- Chhabra, P. S., R. C. Flagan, et al. (2010). "Elemental analysis of chamber organic aerosol using an aerodyne high-resolution aerosol mass spectrometer." Atmos. Chem. Phys. **10**(9): 4111-4131.
- Cocker, D. R., R. C. Flagan, et al. (2001). "State-of-the-Art Chamber Facility for Studying Atmospheric Chemistry." Environmental Science and Technology **35**: 2594-2601.
- Cross, E. S., T. B. Onasch, et al. (2009). "Single particle characterization using a light scattering coupled to a time-of-flight aerosol mass spectrometer." Atmospheric Chemistry and Physics **9**: 7769-7793.
- Eygluent, G., A. Le Person, et al. (2008). "Simple and Reversible Transformation of an APCI/MS/MS Into an Aerosol Mass Spectrometer: Development and Characterization of a New Inlet." Aerosol Science and Technology **42**: 182-193.
- Faulhaber, A. E., B. M. Thomas, et al. (2009). "Characterization of a thermodenuder-particle beam mass spectrometer system for the study of organic aerosol volatility and composition." Atmospheric Measurement Techniques **2**: 15-31.
- Gao, S., M. Keywood, et al. (2004). "Low-Molecular-Weight and Oligomeric Components in Secondary Organic Aerosol from the Ozonolysis of Cycloalkenes and α -Pinene." J. Phys. Chem. A **108**(46): 10147-10164.
- Gao, Y., W. A. I. V. Hall, et al. (2010). "Molecular Composition of Monoterpene Secondary Organic Aerosol at Low Mass Loading." Environ. Sci. Technol. **44**(20): 7897-7902.
- Hall, W. A. I. V. and M. V. Johnston (2010). "Oligomer Content of α -Pinene Secondary Organic Aerosol." Aerosol Sci. Technol. **45**(1): 37-45.

- Jimenez, J. L., M. R. Canagaratna, et al. (2009). "Evolution of Organic Aerosols in the Atmosphere." Science (Washington, DC, U. S.) **326**(5959): 1525-1529.
- Kim, S., R. W. Kramer, et al. (2003). "Graphical Method for Analysis of Ultrahigh-Resolution Broadband Mass Spectra of Natural Organic Matter, the Van Krevelen Diagram." Analytical Chemistry **75**(20): 5336-5344.
- Moini, M., B. L. Jones, et al. (1998). "Sodium Trifluoroacetate as a Tune/Calibration Compound for Positive- and Negative-Ion Electrospray Ionization Mass Spectrometry in the Mass Range 100-4000 Da." Journal of American Society of Mass Spectrometry **9**: 977-980.
- Nguyen, T. B., A. P. Bateman, et al. (2010). "High-resolution mass spectrometry analysis of secondary organic aerosol generated by ozonolysis of isoprene." Atmospheric Environment **44**: 1032-1042.
- Orsini, D. A., Y. Ma, et al. (2003). "Refinements to the particle-into-liquid sampler (PILS) for ground and airborne measurements of water soluble aerosol composition." Atmospheric Environment **37**: 1243-1259.
- Peltier, R. E., R. J. Weber, et al. (2007). "Investigating a Liquid-Based Method for Online Organic Carbon Detection in Atmospheric Particles." Aerosol Science and Technology **41**(12): 1117-1127.
- Sato, K. (2008). "Detection of nitrooxypolyols in secondary organic aerosol formed from the photooxidation of conjugated dienes under high-NO_x conditions." Atmospheric Environment **42**: 6851-6861.
- Sato, K., S. Nakao, et al. (2011). "Secondary organic aerosol formation from the photooxidation of isoprene, 1,3-butadiene, and 2,3-dimethyl-1,3-butadiene under high NO_x conditions." Atmos. Chem. Phys. Discussions **11**: 4313-4354.
- Sato, K., S. Nakao, et al. (2011). "Secondary organic aerosol formation from the photooxidation of isoprene, 1,3-butadiene, and 2,3-dimethyl-1,3-butadiene under high NO_x conditions." Atmos. Chem. Phys. **11**(14): 7301-7317.
- Surratt, J. D., A. W. H. Chan, et al. (2010). "Reactive intermediates revealed in secondary organic aerosol formation from isoprene." Proceedings of the National Academy of Sciences.
- Surratt, J. D., S. M. Murphy, et al. (2006). "Chemical Composition of Secondary Organic Aerosol Formed from the Photooxidation of Isoprene." Journal of Physical Chemistry A **110**: 9665-9690.
- Van Krevelen, D. W. (1950). "Graphical-statistical method for the study of structure and reaction processes of coal." Fuel **29**: 269-284.

Yu, J., D. R. Cocker, III, et al. (1999). "Gas-phase ozone oxidation of monoterpenes: gaseous and particulate products." J. Atmos. Chem. **34**(2): 207-258.

2.6 Tables

Table 2.1. PILS instrument flow-rates

Flow Stream Name	Flow-rate (cm³-min⁻¹)	Flow Stream Composition	Note
Boiler Feed Water	1.6	Pure IC/HPLC Grade Water	a
Impactor Flush Water	0.2	Pure IC/HPLC Grade Water	b
Chamber Sample Flow	15000	Chamber Sample Air Flow	c
Liquid Sample Flow	0.1	Air+Aerosol Sample in water	a
Debubbler Waste Flow	0.05 (approximate)	Air+Aerosol Sample in water	d
Cooling Chamber Waste Flow	0.2 (approximate)	Air+Aerosol Sample in water	d
Nozzle Waste Flow	0.2 (approximate)	Air+Aerosol Sample in water	d
Compressor Inlet	15000	Waste Air Flow	c

a-The boiler feed water flow and impactor flush water are controlled by a calibrated HPLC pump.

b-The impactor flush water is fed by peristaltic pump through 0.0XXX in. diameter tubing where the peristaltic pump rotation rate is adjusted to assure the flowrate is 0.2 ccm. This flowrate is calibrated using traceable volumetric.

c-Both the chamber sample flow and the compressor inlet flow are controlled by a critical orifice of diameter 0.0XXX in.

d-The debubbler waste flow, cooling chamber waste flow, and nozzle waste flow rates are all approximate. These flowrates are fixed by the peristaltic pump tubing, peristaltic pump rotational speed (which is fixed to control the impactor flush water flow), and the available material liquid (air is entrained in all these streams).

Table 2.2. Experimental conditions and results

Run	Compound	[HC]0 (ppb)	[NOx]0 (ppb)	[O3]0 (ppb)	SOAa ($\mu\text{g m}^{-3}$)	SOA Yield	Note
MEZ102309	α -pinene	910	0	85	993	0.20	b
MEZ102709	α -pinene	250	0	68	434	0.31	b
MEZ121509	α -pinene	65	0	85	50	0.14	b
EPA1311A	α -pinene	150	0	157	270	0.32	b
EPA1353A	Isoprene	250	530	0	51	0.07	c

^a to calculate SOA mass concentration from SMPS data a density of 1 was assumed

^b α -pinene ozonolysis experiments were done in the presence of 50 ppb or more of CO as a hydroxyl radical scavenger.

^c isoprene photooxidation experiments were conducted with 3 ppm of H₂O₂ present at the start of the reaction.

Table 2.3. Line Parameters for Van Krevelen Lines shown in Figure 2.6

Line Label	Line Equation (Form: $y=mx+b$)	Correlation Coefficient (R^2)
a	$y=0.3349x+1.2520$	0.9771
b	$y=0.5882x+1.0588$	1.0000
c	$y=2.0000x$	1.0000
d	$y=3.0000x-0.7500$	1.0000
e	$y=-1.8143x+2.9148$	0.9864
f	$y=-0.7206x+2.0855$	0.9937
g	$x=0.8$ (*)	1.0000
h	$y=0.9908x+0.7777$	0.9999
i	$y=1.0225x+0.6237$	0.9964

(*) This line deviates from standard line format because it has no slope, it is a vertical line.

Table 2.4. PILS-ToF Ion Formula Matches for those ions in the mass spectrum shown in Figure 2.5f having an intensity greater than 1000 ion counts

PILS-ToF observed m/z	TOF-MS [M-H] ⁺ ion formula match	Formula Match Error (ppm)	PILS-ToF Ion Counts	References
61.9930	NO ₃	75.4	3973.5	This work
117.0243	C ₅ H ₉ O ₃	-268.4	4189.4	(Lin, Zhang et al. 2012)
119.0391	C ₄ H ₇ O ₄	34.8	4166.1318	(Sato, Nakao et al. 2011)
124.9891	C ₅ HO ₄	17.2	573246.63	This work
125.1282	C ₉ H ₁₇	-43.1	23983.197	This work (line g)
125.9869	C ₄ NO ₄	28.7	3164.6431	This work
126.9938	C ₅ H ₃ O ₄	-77.7	6379.8916	This work (line g)
129.0243	C ₅ H ₅ O ₄	38.7	2809.5815	This work (line g)
146.9714	C ₄ H ₃ O ₆	-150.3	2336.1096	This work (line f)
147.0327				(Surratt, Chan et al. 2010; Sato, Nakao et al. 2011)
	C ₅ H ₇ O ₅	19.1	1804.3802	
175.9861	C ₄ H ₂ NO ₇	13.9	6074.6299	This work
189.0441	C ₇ H ₉ O ₆	19.5	1813.6537	This work
221.0692				(Surratt, Chan et al. 2010; Sato, Nakao et al. 2011)
	C ₈ H ₁₃ O ₇	11.3	3062.5574	
229.0362	C ₁₀ H ₁₃ O ₆	3.4	3062.5574	This work
249.0656				(Surratt, Chan et al. 2010; Sato, Nakao et al. 2011)
	C ₉ H ₁₃ O ₈	15.9	6672.0586	
263.0810				(Surratt, Chan et al. 2010; Sato, Nakao et al. 2011)
	C ₁₀ H ₁₅ O ₈	14.3	3052.1594	
266.0556				(Surratt, Chan et al. 2010; Sato, Nakao et al. 2011)
	C ₈ H ₁₂ NO ₉	14.6	20307.428	
267.0596	C ₁₂ H ₁₁ O ₇	-46.9	1809.6169	This work (line d)
271.0110	C ₁₀ H ₇ O ₉	5.3	1113.276	This work
288.0359	C ₁₀ H ₁₀ NO ₉	-0.8	6348.4302	This work
291.0765	C ₁₁ H ₁₅ O ₉	14.9	3665.0342	(Nguyen, Laskin et al. 2011) (line e)
296.0649	C ₉ H ₁₄ NO ₁₀	8.9	993.20178	(Nguyen, Laskin et al. 2011)
304.0260	C ₁₀ H ₁₀ NO ₁₀	-16.4	1164.1528	(Nguyen, Laskin et al. 2011) (line e)
305.0867	C ₁₂ H ₁₇ O ₉	-3.5	1255.4744	(Nguyen, Laskin et al. 2011)
307.0718	C ₁₁ H ₁₅ O ₁₀	15.3	2348.4895	(Nguyen, Laskin et al. 2011) (line f)
312.0603	C ₉ H ₁₄ NO ₁₁	9.9	1342.1595	This work
321.0861	C ₁₂ H ₁₇ O ₁₀	10.5	3065.6428	(Nguyen, Laskin et al. 2011) (line f)
323.0976				(Surratt, Chan et al. 2010; Sato, Nakao et al. 2011)
	C ₁₂ H ₁₉ O ₁₀	-2.3	2321.6223	
327.0699	C ₉ H ₁₅ N ₂ O ₁₁	5.3	1486.2240	(Sato, Nakao et al. 2011)
333.0363	C ₁₃ H ₁₇ O ₁₀	-18.0	1498.5270	(Nguyen, Laskin et al. 2011)
335.0973	C ₁₃ H ₁₉ O ₁₀	-3.1	1433.1843	(Nguyen, Laskin et al. 2011) (line e)
339.0917	C ₁₂ H ₁₉ O ₁₁	-4.7	1072.0513	This work
349.0812	C ₁₃ H ₁₇ O ₁₁	10.2	1855.1962	This work (line e)

351.0956				(Surratt, Chan et al. 2010; Sato, Nakao et al. 2011)
	$C_{13}H_{19}O_{11}$	6.6	12453.768	al. 2011)
352.0969	$C_{12}H_{18}NO_{11}$	0.8	2142.436	This work
354.0724	$C_{11}H_{16}NO_{12}$	13.1	1073.104	This work
363.0960	$C_{14}H_{19}O_{11}$	7.6	1177.0165	This work
365.1100				(Surratt, Chan et al. 2010; Sato, Nakao et al. 2011)
	$C_{14}H_{21}O_{11}$	3.1	8083.0586	al. 2011)
366.1010	$C_{13}H_{20}NO_{11}$	-8.8	1622.9474	This work (line h)
368.0856				(Surratt, Chan et al. 2010; Sato, Nakao et al. 2011)
	$C_{12}H_{18}NO_{12}$	5.8	28608.205	al. 2011)
369.0887	$C_{16}H_{17}O_{10}$	16.2	4099.4414	This work (line d)
379.0950	$C_{13}H_{19}N_2O_{11}$	-11.7	2133.4917	This work
393.1063	$C_{15}H_{21}O_{12}$	6.3	4478.4185	(Nguyen, Laskin et al. 2011) (line e)
395.1062	$C_{11}H_{23}O_{15}$	4.8	1121.3715	This work (line d)
407.1186	$C_{16}H_{23}O_{12}$	-2.3	2208.0444	(Nguyen, Laskin et al. 2011)
409.1024	$C_{15}H_{21}O_{13}$	8.9	2599.853	This work (line f)
410.0975	$C_{14}H_{20}NO_{13}$	8.5	1597.2347	This work
423.1150	$C_{16}H_{23}O_{13}$	1.5	3583.1565	This work (line f)
425.1244				(Surratt, Chan et al. 2010; Sato, Nakao et al. 2011)
	$C_{16}H_{25}O_{13}$	-13.4	1647.2527	al. 2011)
429.1011	$C_{13}H_{21}N_2O_{14}$	3.0	2092.1863	(Sato, Nakao et al. 2011)
435.1182	$C_{17}H_{23}O_{13}$	8.6	1082.682	This work (line i)
437.1253	$C_{12}H_{25}N_2O_{15}$	-1.7	1494.9421	This work
451.1133	$C_{17}H_{23}O_{14}$	8.9	1765.9613	This work (line e)
453.1250				(Surratt, Chan et al. 2010; Sato, Nakao et al. 2011)
	$C_{17}H_{25}O_{14}$	-0.1	9031.8877	al. 2011)
454.1249	$C_{16}H_{24}NO_{14}$	10.2	2093.5659	This work
465.1252	$C_{18}H_{25}O_{14}$	0.4	1328.2941	This work
467.1386				(Surratt, Chan et al. 2010; Sato, Nakao et al. 2011)
	$C_{18}H_{27}O_{14}$	-4.3	5917.6738	al. 2011)
468.1215	$C_{13}H_{26}NO_{17}$	1.9	1989.0509	This work (line h)
469.1214	$C_{17}H_{25}O_{15}$	3.3	1032.0043	This work (line i)
470.1146				(Surratt, Chan et al. 2010; Sato, Nakao et al. 2011)
	$C_{16}H_{24}NO_{15}$	-1.1	20079.799	al. 2011)
471.1178	$C_{20}H_{23}O_{13}$	7.3	3797.5178	This work (line d)
472.1184	$C_{16}H_{26}NO_{15}$	-26.2	1074.5234	This work
481.1252	$C_{18}H_{25}O_{15}$	11.1	1623.6936	This work
483.1321	$C_{13}H_{27}N_2O_{17}$	1.1	1269.5596	This work
495.1360	$C_{19}H_{27}O_{15}$	0.9	3043.7197	This work (line e)
496.1335	$C_{18}H_{26}NO_{15}$	5.5	900.13403	This work
498.1155	$C_{17}H_{24}NO_{16}$	11.0	1002.9243	This work
500.1232	$C_{17}H_{26}NO_{16}$	-4.9	1045.0215	This work (line i)
509.1464	$C_{15}H_{29}N_2O_{17}$	-1.5	1481.605	This work
511.1320	$C_{19}H_{27}O_{16}$	2.9	1953.6626	This work (line f)
512.1274	$C_{18}H_{26}NO_{16}$	3.2	1458.0984	This work
513.1380	$C_{14}H_{29}N_2O_{18}$	-8.0	1090.8251	This work
525.1438	$C_{20}H_{29}O_{16}$	-4.4	2484.6152	This work (line f)
527.1491	$C_{20}H_{31}O_{16}$	-24.0	1153.5293	(Surratt, Chan et al. 2010; Sato, Nakao et

				al. 2011)
531.1283	$C_{17}H_{27}N_2O_{17}$	-6.1	1529.5437	(Sato, Nakao et al. 2011) (line i)
539.1519	$C_{17}H_{31}O_{19}$	10.1	1109.894	This work (line h)
553.1430	$C_{21}H_{29}O_{17}$	3.5	1280.2749	This work (line e)
555.1539				(Surratt, Chan et al. 2010; Sato, Nakao et al. 2011)
	$C_{21}H_{31}O_{17}$	-5.0	4869.6201	al. 2011)
556.1522	$C_{20}H_{30}NO_{17}$	0.5	1516.0847	This work
567.1535	$C_{22}H_{31}O_{17}$	-5.5	1000.7501	This work
569.1668	$C_{22}H_{33}O_{17}$	-9.6	3299.1602	This work (line h)
570.1480	$C_{17}H_{32}NO_{20}$	-7.6	1535.7621	This work (line h)
572.1445				(Surratt, Chan et al. 2010; Sato, Nakao et al. 2011)
	$C_{20}H_{30}NO_{18}$	-4.1	10293.032	al. 2011)
573.1476	$C_{24}H_{29}O_{16}$	2.6	2614.9775	This work (line d)
583.1538	$C_{22}H_{31}O_{18}$	3.8	1026.4572	This work (line i)
597.1638	$C_{23}H_{33}O_{18}$	-5.7	1781.1512	This work (line e)
613.1606	$C_{23}H_{33}O_{19}$	-2.5	1255.4821	This work (line f)
614.1557	$C_{22}H_{32}NO_{19}$	-2.8	1064.4431	This work (line i)
627.1725	$C_{24}H_{35}O_{19}$	-8.4	1445.8064	This work (line f)
657.1823				(Surratt, Chan et al. 2010; Sato, Nakao et al. 2011)
	$C_{25}H_{37}O_{20}$	-9.3	2447.2239	al. 2011)
671.1933				(Surratt, Chan et al. 2010; Sato, Nakao et al. 2011)
	$C_{26}H_{39}O_{20}$	-16.0	1811.7888	al. 2011)
672.1750	$C_{21}H_{38}NO_{23}$	-13.4	1048.937	This work
674.1723				(Surratt, Chan et al. 2010; Sato, Nakao et al. 2011)
	$C_{24}H_{36}NO_{21}$	-9.2	6289.5747	al. 2011)
675.1766	$C_{28}H_{35}O_{19}$	-1.7	1592.2874	This work (line d)
759.2090				(Surratt, Chan et al. 2010; Sato, Nakao et al. 2011)
	$C_{29}H_{43}O_{23}$	-14.6	1229.4728	al. 2011)
776.2022				(Surratt, Chan et al. 2010; Sato, Nakao et al. 2011)
	$C_{28}H_{42}NO_{24}$	-10.4	2426.967	al. 2011)
878.2288				(Surratt, Chan et al. 2010; Sato, Nakao et al. 2011)
	$C_{32}H_{48}NO_{27}$	-14.9	1219.9783	al. 2011)

2.7 Figures

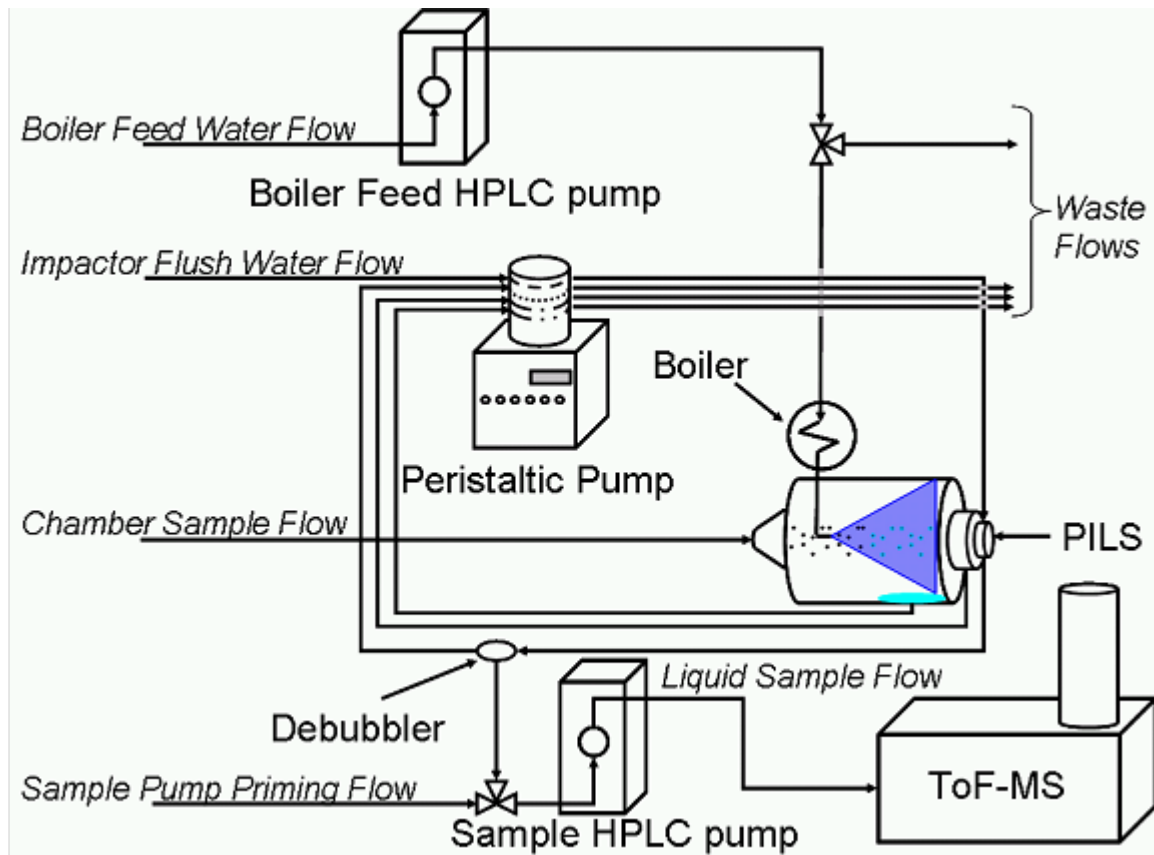


Figure 2.1: Flow diagram of Particle into Liquid Sampling coupled to Time-of-Flight Mass Spectrometry (PILS-ToF)

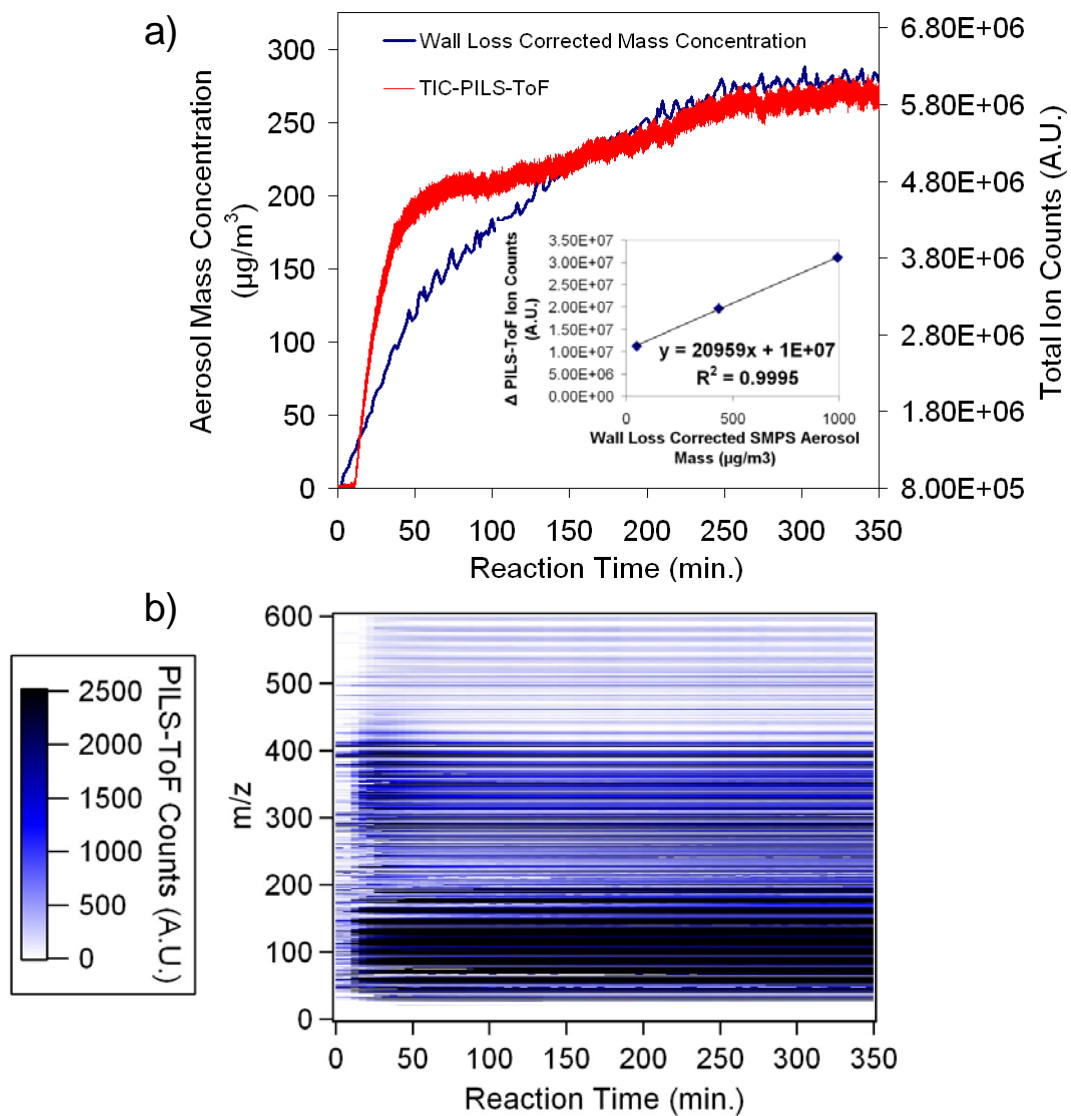


Figure 2.2: a) Plot of the PILS-ToF total measured ion-counts (TIC) and wall-loss corrected aerosol mass formation, as measured by SMPS, during the dark α -pinene ozonolysis, EPA1311A. Inset is the linear correlation of PILS-ToF TIC at maximum to the maximum wall corrected aerosol formation, as measured by SMPS. b) Contour plot of PILS-ToF mass spectrum as a function of reaction time.

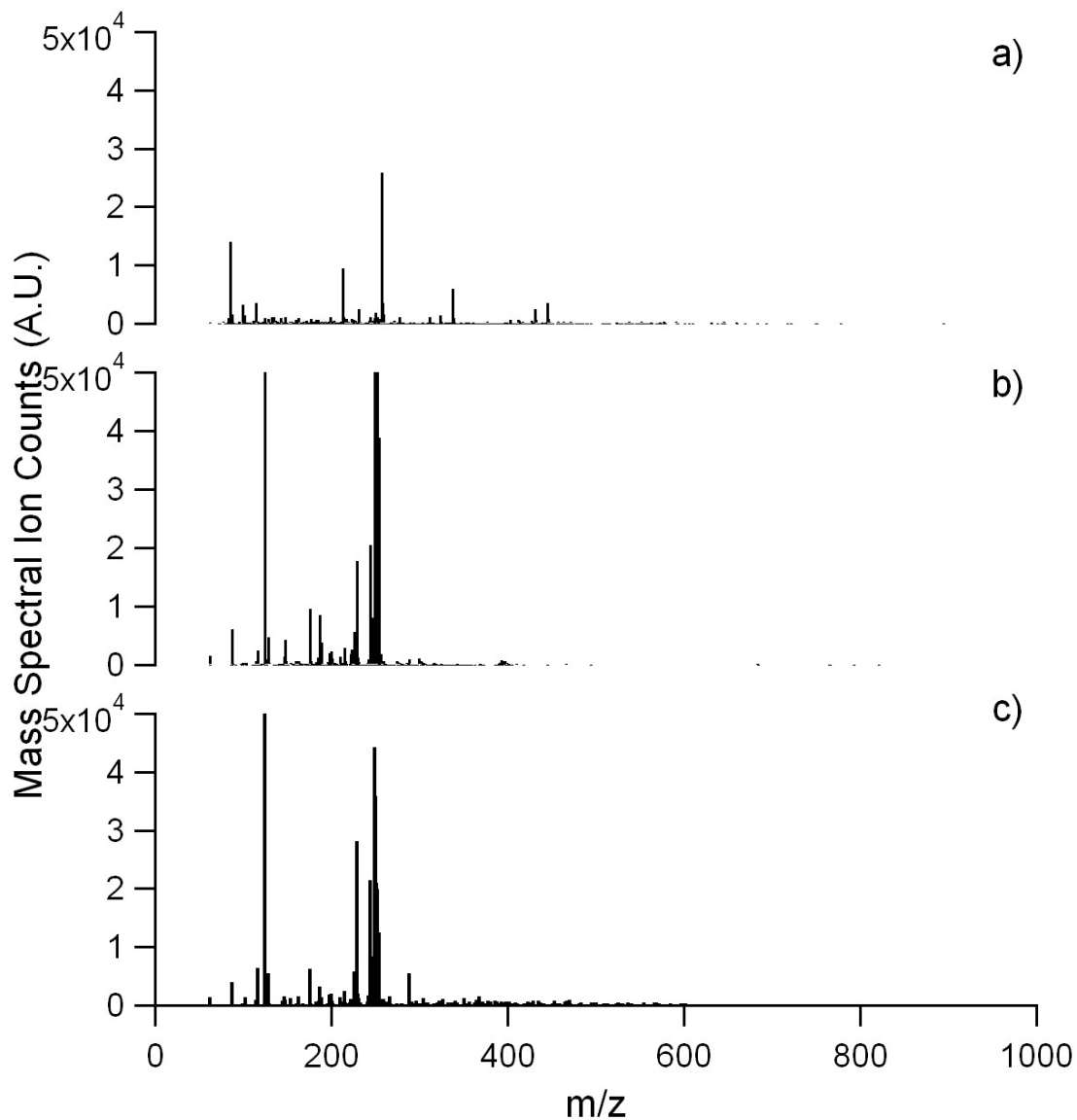


Figure 2.3: Individual PLS-ToF extracted mass spectra for α -pinene ozonolysis run EPA1311A. a) Mass spectra 10 min. into reaction (background). b) Mass spectra 50 min. into reaction. c) Mass spectra 380 min. into reaction.

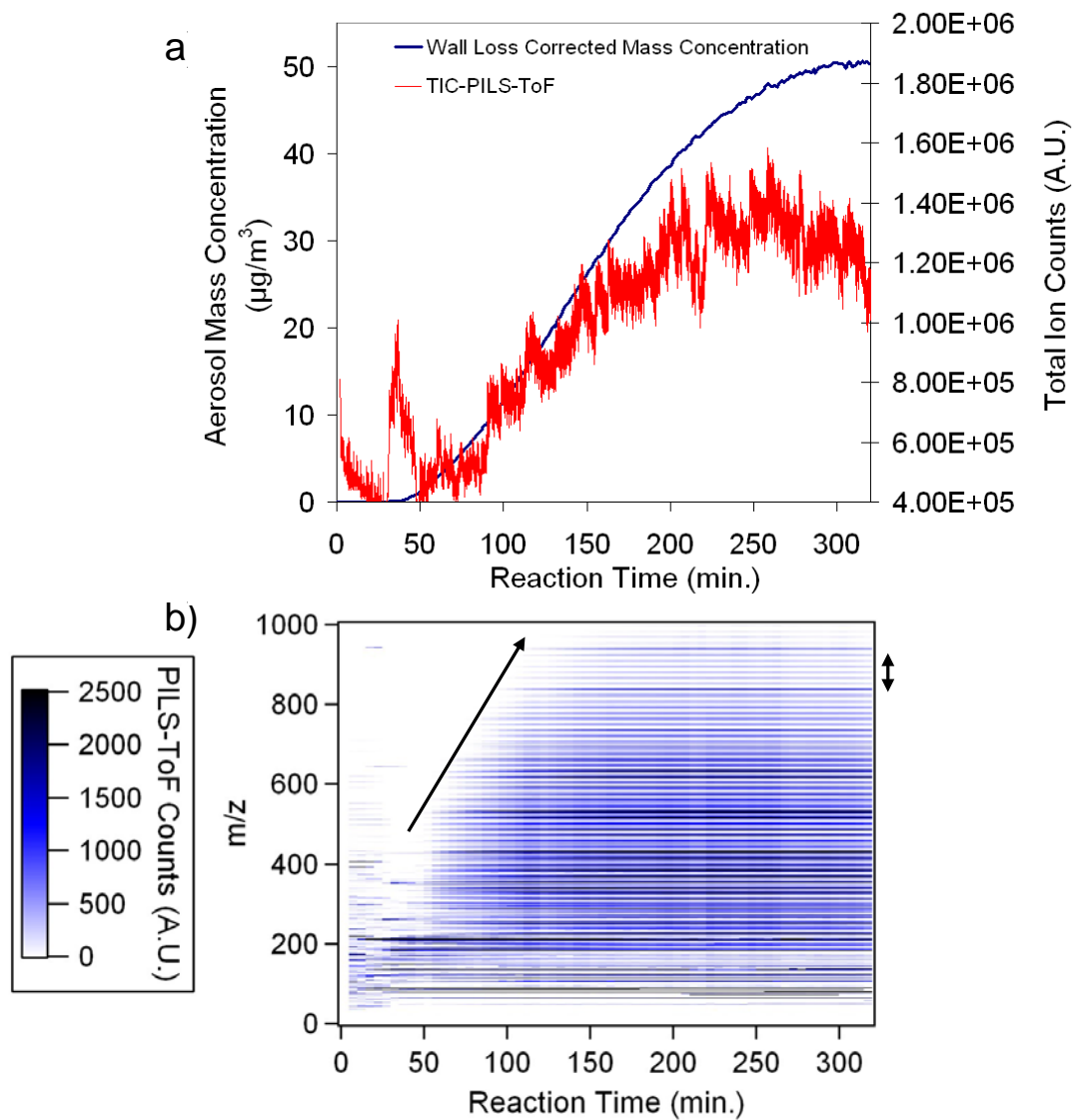


Figure 2.4: a) Plot of the PILS-ToF total measured ion-counts (TIC) and wall-loss corrected aerosol mass formation, as measured by SMPS, during the NO photo-oxidation of isoprene, EPA1353A. b) Contour plot of PILS-ToF mass spectrum as a function of reaction time.

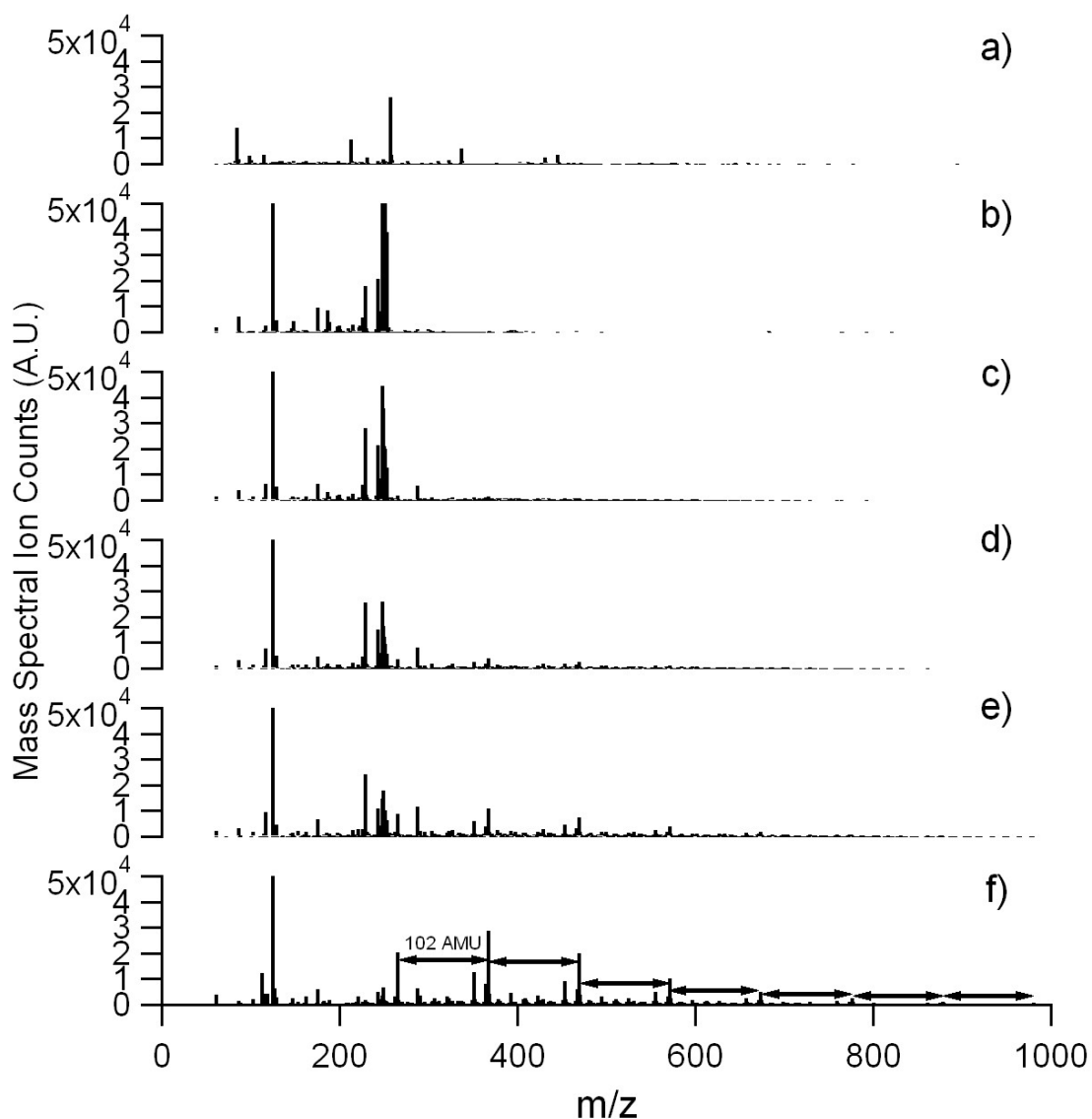


Figure 2.5: Individual PILS-ToF extracted mass spectra for NO photo-oxidation of isoprene, EPA1353A. a) Mass spectra 10 min. into reaction (background). b) Mass spectra 35 min. into reaction. c) Mass spectra 60 min. into reaction. d) Mass spectra 75 min. into reaction. e) Mass spectra 100 min. into reaction. f) Mass spectra 300 min. into reaction.

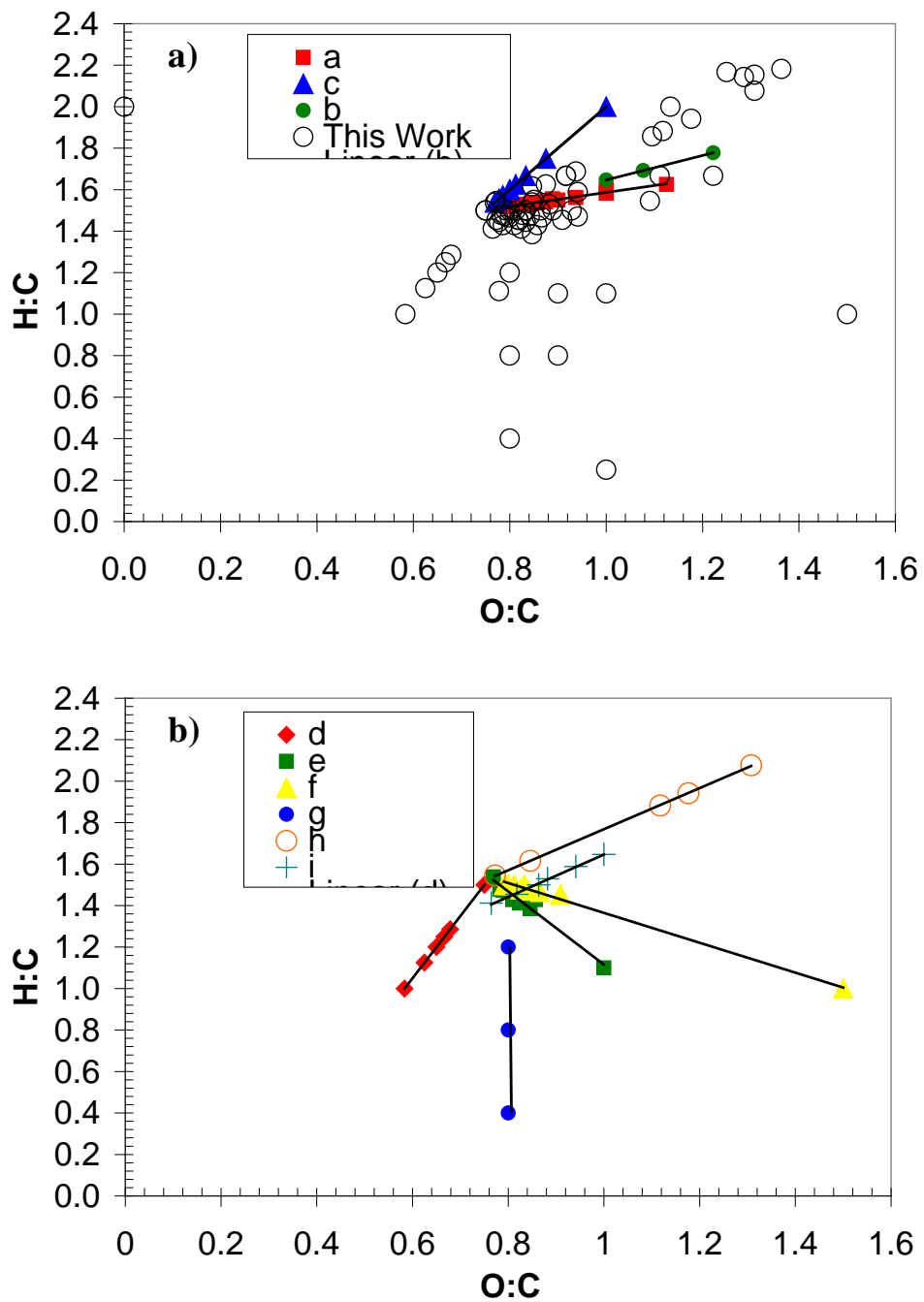


Figure 2.6: Van Krevelen Diagram of the final state (reaction time=300min.) PILS-ToF mass spectra of the NO photo-oxidation of isoprene, EPA1353A. a) represents mass spectral peaks confirmed with the literature compared to this work. b) presents mass spectral peak matches corresponding to new apparent reaction lines observed in this work.

Chapter 3: Characterization of secondary organic aerosol (SOA) from isoprene

3.1 Introduction

It is accepted that isoprene is a significant gas-phase component of the ambient atmosphere, as it is the most abundant non-methane hydrocarbon emitted into the atmosphere (Guenther, Hewitt et al. 1995), and has a propensity for the formation of secondary organic aerosol (SOA) (Claeys, Wang et al. 2004; Edney, Kleindienst et al. 2005; Boege, Miao et al. 2006; Kroll, Ng et al. 2006; Ng, Kroll et al. 2006; Surratt, Murphy et al. 2006; Kleindienst, Lewandowski et al. 2007; Ng, Kwan et al. 2008; Kleindienst, Lewandowski et al. 2009; Rollins, Kiendler-Scharr et al. 2009; Nguyen, Bateman et al. 2010; Surratt, Chan et al. 2010; Nguyen, Laskin et al. 2011; Sato, Nakao et al. 2011; Zhang, Surratt et al. 2011; Borrás and Tortajada-Genaro 2012; Fang, Gong et al. 2012; Liu, Siekmann et al. 2012). The literature reveals, SOA formation from isoprene has been widely studied in recent years, though the focus has been on the photo-oxidation of isoprene (Claeys, Wang et al. 2004; Edney, Kleindienst et al. 2005; Boege, Miao et al. 2006; Kroll, Ng et al. 2006; Ng, Kroll et al. 2006; Surratt, Murphy et al. 2006; Kleindienst, Lewandowski et al. 2009; Surratt, Chan et al. 2010; Nguyen, Laskin et al. 2011; Sato, Nakao et al. 2011; Zhang, Surratt et al. 2011; Borrás and Tortajada-Genaro 2012; Fang, Gong et al. 2012; Liu, Siekmann et al. 2012).

Studies of SOA formation from dark reactions of isoprene with either nitrate radical or ozone, are less prevalent in the literature (Kleindienst, Lewandowski et al. 2007; Ng, Kwan et al. 2008; Rollins, Kiendler-Scharr et al. 2009; Nguyen, Bateman et al.

2010). Though nitrate radical reaction with isoprene has been shown to form a significant amount of aerosol, for example SOA yields of 0.07-.24 (Ng, Kwan et al. 2008), chemical and physical characterization remains incomplete. Kamens et al. posited that little or no SOA would form from isoprene dark ozonolysis gas-phase mechanisms (Kamens, Gery et al. 1982). This assertion has been disputed by more recent reports of SOA yields from isoprene ozonolysis (Kleindienst, Lewandowski et al. 2007; Nguyen, Bateman et al. 2010). These more recent studies of isoprene dark ozonolysis present lower SOA yields than observed here, and include limited chemical and physical property characterization of the formed SOA.

This paper seeks to give a comprehensive and intercomparable experimental overview of dry nucleating SOA from isoprene by utilizing the suite of available instruments at the UCR CE-CERT Environmental Chamber. Here, comparable SOA formation, SOA yield, particle density, particle volatility, AMS elemental ratio, and PILS-ToF SOA chemical speciation measurements are presented for: isoprene photo-oxidation with and without NO in the presence of an additional hydroxyl radical source (H_2O_2), isoprene NO photo-oxidation without an additional hydroxyl radical source (H_2O_2), isoprene dark ozonolysis with and without a hydroxyl scavenger (CO), and isoprene reaction with nitrate radical (added as N_2O_5).

3.2 Materials and Methods

3.2.1 environmental chamber

All experiments were conducted in the UC Riverside/CE-CERT environmental chamber described in detail in Carter et al. (Carter, Cocker et al. 2005). In short, this facility consists of dual 90m³ Teflon® reactors suspended by rigid frames in a temperature controlled enclosure (27±1°C) continuously flushed with dry (a dew point below -40°C) purified air generated by an Aadco 737 series (Cleves, Ohio) air purification system. The top frames are slowly lowered during the experiments to maintain a slight positive differential pressure (0.0100 in. H₂O) between the reactors and the enclosure to minimize dilution and possible contamination of the reactors. 272 115W Sylvania 350 black lights are used as the light source for all photo-oxidation experiments reported the experiments reported.

3.2.2 gas and particle analysis

The Agilent 6890 Gas Chromatograph – Flame Ionization Detector was used to measure concentrations of hydrocarbon reactants and products. NO_x, CO, and O₃ concentrations were monitored using a Thermo Environmental Instruments Inc. model 42C trace level NO-NO₂-NO_y analyzer, Thermo Environmental Instruments Inc. model 48C trace level CO analyzer and O₃ concentration is measured by a Dasibi Environmental Corporation model 1003-AH, respectively. All quantitative gas phase instrumentation is calibrated to a gas standard prior to each chamber experiment.

Particle size distribution between 27 nm and 686 nm was monitored by a custom built Scanning Mobility Particle Sizer (SMPS) similar to that described by (Cocker, Flagan et al. 2001). Particle volatility was monitored with a volatility tandem DMA (VTDMA), in which monodisperse particles of mobility diameter D_{mi} are selected by the 1st DMA followed by transport through a Dekati thermodenuder (TD, residence time: ~17 s, temperature: 100°C). The particle size after the TD (D_{mf}) is then measured by fitting a log-normal size distribution curve from the 2nd SMPS. Volume fraction remaining (VFR) is then calculated as the before and after the TD volume ratio, i.e., $VFR = (D_{mf}/D_{mi})^3$.

Particle effective density was measured with an Aerosol Particle Mass Analyzer (APM, Kanomax) (Ehara, Hagwood et al. 1996) and SMPS in series. The APM is located upstream of the SMPS for improved time resolution and sensitivity (S/N) over the more common configuration of Differential Mobility Analyzer (DMA) – APM (McMurry, Wang et al. 2002; Khalizov, Zhang et al. 2009; Xue, Khalizov et al. 2009). A detailed description of the APM-SMPS system and data algorithms are described elsewhere (Malloy, Nakao et al. 2009).

The high resolution time-of-flight aerosol mass spectrometer (HR-ToF-AMS) (DeCarlo, Kimmel et al. 2006) was operated in high resolution W mode. Elemental analysis (EA) was used to determine the atomic ratio (H/C, O/C, and N/C) of non-refractory organic aerosols (Aiken, DeCarlo et al. 2008).

A Particle-Into-Liquid-Sampler (PILS) (Weber, Orsini et al. 2001; Orsini, Ma et al. 2003) was interfaced with an Agilent 6210 Time-of-Flight Mass Spectrometer (TOFMS), hereafter referred to as the PILS-ToF, equipped with a multimode ionization source for electrospray and atmospheric pressure chemical ionization (ESI/APCI) to provide an on-line accurate mass analysis of water soluble organic compounds (Bateman, Nizkorodov et al. 2010). In order to couple the PILS (Brechtel Manufacturing Inc.) to the TOFMS, the use of HPLC pumps in addition to a commonly used peristaltic pump was critical to overcome the backpressure of the TOFMS inlet and to supply steady flow of water (18.2M Ω , Milli-Q, Millipore) into the boiler. The PILS-ToF system is described in detail else where (Clark et al., 2012). For this study, the TOFMS electrospray ionization sources (ESI) was operated in negative mode with a vaporizer temperature 200 °C, nebulizer pressure 40 psig, corona current 2 μ A, fragmentor voltage 100V. All TOFMS data reported here was acquired using ESI only in negative ion mode.

Occasionally higher mass errors (up to 100 ppm) were observed during sample analysis, which resulted in a consistent shift of mass throughout the mass range of the instrument. Since the extent of the shift can be inferred from repeatedly observed ions (e.g., pyruvic acid), formulas were carefully assigned based on tendency of shift and repeat experiments.

3.3 Results and Discussions

3.3.1 SOA formation

Wall-loss corrected aerosol mass concentration was measured for 25 isoprene experiments. All experiments reported here have the same initial isoprene concentration, $697 \mu\text{g m}^{-3}$ (250ppb). SOA yield (Y) is calculated here as the mass of aerosol formed (wall-loss-corrected) (M_0) divided by mass of hydrocarbon reacted (ΔHC)

$$Y = \frac{M_0}{\Delta HC} \quad (3.1)$$

Table 3.1 presents environmental chamber conditions for the experiments presented here.

3.3.1.1 SOA formation from isoprene photo-oxidation

When looking at SOA formation from isoprene, NO_x photo-oxidation experiments with H_2O_2 as an additional hydroxyl radical source, SOA mass formation and SOA yield are observed to compare well with previous published studies (Kroll, Ng et al. 2006; Surratt, Murphy et al. 2006; Sato, Nakao et al. 2011). Experiments comparable to these previous studies would be: EPA1353A, EPA1392A, EPA1382A, and EPA1303A where HC/ NO_x ratio was approximately 0.5, 1, 2, and 10 respectively. For the high NO_x runs, EPA1353A and 1392A, ozone formation went above the scale of the chamber ozone analysis equipment, 500 ppb; though for EPA1382A and EPA1303A a significant drop, 89 and 359 ppb respectively, in ozone formation was observed as initial NO concentration dropped below 125 ppb (HC/ $\text{NO}_x=2$). For these experiments, an

optimum SOA yield of 0.11 was observed at a HC/NO_x ratio of 1, consistent with Kroll et al. (Kroll, Ng et al. 2006; Hoyle, Boy et al. 2011).

Isoprene NO_x photo-oxidation studies in the literature generally add H₂O₂ or HONO as an additional hydroxyl radical source (Kroll, Ng et al. 2006; Surratt, Murphy et al. 2006; Sato, Nakao et al. 2011), though Sato et al. performed one isoprene NO_x photo-oxidation experiments in the absence of H₂O₂. In this study, the effect of an additional hydroxyl source, H₂O₂, is probed. For a HC/NO_x ratio of 0.5, used in experiments EPA1288A, EPA1288B, and EPA1375A, decreasing initial hydroxyl concentrations, added in the form of H₂O₂ leads to decreased SOA yield. At a HC/NO_x ratio of 0.5 when initial H₂O₂ is 1.5 ppm, as used in EPA1288B, SOA yield is observed to decrease by 0.03. For a HC/NO_x ratio of 1, used in EPA1392A and EPA 1392B, differing initial H₂O₂ concentration is observed to drop in SOA yield by only 0.01. When HC/NO_x ratio is increased to 2, increased H₂O₂ is observed to inhibit SOA formation as can be seen in comparing EPA1382A and EPA1382B. Where EPA1382B, the experiment with the lower initial H₂O₂ concentration, is observed to have a slightly higher SOA yield. As HC/NO_x ratio is increased to 10, as in EPA1303A, EPA1303B, and EPA1397A increased initial H₂O₂ is seen again to increase SOA yield. Although, in comparing EPA1303A and EPA1303B, with initial H₂O₂ concentrations of 3 and 1.5 ppm respectively, the SOA yield decrease with decreasing H₂O₂ is only 0.02. For all experiments for which H₂O₂ was added all isoprene was consumed, though at a slower rate for lower H₂O₂ concentration.

NO_x photo-oxidation experiments performed without H₂O₂ addition forms much less SOA, though for the high NO_x case, EPA1375A, all isoprene was consumed. Very little SOA was formed under low NO_x conditions and no H₂O₂, in experiment EPA1397A. However, EPA1397A formed far more ozone than was formed in comparable experiments with H₂O₂ present, in EPA1303A and EPA1303B.

Hydroxyl radical alone, in the absence of NO_x, has also been reported to form SOA (Kleindienst, Lewandowski et al. 2009). This observation is confirmed here in the isoprene photo-oxidation experiments EPA1467A and EPA1467B. In EPA1467A and EPA1467B, the SOA yields are comparable to low NO_x experiments EPA1303A and EPA1303B respectively.

3.3.1.2 SOA formation from dark reactions of isoprene

Dark ozonolysis of isoprene is rarely reported to form SOA with yields greater than 0.01 (Kleindienst, Lewandowski et al. 2007), though isoprene's gas-phase reactions with ozone have been extensively studied (Paulson, Flagan et al. 1992; Grosjean, Williams et al. 1993; Gutbrod, Kraka et al. 1997; Paulson, Chung et al. 1998; Neeb and Moortgat 1999; Hasson, Ho et al. 2001; Lewin, Johnson et al. 2001). Here a set of experiments is presented, spanning a range of initial concentrations of ozone from 25-250 ppb, both with and without carbon monoxide as a hydroxyl radical scavenger.

Dark ozonolysis experiments EPA1562A and EPA1476A, experiments with initial O₃ concentration of 125 ppb and an excess CO concentration of 150 ppm, are observed to have the highest aerosol yield, 0.06. Though SOA formation from isoprene

dark ozonolysis is reported higher in the experiments here than in the work of Kleindienst et al. (Kleindienst, Lewandowski et al. 2007), it should be noted that Kleindienst et al. do not report SOA yield. Any discrepancies between SOA formation results reported here and those reported by Kleindienst et al. are thought attributable to environmental chamber design and characterization equipment used (Kleindienst, Lewandowski et al. 2007). This high SOA yield from isoprene ozonolysis in the presence of excess CO indicates that ozonolysis isoprene could be a significant contributor to formed SOA, even in the isoprene photo-oxidation experiments above. Figure 3.1a plots SOA yield as it changes with initial ozone concentration, while Figure 3.1b plots isoprene consumption as a function of initial ozone concentration. Figure 3.1 plots observed isoprene consumptions and SOA yields for both ozone only and ozone with CO experiments.

SOA yields for isoprene ozonolysis shown in Figure 3.1a are all 0.01-0.05 higher than those reported previously by Kleindienst et al. (Kleindienst, Lewandowski et al. 2007). Furthermore, 125 ppb of ozone is shown in Figure 3.1a to have the highest yield for the ozone with CO system and the lowest yield for the ozone only system. This high yield from isoprene dark ozonolysis in the presence of CO is likely the result of increased peroxy and alkylperoxy radical chemistry. In contrast, Figure 3.1b shows that isoprene consumption is proportional to initial ozone concentration for both experiments with ozone only and experiments with ozone and CO. This proportional hydrocarbon consumption is an expected result for isoprene ozonolysis.

SOA formation from the reaction of nitrate radical in the dark has been studied by others (Ng, Kwan et al. 2008; Rollins, Kiendler-Scharr et al. 2009). A single isoprene experiment with N_2O_5 , the nitrate radical source, is reported here to serve as a comparator to SOA formation and chemical composition of isoprene photo-oxidation and dark ozonolysis. In comparing the SOA yield result of the dark isoprene with N_2O_5 chamber experiment, provided in Table 3.1, to that of the yields reported by Ng et al. ranging from 0.04-0.24 (Ng, Kwan et al. 2008), the yield of 0.12 observed here appears reasonable. Differences between these two studies are likely attributable to the low RH and the lower excess of initial N_2O_5 present in this experiment, which could lead to the increased formation of organic nitrates opposed to nitric acid.

3.3.2 SOA Physical Characterization

Particle density and particle volatile fraction remaining were measured for a representative subset of the isoprene SOA experiments by APM-SMPS and VTDMA respectively. The physical and chemical SOA characterization data is summarized in Table 3.2. It should be noted that particle density and VFR are reported as a mean of measurements after particle nucleation. Error bars represent the minimum and maximum observed values after particle nucleation.

Figure 3.2 shows the results of particle density, Figure 3.2a, and particle VFR, Figure 3.2b as a function of initial NO concentration for isoprene photo-oxidation experiments. Particle density is observed to vary little regardless of initial NO concentration or the presence of H_2O_2 . The observed density range for isoprene photo-

oxidation experiments of 1.32-1.45 is in the typical range for hydrocarbon SOA (Nakao, Tang et al. 2012).

Particle VFR increases within increasing initial NO concentration (Figure 3.2b). This decrease in particle volatility is attributed to increased formation of highly oxygenated and high molecular weight nitro-oligoesters and oligoesters. Previous reports, and results shown in the SOA chemical characterization section here, show that decreasing HC:NO_x ratio leads to increasing SOA nitro-oligoester content which in-turn correlates in Figure 3.2b to decreased particle volatility (Surratt, Murphy et al. 2006; Sato, Nakao et al. 2011).

Figure 3.3 shows the results for particle density (Figure 3.3a) and particle VFR (Figure 3.3b) as a function of initial O₃ concentration for dark experiments. Particle density (Figure 3.3a) compares favorably to particle density from isoprene photo-oxidation (Figure 3.2a) supporting the assertion that particle density for isoprene SOA is consistent, within experimental error, for all reaction types performed. Similarly, isoprene N₂O₅ density (Figure 3.3a) is also shown to be consistent with photooxidation and ozonolysis density measurements.

In contrast, particle VFR for dark isoprene ozonolysis experiments, shown in Figure 3.3b, is significantly less than that observed in isoprene photo-oxidation experiments. Isoprene ozonolysis is shown (Section 3.3) to form smaller molecular weight particle-phase compounds than isoprene photo-oxidation consistent with decreased VFR. Additionally, 3.3b shows the VFR for the reaction of isoprene with

N_2O_5 in the dark is quantitatively comparable to the isoprene photo-oxidation experiments.

3.3.3 SOA chemical characterization

Two mass spectral particle characterization methods are compared here, the AMS and the PILS-ToF. For gross chemical characterization of O:C, H:C, and N:C ratios of particle composition the two methods generally agree (Table 3.2). The AMS is used here to give gross quantitative chemical description through the elemental ratios, O:C, H:C, and N:C. The PILS-ToF is used here for qualitative chemical speciation of the particle phase products. AMS and PILS-ToF calculated average particle elemental ratios H:C, O:C, and N:C ratios are presented in Table 3.2.

3.3.3.1 SOA AMS characterization

The calculated AMS H:C and O:C ratios are observed to be invariant for photo-oxidation experiments performed in the presence of H_2O_2 (Table 3.2). AMS N:C ratio for these experiments are observed to increase with increasing NO up to an initial NO concentration of 125 ppb, corresponding to a isoprene to NO molar ratio of 2. As initial NO concentration is increased above 125 ppb the AMS N:C ratio is observed to plateau, within measurement error. AMS elemental H:C and O:C ratios compare well with a study by Chhabra et al. (Chhabra, Ng et al. 2011). However, the AMS N:C ratios reported here are as much as three time higher than that for any isoprene photo-oxidation experimental observation by Chhabra et al. (Chhabra, Ng et al. 2011). This discrepancy between the N:C results reported here and those reported by Chhabra et al. are

attributable to application of the AMS data analysis algorithms that deal with organic nitrate mass spectral fragments (Aiken, DeCarlo et al. 2008).

NO photo-oxidation experiments performed without H₂O₂, EPA1375A and 1397A, are observed to have the same AMS H:C ratios as those experiments with H₂O₂; while the AMS O:C ratios of the NO photo-oxidation experiments without H₂O₂ are lower. In contrast, the AMS N:C ratio for the NO photo-oxidation experiments without H₂O₂ increases in comparison to the corresponding initial NO concentration of the photo-oxidation experiments with H₂O₂. This increased AMS N:C ratio and decreased O:C ratio is attributed to the increased selectivity and yield in the formation of nitro-oligoesters opposed to oligoesters, this attribution is further supported by the PILS-ToF speciation below.

Table 3.2 shows AMS H:C ratio for isoprene dark ozonolysis experiments (Table 3.2) is consistent with that observed for the photo-oxidation experiments. However, the observed O:C ratio for the dark ozonolysis experiments is generally less than the O:C ratio of the isoprene photo-oxidation experiments, regardless of O₃ concentration or the presence of hydroxyl scavenger (CO). This lower AMS O:C ratio is posited to be due to the formation of smaller molecular weight higher volatility oxygenated compounds and less oligomer formation as supported by the PILS-ToF chemical speciation (Section 3.3.2).

In the reaction of isoprene with nitrate radical (EPA1560A) the H:C and O:C ratios broadly fall in line with the isoprene photo-oxidation experiments. Surprisingly,

the N:C ratio for EPA1560A is significantly lower than any NO photo-oxidation experiment, an observation that does not compare well to the literature and the PILS-ToF results presented here (Ng, Kwan et al. 2008). This disagreement between the N:C ratio reported by the AMS and that reported by the PILS-ToF could be attributable again to the AMS organic nitrate data analysis algorithm or the non-quantitative ionization of the PILS-ToF.

3.3.3.2 PILS-ToF Characterization

PILS-ToF characterization was performed for a representative set of the isoprene SOA experiments. It should be noted that the PILS-ToF will observe both water soluble SOA and some water soluble gas-phase compounds, as no denuder is used in PILS sampling. Table 3.2 summarizes PILS-ToF elemental analysis results, H:C, O:C, and N:C ratios. The specific percentage of the PILS-ToF signal that has been matched to specific ions and the average observed molecular weight is also provided. In broadly comparing the PILS-ToF elemental analysis to the AMS elemental analysis, specific discrepancies can be seen among H:C and N:C ratios in addition to specific similarities. These will be discussed on a case by case basis. Typically, the PILS-ToF O:C ratios for all experiments here are significantly higher than the AMS O:C ratios. These general comments transcend isoprene dark ozonolysis and photo-oxidation.

Table 3.3 gives the PILS-ToF observed m/z, the corresponding ion match, the experiments the ion was observed, and the literature reference if the ion or a corresponding molecule was previously observed. PILS-ToF ion matches presented in

Table 3.3 and the Van Krevelen Plots in Figure 3.5, 3.7, and 3.9, are for ions with intensity above 1000 ion counts. The decision to limit presentation and analysis of PILS-ToF data to mass spectral peaks above 1000 counts lowers the probability of analyzing instrumental artifact ions and makes data analysis more manageable.

3.3.3.2.a PILS-ToF Characterization of Isoprene Photo-oxidation

Figure 3.4 gives the observed final state PILS-ToF mass spectra for isoprene photo-oxidation experiments. Four of these NO photo-oxidation experiments were performed with added H₂O₂. For these four photo-oxidation experiments, the intensity of the signal, especially above 800 m/z, trends with suspended aerosol mass as measured by SMPS.

Figure 3.4a and Figure 3.4b, corresponding to the PILS-ToF mass spectra of EPA1353A and EPA1392A, show clear repetitive patterns in the mass spectra corresponding to nitro-oligoesters and oligoesters. Detailed specific nitro-oligoesters and oligoesters reaction products observed by PILS-ToF in the high NO case of isoprene photo-oxidation are discussed in greater detail in Clark et al. (Clark, Nakao et al. 2012). The higher PILS-ToF intensity corresponding to these higher-order oligoester and nitro-oligoesters is consistent with larger observed aerosol mass formation of lower volatility particles (Sections 3.3.1.1 and 3.3.2). A significant decrease in the intensity of the higher order repetitive patterns, indicative of large oligomer formation is observed (Figure 3.4c). EPA1382A has similar SOA mass formation as EPA1353A and 6 $\mu\text{g m}^{-3}$ less SOA mass formation than EPA1392 though the PILS-ToF mass spectra indicates lower order and

lower intensity oligomer formation. Furthermore, the lower PILS-ToF intensity at lower m/z observed in EPA1382A corresponds to a lower observed VFR, discussed in section 3.2, indicating a lower volatility SOA. The larger intensity signal at smaller m/z and less prevalent oligomer signal observed in Figure 3.4c-e, is indicative of increased hydroxyl chemistry and decreased alkyl peroxy radical chemistry, the chemistry responsible for nitro-oligoester formation.

Observed ions from PILS-ToF mass spectra (Figure 3.4d and 3.4e) for low NO_x or no NO_x conditions (EPA1303A and EPA1467A, respectively), are all shifted below an m/z of 500. The low NO_x and no NO_x photo-oxidation experiments still have SOA mass formations of 56 $\mu\text{g m}^{-3}$ and 55 $\mu\text{g m}^{-3}$, respectively, similar to SOA mass formation from high NO_x experiments. Furthermore, the no NO_x experiment with H₂O₂ has higher volatility particles (lower VFR) than those produced from high NO_x+H₂O₂ experiments. The lower m/z ions for no NO_x and low NO_x experiments are identified as smaller, highly oxygenated hydrocarbons, consistent with a more semi-volatile SOA.

Experiments EPA1375A (high NO_x) and EPA1397A (low NO_x) correspond to NO photo-oxidation runs performed in the absence of H₂O₂. The PILS-ToF mass spectra (EPA1375A) exhibits the same repetitive oligomeric structure observed for high NO_x experiments performed in the presence of H₂O₂. Though the PILS-ToF mass spectral patterns are consistent, the PILS-ToF mass spectral intensity is greatly decreased without H₂O₂ addition, consistent with observed decreases in SOA mass without H₂O₂.

The PILS-ToF mass spectral results for EPA1397A, a photo-oxidation experiment with low NO_x (25 ppb) and no H₂O₂ (Figure 3.4g) is significantly different than any of the other photo-oxidation experiments. The repetitive m/z pattern is not assigned to a condensation oligomerization with a monomer subunit. Rather, the higher m/z ions observed are assigned to both oxygenated and nitrogenated hydrocarbons. The incorporation of nitrogen in the SOA formed, a somewhat unexpected result, is also supported by both AMS elemental analysis.

In specifically comparing and contrasting PILS-ToF elemental analysis of the mass spectra presented in Figure 3.4 to the AMS elemental ratios for isoprene photo-oxidation experiments, we find that H:C ratios are within experimental error for experiments with HC/NO_x ratio of 2 or higher (EPA1382A, EPA1303A, EPA1467A, and EPA1397A). The isoprene photo-oxidation experiments where AMS and PILS-ToF elemental H:C analysis do not agree are where HC/NO_x ratio below 2 (EPA1353A, EPA1392A, and EPA1375A). In calculating the PILS-ToF elemental ratio, as performed in Clark et al. (Clark, Nakao et al. 2012), a weighted average is used. In the case of EPA1353A, EPA1392A, and EPA1375A the total PILS-ToF ion counts are dominated by m/z 125, which makes up 49%, 15%, and 45% of the ion counts respectively, which is matched in all three cases to the ion [C₅H₄O]⁻. If this likely semi-volatile or volatile compound [C₅H₄O]⁻ is removed from the elemental analysis for EPA1353A, EPA1392A, and EPA1375A, the PILS-ToF H:C ratios are calculated to be 1.45, 1.51, and 1.18 respectively. These new PILS-ToF H:C ratios match, within experimental error, the AMS H:C ratios.

As previously stated, the calculated PILS-ToF O:C ratios are much higher than the observed AMS O:C ratios for all isoprene photo-oxidation experiments except the isoprene low NO (25 ppb) photo-oxidation experiment performed in the absence of H₂O₂ (EPA 1397A). The discrepancy between the PILS-ToF O:C and AMS O:C ratio is attributed to the weighting of the PILS-ToF O:C ratio by the ion individual ion intensity; small semi-volatile or vapor phase ions may be disproportionately weighting the O:C ratio to a higher O:C ratio. N:C ratios for both PILS-ToF and AMS are highly dependent on specific individual ions; this ion specificity lends itself to biased uncertainties though, AMS and PILS-ToF AMS N:C ratios broadly agree.

Van Krevelen plots (Figure 3.5) are provided to summarize H:C and O:C ratios for select isoprene-NO_x photooxidation experiments, with the color intensity indicating the observed ion intensity. Specific PILS-ToF ion matches are provided in Table 3.3. It should be noted that the left hand column of Van Krevelen plots (Figure 3.5) are for experiments done with H₂O₂ and the right hand column are experiments done without H₂O₂. Furthermore, initial experimental NO increases for the Van Krevelen plots (Figure 3.5) from bottom (no NO) to top (highest NO- 500 ppb). In comparing the Van Krevelen plots for no NO and low NO (Figure 3.5d and 3.5e), done in the presence of H₂O₂, little difference is observed between them. This similarity indicates that the formation of SOA component species in the low-NO_x experiment is dominated by hydroxyl chemistry. When looking at Figure 3.5b and Figure 3.5a, representing a medium NO_x (EPA1382A-250 ppb) and high NO_x experiment (EPA1353A-500 ppb)

respectively, a transition is prevalent to a more concentrated grouping of molecular matches.

The Van Krevelen plot for optimum SOA yield (Figure 3.5b), corresponding to EPA1382A done with 125 ppb of initial NO in the presence of H₂O₂, has many more molecular matches with increased mass spectral intensity. This increased number of identified PILS-ToF ions in EPA1382A correlates to the highest SOA mass formation. What is seen in Figure 3.5b is a swarm of molecular matches lying in the center of the Van Krevelen diagram. This swarm of ions is thought to be indicative of optimum SOA formation in isoprene photo-oxidation. This optimum SOA formation balances both formation of smaller oxygenated species from hydroxyl chemistry as in the case of low NO_x experiments (EPA1467A and EPA1303A) and oligomer formation in the high NO_x experiment (EPA1353A).

Figure 3.5a, the PILS-ToF Van Krevelen diagram for EPA1353A a high NO_x (500 ppb) photo-oxidation experiment done in the presence of H₂O₂, has been analyzed in detail in previous work by Clark et al. (Clark, Nakao et al. 2012). In Figure 3.5a the swarm of molecular matches is further focused along the centerline of the plot. The oligoester and nitro-oligoester species discussed in previous works (Surratt, Murphy et al. 2006; Surratt, Chan et al. 2010; Sato, Nakao et al. 2011) lie in the swarm along the center line of the Van Krevelen diagram, with the nitro-oligoesters lying in the upper right of the diagram. The intense ions lying in the bottom right of Figure 3.5a, below the ion swarm around the center-line, correspond to the molecular matches C₅H₂O₄, C₅H₄O₄,

C₄H₁NO₄, and C₅H₃NO₇ that make up 47%, 0.5%, 0.5%, and 0.3% of the total PILS-ToF ion counts respectively.

Figure 3.5e and Figure 3.5f show Van Krevelen diagrams of PILS-ToF mass spectra for EPA1375A and EPA1397A, which correspond to a high NO (500 ppb) and low NO (25 ppb) experiment respectively both done in the absence of H₂O₂. Figure 3.5f looks comparable to Figure 3.5c, but this is not the case. PILS-ToF molecular matches for the experiment done in the absence of NO (Figure 3.5f-EPA1397A), shown in detail in Table 3.3, correspond to small nitrogen containing oxygenated species. In the Van Krevelen diagram for the experimental case of low NO (25 ppb) with H₂O₂ (Figure 3.5c), molecular matches for small oxygenated species containing no nitrogen are observed. These observed ion species differences are seen more prevalently in contrasting the PILS-ToF mass spectra in Figure 3.4d and Figure 3.4g. In contrast, Figure 3.5f is very similar to Figure 3.5d. In comparing the PILS-ToF ion matches for these two experiments it is seen that 92% of the matched ions counts in Figure 3.5f, the PILS-ToF Van Krevelen diagram for the high NO_x (EPA1375A) experiment done in the absence of H₂O₂, agree with Figure 3.5d for a high NO_x experiment done in the presence of H₂O₂ (EPA1353A).

3.3.3.2.b PILS-ToF characterization of isoprene dark reactions

The results of experiment Isoprene dark ozonolysis experiments PILS-ToF mass spectra with (EPA 1425A, EPA 1562A, and EPA 1480A; Figure 3.6a-c) and without (EPA 1438A, EPA 1445A, and EPA 1473A; Figure 3.6d-f) hydroxyl scavenger (CO)

present are compared. All dark ozonolysis PILS-ToF mass spectra, regardless of initial O₃ concentration or hydroxyl scavenger, matches (90-100%) closely with the PILS-ToF molecular matches for the isoprene no-NO_x H₂O₂ photo-oxidation experiment (EPA 1467A). No significant ion signals were observed from m/z 600-1200 so only m/z upto 600 are shown. The intensity of the PILS-ToF mass spectra increases as ozone concentration is increased, consistent with increasing SOA formation in the experiment. Generally, the mass spectra exhibit similar features with and without the hydroxyl radical present with the majority of m/z intensity below 300 AMU. In comparing the PILS-ToF mass spectra for both of the highest ozone concentration experiments done (Figure 3.6a and Figure 3.6d), both with and without CO (EPA1425A and EPA1438A), it appears that the ion intensity is increased below 300 m/z for the no CO experiment. This result is expected as aerosol formation is higher for the experiment done without CO (EPA1438A). However, for the two lower O₃ concentration experiments without CO present (Figure 3.6ef), higher m/z peaks at 413.16645 (C₂₃H₂₆O₇), 427.1821 (C₁₇H₃₂O₁₂), 457.22905 (C₁₉H₃₈O₁₂), and 471.2447 (C₂₀H₂₄O₁₃) are observed.

Van Krevelen plots for the six dark ozonolysis experiments (Figure 3.7) representing the end of the experiment with corresponding individual ion matches (Table 3.3) are also presented. EPA1425A, EPA1562A, and EPA1480A, dark ozonolysis experiments done in the presence of CO with initial O₃ concentrations of 250 ppb, 125 ppb, and 25 ppb respectively. Figure 3.7d-f correspond to the Van Krevelen plots of PILS-ToF ion matches for EPA1438A, EPA1445A, EPA1473A, dark ozonolysis

experiments done in the absence of CO with initial O₃ concentrations of 250 ppb, 125 ppb, and 25 ppb respectively.

The number of ions and total ion intensity for both Figure 3.7a-c and Figure 3.7d-f, from experiments ranging in initial O₃ concentration performed with and without CO scales with SOA mass concentration and therefore initial O₃ concentration. Few chemical speciation differences are observed when closely analyzing the Van Krevelen diagrams. The detailed ion matches corresponding to the PILS-ToF mass spectra (Figure 3.8) of a dark N₂O₅ (used as a nitrate radical source) reaction with isoprene are provided in Table 3.3. PILS-ToF mass spectral data was collected up to m/z 1200; however, no significant ion-intensity is observed above m/z 600. The mass spectra in Figure 3.8 shows little signs of repeating oligomer ion pattern observed in the high-NO_x photooxidation experiments discussed above (Figure 3.4a,b,f). Nitrate anion, at m/z 61.9884, is observed to make up 9% of the total observed PILS-ToF ion intensity. This significant abundance of nitrate is important to note as it is observed to cluster with other formed ions in the ToF-MS. The nitrate ion clusters in Figure 3.8 identified are at m/z 557.0670, 512.0705, 433.0785, 333.0241, and 257.0338. These nitrate ion clusters correlate to the parent ions at m/z 494.0496, 449.0645, 370.0739, 270.0215, and 194.0306, which are matched to the molecules C₅H₉N₁O₇, C₅H₉N₃O₁₀, C₁₀H₁₆N₃O₁₂, C₁₀H₁₈N₄O₁₆, and C₁₀H₁₇N₅O₁₈. These ions and molecular matches have all been observed previously by Ng et al. (Ng, Kwan et al. 2008).

Ions previously observed by Ng et al. make up 18% of the observed ion intensity (Ng, Kwan et al. 2008). An additional 28% of the ions from N₂O₅ dark oxidation are consistent with ions observed in the literature for other isoprene SOA systems, both photo-oxidation and dark ozonolysis (Rollins, Kiendler-Scharr et al. 2009; Nguyen, Bateman et al. 2010; Clark, Nakao et al. 2012; Fang, Gong et al. 2012).

Figure 3.9 gives the Van Krevelen plot for the reaction of isoprene and N₂O₅, experiment EPA1560A. Figure 3.9 shows many ions hovering around the centerline of the Van Krevelen diagram with some additional orderly ion lines in the lower right of the diagram. Generally, the Van Krevelen diagram for the dark reaction of N₂O₅ (Figure 3.9) appears similar to the Van Krevelen diagram in for the high NO-H₂O₂ photooxidation (Figure 3.5a). The consistency between the two plots is indicative of increased abundance of higher molecular weight oxygenated and nitro-oxygenated molecules, though most of these molecules are inconsistent with the oligoesters and nitro-oligoesters observed in high NO isoprene photo-oxidation experiments. Indeed, no apparent oligomers were observed by the PILS-ToF in the dark reaction of N₂O₅ with isoprene. It should be noted again that the VFR for EPA1560A, 0.53, is higher than that reported for dark ozonolysis experiments and within the observational range for isoprene NO photo-oxidation experiment, 0.5-0.71. This point furthers the assertion that nitro-oxygenated compounds lead to lower volatility aerosol.

3.4 Conclusions

This work presents an intercomparable set of SOA formation experiments from isoprene all performed in the CE-CERT environmental chambers. For a representative subset of these isoprene experiments, a suite of physical and chemical characterization techniques were employed that provided insight into the SOA yield, mass formation, density, volatility, and chemical speciation.

Increasing OH concentration during NO photooxidation of isoprene increased SOA mass formation with observable chemical and physical differences. For the SOA photo-oxidation experiments, a strong trend toward decreasing volatility was observed as initial NO concentration was increased and was attributed to increased nitro-oligoester concentrations. Furthermore, the optimum in SOA formation and yield for isoprene photo-oxidation experiments is observed at HC/NO_x ratio of 1. This optimum SOA formation is shown through chemical speciation to be a balance between formations of small oxygenated hydrocarbons typical of low NO_x chemistry coupled to the incorporation of nitrogen into the SOA to form higher order nitro-oligoesters typical of high NO_x experiments.

Though SOA formation and yields for isoprene photo-oxidation broadly matched previous work (Surratt, Murphy et al. 2006; Sato, Nakao et al. 2011), SOA yields and mass formation from isoprene dark ozonolysis are observed here to be higher than previous reports (Kleindienst, Lewandowski et al. 2007). Dark ozonolysis of isoprene was shown to form SOA with a higher volatility than that formed through isoprene photo-

oxidation attributed to the prominence of small molecular weight less oxygenated chemical species observed by the PILS-ToF. The chemical composition of SOA formed through dark ozonolysis of isoprene, both with and without CO a hydroxyl scavenger present, broadly compares to the chemical composition of SOA formed from the photo-oxidation of isoprene with hydroxyl radical alone (photo-oxidation with H_2O_2 in the absence of NO).

SOA formation through the dark reaction of isoprene with nitrate radical, added to the environmental chamber as N_2O_5 , is comparable to previous work (Ng, Kwan et al. 2008). Physical characterization, VFR and density, of the SOA formed through dark reaction of isoprene with N_2O_5 are observed to compare with that of high NO photo-oxidation experiments. PILS-ToF chemical characterization shows that chemical species making up the SOA formed are largely highly nitrogenated compounds. The SOA from isoprene and nitrate radical is observed to contain much more nitrogen than isoprene NO photo-oxidation experiments with no clear repeating nitro-oligoesters. The physical and chemical characterization data for the dark reaction of N_2O_5 with isoprene generally supports the assertion that increased prevalence of nitrogenous species in the SOA leads to decreased SOA volatility in isoprene systems.

Here it can be seen that significant SOA can be formed not only in NO photo-oxidation of isoprene, but during hydroxyl radical only photo-oxidation of isoprene, dark ozonolysis of isoprene, and dark nitrate radical reaction of isoprene. Finally, the SOA

formation, physical, and chemical data presented here provides information to be used in atmospheric models and SOA chemical mechanisms for reaction with isoprene.

3.5 Reference

- Aiken, A. C., P. F. DeCarlo, et al. (2008). "O/C and OM/OC Ratios of Primary, Secondary, and Ambient Organic Aerosols with High-Resolution Time-of-Flight Aerosol Mass Spectrometry." Environmental Science & Technology **42**(12): 4478-4485.
- Bateman, A. P., S. A. Nizkorodov, et al. (2010). "High-Resolution Electro-spray Ionization Mass Spectrometry Analysis of Water-Soluble Organic Aerosols Collected with a Particle into Liquid Sampler." Analytical Chemistry **82**(19): 8010-8016.
- Boege, O., Y. Miao, et al. (2006). "Formation of secondary organic particle phase compounds from isoprene gas-phase oxidation products: An aerosol chamber and field study." Atmospheric Environment **40**(14): 2501-2509.
- Borras, E. and L. A. Tortajada-Genaro (2012). "Determination of oxygenated compounds in secondary organic aerosol from isoprene and toluene smog chamber experiments." Int. J. Environ. Anal. Chem. **92**(1): 110-124.
- Carter, W. P. L., D. R. I. Cocker, et al. (2005). "A new environmental chamber for the evaluation of gas-phase chemical mechanisms and secondary aerosol formation." Atmospheric Environment **39**: 7768-7788.
- Chhabra, P. S., N. L. Ng, et al. (2011). "Elemental composition and oxidation of chamber organic aerosol." Atmos. Chem. Phys. **11**(17): 8827-8845.
- Claeys, M., W. Wang, et al. (2004). "Formation of secondary organic aerosols from isoprene and its gas-phase oxidation products through reaction with hydrogen peroxide." Atmospheric Environment **38**(25): 4093-4098.
- Clark, C. H., S. Nakao, et al. (2012). "A real-time study of the particle phase products of the dark ozonolysis of α -pinene and the photo oxidation of isoprene by particle into liquid sampling directly coupled to a time of flight mass spectrometer (PILS-ToF)." Aerosol Sci. Technol. **In preparation.**
- Cocker, D. R., R. C. Flagan, et al. (2001). "State-of-the-Art Chamber Facility for Studying Atmospheric Chemistry." Environmental Science and Technology **35**: 2594-2601.

- DeCarlo, P. F., J. R. Kimmel, et al. (2006). "Field-Deployable, High-Resolution, Time-of-Flight Aerosol Mass Spectrometer." Analytical Chemistry **78**(24): 8281-8289.
- Edney, E. O., T. E. Kleindienst, et al. (2005). "Formation of 2-methyl tetrols and 2-methylglyceric acid in secondary organic aerosol from laboratory irradiated isoprene/NOX/SO2/air mixtures and their detection in ambient PM2.5 samples collected in the eastern United States." Atmospheric Environment **39**(29): 5281-5289.
- Ehara, K., C. Hagwood, et al. (1996). "Novel method to classify aerosol particles according to their mass-to-charge ratio" Aerosol particle mass analyser." Journal of Aerosol Science **27**(2): 217-234.
- Fang, W., L. Gong, et al. (2012). "Measurements of Secondary Organic Aerosol Formed from OH-initiated Photo-oxidation of Isoprene Using Online Photoionization Aerosol Mass Spectrometry." Environmental Science & Technology **46**(7): 3898-3904.
- Guenther, A., C. N. Hewitt, et al. (1995). "A global model of natural volatile organic compound emissions." Journal of Geophysical Research **100**: 8873-8892.
- Hoyle, C. R., M. Boy, et al. (2011). "A review of the anthropogenic influence on biogenic secondary organic aerosol." Atmos. Chem. Phys. **11**: 321-343.
- Kamens, R. M., M. W. Gery, et al. (1982). "Ozone-isoprene reactions: Product formation and aerosol potential." International Journal of Chemical Kinetics **14**(9): 955-975.
- Kleindienst, T. E., M. Lewandowski, et al. (2007). "Ozone-isoprene reaction: Re-examination of the formation of secondary organic aerosol." Geophysical Research Letters **34**.
- Kleindienst, T. E., M. Lewandowski, et al. (2009). "The formation of secondary organic aerosol from the isoprene + OH reaction in the absence of NOx." Atmos. Chem. Phys. **9**(17): 6541-6558.
- Kroll, J. H., N. L. Ng, et al. (2006). "Secondary Organic Aerosol Formation from Isoprene Photooxidation." Environmental Science & Technology **40**(6): 1869-1877.
- Liu, Y., F. Siekmann, et al. (2012). "Oligomer and SOA formation through aqueous phase photooxidation of methacrolein and methyl vinyl ketone." Atmospheric Environment **49**(0): 123-129.

- Malloy, Q. G. J., S. Nakao, et al. (2009). "Real-Time Aerosol Density Determination Utilizing a Modified Scanning Mobility Particle Sizer-Aerosol Particle Mass Analyzer System." Aerosol Science and Technology **43**: 673-678.
- Nakao, S., P. Tang, et al. (2012). "Density and elemental ratios of secondary organic aerosol: application of a density prediction method." Atmospheric Environment **In Review**.
- Ng, N. L., J. H. Kroll, et al. (2006). "Contribution of First- versus Second-Generation Products to Secondary Organic Aerosols Formed in the Oxidation of Biogenic Hydrocarbons." Environmental Science & Technology **40**(7): 2283-2297.
- Ng, N. L., A. J. Kwan, et al. (2008). "Secondary organic aerosol (SOA) formation from reaction of isoprene with nitrate radicals (NO₃)." Atmos. Chem. Phys. **8**(14): 4117-4140.
- Nguyen, T. B., A. P. Bateman, et al. (2010). "High-resolution mass spectrometry analysis of secondary organic aerosol generated by ozonolysis of isoprene." Atmospheric Environment **44**: 1032-1042.
- Nguyen, T. B., J. Laskin, et al. (2011). "Nitrogen-containing Organic Compounds and Oligomers in Secondary Organic Aerosol Formed by Photooxidation of Isoprene." Environ. Sci. Technol. **45**(16): ACS Just Accepted.
- Orsini, D. A., Y. Ma, et al. (2003). "Refinements to the particle-into-liquid sampler (PILS) for ground and airborne measurements of water soluble aerosol composition." Atmospheric Environment **37**: 1243-1259.
- Rollins, A. W., A. Kiendler-Scharr, et al. (2009). "Isoprene oxidation by nitrate radical: alkyl nitrate and secondary organic aerosol yields." Atmos. Chem. Phys. **9**(18): 6685-6703.
- Sato, K., S. Nakao, et al. (2011). "Secondary organic aerosol formation from the photooxidation of isoprene, 1,3-butadiene, and 2,3-dimethyl-1,3-butadiene under high NO_x conditions." Atmos. Chem. Phys. **11**(14): 7301-7317.
- Surratt, J. D., A. W. H. Chan, et al. (2010). "Reactive intermediates revealed in secondary organic aerosol formation from isoprene." Proceedings of the National Academy of Sciences.

- Surratt, J. D., S. M. Murphy, et al. (2006). "Chemical Composition of Secondary Organic Aerosol Formed from the Photooxidation of Isoprene." Journal of Physical Chemistry A **110**: 9665-9690.
- Weber, R. J., D. Orsini, et al. (2001). "A Particle-into-Liquid Collector for Rapid Measurement of Aerosol Bulk Chemical Composition." Aerosol Science and Technology **35**(3): 718-727.
- Zhang, H., J. D. Surratt, et al. (2011). "Effect of relative humidity on SOA formation from isoprene/NO photooxidation: enhancement of 2-methylglyceric acid and its corresponding oligoesters under dry conditions." Atmos. Chem. Phys. **11**(13): 6411-6424.

3.6 Tables

Table 3.1. Experimental conditions and aerosol mass and yield results

Run ^a	ΔHC ($\mu\text{g m}^{-3}$)	$[\text{NO}]_0$ (ppb)	$[\text{H}_2\text{O}_2]_0^b$ (ppm)	$[\text{O}_3]^c$ (ppb)	$[\text{CO}]_0$ (ppm)	Final SOA ^c ($\mu\text{g m}^{-3}$)	SOA Yield	Reaction Notes
EPA1288A	697	500	3	500+	0	68	0.10	photo-oxidation
EPA1288B	697	500	1.5	500+	0	48	0.07	photo-oxidation
EPA1353A ^d	697	500	3	500+	0	68	0.10	photo-oxidation
EPA1271A	697	250	3	500+	0	74	0.11	photo-oxidation
EPA1392A	697	250	3	500+	0	74	0.11	photo-oxidation
EPA1392B	697	250	1.5	500+	0	70	0.10	photo-oxidation
EPA1411A	697	250	3	500+	0	79	0.11	photo-oxidation
EPA1382A	697	125	3	410	0	68	0.09	photo-oxidation
EPA1382B	697	125	1.5	419	0	72	0.10	photo-oxidation
EPA1303A	697	25	3	154	0	56	0.08	photo-oxidation
EPA1303B	697	25	1.5	151	0	40	0.06	photo-oxidation
EPA1467A	697	0	3	21	0	55	0.08	photo-oxidation
EPA1467B	697	0	1.5	13	0	44	0.06	photo-oxidation
EPA1375A	697	500	0	500+	0	18	0.03	photo-oxidation
EPA1397A	669	25	0	472	0	4	0.01	photo-oxidation
EPA1425A	557	0	0	250	160	8	0.01	dark ozonolysis
EPA1480A	139	0	0	25	150	3	0.02	dark ozonolysis
EPA1398A	501	0	0	175	0	9	0.02	dark ozonolysis
EPA1438A	323	0	0	250	0	14	0.04	dark ozonolysis
EPA1440A	334	0	0	125	0	6	0.02	dark ozonolysis
EPA1445A	394	0	0	125	0	7	0.02	dark ozonolysis
EPA1473A	56	0	0	25	0	1	0.02	dark ozonolysis
EPA1476A	336	0	0	125	150	20	0.06	dark ozonolysis
EPA1562A	362	0	0	125	150	21	0.06	dark ozonolysis
EPA1560A	343	0	0	380	0	42	0.12	Dark N ₂ O ₅ , Initial N ₂ O ₅ =270 ppb

^aExperiments were conducted at $300 \pm 1\text{K}$. ^bInitial H₂O₂ concentration is not measured, but estimated by isoprene decay. ^cFor photo-oxidation this is the final observed O₃ concentration; for dark ozonolysis this is the initial O₃ concentration. ^dThis assumes an average measured density of 1.34 g cm^{-3} .

^dSome data from this experiment has been previously published (Clark, Nakao et al. 2012)

Table 3.2. Summary of SOA chemical and physical characterization data

Run	Density (g cm ⁻³)	VFR	AMS H:C	AMS O:C	AMS N:C	PILS-ToF H:C	PILS-ToF O:C	PILS-ToF N:C	PILS- ToF Percent Ions Matched	Notes
EPA1288A	1.32	-	1.50 ±0.10	0.55 ±0.05	0.09 ±0.04	-	-	-	-	b, d
EPA1353A	-	0.71	-	-	-	0.66	0.82	0.02	78	a, c
EPA1271A	1.34	-	1.53 ±0.08	0.54 ±0.08	0.08 ±0.04	-	-	-	-	b, d
EPA1392A	1.35	0.71	1.51 ±0.12	0.48 ±0.15	0.03 ±0.02	1.51	0.91	0.04	72	
EPA1411A	1.34	0.73	1.49 ±0.20	0.45 ±0.15	0.09 ±0.04	-	-	-	-	d
EPA1382A	1.36	0.63	1.65 ±0.20	0.38 ±0.15	0.12 ±0.03	1.41	0.89	0.03	78	
EPA1303A	1.33	-	1.55 ±0.20	0.48 ±0.06	0.04 ±0.02	1.39	0.87	0.01	73	b
EPA1467A	1.34	0.48	1.72 ±0.20	0.45 ±0.05	0.00	1.40	0.80	0.00	84	
EPA1375A	1.35	0.50	1.60 ±0.20	0.35 ±0.10	0.13 ±0.05	0.61	0.84	0.02	77	
EPA1397A	1.41	0.47	1.55 ±0.20	0.48 ±0.10	0.07 ±0.03	1.38	0.62	0.02	82	
EPA1425A	1.36	0.12	1.43 ±0.20	0.25 ±0.10	0.00	1.29	0.76	0.00	64	
EPA1480A	-	-	-	-	-	0.78	0.70	0.00	15	a, b, c
EPA1398A	1.38	-	1.50 ±0.15	0.29 ±0.10	0.00	1.27	0.68	0.00	62	b
EPA1438A	1.36	0.14	1.58 ±0.20	0.30 ±0.08	0.00	1.27	0.76	0.00	74	
EPA1440A	-	0.12	1.52 ±0.15	0.25 ±0.08	0.00	-	-	-	-	a, c, d
EPA1445A	1.36	0.14	-	-	-	1.49	0.69	0.00	64	c
EPA1473A	-	-	-	-	-	1.26	0.64	0.00	56	a, b, c
EPA1476A	-	-	1.54 ±0.20	0.31 ±0.05	0.00	-	-	-	-	d
EPA1562A	1.45	-	1.52 ±0.18	0.33 ±0.05	0.00	1.26	0.89	0.00	59	b
EPA1560A	1.39	0.53	1.47 ±0.15	0.40 ±0.08	0.01 ±0.005	1.07	1.03	0.17	70	

a-no APM-SMPS data available, b-no VTDMA data available, c-no AMS data available, d-no PILS-ToF data available

Table 3.3. PILS-ToF mass spectral ion matches with the corresponding correlations experiments in Table 3.1 and literature references

PILS-ToF observed m/z	TOF-MS ion formula match	Experiment Observed	References
61.9930	NO ₃	EPA1353A, EPA1375A, EPA1560A	(Ng, Kwan et al. 2008)
69.0352	C ₄ H ₅ O	EPA1425A	(Nguyen, Bateman et al. 2010)
71.0146	C ₃ H ₃ O ₂	EPA1425A, EPA1438A	(Nguyen, Bateman et al. 2010)
72.9941	C ₂ HO ₃	EPA1425A, EPA1562A	
73.0296	C ₃ H ₅ O ₂	EPA1467A, EPA1425A, EPA1562A, EPA1445A, EPA1438A	(Nguyen, Bateman et al. 2010)
75.0095	C ₂ H ₃ O ₃	EPA1467A, EPA1425A, EPA1398A, EPA1562A, EPA1445A, EPA1438A, EPA1382A, EPA1303A, EPA1397A	(Nguyen, Bateman et al. 2010)
79.0045	C ₅ H ₃ O	EPA1425A	
83.0543	C ₅ H ₇ O	EPA1398A, EPA1438A, EPA1397A	
85.0300	C ₄ H ₅ O ₂	EPA1467A, EPA1425A, EPA1398A, EPA1562A, EPA1473A, EPA1445A, EPA1438A, EPA1382A, EPA1303A, EPA1397A	(Nguyen, Bateman et al. 2010)
87.0095	C ₃ H ₃ O ₃	EPA1467A, EPA1425A, EPA1398A, EPA1562A, EPA1473A, EPA1445A, EPA1438A, EPA1392A, EPA1382A, EPA1303A, EPA1397A, EPA1375A	(Nguyen, Bateman et al. 2010)
88.0263	C ₆ H ₂ N	EPA1382A, EPA1397A	
89.0247	C ₃ H ₅ O ₃	EPA1467A, EPA1425A, EPA1398A, EPA1562A, EPA1445A, EPA1438A, EPA1382A, EPA1303A, EPA1397A	(Nguyen, Bateman et al. 2010)
91.0043	C ₂ H ₃ O ₄	EPA1467A, EPA1425A, EPA1398A, EPA1562A, EPA1445A, EPA1438A, EPA1303A	
95.0152	C ₅ H ₃ O ₂	EPA1397A	
96.9662	C ₄ HO ₃	EPA1398A, EPA1473A, EPA1397A	
97.0306	C ₅ H ₅ O ₂	EPA1425A, EPA1398A, EPA1473A, EPA1445A, EPA1438A, EPA1382A, EPA1397A	(Fang, Gong et al. 2012)
99.0438	C ₅ H ₇ O ₂	EPA1467A, EPA1425A, EPA1398A, EPA1562A, EPA1473A, EPA1445A, EPA1438A, EPA1397A	(Fang, Gong et al. 2012)
101.0253	C ₄ H ₅ O ₃	EPA1467A, EPA1425A, EPA1398A, EPA1562A, EPA1473A, EPA1445A, EPA1438A, EPA1382A, EPA1303A, EPA1397A	(Nguyen, Bateman et al. 2010)
103.0079	C ₄ H ₇ O ₃	EPA1467A, EPA1425A, EPA1398A, EPA1562A, EPA1473A, EPA1445A, EPA1438A, EPA1392A, EPA1382A, EPA1303A, EPA1397A, EPA1375A	(Fang, Gong et al. 2012)
105.0189	C ₃ H ₅ O ₄	EPA1467A, EPA1425A, EPA1398A, EPA1438A, EPA1303A, EPA1397A	

109.0514	$C_6H_5O_2$	EPA1438A	
111.0321	$C_5H_3O_3$	EPA1425A, EPA1398A, EPA1438A	(Fang, Gong et al. 2012)
113.0216	$C_5H_5O_3$	EPA1467A, EPA1425A, EPA1398A, EPA1562A, EPA1445A, EPA1438A, EPA1382A, EPA1303A, EPA1397A	(Fang, Gong et al. 2012)
114.0537	$C_4H_4NO_3$	EPA1397A	
115.0364	$C_5H_7O_3$	EPA1467A, EPA1425A, EPA1398A, EPA1562A, EPA1473A, EPA1445A, EPA1438A, EPA1392A, EPA1382A, EPA1303A, EPA1397A	(Fang, Gong et al. 2012)
117.0229	$C_5H_9O_3$	EPA1353A, EPA1467A, EPA1425A, EPA1398A, EPA1562A, EPA1445A, EPA1438A, EPA1392A, EPA1382A, EPA1303A, EPA1397A, EPA1375A	(Lin, Zhang et al. 2012)
118.0831	$C_4H_8NO_3$	EPA1397A	
119.0350	$C_4H_7O_4$	EPA1353A, EPA1425A, EPA1438A, EPA1392A, EPA1382A, EPA1303A, EPA1397A	(Sato, Nakao et al. 2011)
120.0566	$C_4H_{10}NO_3$	EPA1382A	
121.0289	$C_7H_5O_2$	EPA1425A, EPA1398A, EPA1562A, EPA1473A, EPA1445A, EPA1397A	
123.0371	$C_7H_7O_2$	EPA1467A, EPA1425A, EPA1398A, EPA1438A	
124.9891	C_5HO_4	EPA1353A, EPA1425A, EPA1480A, EPA1438A, EPA1382A, EPA1560A	
125.1282	C_9H_{17}	EPA1353A, EPA1392A, EPA1375A	
125.9869	C_4NO_4	EPA1353A, EPA1392A, EPA1375A	
126.0292	$C_5H_4NO_3$	EPA1397A	
126.9938	$C_5H_3O_4$	EPA1353A, EPA1425A, EPA1398A, EPA1562A, EPA1473A, EPA1445A, EPA1438A, EPA1392A, EPA1397A, EPA1375A, EPA1560A	(Fang, Gong et al. 2012)
129.0243	$C_5H_5O_4$	EPA1353A, EPA1467A, EPA1398A, EPA1562A, EPA1473A, EPA1445A, EPA1438A, EPA1392A, EPA1382A, EPA1303A, EPA1397A, EPA1375A	
130.0560	$C_5H_8N_1O_3$	EPA1397A	
131.0342	$C_5H_7O_4$	EPA1467A, EPA1425A, EPA1398A, EPA1562A, EPA1473A, EPA1445A, EPA1438A, EPA1382A, EPA1303A, EPA1397A	(Fang, Gong et al. 2012)
133.0154	$C_5H_9O_4$	EPA1467A, EPA1425A, EPA1398A, EPA1438A, EPA1382A, EPA1303A, EPA1397A	
135.0436	$C_8H_7O_2$	EPA1467A, EPA1425A, EPA1398A, EPA1473A, EPA1438A, EPA1303A, EPA1397A	
137.0630	$C_8H_9O_2$	EPA1467A, EPA1425A, EPA1398A, EPA1562A, EPA1473A, EPA1445A, EPA1438A, EPA1303A, EPA1397A	
138.0612	$C_7H_8NO_2$	EPA1397A	

139.0193	$C_3H_7O_6$	EPA1425A, EPA1438A	
141.0332	$C_3H_9O_6$	EPA1425A, EPA1398A, EPA1562A, EPA1473A, EPA1438A	
143.0683	$C_7H_{11}O_3$	EPA1467A, EPA1425A, EPA1480A, EPA1473A, EPA1445A, EPA1438A, EPA1382A, EPA1303A, EPA1397A	
145.0501	$C_5H_5O_5$	EPA1467A, EPA1425A, EPA1398A, EPA1562A, EPA1473A, EPA1445A, EPA1438A, EPA1382A, EPA1303A, EPA1397A	(Fang, Gong et al. 2012)
146.9714	$C_4H_3O_6$	EPA1353A, EPA1480A, EPA1560A	
147.0327	$C_5H_7O_5$	EPA1353A, EPA1467A, EPA1425A, EPA1398A, EPA1562A, EPA1473A, EPA1445A, EPA1438A, EPA1392A, EPA1382A, EPA1303A, EPA1397A, EPA1375A	(Surratt, Chan et al. 2010)
149.0465	$C_5H_9O_5$	EPA1467A, EPA1438A, EPA1398A, EPA1382A, EPA1303A, EPA1397A	
150.0389	$C_3H_4NO_6$	EPA1397A	
151.0349	$C_8H_7O_3$	EPA1467A, EPA1438A	
153.0517	$C_8H_9O_3$	EPA1467A, EPA1425A, EPA1398A, EPA1438A	
154.0233	$C_6H_4NO_4$	EPA1382A	
155.0446	$C_7H_7O_4$	EPA1425A, EPA1398A, EPA1438A, EPA1303A	
156.0498	$C_9H_2NO_2$	EPA1397A	
157.0451	$C_7H_9O_4$	EPA1467A, EPA1425A, EPA1398A, EPA1473A, EPA1438A, EPA1392A, EPA1382A, EPA1303A, EPA1397A, EPA1375A	(Nguyen, Bateman et al. 2010)
159.0402	$C_{10}H_7O_2$	EPA1467A, EPA1425A, EPA1473A, EPA1438A, EPA1382A, EPA1303A, EPA1397A	
159.9251	$C_4H_2NO_6$	EPA1397A	
161.0454	$C_9H_5O_3$	EPA1467A, EPA1425A, EPA1398A, EPA1562A, EPA1445A, EPA1438A, EPA1382A, EPA1303A, EPA1397A	
162.9701	$C_4H_3O_7$	EPA1375A	
163.0345	$C_9H_7O_3$	EPA1467A, EPA1398A, EPA1562A, EPA1473A, EPA1445A, EPA1303A, EPA1397A	
165.0274	$C_8H_5O_4$	EPA1467A, EPA1425A, EPA1398A, EPA1473A, EPA1438A, EPA1382A, EPA1397A	
165.0531	$C_6H_{13}O_5$	EPA1303A	
167.0658	$C_9H_{11}O_3$	EPA1425A, EPA1398A, EPA1438A	
169.0611	$C_8H_9O_4$	EPA1425A, EPA1398A, EPA1473A, EPA1438A, EPA1397A	
171.0616	$C_8H_{11}O_4$	EPA1467A, EPA1425A, EPA1398A, EPA1473A, EPA1445A, EPA1438A, EPA1303A, EPA1397A	

173.0446	$C_7H_9O_5$	EPA1467A, EPA1425A, EPA1398A, EPA1562A, EPA1473A, EPA1438A, EPA1382A, EPA1303A, EPA1397A
175.0405	$C_{10}H_7O_3$	EPA1467A, EPA1425A, EPA1398A, EPA1473A, EPA1438A, EPA1392A, EPA1382A, EPA1303A, EPA1397A
175.9861	$C_4H_2NO_7$	EPA1353A, EPA1382A, EPA1375A
177.0451	$C_6H_9O_6$	EPA1467A, EPA1438A, EPA1382A, EPA1303A, EPA1397A
179.0322	$C_5H_7O_7$	EPA1473A, EPA1438A
181.0408	$C_9H_9O_4$	EPA1425A, EPA1398A, EPA1438A, EPA1397A
182.0559	$C_9H_{12}NO_3$	EPA1382A, EPA1375A
183.0817	$C_6H_{15}O_6$	EPA1425A, EPA1398A, EPA1562A, EPA1473A, EPA1445A, EPA1392A, EPA1382A, EPA1397A
184.0188	$C_3H_6NO_8$	EPA1392A, EPA1382A, EPA1397A, EPA1375A
185.0619	$C_{12}H_9O_2$	EPA1467A, EPA1425A, EPA1398A, EPA1562A, EPA1473A, EPA1445A, EPA1438A, EPA1303A, EPA1397A, EPA1560A
186.0358	$C_7H_8NO_5$	EPA1392A, EPA1382A, EPA1375A
187.0599	$C_8H_{11}O_5$	EPA1467A, EPA1425A, EPA1398A, EPA1562A, EPA1480A, EPA1473A, EPA1445A, EPA1438A, EPA1382A, EPA1303A, EPA1397A
189.0410	$C_7H_9O_6$	EPA1353A, EPA1467A, EPA1398A, EPA1562A, EPA1473A, EPA1445A, EPA1438A, EPA1392A, EPA1382A, EPA1303A, EPA1397A
191.0319	$C_{10}H_7O_4$	EPA1467A, EPA1425A, EPA1438A, EPA1382A, EPA1303A
193.0407	$C_6H_9O_7$	EPA1467A, EPA1438A, EPA1382A, EPA1303A
194.0366	$C_5H_8NO_7$	EPA1560A
195.0519	$C_6H_{11}O_7$	EPA1467A, EPA1398A, EPA1438A, EPA1303A
197.1012	$C_7H_{17}O_6$	EPA1467A, EPA1425A, EPA1398A, EPA1438A, EPA1392A, EPA1382A, EPA1397A
198.0503	$C_8H_8NO_5$	EPA1382A
199.0892	$C_6H_{15}O_7$	EPA1467A, EPA1425A, EPA1398A, EPA1562A, EPA1473A, EPA1445A, EPA1438A, EPA1392A, EPA1382A, EPA1397A
200.0598	$C_4H_{10}NO_8$	EPA1303A
201.0699	$C_9H_{13}O_5$	EPA1467A, EPA1425A, EPA1398A, EPA1562A, EPA1480A, EPA1473A, EPA1445A, EPA1438A, EPA1382A, EPA1303A, EPA1397A

(Nguyen, Bateman et al. 2010; Nguyen, Laskin et al. 2011)

203.0570	$C_8H_{11}O_6$	EPA1467A, EPA1425A, EPA1398A, EPA1562A, EPA1480A, EPA1473A, EPA1438A, EPA1392A, EPA1382A, EPA1303A, EPA1397A	
204.1369	$C_8H_{14}NO_5$	EPA1397A	
205.0459	$C_{11}H_9O_4$	EPA1467A, EPA1425A, EPA1398A, EPA1438A, EPA1382A, EPA1303A, EPA1397A	
207.0534	$C_7H_{11}O_7$	EPA1467A, EPA1382A, EPA1303A, EPA1397A	
209.0616	$C_{14}H_9O_2$	EPA1467A, EPA1398A, EPA1438A	
210.0553	$C_9H_8NO_5$	EPA1382A	
211.0596	$C_{10}H_{11}O_5$	EPA1467A, EPA1425A, EPA1438A	
212.0571	$C_5H_{10}NO_8$	EPA1303A, EPA1397A	
213.0740	$C_{10}H_{13}O_5$	EPA1467A, EPA1398A, EPA1562A, EPA1473A, EPA1445A, EPA1382A, EPA1397A	
214.1604	$C_{10}H_{16}NO_4$	EPA1397A	
215.0858	$C_{10}H_{15}O_5$	EPA1467A, EPA1425A, EPA1398A, EPA1562A, EPA1480A, EPA1473A, EPA1445A, EPA1438A, EPA1392A, EPA1382A, EPA1397A	
217.0782	$C_{13}H_{13}O_3$	EPA1467A, EPA1425A, EPA1398A, EPA1562A, EPA1480A, EPA1438A, EPA1382A, EPA1303A, EPA1397A	
218.1581	$C_9H_{16}NO_5$	EPA1397A	
219.0530	$C_8H_{11}O_7$	EPA1467A, EPA1425A, EPA1398A, EPA1473A, EPA1438A, EPA1392A, EPA1382A, EPA1303A, EPA1397A	
221.0690	$C_8H_{13}O_7$	EPA1353A, EPA1467A, EPA1425A, EPA1398A, EPA1392A, EPA1382A, EPA1303A, EPA1397A, EPA1375A	(Surratt, Chan et al. 2010; Sato, Nakao et al. 2011)
222.0948	$C_{11}H_{12}NO_4$	EPA1382A	
223.0523	$C_7H_{11}O_8$	EPA1467A, EPA1382A, EPA1303A, EPA1560A	
225.0637	$C_7H_{13}O_8$	EPA1467A, EPA1303A	
226.0708	$C_{10}H_{12}NO_5$	EPA1382A, EPA1397A	
227.0554	$C_{10}H_{11}O_6$	EPA1467A, EPA1425A, EPA1398A, EPA1438A, EPA1382A, EPA1303A	
228.0566	$C_5H_{10}NO_9$	EPA1303A, EPA1397A	
229.0701	$C_9H_9O_7$	EPA1353A, EPA1467A, EPA1425A, EPA1398A, EPA1562A, EPA1480A, EPA1473A, EPA1445A, EPA1438A, EPA1392A, EPA1382A, EPA1303A, EPA1375A, EPA1560A	
230.0688	$C_5H_{12}NO_9$	EPA1303A	
231.1087	$C_{14}H_{15}O_3$	EPA1425A, EPA1398A, EPA1562A, EPA1480A, EPA1392A, EPA1382A, EPA1397A	

232.1762	$C_{10}H_{18}NO_5$	EPA1397A	
233.0679	$C_9H_{13}O_7$	EPA1467A, EPA1425A, EPA1398A, EPA1562A, EPA1473A, EPA1438A, EPA1392A, EPA1382A, EPA1303A	
234.9842	$C_{10}H_3O_7$	EPA1480A	
235.0041	$C_{14}H_3O_4$	EPA1467A, EPA1425A, EPA1398A, EPA1438A, EPA1392A, EPA1382A, EPA1303A, EPA1397A	
236.0772	$C_{11}H_{10}NO_5$	EPA1382A	
237.0649	$C_8H_{13}O_8$	EPA1467A, EPA1392A, EPA1382A, EPA1303A	
238.0893	$C_{11}H_{12}NO_5$	EPA1382A	
239.0229	$C_5H_7N_2O_9$	EPA1560A	(Ng, Kwan et al. 2008)
239.0774	$C_8H_{15}O_8$	EPA1467A, EPA1473A, EPA1392A, EPA1382A, EPA1303A, EPA1397A	
239.1684	$C_{10}H_{23}O_6$	EPA1445A	
240.0654	$C_{10}H_{10}NO_6$	EPA1382A	
241.0383	$C_5H_9N_2O_9$	EPA1560A	(Rollins, Kiendler-Scharr et al. 2009)
241.0643	$C_{11}H_{13}O_6$	EPA1467A, EPA1382A, EPA1303A	
243.9369	$C_7H_2NO_9$	EPA1375A	
242.0700	$C_{13}H_8NO_4$	EPA1382A, EPA1303A	
243.0546	$C_{10}H_{11}O_7$	EPA1467A, EPA1425A, EPA1398A, EPA1438A, EPA1303A	
243.9312	$C_7H_2NO_9$	EPA1382A, EPA1397A, EPA1375A	
245.0699	$C_{10}H_{13}O_7$	EPA1425A, EPA1398A, EPA1438A, EPA1303A, EPA1560A	(Nguyen, Bateman et al. 2010)
245.9275	$C_7H_4NO_9$	EPA1382A, EPA1375A	
247.0792	$C_{10}H_{15}O_7$	EPA1467A, EPA1425A, EPA1398A, EPA1562A, EPA1473A, EPA1445A, EPA1438A, EPA1382A, EPA1303A	
248.9064	$C_{10}H_1O_8$	EPA1392A, EPA1382A, EPA1375A	
249.0623	$C_9H_{13}O_8$	EPA1353A, EPA1467A, EPA1425A, EPA1398A, EPA1473A, EPA1438A, EPA1392A, EPA1382A, EPA1303A, EPA1397A, EPA1375A	(Surratt, Chan et al. 2010; Sato, Nakao et al. 2011)
250.0763	$C_8H_{12}NO_8$	EPA1392A, EPA1382A, EPA1375A	
251.0791	$C_9H_{15}O_8$	EPA1467A, EPA1438A, EPA1382A, EPA1303A, EPA1375A	
252.0506	$C_7H_{10}NO_9$	EPA1392A, EPA1382A	
253.0697	$C_9H_{15}O_8$	EPA1467A, EPA1303A	(Lin, Zhang et al. 2012)
254.0707	$C_7H_{12}NO_9$	EPA1303A	
255.0769	$C_{10}H_{21}O_7$	EPA1467A, EPA1438A, EPA1382A, EPA1303A	
257.0338*	$C_5H_8NO_7$ + NO_3	EPA1560A	(Ng, Kwan et al. 2008)
257.0400	$C_{10}H_9O_8$	EPA1392A, EPA1382A	

257.1175	$C_8H_{17}O_9$	EPA1303A	
257.1802	$C_{14}H_{25}O_4$	EPA1398A, EPA1397A	
258.2325	$C_{13}H_{24}NO_4$	EPA1397A	
259.0706	$C_7H_{15}O_9$	EPA1467A, EPA1425A, EPA1398A, EPA1438A, EPA1392A, EPA1382A, EPA1303A, EPA1560A	
260.0286	$C_8H_6NO_9$	EPA1392A, EPA1382A	
261.0786	$C_7H_{15}O_{10}$	EPA1467A, EPA1425A, EPA1398A, EPA1438A, EPA1382A, EPA1303A	
263.0755	$C_{10}H_{15}O_8$	EPA1353A, EPA1467A, EPA1425A, EPA1398A, EPA1438A, EPA1392A, EPA1382A, EPA1303A, EPA1397A, EPA1375A	(Surratt, Chan et al. 2010; Sato, Nakao et al. 2011)
264.0893	$C_9H_{14}NO_8$	EPA1392A, EPA1382A	
265.0681	$C_{13}H_{13}O_6$	EPA1467A, EPA1438A, EPA1382A, EPA1303A	
266.0556	$C_8H_{12}NO_9$	EPA1353A, EPA1392A, EPA1382A, EPA1303A, EPA1397A, EPA1375A	(Surratt, Chan et al. 2010; Sato, Nakao et al. 2011)
267.0596	$C_{12}H_{11}O_7$	EPA1353A, EPA1467A, EPA1392A, EPA1382A, EPA1303A, EPA1397A, EPA1375A	
268.0887	$C_8H_{14}NO_9$	EPA1382A	
269.0882	$C_9H_{17}O_9$	EPA1467A	
271.0110	$C_{10}H_7O_9$	EPA1353A, EPA1438A, EPA1382A, EPA1303A, EPA1375A	
272.0445	$C_{10}H_{10}NO_8$	EPA1560A	
272.0826	$C_7H_{14}NO_{10}$	EPA1303A	
273.1136	$C_8H_{17}O_{10}$	EPA1398A, EPA1438A, EPA1303A, EPA1397A	
274.0247	$C_9H_8NO_9$	EPA1560A	
275.0777	$C_{11}H_{15}O_8$	EPA1467A, EPA1425A, EPA1398A, EPA1382A, EPA1303A, EPA1397A, EPA1560A	
277.1113	$C_{15}H_{17}O_5$	EPA1467A, EPA1398A, EPA1392A, EPA1382A, EPA1303A, EPA1397A, EPA1375A	
278.0951	$C_6H_{16}NO_{11}$	EPA1382A, EPA1397A	
279.0727	$C_{10}H_{15}O_9$	EPA1467A, EPA1425A, EPA1398A, EPA1392A, EPA1382A, EPA1303A	
280.1011	$C_{13}H_{14}NO_6$	EPA1382A	
281.0869	$C_{10}H_{17}O_9$	EPA1467A, EPA1382A	
282.1089	$C_9H_{16}NO_9$	EPA1382A	
283.0803	$C_{13}H_{15}O_7$	EPA1467A, EPA1382A, EPA1303A	
284.0837	$C_8H_{14}NO_{10}$	EPA1303A	
285.0895	$C_{13}H_{17}O_7$	EPA1467A, EPA1303A	
286.0240	$C_{10}H_8NO_9$	EPA1560A	
286.0551	$C_7H_{12}NO_{11}$	EPA1382A	
287.1224	$C_{12}H_{15}O_8$	EPA1438A, EPA1382A, EPA1303A, EPA1397A	

288.0359	$C_{10}H_{10}NO_9$	EPA1353A, EPA1392A, EPA1382A, EPA1303A, EPA1397A, EPA1375A, EPA1560A	
289.0847	$C_{19}H_{13}O_3$	EPA1467A, EPA1425A, EPA1398A, EPA1438A, EPA1392A, EPA1382A, EPA1303A, EPA1397A	
291.0765	$C_{11}H_{15}O_9$	EPA1353A, EPA1467A, EPA1438A, EPA1392A, EPA1382A, EPA1303A, EPA1375A	(Nguyen, Laskin et al. 2011)
292.1077	$C_7H_{18}NO_{11}$	EPA1382A	
293.0801	$C_{10}H_{13}O_{10}$	EPA1467A, EPA1425A, EPA1438A, EPA1392A, EPA1382A, EPA1303A	(Nguyen, Bateman et al. 2010)
294.0888	$C_{13}H_{12}NO_7$	EPA1382A	
295.0974	$C_{10}H_{15}O_{10}$	EPA1382A	
296.0649	$C_9H_{14}N_1O_{10}$	EPA1353A, EPA1392A, EPA1382A	(Nguyen, Laskin et al. 2011)
297.2479	$C_{17}H_{29}O_4$	EPA1445A	
298.0901	$C_9H_{16}NO_{10}$	EPA1392A, EPA1382A, EPA1303A	
299.1579	$C_{11}H_{23}O_9$	EPA1303A	
301.0436	$C_{11}H_9O_{10}$	EPA1392A	
301.1382	$C_{13}H_{17}O_8$	EPA1438A, EPA1382A, EPA1303A	
302.0193	$C_{10}H_8NO_{10}$	EPA1560A	
303.1161	$C_9H_{19}O_{11}$	EPA1398A, EPA1438A, EPA1382A, EPA1303A	
304.0260	$C_{10}H_{10}N_1O_{10}$	EPA1353A, EPA1392A, EPA1382A, EPA1303A, EPA1375A, EPA1560A	(Nguyen, Laskin et al. 2011)
305.0867	$C_{12}H_{17}O_9$	EPA1353A, EPA1467A, EPA1438A, EPA1392A, EPA1382A, EPA1303A, EPA1397A, EPA1375A	(Nguyen, Laskin et al. 2011)
306.1163	$C_8H_{20}NO_{11}$	EPA1382A	
307.0718	$C_{11}H_{15}O_{10}$	EPA1353A, EPA1467A, EPA1392A, EPA1382A, EPA1303A, EPA1375A	(Nguyen, Laskin et al. 2011)
308.1061	$C_{10}H_{14}NO_{10}$	EPA1382A	
309.0910	$C_{11}H_{17}O_{10}$	EPA1467A, EPA1392A, EPA1382A, EPA1303A	
310.1038	$C_{17}H_{12}NO_5$	EPA1382A	
311.0990	$C_{10}H_{15}O_{11}$	EPA1382A	
311.2097	$C_{14}H_{31}O_7$	EPA1562A, EPA1473A, EPA1438A, EPA1397A	
312.0603	$C_9H_{14}NO_{11}$	EPA1353A, EPA1392A, EPA1382A	
313.1279	$C_{18}H_{17}O_5$	EPA1303A	
314.0959	$C_9H_{16}NO_{11}$	EPA1303A	
315.1410	$C_{10}H_{19}O_{11}$	EPA1438A, EPA1303A	
317.1160	$C_9H_{17}O_{12}$	EPA1398A, EPA1438A, EPA1382A, EPA1303A	
319.0997	$C_9H_{19}O_{12}$	EPA1467A, EPA1438A, EPA1392A, EPA1382A, EPA1303A	
321.0861	$C_{12}H_{17}O_{10}$	EPA1353A, EPA1467A, EPA1392A, EPA1382A, EPA1303A, EPA1375A	(Nguyen, Laskin et al. 2011)

322.1235	$C_8H_{20}NO_{12}$	EPA1382A	
323.0976	$C_{12}H_{19}O_{10}$	EPA1353A, EPA1467A, EPA1392A, EPA1382A, EPA1303A, EPA1397A, EPA1375A	(Surratt, Chan et al. 2010; Sato, Nakao et al. 2011)
324.1217	$C_{11}H_{18}NO_{10}$	EPA1382A	
325.1084	$C_{11}H_{17}O_{11}$	EPA1382A	
326.0992	$C_{10}H_{16}NO_{11}$	EPA1382A	
327.0699	$C_9H_{15}N_2O_{11}$	EPA1353A, EPA1392A, EPA1382A, EPA1397A, EPA1375A	(Sato, Nakao et al. 2011)
327.3202	$C_{20}H_{39}O_3$	EPA1398A	
328.3745	$C_{19}H_{38}NO_3$	EPA1397A	
329.1407	$C_{11}H_{21}O_{11}$	EPA1303A, EPA1397A	
331.1483	$C_{14}H_{19}O_9$	EPA1438A, EPA1382A, EPA1303A	
333.0241*	$C_5H_8N_3O_{10} + NO_3$	EPA1560A	(Ng, Kwan et al. 2008)
333.0363	$C_{13}H_{17}O_{10}$	EPA1353A, EPA1467A, EPA1398A, EPA1562A, EPA1438A, EPA1392A, EPA1382A, EPA1303A, EPA1375A	(Nguyen, Laskin et al. 2011)
334.0552	$C_8H_{16}NO_{13}$	EPA1392A, EPA1382A	
335.0973	$C_{13}H_{19}O_{10}$	EPA1353A, EPA1467A, EPA1438A, EPA1392A, EPA1382A, EPA1303A, EPA1375A	(Nguyen, Laskin et al. 2011)
336.1283	$C_{12}H_{18}NO_{10}$	EPA1382A	
337.0958	$C_{12}H_{17}O_{11}$	EPA1467A, EPA1392A, EPA1382A, EPA1397A	
338.1190	$C_8H_{20}NO_{13}$	EPA1382A, EPA1397A	
339.0917	$C_7H_{19}N_2O_{13}$	EPA1353A, EPA1392A, EPA1382A	
340.1257	$C_{11}H_{18}NO_{11}$	EPA1382A	
341.1058	$C_{11}H_{17}O_{12}$	EPA1382A	
343.1077	$C_{11}H_{19}O_{12}$	EPA1382A, EPA1303A	
345.1576	$C_{12}H_{25}O_{11}$	EPA1398A, EPA1303A, EPA1397A	
347.1537	$C_{14}H_{19}O_{10}$	EPA1438A, EPA1382A, EPA1303A	
349.0812	$C_{13}H_{17}O_{11}$	EPA1353A, EPA1467A, EPA1438A, EPA1392A, EPA1382A, EPA1303A, EPA1375A	
350.1284	$C_9H_{20}NO_{13}$	EPA1382A	
351.0956	$C_{13}H_{19}O_{11}$	EPA1353A, EPA1467A, EPA1392A, EPA1382A, EPA1303A, EPA1375A	(Surratt, Chan et al. 2010; Sato, Nakao et al. 2011)
352.0969	$C_{12}H_{18}NO_{11}$	EPA1353A, EPA1392A, EPA1382A, EPA1375A	
353.1153	$C_{13}H_{21}O_{11}$	EPA1392A, EPA1382A	
354.0724	$C_{11}H_{16}NO_{12}$	EPA1353A	
356.1011	$C_{15}H_{18}NO_9$	EPA1560A	
357.1601	$C_{13}H_{25}O_{11}$	EPA1303A	
359.2355	$C_{13}H_{27}O_{11}$	EPA1397A	
361.1443	$C_{15}H_{21}O_{10}$	EPA1303A	
363.0960	$C_{14}H_{19}O_{11}$	EPA1353A, EPA1438A, EPA1392A, EPA1382A, EPA1303A	
364.1384	$C_{10}H_{22}NO_{13}$	EPA1382A	

365.1100	$C_{14}H_{21}O_{11}$	EPA1353A, EPA1392A, EPA1382A, EPA1303A, EPA1375A	(Surratt, Chan et al. 2010; Sato, Nakao et al. 2011)
366.1010	$C_{13}H_{20}NO_{11}$	EPA1353A, EPA1392A, EPA1382A, EPA1375A	
367.1114	$C_{13}H_{19}O_{12}$	EPA1392A	
368.0856	$C_{12}H_{18}NO_{12}$	EPA1353A, EPA1392A, EPA1382A, EPA1375A	(Surratt, Chan et al. 2010; Sato, Nakao et al. 2011)
369.0887	$C_{16}H_{17}O_{10}$	EPA1353A, EPA1392A, EPA1382A, EPA1375A	
370.0828	$C_{10}H_{16}N_3O_{12}$	EPA1560A	(Ng, Kwan et al. 2008)
370.1033	$C_{12}H_{20}NO_{12}$	EPA1392A, EPA1382A	
372.1027	$C_{11}H_{18}NO_{13}$	EPA1382A	
373.1208	$C_{12}H_{21}O_{13}$	EPA1382A, EPA1303A	
375.1514	$C_{12}H_{23}O_{13}$	EPA1382A, EPA1303A	
377.1490	$C_{12}H_{25}O_{13}$	EPA1382A, EPA1303A	
378.0847	$C_{13}H_{16}NO_{12}$	EPA1392A, EPA1382A	
379.0950	$C_{13}H_{19}N_2O_{11}$	EPA1353A, EPA1392A, EPA1382A, EPA1303A, EPA1375A	
380.1108	$C_{13}H_{18}NO_{12}$	EPA1392A, EPA1382A	
381.1183	$C_{14}H_{21}O_{12}$	EPA1392A, EPA1382A	
382.1126	$C_{13}H_{20}NO_{12}$	EPA1392A, EPA1382A	
384.1147	$C_9H_{22}NO_{15}$	EPA1392A, EPA1382A	
386.0779	$C_{10}H_{16}N_3O_{13}$	EPA1560A	(Ng, Kwan et al. 2008)
387.1705	$C_{14}H_{27}O_{12}$	EPA1303A	
388.0924	$C_{15}H_{18}NO_{11}$	EPA1560A	
389.1826	$C_{13}H_{25}O_{13}$	EPA1382A, EPA1303A	
391.1584	$C_{13}H_{27}O_{13}$	EPA1382A, EPA1303A	
393.1063	$C_{15}H_{21}O_{12}$	EPA1353A, EPA1392A, EPA1382A, EPA1375A	(Nguyen, Laskin et al. 2011)
394.1193	$C_{14}H_{20}NO_{12}$	EPA1392A, EPA1382A	
395.1062	$C_{11}H_{23}O_{15}$	EPA1353A, EPA1392A, EPA1382A	
396.1011	$C_{13}H_{18}NO_{13}$	EPA1392A, EPA1382A	
397.1433	$C_{11}H_{25}O_{15}$	EPA1382A	
398.1104	$C_{13}H_{20}NO_{13}$	EPA1392A, EPA1382A	
399.2687	$C_{14}H_{27}N_2O_{11}$	EPA1397A	
400.1241	$C_{13}H_{22}NO_{13}$	EPA1392A, EPA1382A	
401.1526	$C_{14}H_{25}O_{13}$	EPA1382A, EPA1303A	
402.0739	$C_{15}H_{16}NO_{12}$	EPA1560A	
403.1783	$C_{14}H_{27}O_{13}$	EPA1303A	
404.0883	$C_{15}H_{18}NO_{12}$	EPA1560A	
405.1638	$C_{13}H_{25}O_{14}$	EPA1382A, EPA1303A	
407.1186	$C_{16}H_{23}O_{12}$	EPA1353A, EPA1392A, EPA1382A, EPA1303A, EPA1375A	(Nguyen, Laskin et al. 2011)
408.1303	$C_{15}H_{22}NO_{12}$	EPA1392A	
409.1024	$C_{15}H_{21}O_{13}$	EPA1353A, EPA1392A, EPA1382A, EPA1375A	
410.0975	$C_{14}H_{20}NO_{13}$	EPA1353A, EPA1392A, EPA1382A	
411.1286	$C_{15}H_{23}O_{13}$	EPA1392A	
412.1492	$C_{11}H_{26}NO_{15}$	EPA1382A	
413.1982	$C_{16}H_{29}O_{12}$	EPA1473A, EPA1445A, EPA1382A, EPA1397A	

414.1472	$C_{10}H_{24}NO_{16}$	EPA1382A, EPA1397A	
417.1850	$C_{15}H_{29}O_{13}$	EPA1303A, EPA1397A	
419.1702	$C_{14}H_{27}O_{14}$	EPA1382A, EPA1303A	
420.083	$C_{15}H_{18}NO_{13}$	EPA1560A	
421.1349	$C_{13}H_{25}O_{15}$	EPA1392A, EPA1382A, EPA1303A	
422.1519	$C_{12}H_{24}NO_{15}$	EPA1382A	
423.1150	$C_{16}H_{23}O_{13}$	EPA1353A, EPA1392A, EPA1382A, EPA1375A	
424.1293	$C_{15}H_{22}NO_{13}$	EPA1392A, EPA1382A	
425.1244	$C_{16}H_{25}O_{13}$	EPA1353A, EPA1392A, EPA1382A, EPA1375A	(Surratt, Chan et al. 2010; Sato, Nakao et al. 2011)
426.1266	$C_{11}H_{24}NO_{16}$	EPA1392A, EPA1382A	
427.2134	$C_{17}H_{31}O_{12}$	EPA1473A, EPA1445A, EPA1397A	
428.1522	$C_{11}H_{26}NO_{16}$	EPA1382A, EPA1397A	
429.1011	$C_{13}H_{21}N_2O_{14}$	EPA1353A, EPA1392A, EPA1392A, EPA1382A, EPA1375A	(Sato, Nakao et al. 2011)
429.1697	$C_{16}H_{29}O_{13}$	EPA1425A	
430.1206	$C_{10}H_{24}NO_{17}$	EPA1392A, EPA1382A	
431.2343	$C_{17}H_{35}O_{12}$	EPA1398A, EPA1397A	
432.3087	$C_{23}H_{30}NO_7$	EPA1397A	
433.0785*	$C_{10}H_{16}N_3O_{12} + NO_3$	EPA1560A	(Ng, Kwan et al. 2008)
433.1583	$C_{15}H_{29}O_{14}$	EPA1425A, EPA1303A	
434.0809	$C_{12}H_{20}NO_{16}$	EPA1560A	
435.1182	$C_{17}H_{23}O_{13}$	EPA1353A, EPA1392A, EPA1382A, EPA1303A, EPA1560A	
437.1253	$C_{12}H_{25}N_2O_{15}$	EPA1353A, EPA1392A, EPA1382A	
438.1614	$C_{12}H_{24}NO_{16}$	EPA1382A	
439.1293	$C_{16}H_{23}O_{14}$	EPA1392A, EPA1382A	
440.1234	$C_{15}H_{22}NO_{14}$	EPA1392A, EPA1382A	
441.1402	$C_{16}H_{25}O_{14}$	EPA1392A, EPA1382A	
442.1674	$C_{12}H_{28}NO_{16}$	EPA1382A	
445.1526	$C_{11}H_{25}O_{18}$	EPA1382A, EPA1397A	
446.3258	$C_{17}H_{36}NO_{12}$	EPA1397A	
447.1638	$C_{30}H_{23}O_4$	EPA1425A, EPA1398A	
449.0735	$C_{10}H_{17}N_4O_{16}$	EPA1560A	(Ng, Kwan et al. 2008)
449.1730	$C_{15}H_{29}O_{15}$	EPA1382A	
450.0758	$C_{12}H_{20}NO_{17}$	EPA1560A	
451.1133	$C_{17}H_{23}O_{14}$	EPA1353A, EPA1392A, EPA1382A, EPA1560A	
453.1250	$C_{17}H_{25}O_{14}$	EPA1353A, EPA1392A, EPA1382A, EPA1375A	(Surratt, Chan et al. 2010; Sato, Nakao et al. 2011)
454.1249	$C_{16}H_{24}NO_{14}$	EPA1353A, EPA1392A, EPA1382A, EPA1375A	
455.1474	$C_{12}H_{27}N_2O_{16}$	EPA1392A, EPA1382A	
456.1250	$C_{19}H_{22}NO_{12}$	EPA1392A, EPA1382A	
457.2582	$C_{19}H_{37}O_{12}$	EPA1473A, EPA1445A, EPA1382A, EPA1397A	
461.1603	$C_{27}H_{25}O_7$	EPA1425A, EPA1398A	
463.1785	$C_{15}H_{27}O_{16}$	EPA1382A	
465.0689	$C_{15}H_{17}N_2O_{15}$	EPA1560A	

465.1252	$C_{18}H_{25}O_{14}$	EPA1353A, EPA1392A, EPA1382A	
467.0832	$C_{15}H_{19}N_2O_{15}$	EPA1560A	
467.1386	$C_{18}H_{27}O_{14}$	EPA1353A, EPA1392A, EPA1382A, EPA1375A	(Surratt, Chan et al. 2010; Sato, Nakao et al. 2011)
468.1215	$C_{13}H_{26}NO_{17}$	EPA1353A, EPA1392A, EPA1382A	
469.1214	$C_{17}H_{25}O_{15}$	EPA1353A, EPA1392A, EPA1382A	
470.1344	$C_{13}H_{28}NO_{17}$	EPA1560A	
470.1146	$C_{16}H_{24}NO_{15}$	EPA1353A, EPA1392A, EPA1382A, EPA1375A	(Surratt, Chan et al. 2010; Sato, Nakao et al. 2011)
471.1178	$C_{20}H_{23}O_{13}$	EPA1353A, EPA1473A, EPA1392A, EPA1382A, EPA1397A	
471.3020	$C_{20}H_{39}O_{12}$	EPA1445A, EPA1375A	
472.1185	$C_{12}H_{26}NO_{18}$	EPA1353A, EPA1392A, EPA1382A	
477.1925	$C_{16}H_{29}O_{16}$	EPA1382A	
478.0657	$C_{13}H_{20}NO_{18}$	EPA1560A	
479.1897	$C_{16}H_{31}O_{16}$	EPA1382A	
481.1252	$C_{18}H_{25}O_{15}$	EPA1353A, EPA1392A, EPA1382A	
482.1433	$C_{14}H_{28}NO_{17}$	EPA1392A, EPA1382A	
483.1321	$C_{13}H_{27}N_2O_{17}$	EPA1353A, EPA1392A, EPA1382A	
484.1449	$C_{17}H_{26}NO_{15}$	EPA1392A	
485.1809	$C_{14}H_{29}O_{18}$	EPA1382A	
486.1450	$C_{13}H_{28}NO_{18}$	EPA1392A, EPA1382A, EPA1560A	
491.1859	$C_{16}H_{31}N_2O_{15}$	EPA1392A, EPA1382A	
494.0631	$C_{10}H_{16}N_5O_{18}$	EPA1560A	(Ng, Kwan et al. 2008)
495.1360	$C_{19}H_{27}O_{15}$	EPA1353A, EPA1392A, EPA1382A, EPA1375A	
496.1335	$C_{18}H_{26}NO_{15}$	EPA1353A, EPA1392A, EPA1382A	
497.1545	$C_{15}H_{29}O_{18}$	EPA1392A, EPA1382A	
498.1155	$C_{17}H_{24}NO_{16}$	EPA1353A, EPA1392A, EPA1382A	
499.1843	$C_{15}H_{31}O_{18}$	EPA1382A	
500.1232	$C_{17}H_{26}NO_{16}$	EPA1353A, EPA1392A, EPA1382A	
501.1417	$C_{13}H_{29}N_2O_{18}$	EPA1560A	
502.1554	$C_{17}H_{28}NO_{16}$	EPA1392A, EPA1382A	
507.2038	$C_{17}H_{31}O_{17}$	EPA1382A	
509.1464	$C_{15}H_{29}N_2O_{17}$	EPA1353A, EPA1392A, EPA1382A	
510.2006	$C_{16}H_{32}NO_{17}$	EPA1382A	
511.1320	$C_{19}H_{27}O_{16}$	EPA1353A, EPA1392A, EPA1382A	
512.0705*	$C_{10}H_{17}N_4O_{16} +$ NO_3	EPA1560A	
512.1274	$C_{18}H_{26}NO_{16}$	EPA1353A, EPA1392A, EPA1382A	(Ng, Kwan et al. 2008)
513.1380	$C_{14}H_{29}N_2O_{18}$	EPA1353A, EPA1392A, EPA1382A, EPA1560A	
514.1883	$C_{14}H_{28}NO_{19}$	EPA1382A	
517.1370	$C_{13}H_{29}N_2O_{19}$	EPA1560A	
523.1653	$C_{17}H_{31}O_{18}$	EPA1392A, EPA1382A	
525.1438	$C_{20}H_{29}O_{16}$	EPA1353A, EPA1392A, EPA1382A, EPA1375A	
526.1612	$C_{19}H_{28}NO_{16}$	EPA1392A, EPA1382A	
527.1491	$C_{20}H_{31}O_{16}$	EPA1353A, EPA1392A, EPA1382A, EPA1375A	(Surratt, Chan et al. 2010; Sato, Nakao et al. 2011)
528.1549	$C_{15}H_{30}NO_{19}$	EPA1392A, EPA1382A	

531.1283	$C_{17}H_{27}N_2O_{17}$	EPA1353A, EPA1392A, EPA1382A, EPA1375A	(Sato, Nakao et al. 2011)
532.1533	$C_{14}H_{30}NO_{20}$	EPA1392A, EPA1382A	
533.1316	$C_{13}H_{29}N_2O_{20}$	EPA1560A	
537.1699	$C_{20}H_{29}N_2O_{15}$	EPA1392A, EPA1397A	
539.1519	$C_{17}H_{31}O_{19}$	EPA1353A, EPA1392A, EPA1382A	
541.1632	$C_{19}H_{29}N_2O_{16}$	EPA1392A, EPA1382A	
542.1561	$C_{19}H_{28}N_1O_{17}$	EPA1392A, EPA1382A	
543.1723	$C_{15}H_{31}N_2O_{19}$	EPA1392A, EPA1382A	
549.12683	$C_{13}H_{29}N_2O_{21}$	EPA1560A	
551.4142	$C_{25}H_{43}O_{13}$	EPA1397A	
553.1430	$C_{21}H_{29}O_{17}$	EPA1353A, EPA1392A, EPA1382A	
555.1539	$C_{21}H_{31}O_{17}$	EPA1353A, EPA1392A, EPA1382A, EPA1375A	(Surratt, Chan et al. 2010; Sato, Nakao et al. 2011)
556.1522	$C_{20}H_{30}NO_{17}$	EPA1353A, EPA1392A, EPA1382A	
580.1325	$C_{10}H_{16}N_5O_{18}$	EPA1560A	
557.0560*	$C_{10}H_{16}N_5O_{18}$ + NO_3	EPA1560A	(Ng, Kwan et al. 2008)
557.1795	$C_{17}H_{33}O_{20}$	EPA1392A, EPA1382A	
558.1591	$C_{23}H_{28}NO_{15}$	EPA1392A	
567.1535	$C_{22}H_{31}O_{17}$	EPA1353A, EPA1392A, EPA1382A	
569.1668	$C_{22}H_{33}O_{17}$	EPA1353A, EPA1392A, EPA1382A, EPA1375A	
570.1480	$C_{17}H_{32}NO_{20}$	EPA1353A, EPA1392A, EPA1382A	
571.1763	$C_{20}H_{31}N_2O_{17}$	EPA1392A, EPA1382A	
572.1445	$C_{20}H_{30}NO_{18}$	EPA1353A, EPA1392A, EPA1382A, EPA1375A	(Surratt, Chan et al. 2010; Sato, Nakao et al. 2011)
573.1476	$C_{24}H_{29}O_{16}$	EPA1353A, EPA1392A, EPA1382A	
574.1711	$C_{27}H_{28}NO_{13}$	EPA1392A	
580.1325	$C_{18}H_{30}NO_{20}$	EPA1560A	
581.2292	$C_{19}H_{33}O_{20}$	EPA1382A	
583.1538	$C_{22}H_{31}O_{18}$	EPA1353A, EPA1392A, EPA1382A	
584.2215	$C_{18}H_{34}NO_{20}$	EPA1382A	
585.1851	$C_{17}H_{33}N_2O_{20}$	EPA1392A, EPA1382A	
586.1768	$C_{21}H_{32}NO_{18}$	EPA1392A, EPA1382A	
588.1760	$C_{17}H_{34}NO_{21}$	EPA1392A, EPA1382A	
595.2362	$C_{20}H_{35}O_{20}$	EPA1382A	
597.1638	$C_{23}H_{33}O_{18}$	EPA1353A, EPA1392A, EPA1382A	
599.1873	$C_{19}H_{35}O_{21}$	EPA1392A, EPA1382A	
600.1710	$C_{25}H_{30}NO_{16}$	EPA1392A, EPA1382A	
602.1780	$C_{21}H_{32}NO_{19}$	EPA1392A, EPA1382A	
604.1859	$C_{21}H_{34}NO_{19}$	EPA1392A, EPA1382A	
611.1964	$C_{19}H_{35}N_2O_{20}$	EPA1392A, EPA1382A	
613.1606	$C_{23}H_{33}O_{19}$	EPA1353A, EPA1392A, EPA1382A	
614.1557	$C_{22}H_{32}NO_{19}$	EPA1353A, EPA1392A	
615.1923	$C_{18}H_{35}N_2O_{21}$	EPA1392A	
625.2459	$C_{21}H_{37}O_{21}$	EPA1382A	
627.1725	$C_{24}H_{35}O_{19}$	EPA1353A, EPA1392A, EPA1382A	
628.1896	$C_{23}H_{34}NO_{19}$	EPA1392A	

629.2044	$C_{19}H_{37}N_2O_{21}$	EPA1392A, EPA1382A	
630.1853	$C_{26}H_{32}NO_{17}$	EPA1392A	
432.3087	$C_{23}H_{30}NO_7$	EPA1397A	
633.1836	$C_{21}H_{33}N_2O_{20}$	EPA1392A, EPA1382A	
641.2061	$C_{20}H_{37}N_2O_{21}$	EPA1392A, EPA1382A	
643.1979	$C_{24}H_{35}O_{20}$	EPA1392A	
645.2017	$C_{19}H_{37}N_2O_{22}$	EPA1392A	
645.4517	$C_{23}H_{49}O_{20}$	EPA1397A	
646.4539	$C_{26}H_{48}NO_{17}$	EPA1397A	
655.1998	$C_{18}H_{39}O_{25}$	EPA1392A	
657.1823	$C_{25}H_{37}O_{20}$	EPA1353A, EPA1392A, EPA1382A, EPA1375A	(Surratt, Chan et al. 2010; Sato, Nakao et al. 2011)
658.2070	$C_{24}H_{36}NO_{20}$	EPA1392A	
659.2118	$C_{21}H_{39}O_{23}$	EPA1392A, EPA1397A	
660.4719	$C_{27}H_{50}NO_{17}$	EPA1397A	
669.2075	$C_{21}H_{37}N_2O_{22}$	EPA1392A	
671.1933	$C_{26}H_{39}O_{20}$	EPA1353A, EPA1392A, EPA1382A, EPA1375A	(Surratt, Chan et al. 2010; Sato, Nakao et al. 2011)
672.1750	$C_{17}H_{38}NO_{26}$	EPA1353A, EPA1392A	
673.2079	$C_{25}H_{37}O_{21}$	EPA1392A	
674.1723	$C_{24}H_{36}NO_{21}$	EPA1353A, EPA1392A, EPA1382A, EPA1375A	(Surratt, Chan et al. 2010; Sato, Nakao et al. 2011)
675.1766	$C_{28}H_{35}O_{19}$	EPA1353A, EPA1392A	
685.2107	$C_{19}H_{41}O_{26}$	EPA1392A	
687.2172	$C_{21}H_{39}N_2O_{23}$	EPA1392A	
699.2192	$C_{22}H_{39}N_2O_{23}$	EPA1392A	
701.2191	$C_{23}H_{41}O_{24}$	EPA1392A	
704.2100	$C_{25}H_{38}NO_{22}$	EPA1392A	
713.2286	$C_{23}H_{41}N_2O_{23}$	EPA1392A	
715.2197	$C_{20}H_{43}O_{27}$	EPA1392A	
729.2282	$C_{23}H_{41}N_2O_{24}$	EPA1392A	
731.2339	$C_{24}H_{43}O_{25}$	EPA1392A	
735.2167	$C_{25}H_{39}N_2O_{23}$	EPA1392A	
759.2090	$C_{29}H_{43}O_{23}$	EPA1353A, EPA1392A, EPA1375A	(Surratt, Chan et al. 2010; Sato, Nakao et al. 2011)
760.2394	$C_{28}H_{42}NO_{23}$	EPA1392A	
773.2530	$C_{25}H_{45}N_2O_{25}$	EPA1392A	
774.2421	$C_{25}H_{44}NO_{26}$	EPA1392A	
776.2022	$C_{28}H_{42}NO_{24}$	EPA1353A, EPA1392A, EPA1375A	(Surratt, Chan et al. 2010; Sato, Nakao et al. 2011)
777.2374	$C_{25}H_{45}O_{27}$	EPA1392A	
801.2545	$C_{26}H_{45}N_2O_{26}$	EPA1392A	
861.274	$C_{28}H_{49}N_2O_{28}$	EPA1392A	
875.2851	$C_{29}H_{51}N_2O_{28}$	EPA1392A	
878.2288	$C_{32}H_{48}NO_{27}$	EPA1353A, EPA1392A	(Surratt, Chan et al. 2010; Sato, Nakao et al. 2011)
980.3003	$C_{36}H_{54}NO_{30}$	EPA1392A	(Surratt, Chan et al. 2010; Sato, Nakao et al. 2011)

3.7 Figures

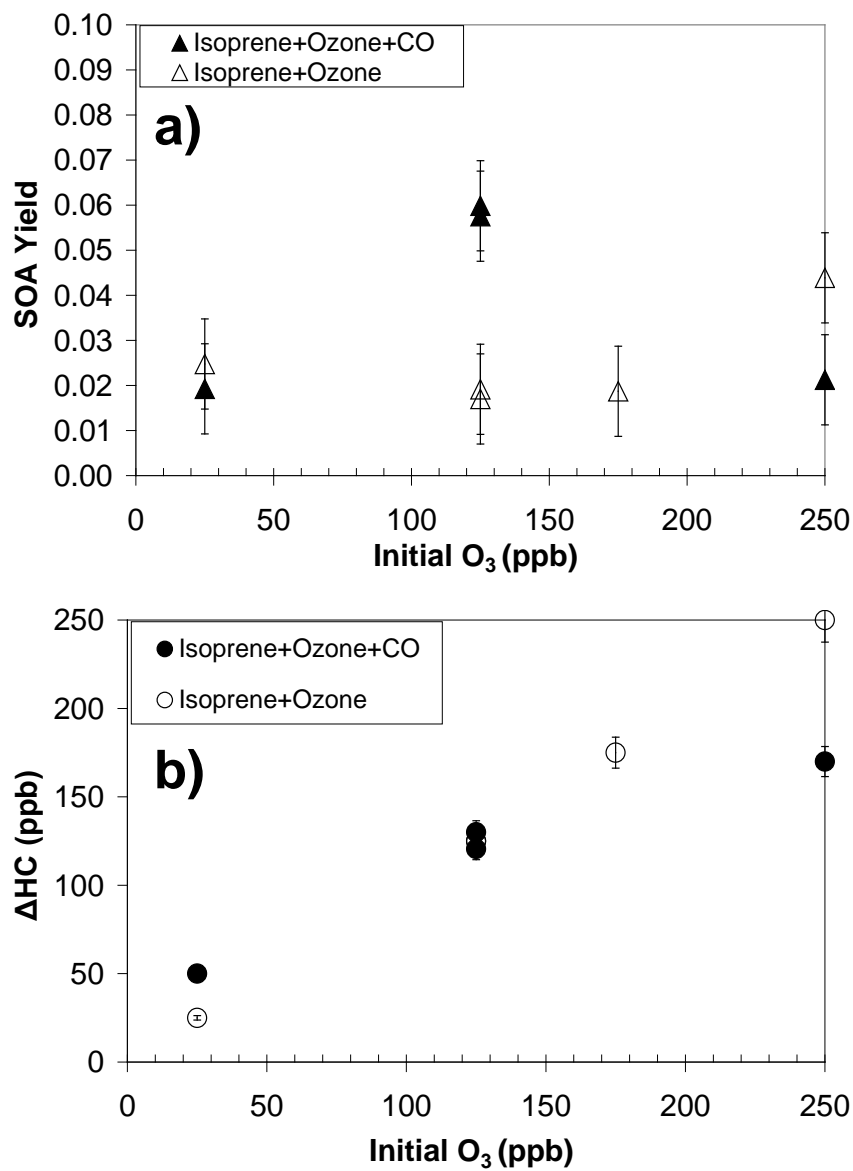


Figure 3.1: Final (a) SOA yield and (b) isoprene consumption (ΔHC) shown as a function of experimental initial ozone concentration for isoprene dark ozonolysis experiments

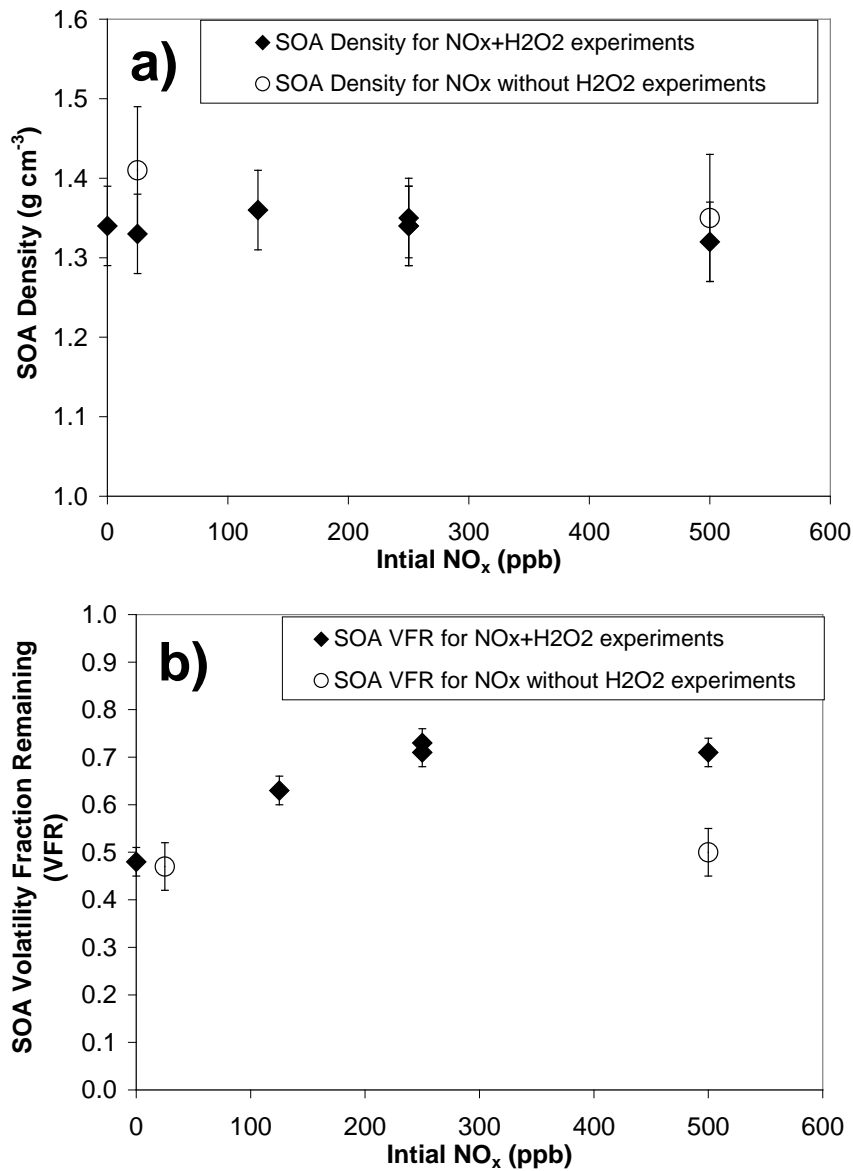


Figure 3.2: Final SOA (a) particle density as measured by APM-SMPS and (b) particle volatility fraction remaining (VFR) as measured by VTDMA as a function of initial NO concentration for isoprene photo-oxidation experiments

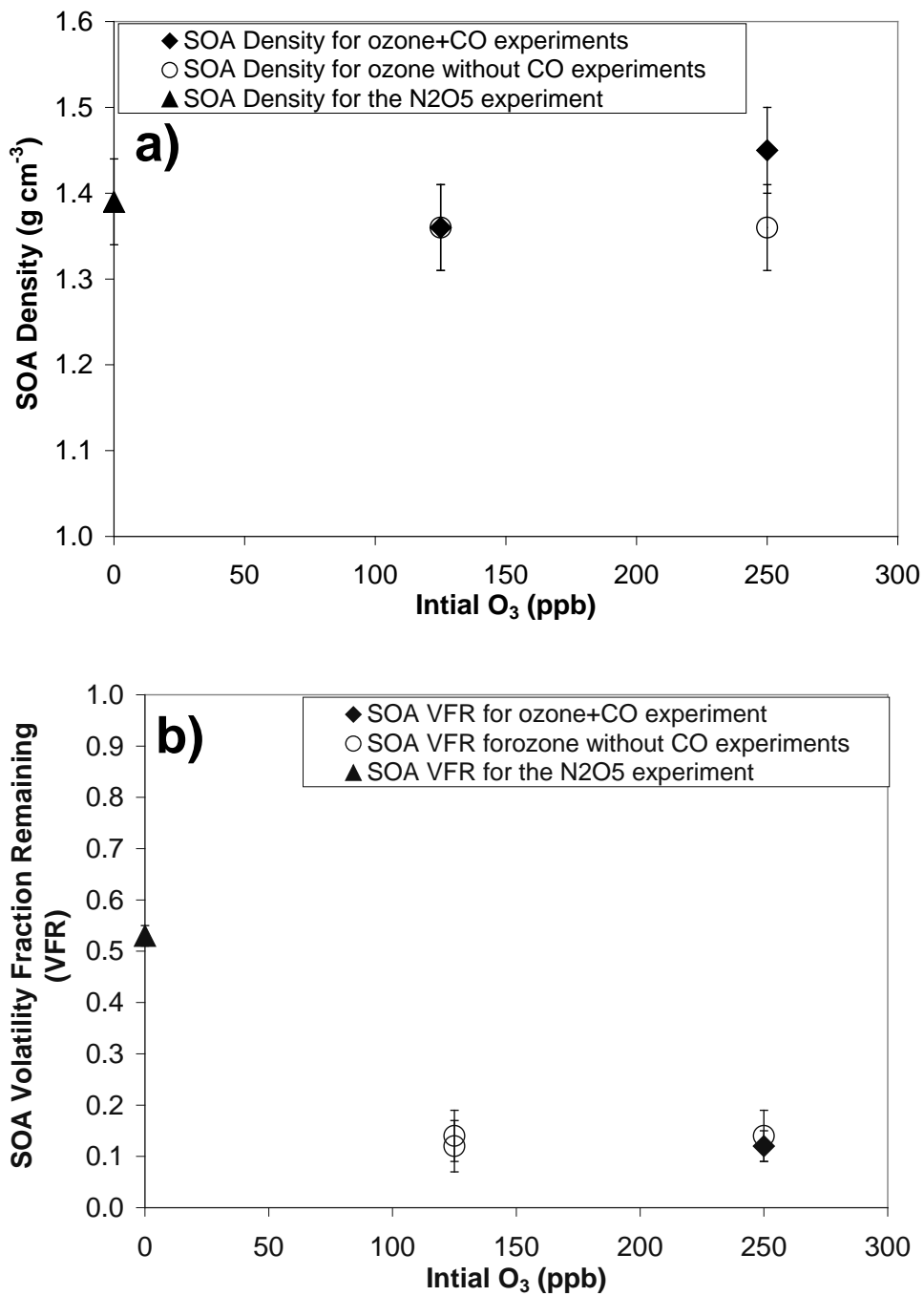


Figure 3.3: Final SOA (a) particle density as measured by APM-SMPS and (b) particle volatility fraction remaining (VFR) as measured by VTDMA as a function of initial ozone concentration for isoprene dark ozonolysis and dark N_2O_5 experiments

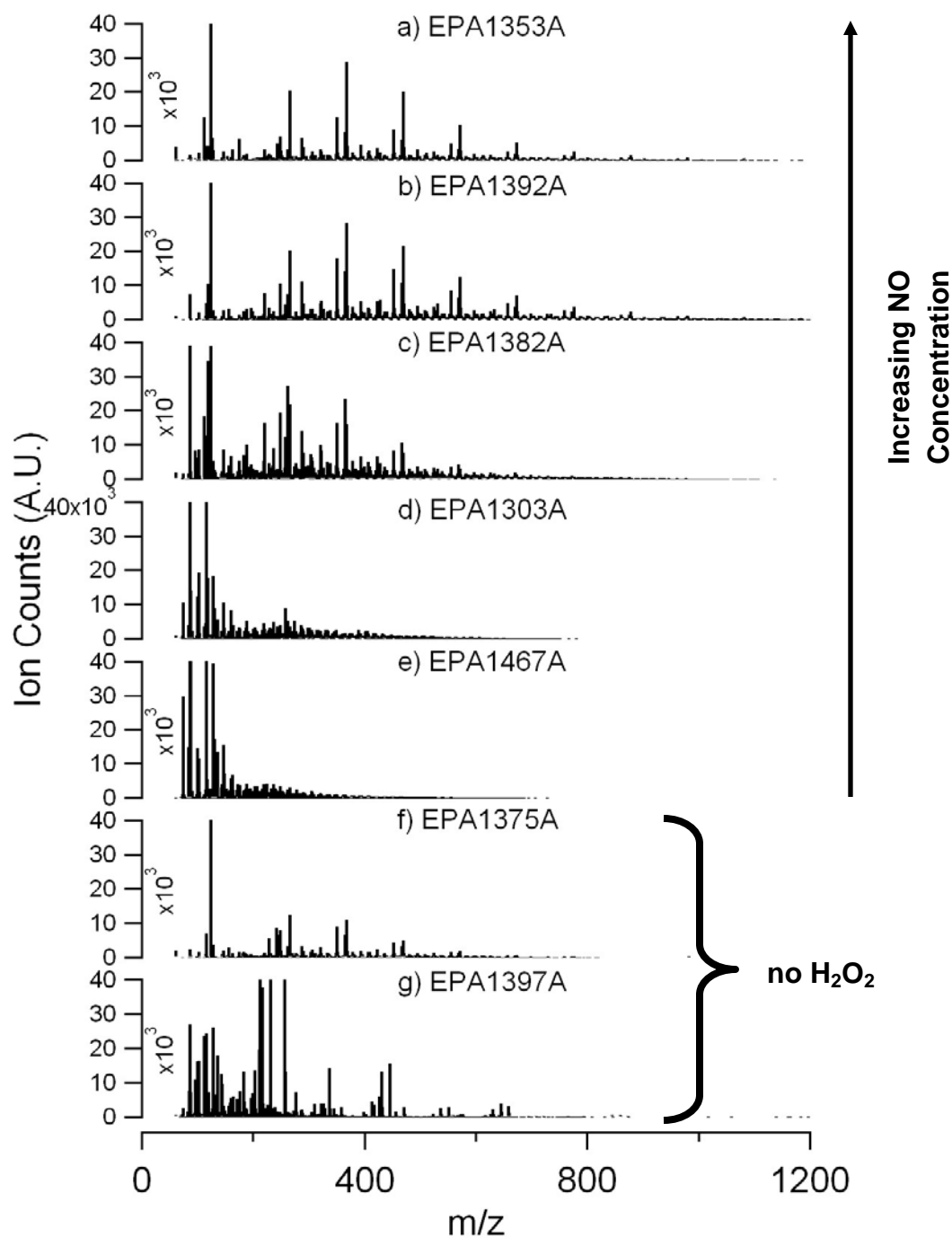


Figure 3.4: PILS-ToF mass spectra for isoprene photo-oxidation experiments (a) EPA1353A, (b) EPA1392A, (c) EPA1382A, (d) EPA1303A, (e) EPA1467A, (f) EPA1375A, and (g) EPA1397A

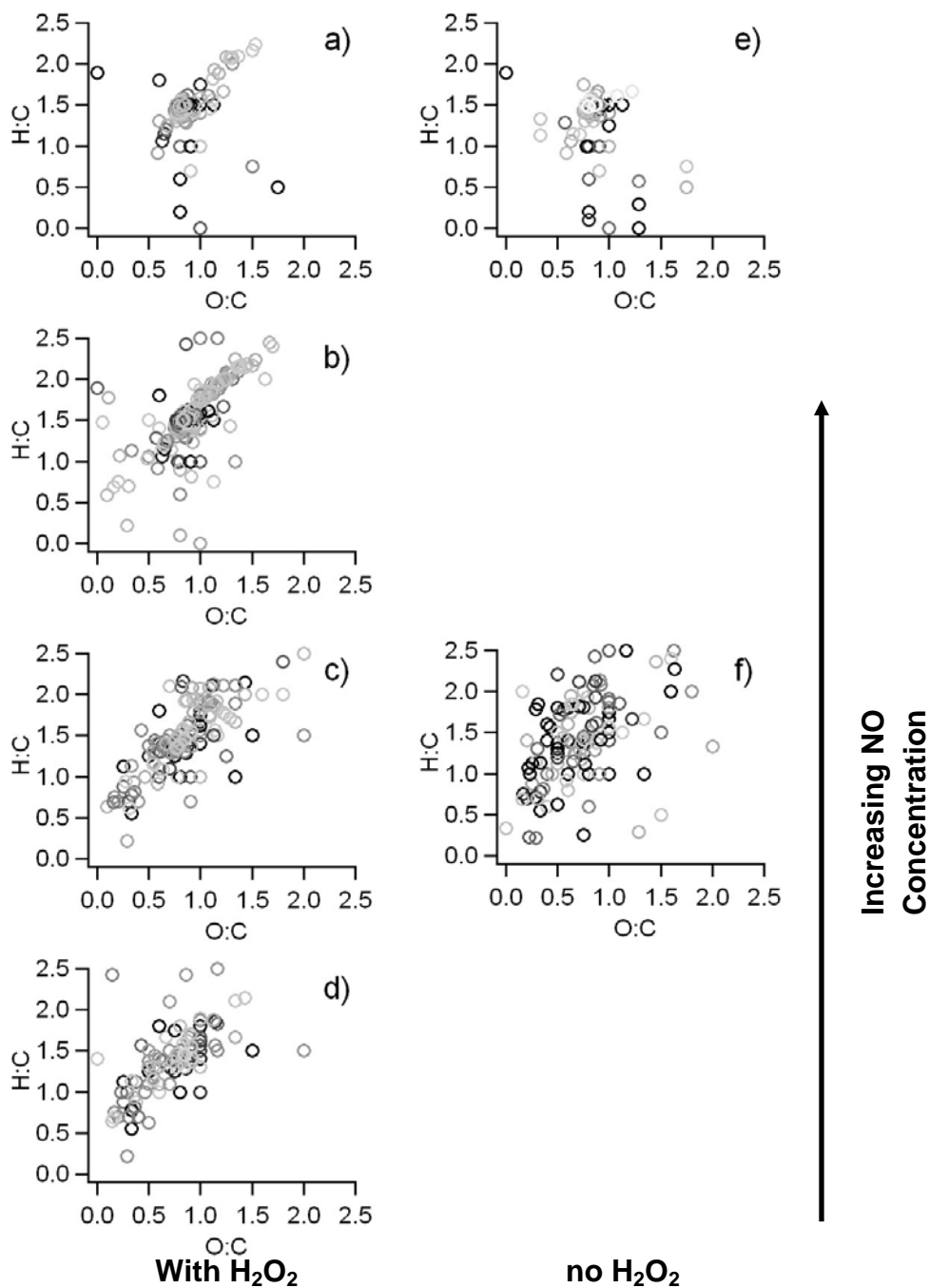


Figure 3.5: PILS-ToF ion matches presented as Van Krevelen Plots for isoprene photo-oxidation experiments (a) EPA1353A, (b) EPA1382A, (c) EPA1303A, (d) EPA1467A, (e) EPA1375A, and (f) EPA1397A. *Note mass spectral intensity of an individual ion is presented through a gradient gray scale, where white represents no ion intensity, black represents an ion intensity of 5000 counts or above.

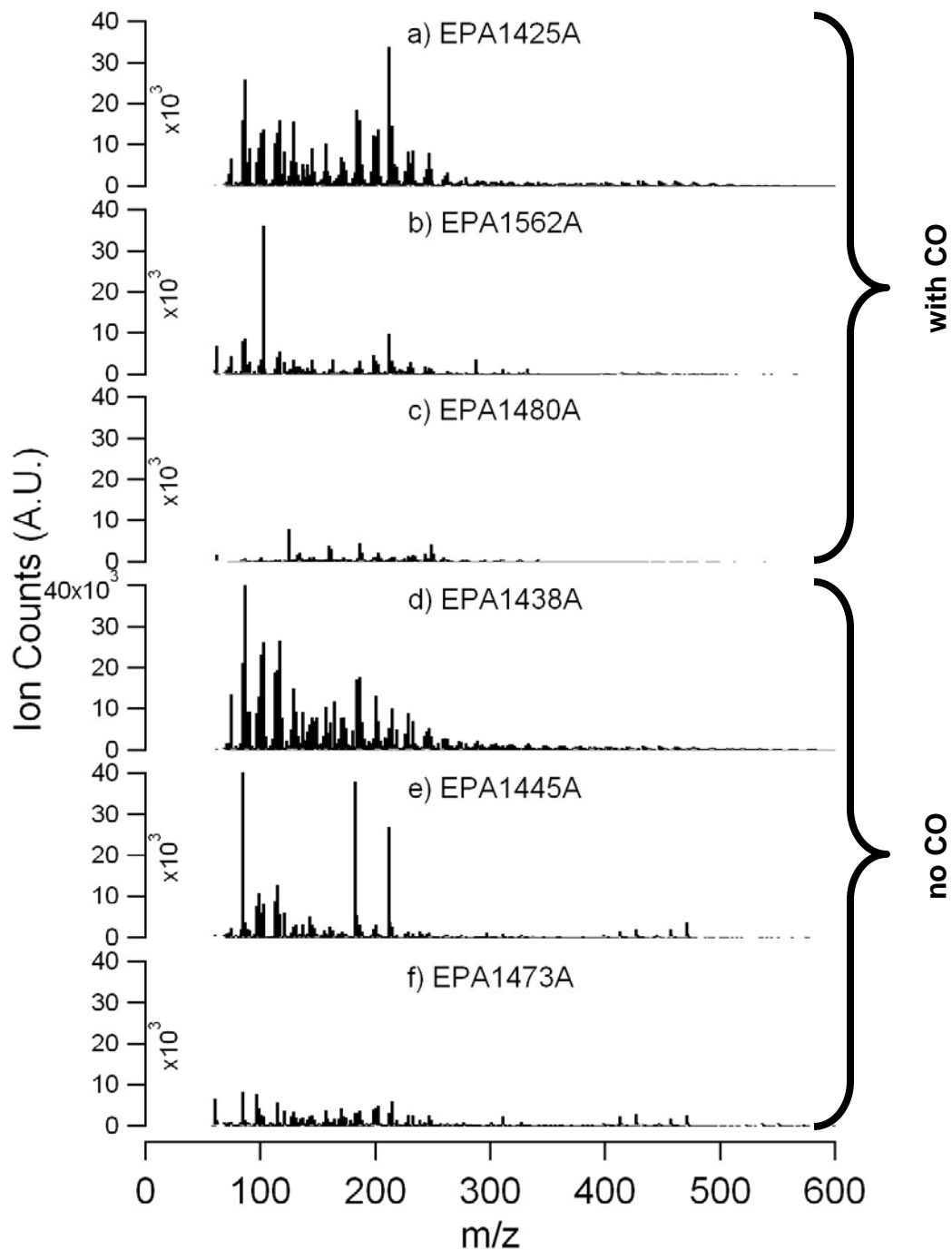


Figure 3.6: PILS-ToF mass spectra for isoprene dark ozonolysis experiments (a) EPA1425A, (b) EPA1562A, (c) EPA1480A, (d) EPA1428A, (e) EPA1445A, and (f) EPA1473A

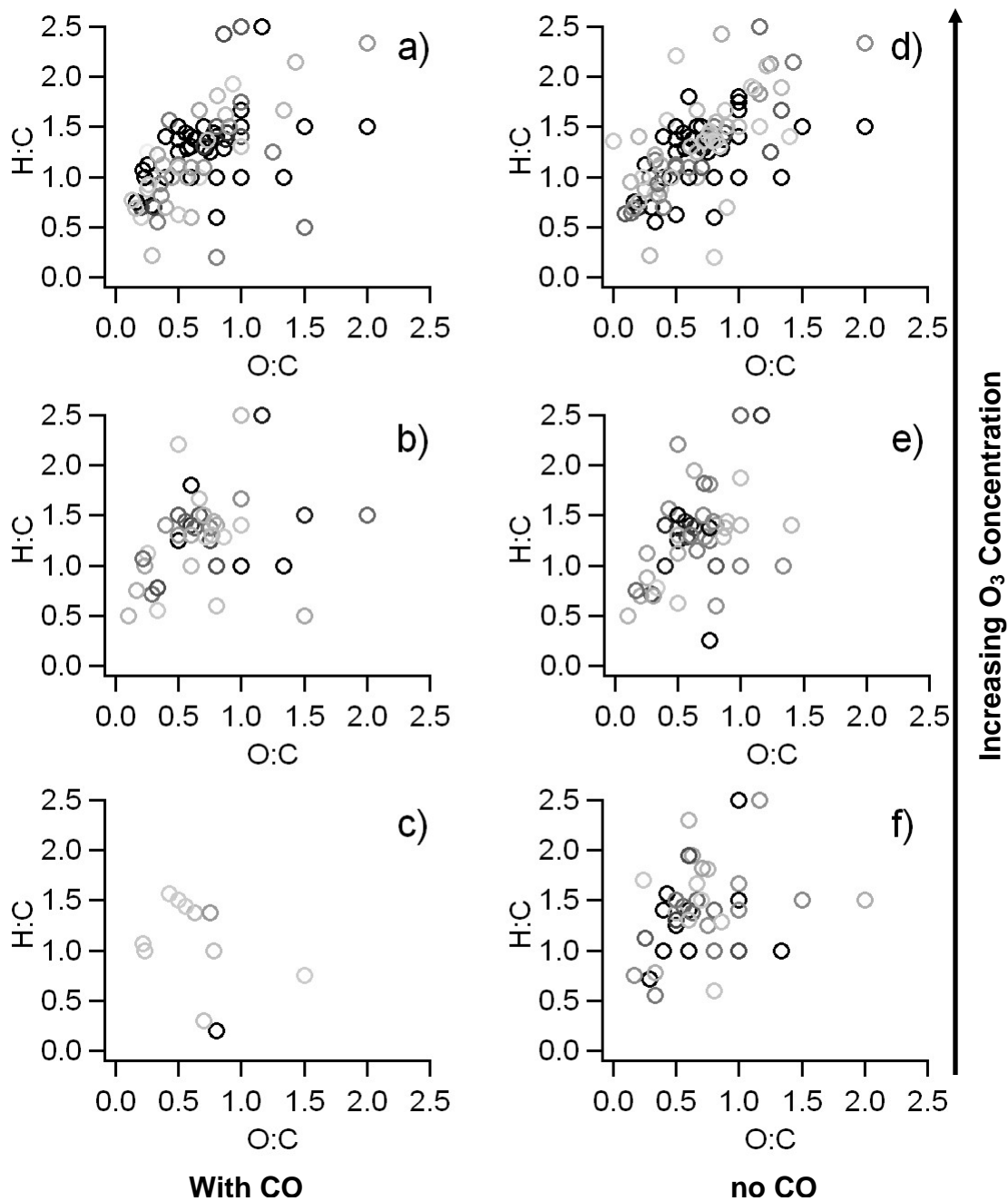


Figure 3.7: PILS-ToF ion matches presented as Van Krevelen Plots for isoprene dark ozonolysis experiments (a) EPA1425A, (b) EPA1562A, (c) EPA1480A, (d) EPA1428A, (e) EPA1445A, and (f) EPA1473A. *Note mass spectral intensity of an individual ion is presented through a gradient gray scale, where white represents no ion intensity, black represents an ion intensity of 5000 counts or above.

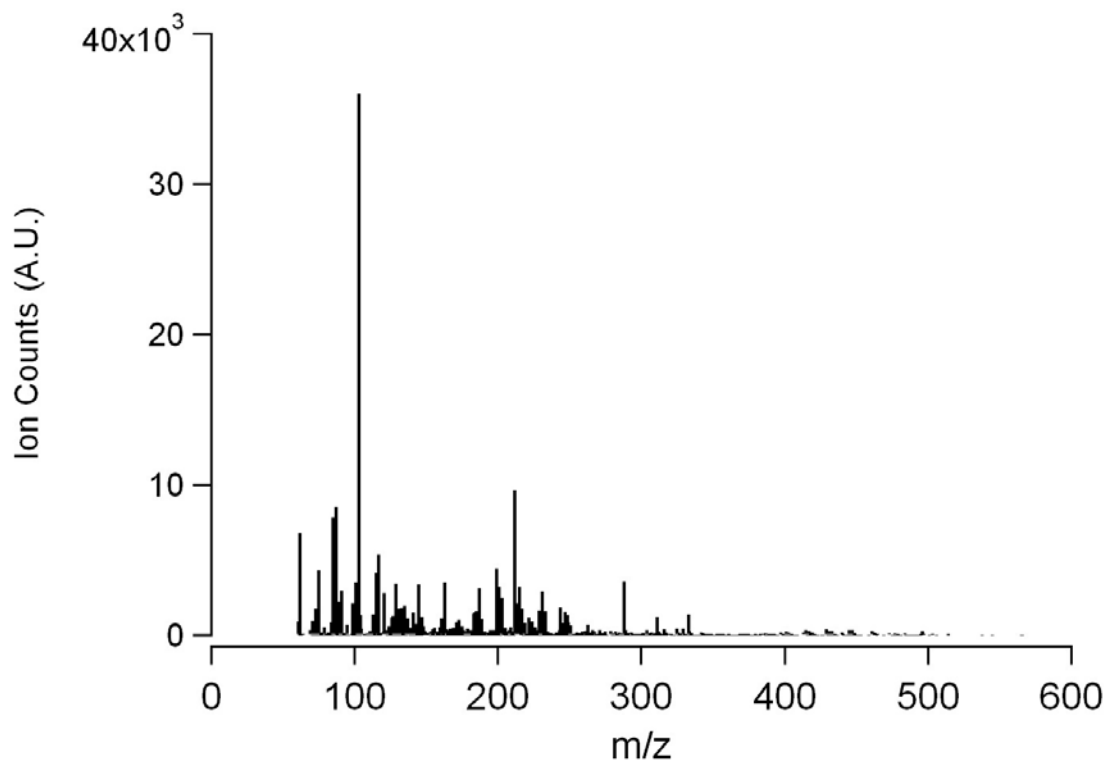


Figure 3.8: PILS-ToF mass spectra for isoprene dark reaction of isoprene and N₂O₅, EPA1562A

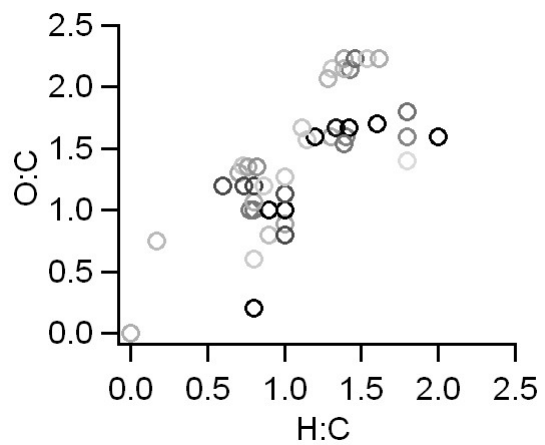


Figure 3.9: PILS-ToF ion matches presented as Van Krevelen Plots for dark reaction of isoprene and N₂O₅, EPA1562

Chapter 4: Temperature effects on secondary organic aerosol (SOA) from the dark ozonolysis and NO photo-oxidation of Isoprene

4.1 Introduction

Isoprene is the most abundant non-methane hydrocarbon observed in the atmosphere (Guenther, Hewitt et al. 1995). Isoprene is found in the ambient in a diverse geography with varying meteorological, gas-phase oxidant concentration, and geographical environments, from boreal forests (Sjostedt, Slowik et al. 2011) to oil tanker emissions (Agrawal, Welch et al. 2008). It is therefore important to study SOA formation from isoprene under varying oxidizing conditions, humidity, and temperatures. Many have studied the effect of various oxidizing environments including, O₃, NO, nitrate radical, and hydroxyl radical (Surratt, Murphy et al. 2006; Ng, Kwan et al. 2008; Nguyen, Bateman et al. 2010; Sato, Nakao et al. 2011; Clark, Nakao et al. 2012). The effect of humidity on SOA formation from isoprene has also been probed (Zhang, Surratt et al. 2011). However, no set of temperature controlled environmental chamber experiments on isoprene SOA formation to probe reaction temperature effects appear in the literature. Here the CE-CERT temperature controlled environmental chamber (Carter, Cocker et al. 2005) is used to study the effect of reaction temperature on the chemical and physical properties of SOA formed from isoprene photo-oxidation and dark ozonolysis.

4.2 Materials and Methods

4.2.1 environmental chamber

All experiments were conducted in the UC Riverside/CE-CERT environmental chamber described in detail in Carter et al. (Carter, Cocker et al. 2005). In short, this facility consists of dual 90m³ Teflon® reactors suspended by rigid frames in a temperature controlled enclosure (27±1°C) continuously flushed with dry (a dew point below -40°C) purified air generated by an Aadco 737 series (Cleves, Ohio) air purification system. The top frames are slowly lowered during the experiments to maintain a slight positive differential pressure (0.0100 in. H₂O) between the reactors and the enclosure to minimize dilution and possible contamination of the reactors. 350 115W Sylvania black lights are used as the light source for photo-oxidation experiments. Different numbers of light bulbs are used to match the NO₂ photolysis rate at different temperatures as described by Qi et al. (Qi, Nakao et al. 2010). Unless otherwise noted, photolysis rate was controlled at 0.29 min⁻¹ by using differing number of bulbs. A known volume of high purity liquid hydrocarbon precursor (isoprene: Sigma-Aldrich, 99.5%) is injected through a heated glass injection manifold system and flushed into the chamber with pure N₂.

4.2.2 gas and particle analysis

The Agilent 6890 Gas Chromatograph – Flame Ionization Detector was used to measure concentrations of hydrocarbon reactants and products. NO_x, CO, and O₃ concentrations were monitored using a Thermo Environmental Instruments Inc. model

42C trace level NO-NO₂-NO_y analyzer, Thermo Environmental Instruments Inc. model 48C trace level CO analyzer and O₃ concentration is measured by a Dasibi Environmental Corporation model 1003-AH, respectively. All quantitative gas phase instrumentation is calibrated to a gas standard prior to each chamber experiment.

Particle size distribution between 27 nm and 686 nm was monitored by a custom built Scanning Mobility Particle Sizer (SMPS) similar to that described by (Cocker, Flagan et al. 2001). Particle volatility was monitored with a volatility tandem DMA (VTDMA), in which monodisperse particles of mobility diameter D_{mi} are selected by the 1st DMA followed by transport through a Dekati thermodenuder (TD, residence time: ~17 s, temperature: 100°C). The particle size after the TD (D_{mf}) is then measured by fitting a log-normal size distribution curve from the 2nd SMPS. Volume fraction remaining (VFR) is then calculated as the before and after the TD volume ratio, i.e., $VFR = (D_{mf}/D_{mi})^3$.

Particle effective density was measured with an Aerosol Particle Mass Analyzer (APM, Kanomax) (Ehara, Hagwood et al. 1996) and SMPS in series. The APM is located upstream of the SMPS for improved time resolution and sensitivity (S/N) over the more common configuration of Differential Mobility Analyzer (DMA) – APM (McMurry, Wang et al. 2002; Khalizov, Zhang et al. 2009; Xue, Khalizov et al. 2009). A detailed description of the APM-SMPS system and data algorithms are described elsewhere (Malloy, Nakao et al. 2009).

The high resolution time-of-flight aerosol mass spectrometer (HR-ToF-AMS) (DeCarlo, Kimmel et al. 2006) was operated in high resolution W mode. Elemental analysis (EA) was used to determine the atomic ratio (H/C, O/C, and N/C) of non-refractory organic aerosols (Aiken, DeCarlo et al. 2008).

A Particle-Into-Liquid-Sampler (PILS) (Weber, Orsini et al. 2001; Orsini, Ma et al. 2003) was interfaced with an Agilent 6210 Time-of-Flight Mass Spectrometer (TOFMS), hereafter referred to as the PILS-ToF, equipped with a multimode ionization source for electrospray and atmospheric pressure chemical ionization (ESI/APCI) to provide an on-line accurate mass analysis of water soluble organic compounds (Bateman, Nizkorodov et al. 2010). In order to couple the PILS (Brechtel Manufacturing Inc.) to the TOFMS, the use of HPLC pumps in addition to a commonly used peristaltic pump was critical to overcome the backpressure of the TOFMS inlet and to supply steady flow of water (18.2M Ω , Milli-Q, Millipore) into the boiler. The PILS-ToF system is described in detail else where (Clark et al., 2012). For this study, the TOFMS electrospray ionization sources (ESI) was operated in negative mode with a vaporizer temperature 200 °C, nebulizer pressure 40 psig, corona current 2 μ A, fragmentor voltage 100V. All TOFMS data reported here was acquired using ESI only in negative ion mode.

Occasionally higher mass errors (up to 100 ppm) were observed during sample analysis, which resulted in a consistent shift of mass throughout the mass range of the instrument. Since the extent of the shift can be inferred from repeatedly observed ions

(e.g., methyl vinyl ketone), formulas were carefully assigned based on tendency of shift and repeat experiments.

4.3 Results and Discussions

4.3.1 SOA formation

Wall-loss corrected aerosol mass concentration was measured for 13 isoprene experiments. All experiments reported here have the same initial isoprene concentration, $697 \mu\text{g m}^{-3}$ (250ppb). SOA yield (Y) is calculated here as the mass of aerosol formed (wall-loss-corrected) (M_0) divided by mass of hydrocarbon reacted (ΔHC)

$$Y = \frac{M_0}{\Delta HC} \quad (4.1)$$

Table 4.1 presents environmental chamber conditions for the experiments presented here.

In Figure 4.1 the effect of environmental chamber reaction temperature on SOA yield is shown for both photo-oxidation and dark ozonolysis experiments. SOA yield decreases in Figure 4.1 by more than 2-fold between a reaction temperature of 278 K and 300 K for NO + H₂O₂ photo-oxidation, H₂O₂ only photo-oxidation, and dark ozonolysis. This result supports a volatility driven process indicating the isoprene SOA at 278 K is made up of many semi-volatile species. Between 300 K and 313 K SOA yield for isoprene NO photo-oxidation and isoprene dark ozonolysis is observed to vary little, within experimental error, indicating that SOA at 300K is far less volatile. For H₂O₂ photo-oxidation of isoprene, SOA yield is observed to be at a minimum at 300K. It

should be noted that SOA yield for H₂O₂ photo-oxidation lies directly beneath the result for NO photo-oxidation. This minimum in SOA yield for H₂O₂ oxidation observed at 300K is a confounding result, but could be caused by Arrhenius effect on rates of side reactions that lead to lower volatility, potentially oligomer-like, products.

4.3.2 SOA physical characterization

Particle density and particle volatile fraction remaining were measured for a representative subset of the isoprene SOA experiments by APM-SMPS and VTDMA respectively. The physical and chemical SOA characterization data is summarized in Table 4.2. It should be noted that particle density and VFR are reported as a mean of measurements after particle nucleation, with error-bars indicating the observed deviation from this mean.

SOA density, as measured by the APM-SMPS, is provided in Figure 4.2 for all three isoprene oxidant systems. Observed particle density decreases for all oxidation systems between environmental chamber reaction temperatures 278 K and 300 K, but does not change, within experimental error between reaction temperatures 300 K and 313 K. This plateau trend is consistent with the SOA yield results in Figure 4.1. This result indicates that the semi-volatile species formed in the gas phase oxidation of isoprene, observed in greater quantities at low reaction temperature, have higher densities.

Figure 4.3 plots SOA volatile fraction remaining (VFR) for all three isoprene oxidation systems, and generally VFR is seen to increase with temperature for all three of these systems. In assessing specific heuristics of this increase in Figure 4.3, isoprene NO

+ H₂O₂ photo-oxidation VFR is observed at the same value at 300 K and 313 K, indicating little change in particle volatility at higher temperature. No VFR data is available for isoprene dark ozonolysis at 278 K and 300 K as aerosol signal was too low. However, the VFR observed at 313 K is in line with the other isoprene oxidation experiments indicating a non-volatile SOA core. For H₂O₂ photo-oxidation of isoprene data is unavailable for the high temperature case of 313K, never the less, VFR is observed to increase by 5 times between 278 K and 300K showing a significant drop in particle volatility. Overall, the high particle volatilities at low temperature indicate that the SOA is made up semi-volatile species. The trend of the SOA VFR results is in-line with the SOA yield and density. It hypothesized that upon heating the SOA reaction less semi-volatile species are present in the particle phase and reactions are occurring faster leading to an aerosol made of more oligomer products of much lower volatility. This hypothesis will be further supported by PILS-ToF chemical characterization.

4.3.3 SOA chemical characterization

Two mass spectral particle characterization methods are compared here, the AMS and the PILS-ToF. The AMS is used here to give gross quantitative chemical description through the elemental ratios, O:C, H:C, and N:C. The PILS-ToF is used here for qualitative chemical speciation of the particle phase products. AMS and PILS-ToF calculated average particle elemental ratios H:C, O:C, and N:C ratios are presented in Table 4.2. For gross chemical characterization of O:C, H:C, and N:C ratios of particle composition by the two methods generally agree, with the PILS-ToF reporting slightly higher O:C ratios for most of the isoprene SOA experiments. The exception being

isoprene NO + H₂O₂ photo-oxidation where, regardless of reaction temperature, the PILS-ToF observed H:C ratio is approximately 0.5 less than that observed by AMS. Table 4.2 shows that AMS elemental ratios appear unaffected by reaction temperature within the error of the data.

Figure 4.4 gives the PILS-ToF mass spectra for isoprene NO + H₂O₂ photo-oxidation experiments at two reaction temperatures, 300 K and 278 K. Figure 4.4a is the PILS-ToF mass spectra of NO + H₂O₂ photo-oxidation experiment EPA1353A performed at a reaction temperature of 300 K. For NO + H₂O₂ photo-oxidation performed at 300K, the PILS-ToF mass spectra is observed to have a clear pattern of repeating ion peaks indicative of oligomerization. It should be noted that the data reported in Figure 4.4a as been presented and discussed elsewhere (Clark, Nakao et al. 2012; Clark, Nakao et al. 2012) and used here as a base of comparison.

In contrast Figure 4.4b, PILS-ToF mass spectra of an isoprene NO + H₂O₂ photo-oxidation experiment EPA1559A performed at 278 K, does not have the same evident repeating pattern of PILS-ToF mass spectral peaks indicative of oligomerization. That is not to say that oligomers are not present in Figure 4.4b. Detailed PILS-ToF molecular formula matching provided in Figure 4.7 and Table 4.3 show that there are oligomers observed in Figure 4.4b, but clearly not as many. Instead the PILS-ToF mass spectra in Figure 4.4b is seen to be shifted to a lower molecular weight with a broad diverse “hump” of peaks observed between m/z 200 and m/z 600. It is thought that these smaller molecular weight species correlate to semi-volatiles. It is further hypothesized that SOA

formation at 278 K is dominated by the condensation of semi-volatiles with reaction rates of oligomerization slowed by kinetic effects of decreased temperature and decreased concentrations of oligomer precursors.

PILS-ToF mass spectra of isoprene H₂O₂ photo-oxidation experiments performed in the absence of initial NO at varying temperatures are provided in Figure 4.4. In Figure 4.5a, isoprene H₂O₂ photo-oxidation experiment EPA1566A performed at 313 K, mass spectral peak intensity is observed to lie completely below m/z 400, with most mass spectral peak intensity falling below m/z 200. In Figure 4.5b, photo-oxidation experiment EPA1467A performed at 300 K in the absence of initial NO, larger m/z are observed with the mass spectral intensity existing in another broad “hump” of mass spectral peaks between m/z 100 and m/z 400. The PILS-ToF mass spectra of the H₂O₂ photo-oxidation experiment EPA1556A performed at 278 K is provided in Figure 4.5c. Figure 4.5c shows a further mass spectral intensity increase at higher molecular weights in comparison to Figures 4.5a and 4.5b. Furthermore, the mass spectral “hump” observed in Figure 4.5b has decreased with discrete high intensity and higher m/z peaks taking its place. In contrast to the PILS-ToF mass spectral results for the NO + H₂O₂ photo-oxidation, PILS-ToF mass spectral peak intensity for the H₂O₂ only system increases at all m/z, including high m/z; a result indicative a volatility driven process. PILS-ToF results provided in Figure 4.5a do not appear to be indicative of a high molecular weight low-volatility aerosol.

Figure 4.6 shows PILS-ToF mass spectral results for isoprene dark ozonolysis experiments at 3 temperatures, 313 K, 300 K, and 278 K. In Figure 4.6a, isoprene dark ozonolysis experiment EPA1563A performed at 313K, nearly all mass spectral intensity is observed below 400 m/z. Although in Figure 4.6b, the PILS-ToF mass spectra for isoprene dark ozonolysis experiment EPA1563A performed at 300K, mass spectral intensity is again generally below m/z 400 with two sets of peaks at higher m/z ranges observed between m/z 400-500 and m/z 600-700. For Figure 4.6c, the PILS-ToF mass spectra for isoprene dark ozonolysis experiment EPA1563A performed at 278K, overall mass spectral intensity appears to increase below m/z 400 while the mass spectral peaks observed in Figure 4.6b above m/z 400 are present but far less intense. Like the case of H₂O₂ photo-oxidation, the change in PILS-ToF mass spectra with temperature observed in Figure 4.6 for isoprene dark ozonolysis support a SOA formation process driven by chemical species volatility, not reactions forming high molecular weight chemical species.

Figure 4.7 gives Van Krevelen diagrams of molecular matches for PILS-ToF mass spectral ions (Van Krevelen 1950) observed to have intensity greater than 1000 ion counts in Figure 4.4, the PILS-ToF mass spectra for isoprene NO + H₂O₂ photo-oxidation experiments. The observed intensity in Figure 4.7 is provided by a grey scale, where a black open circle represents a molecular match at 5000 ion counts and above and no circle (white) represents zero ion counts. Furthermore, it should be noted that the details of the mass spectral peaks observed in Figure 4.7 are provided in Table 4.3. In comparing Figure 4.7a and 4.7b, for isoprene NO + H₂O₂ photo-oxidation experiments

EPA1353A and EPA1559A performed at 300 K and 278 K respective, show the same general focal point at O:C=1 and H:C=1.5. However where Figure 4.7a and 4.7b differ, is in the quadrant below O:C=1 and H:C=1.5 where many more points are observed in this quadrant in Figure 4.7b. It is hypothesized that these points with lower O:C and H:C observed in Figure 4.7b correlate to higher volatility species.

Van Krevelen diagrams of molecular matches to PILS-ToF mass spectral ions observed at intensities above 1000 ion counts observed in Figure 4.5, for isoprene H₂O₂ photo-oxidation experiments done in the absence of initial NO, are provided in Figure 4.8. The mass spectral intensity of molecular matches is provided by a grey scale as in Figure 4.7. The detailed molecular matches in Figure 4.8 are presented in Table 4.3. In comparing the Figures 4.7a-c, for experiments H₂O₂ photo-oxidation experiments EPA1566A, EPA1467A, and EPA1556 performed at 313 K, 300 K, and 278 K respectively, some trends can be observed. First, though the eye is drawn to the focal point in all three Van Krevelen diagrams at O:C=1.0 and H:C=2.0 matched to the molecule C₅H₁₀O₅, most of the molecules and mass spectral intensity lies in the quadrant below O:C=1.0 and H:C=2.0. The molecular abundance and intensities grow in the lower left quadrant of Figure 4.7a-c as temperature decreases. Indicating, as was hypothesized for NO + H₂O₂ photo-oxidation, that semi-volatile species occur at lower O:C and H:C. These molecules below an O:C=1.0 and H:C=2.0 are shown in Table 4.3 to be small less oxygenated hydrocarbons. Never the less, three clear lines also grow in intensity and length in Figure 4.7a-c as temperature decreases, these lines occur at O:C=1, H:C=2 and H:C = -(O:C) + 3.

Figure 4.9 gives Van Krevelen diagrams of molecular matches for PILS-ToF mass spectral ions observed to have intensity greater than 1000 ion counts in Figure 4.4, the PILS-ToF mass spectra for isoprene dark ozonolysis experiments. The observed intensity in Figure 4.8 is provided by a grey scale as in Figures 4.6 and 4.7. Furthermore, it should be noted that the details of the mass spectral peaks observed in Figure 4.9 are provided in Table 4.3. In comparing Figure 4.9a-c, for isoprene dark ozonolysis experiments EPA1563A, EPA1445A, and EPA1483A performed at 313 K, 300 K and 278 K respectively, show a focal point, as observed in Figure 4.8, at O:C=1 and H:C=2. The molecular abundance and intensities grow in the lower left quadrant of Figure 4.7a-c, below O:C=1 and H:C=2, as temperature decreases. This result indicates, as was hypothesis for the photo-oxidation systems, that semi-volatile species occur at lower O:C and H:C.

4.4 Conclusions

SOA yield, density, volatility, and PILS-ToF chemical speciation are shown as a function of reaction temperature for isoprene NO + H₂O₂ photo-oxidation, H₂O₂ photo-oxidation done in the absence of initial NO, and dark ozonolysis. SOA yield is observed to increase as reaction temperature is dropped from 300 K to 278K for all three isoprene oxidation systems. However, as reaction temperature is increased from 300 K to 313 K SOA yield is observed to remain relatively unchanged for all three oxidant systems. SOA Density decreases as reaction temperature is increased from 278 K to 300 K, but is stable for further reaction temperature increase from 300 K to 313K for all isoprene oxidation systems. SOA volatility follows the trend expected from SOA yield and

density results; where isoprene SOA volatility decreases when reaction temperature is increased from 278 K to 300 K, but appears to remain stable as reaction temperature is increased from 300 K to 313 K.

AMS average SOA elemental ratios appear to be unaffected by changes in reaction temperature. However, specific qualitative PILS-ToF speciation reveals that as temperature decreases mass spectral matches correlating to lower H:C and O:C ratios are observed, a result consistent for all three isoprene oxidation systems reported here. In the case of $\text{NO} + \text{H}_2\text{O}_2$, photo-oxidation oligomer production decreases as temperature decreases indicating a strong kinetic effect.

4.5 Reference

- Agrawal, H., W. A. Welch, et al. (2008). "Emission Measurements from a Crude Oil Tanker at Sea." Environmental Science & Technology **42**(19): 7098-7103.
- Aiken, A. C., P. F. DeCarlo, et al. (2008). "O/C and OM/OC Ratios of Primary, Secondary, and Ambient Organic Aerosols with High-Resolution Time-of-Flight Aerosol Mass Spectrometry." Environmental Science & Technology **42**(12): 4478-4485.
- Bateman, A. P., S. A. Nizkorodov, et al. (2010). "High-Resolution Electro-spray Ionization Mass Spectrometry Analysis of Water-Soluble Organic Aerosols Collected with a Particle into Liquid Sampler." Analytical Chemistry **82**(19): 8010-8016.
- Carter, W. P. L., D. R. I. Cocker, et al. (2005). "A new environmental chamber for the evaluation of gas-phase chemical mechanisms and secondary aerosol formation." Atmospheric Environment **39**: 7768-7788.
- Clark, C. H., S. Nakao, et al. (2012). "A real-time study of the particle phase products of the dark ozonolysis of α -pinene and the photo oxidation of isoprene by particle into liquid sampling directly coupled to a time of flight mass spectrometer (PILS-ToF)." Aerosol Sci. Technol. **In preparation.**
- Clark, C. H., S. Nakao, et al. (2012). "Characterization of secondary organic aerosol (SOA) from isoprene as formed in the University of California, Riverside College of Engineering Center for Environmental Research and Technology (UCR CE-CERT) atmospheric chamber." In Preparation.
- Cocker, D. R., R. C. Flagan, et al. (2001). "State-of-the-Art Chamber Facility for Studying Atmospheric Chemistry." Environmental Science and Technology **35**: 2594-2601.
- DeCarlo, P. F., J. R. Kimmel, et al. (2006). "Field-Deployable, High-Resolution, Time-of-Flight Aerosol Mass Spectrometer." Analytical Chemistry **78**(24): 8281-8289.
- Ehara, K., C. Hagwood, et al. (1996). "Novel method to classify aerosol particles according to their mass-to-charge ratio—Aerosol particle mass analyser." Journal of Aerosol Science **27**(2): 217-234.

- Guenther, A., C. N. Hewitt, et al. (1995). "A global model of natural volatile organic compound emissions." Journal of Geophysical Research **100**: 8873-8892.
- Malloy, Q. G. J., S. Nakao, et al. (2009). "Real-Time Aerosol Density Determination Utilizing a Modified Scanning Mobility Particle Sizer-Aerosol Particle Mass Analyzer System." Aerosol Science and Technology **43**: 673-678.
- Ng, N. L., A. J. Kwan, et al. (2008). "Secondary organic aerosol (SOA) formation from reaction of isoprene with nitrate radicals (NO₃)." Atmos. Chem. Phys. **8**(14): 4117-4140.
- Nguyen, T. B., A. P. Bateman, et al. (2010). "High-resolution mass spectrometry analysis of secondary organic aerosol generated by ozonolysis of isoprene." Atmospheric Environment **44**: 1032-1042.
- Orsini, D. A., Y. Ma, et al. (2003). "Refinements to the particle-into-liquid sampler (PILS) for ground and airborne measurements of water soluble aerosol composition." Atmospheric Environment **37**: 1243-1259.
- Qi, L., S. Nakao, et al. (2010). "Temperature effect on physical and chemical properties of secondary organic aerosol from m-xylene photooxidation." Atmos. Chem. Phys. **10**(8): 3847-3854.
- Sato, K., S. Nakao, et al. (2011). "Secondary organic aerosol formation from the photooxidation of isoprene, 1,3-butadiene, and 2,3-dimethyl-1,3-butadiene under high NO_x conditions." Atmos. Chem. Phys. **11**(14): 7301-7317.
- Sjostedt, S. J., J. G. Slowik, et al. (2011). "Diurnally resolved particulate and VOC measurements at a rural site: indication of significant biogenic secondary organic aerosol formation." Atmos. Chem. Phys. **11**(12): 5745-5760.
- Surratt, J. D., S. M. Murphy, et al. (2006). "Chemical Composition of Secondary Organic Aerosol Formed from the Photooxidation of Isoprene." Journal of Physical Chemistry A **110**: 9665-9690.
- Van Krevelen, D. W. (1950). "Graphical-statistical method for the study of structure and reaction processes of coal." Fuel **29**: 269-284.
- Weber, R. J., D. Orsini, et al. (2001). "A Particle-into-Liquid Collector for Rapid Measurement of Aerosol Bulk Chemical Composition." Aerosol Science and Technology **35**(3): 718-727.

Zhang, H., J. D. Surratt, et al. (2011). "Effect of relative humidity on SOA formation from isoprene/NO photooxidation: enhancement of 2-methylglyceric acid and its corresponding oligoesters under dry conditions." Atmos. Chem. Phys. **11**(13): 6411-6424.

4.6 Tables

Table 4.1. Experimental conditions and results

Run	Temperature (K)	ΔHC ($\mu\text{g m}^{-3}$)	$[\text{NO}]_0$ (ppb)	$[\text{H}_2\text{O}_2]_0^{\text{a}}$ (ppm)	$[\text{O}_3]_0$ (ppb)	Final SOA ^b ($\mu\text{g m}^{-3}$)	SOA Yield	Reaction Notes
EPA1483A	278	418	0	0	125	25	0.06	dark ozonolysis
EPA1556A	278	669	0	3	0	196	0.29	photo-oxidation
EPA1559A	278	697	500	3	0	288	0.41	photo-oxidation
EPA1445A ^c	300	394	0	0	125	7	0.02	dark ozonolysis
EPA1440A ^c	300	334	0	0	125	6	0.02	dark ozonolysis
EPA1353A ^{c, d}	300	697	500	3	0	68	0.10	photo-oxidation
EPA1288A ^{c, d}	300	697	500	3	0	68	0.10	photo-oxidation
EPA1567A	300	585	0	3	0	15	0.03	photo-oxidation
EPA1467A ^{c, d}	300	697	0	3	0	55	0.08	photo-oxidation
EPA1563A	313	418	0	0	125	10	0.02	dark ozonolysis
EPA1505A	313	446	0	0	125	5	0.01	dark ozonolysis
EPA1566A	313	557	0	3	0	3	0.01	photo-oxidation
EPA1508A	313	362	500	3	0	42	0.12	photo-oxidation

^aInitial H_2O_2 concentration is not measured, but estimated by isoprene decay. ^bThis assumes an average measured density of 1.34 g cm^{-3} . ^cThis data previously has been published (Clark, Nakao et al. 2012). ^dLight intensity was higher in these experiment with an estimated NO_2 photolysis rate of 0.51 min^{-1}

Table 4.2. Summary of SOA chemical and physical characterization data

Run	Density (g cm ⁻³)	VFR	AMS H:C	AMS O:C	AMS N:C	PILS-ToF H:C	PILS-ToF O:C	PILS-ToF N:C	PILS- ToF Percent Ions Matched	Notes
EPA1483A	-	-	1.40 ±0.10	0.20 ±0.06	0.00	1.44	0.53	0.00	83	a, b
EPA1556A	1.49	0.12	1.55 ±0.20	0.30 ±0.08	0.00	1.63	0.85	0.00	71	
EPA1559A	1.46	0.31	1.52 ±0.10	0.51 ±0.10	0.05 ±0.04	0.96	0.81	0.03	68	
EPA1445A	1.36	-	-	-	-	1.33	0.66	0.00	64	c
EPA1440A	-	-	1.52 ±0.15	0.25 ±0.08	0.00	-	-	-	-	a, c, d
EPA1353A	-	0.71	-	-	-	0.81	0.82	0.02	78	a, c
EPA1288A	1.32	-	1.50 ±0.10	0.55 ±0.05	0.09 ±0.04	-	-	-	-	b, d
EPA1567A	1.45	-	1.48 ±0.20	0.31 ±0.12	0.00	-	-	-	-	b, d
EPA1467A	1.34	0.48	1.72 ±0.20	0.45 ±0.05	0.00	1.62	0.80	0.00	84	
EPA1505A	1.36	0.63	-	-	-	-	-	-	-	c, d
EPA1563A	-	-	1.46 ±0.20	0.29 ±0.12	0.00	1.53	0.76	0.00	75	a, b
EPA1566A	1.38	-	1.45 ±0.18	0.19 ±0.10	0.00	1.42	0.74	0.00	89	b
EPA1508A	1.31	0.73	-	-	-	-	-	-	-	c, d

III a-no APM-SMPS data available, b-no VTDMA data available, c-no AMS data available, d-no PILS-ToF data available

Table 4.3. PILS-ToF mass spectral ion matches with the corresponding correlations experiments in Table 4.1 and literature references

PILS-ToF observed m/z	TOF-MS ion formula match	Experiment Observed	References
61.9930	NO ₃	EPA1353A,EPA1559A	(Ng, Kwan et al. 2008)
69.0352	C ₄ H ₅ O	EPA1563A, EPA1556A, EPA1566A	(Nguyen, Bateman et al. 2010)
71.0146	C ₃ H ₃ O ₂	EPA1563A, EPA1556A, EPA1566A	(Nguyen, Bateman et al. 2010)
72.9941	C ₂ HO ₃	EPA1563A	
73.0296	C ₃ H ₅ O ₂	EPA1445A, EPA1483A, EPA1563A, EPA1556A, EPA1566A	(Nguyen, Bateman et al. 2010)
75.0095	C ₂ H ₃ O ₃	EPA1445A, EPA1483A, EPA1563A, EPA1556A, EPA1566A	(Nguyen, Bateman et al. 2010)
79.0045	C ₅ H ₃ O	EPA1483A	
83.0543	C ₅ H ₇ O	EPA1483A	
85.0300	C ₄ H ₅ O ₂	EPA1467A, EPA1445A, EPA1483A, EPA1563A, EPA1556A, EPA1566A	(Nguyen, Bateman et al. 2010)
87.0095	C ₃ H ₃ O ₃	EPA1467A, EPA1445A, EPA1483A, EPA1563A, EPA1556A, EPA1566A	(Nguyen, Bateman et al. 2010)
89.0247	C ₃ H ₅ O ₃	EPA1467A, EPA1445A, EPA1483A, EPA1563A, EPA1556A, EPA1566A	(Nguyen, Bateman et al. 2010)
91.0043	C ₂ H ₃ O ₄	EPA1467A, EPA1445A, EPA1563A, EPA1556A, EPA1566A	
95.0152	C ₆ H ₇ O	EPA1483A	
97.0306	C ₅ H ₅ O ₂	EPA1445A, EPA1483A, EPA1563A, EPA1556A, EPA1566A	(Fang, Gong et al. 2012)
98.0360	C ₄ H ₅ O ₂ ¹³ C	EPA1483A	(Fang, Gong et al. 2012)
99.0438	C ₅ H ₇ O ₂	EPA1467A, EPA1445A, EPA1483A, EPA1563A, EPA1556A, EPA1566A	(Fang, Gong et al. 2012)
101.0253	C ₄ H ₅ O ₃	EPA1467A, EPA1445A, EPA1483A, EPA1563A, EPA1556A, EPA1566A	(Nguyen, Bateman et al. 2010)
103.0147	C ₃ H ₃ O ₄	EPA1556A	(Nguyen, Bateman et al. 2010)
103.0499	C ₄ H ₇ O ₃	EPA1467A, EPA1445A, EPA1483A, EPA1563A, EPA1556A, EPA1566A	(Fang, Gong et al. 2012)
105.0189	C ₃ H ₅ O ₄	EPA1467A, EPA1483A	
111.0168	C ₅ H ₃ O ₃	EPA1566A	(Fang, Gong et al. 2012)
111.0321	C ₆ H ₇ O ₂	EPA1483A	
113.0216	C ₅ H ₅ O ₃	EPA1467A, EPA1445A, EPA1483A, EPA1563A, EPA1556A, EPA1566A	(Fang, Gong et al. 2012)
115.0364	C ₅ H ₇ O ₃	EPA1467A, EPA1445A, EPA1483A, EPA1563A, EPA1556A, EPA1566A	(Fang, Gong et al. 2012)
116.9973	C ₃ HO ₅	EPA1556A	
117.0229	C ₅ H ₉ O ₃	EPA1353A, EPA1467A, EPA1445A, EPA1556A	(Lin, Zhang et al. 2012)
117.0436	C ₄ H ₆ O ₄	EPA1483A, EPA1563A, EPA1556A	(Nguyen, Bateman et al. 2010)

119.0350	C ₄ H ₇ O ₄	EPA1353A, EPA1483A, EPA1563A, EPA1556A, EPA1566A, EPA1559A	(Sato, Nakao et al. 2011)
121.0289	C ₇ H ₅ O ₂	EPA1445A, EPA1483A, EPA1563A, EPA1556A	
123.0371	C ₇ H ₇ O ₂	EPA1467A, EPA1483A	
124.9891	C ₅ HO ₄	EPA1353A, EPA1559A	
125.1282	C ₉ H ₁₇	EPA1353A	
125.9869	C ₄ NO ₄	EPA1353A, EPA1559A	
126.9938	C ₅ H ₃ O ₄	EPA1353A, EPA1445A, EPA1483A, EPA1559A	(Fang, Gong et al. 2012)
127.0365	C ₇ H ₇ O ₃	EPA1563A	
127.0488	C ₆ H ₇ O ₃	EPA1556A, EPA1566A	
129.0243	C ₅ H ₅ O ₄	EPA1353A, EPA1467A, EPA1445A, EPA1566A, EPA1559A	
129.0569	C ₆ H ₉ O ₃	EPA1483A, EPA1563A, EPA1556A	
130.0602	C ₅ H ₉ O ₃ ¹³ C	EPA1483A, EPA1556A, EPA1566A	
131.0342	C ₅ H ₇ O ₄	EPA1467A, EPA1445A, EPA1483A, EPA1563A, EPA1556A, EPA1566A	(Fang, Gong et al. 2012)
133.0154	C ₅ H ₉ O ₄	EPA1467A	
133.0252	C ₃ H ₅ O ₅	EPA1483A	(Nguyen, Bateman et al. 2010)
133.0169	C ₄ H ₅ O ₅	EPA1563A, EPA1556A	
135.0436	C ₈ H ₇ O ₂	EPA1467A, EPA1483A, EPA1556A	
137.0630	C ₈ H ₉ O ₂	EPA1467A, EPA1445A, EPA1483A, EPA1563A, EPA1556A, EPA1566A	
139.0513	C ₇ H ₇ O ₃	EPA1483A	
141.0572	C ₇ H ₉ O ₃	EPA1483A, EPA1563A, EPA1556A	
143.0392	C ₆ H ₇ O ₄	EPA1563A, EPA1566A	
143.0556	C ₁₀ H ₇ O	EPA1483A	
143.0683	C ₇ H ₁₁ O ₃	EPA1467A, EPA1445A	
143.0683	C ₇ H ₁₁ O ₃	EPA1467A, EPA1445A	(Fang, Gong et al. 2012)
145.0283	C ₅ H ₅ O ₅	EPA1556A, EPA1559A	
145.0394	C ₉ H ₅ O ₂	EPA1556A, EPA1566A	
145.0517	C ₆ H ₉ O ₄	EPA1483A, EPA1563A	
146.9714	C ₄ H ₃ O ₆	EPA1353A	
147.0327	C ₅ H ₇ O ₅	EPA1353A, EPA1467A, EPA1445A, EPA1483A, EPA1563A, EPA1556A, EPA1566A, EPA1559A	(Surratt, Chan et al. 2010)
149.0465	C ₅ H ₉ O ₅	EPA1467A, EPA1483A, EPA1556A, EPA1566A	
151.0349	C ₈ H ₇ O ₃	EPA1467A	
151.0608	C ₁₂ H ₇	EPA1483A	
151.0712	C ₅ H ₁₁ O ₅	EPA1556A	
153.0462	C ₁₁ H ₅ O	EPA1566A	
153.0517	C ₈ H ₉ O ₃	EPA1467A, EPA1483A	
155.0416	C ₇ H ₇ O ₄	EPA1563A, EPA1556A, EPA1566A	
155.0632	C ₈ H ₁₁ O ₃	EPA1483A	

157.0451	$C_7H_9O_4$	EPA1467A, EPA1483A, EPA1563A, EPA1556A, EPA1566A	(Nguyen, Bateman et al. 2010)
159.0402	$C_{10}H_7O_2$	EPA1467A, EPA1483A, EPA1563A, EPA1556A, EPA1566A	
161.0454	$C_9H_5O_3$	EPA1467A, EPA1445A	
161.0500	$C_6H_9O_5$	EPA1483A, EPA1563A, EPA1556A, EPA1566A	
163.0345	$C_9H_7O_3$	EPA1467A, EPA1445A	
163.0388	$C_5H_7O_6$	EPA1556A	
163.0688	$C_6H_{11}O_5$	EPA1556A	
165.0274	$C_8H_5O_4$	EPA1467A	
165.0531	$C_5H_9O_6$	EPA1483A, EPA1556A	
167.0658	$C_9H_{11}O_3$	EPA1483A, EPA1556A	
169.0581	$C_8H_9O_6$	EPA1563A	
169.0734	$C_9H_{13}O_3$	EPA1483A, EPA1556A	
171.0616	$C_8H_{11}O_4$	EPA1467A, EPA1445A, EPA1483A, EPA1563A, EPA1556A, EPA1566A	
173.0446	$C_7H_9O_5$	EPA1467A, EPA1483A, EPA1563A, EPA1556A, EPA1566A	
175.0405	$C_{10}H_7O_3$	EPA1467A, EPA1563A, EPA1559A	
175.0608	$C_7H_{11}O_5$	EPA1483A, EPA1556A	
175.9861	$C_4H_2NO_7$	EPA1353A	
177.0451	$C_6H_9O_6$	EPA1467A	
177.0642	$C_{10}H_9O_3$	EPA1556A	
177.0775	$C_7H_{13}O_5$	EPA1566A	
179.0677	$C_6H_{11}O_6$	EPA1556A	
181.0643	$C_9H_9O_4$	EPA1556A	
181.0752	$C_{10}H_{13}O_3$	EPA1483A, EPA1556A	
183.0817	$C_{10}H_{15}O_3$	EPA1445A, EPA1483A, EPA1563A, EPA1556A	
183.00032	$C_7H_3O_6$	EPA1559A	
185.0619	$C_{12}H_9O_2$	EPA1467A, EPA1445A, EPA1563A	
185.0805	$C_9H_{13}O_4$	EPA1483A, EPA1556A, EPA1566A	
186.0358	$C_7H_8NO_5$	EPA1392A, EPA1382A, EPA1375A	
186.0819	$C_8H_9O_4^{13}C$	EPA1483A	
187.0599	$C_8H_{11}O_5$	EPA1467A, EPA1445A, EPA1483A, EPA1563A, EPA1556A, EPA1566A	
189.0410	$C_7H_9O_6$	EPA1353A, EPA1467A, EPA1445A, EPA1483A, EPA1563A, EPA1556A, EPA1559A	(Nguyen, Bateman et al. 2010; Nguyen, Laskin et al. 2011)
191.0319	$C_{10}H_7O_4$	EPA1467A, EPA1483A	
191.0768	$C_7H_{11}O_6$	EPA1556A	
193.0407	$C_6H_9O_7$	EPA1467A	
195.0519	$C_6H_{11}O_7$	EPA1467A, EPA1556A, EPA1566A	
197.0811	$C_6H_{13}O_7$	EPA1556A	
197.1012	$C_7H_{17}O_6$	EPA1467A	
197.1090	$C_{11}H_{17}O_3$	EPA1483A	

198.1031	$C_{10}H_{17}O_3^{13}C$	EPA1483A	
199.0892	$C_{13}H_{11}O_2$	EPA1467A, EPA1445A, EPA1483A, EPA1563A	
199.1024	$C_{10}H_{15}O_4$	EPA1556A	
199.1630	$C_{12}H_{23}O_2$	EPA1563A	
200.0987	$C_{12}H_{11}O_2^{13}C$	EPA1483A	
201.0699	$C_9H_{13}O_5$	EPA1467A, EPA1445A, EPA1483A, EPA1563A, EPA1556A, EPA1566A	
203.0570	$C_8H_{11}O_6$	EPA1467A, EPA1483A, EPA1563A, EPA1556A, EPA1566A	
205.0459	$C_{11}H_9O_4$	EPA1467A, EPA1556A	
205.0659	$C_{15}H_9O$	EPA1483A	
207.0534	$C_7H_{11}O_7$	EPA1467A	
209.0616	$C_{14}H_9O_2$	EPA1467A, EPA1563A	
211.0596	$C_{10}H_{11}O_5$	EPA1467A, EPA1483A, EPA1556A	
213.0740	$C_{10}H_{13}O_5$	EPA1467A, EPA1445A, EPA1556A	
215.0383	$C_7H_3O_4$	EPA1559A	
215.0858	$C_{10}H_{15}O_5$	EPA1467A, EPA1445A, EPA1483A, EPA1563A, EPA1556A	
217.0782	$C_{13}H_{13}O_3$	EPA1467A, EPA1483A, EPA1563A, EPA1556A	
219.0530	$C_8H_{11}O_7$	EPA1467A, EPA1563A	
219.0691	$C_{12}H_{11}O_4$	EPA1483A, EPA1559A	
219.0977	$C_9H_{15}O_6$	EPA1556A	
221.0690	$C_8H_{13}O_7$	EPA1353A, EPA1467A, EPA1483A, EPA1559A	(Surratt, Chan et al. 2010; Sato, Nakao et al. 2011)
223.0523	$C_7H_{11}O_8$	EPA1467A	
225.0637	$C_7H_{13}O_8$	EPA1467A, EPA1556A	
227.0554	$C_{10}H_{11}O_6$	EPA1467A, EPA1483A, EPA1563A	
227.0914	$C_{11}H_{15}O_5$	EPA1556A	
229.0701	$C_{10}H_{13}O_6$	EPA1353A, EPA1467A, EPA1445A, EPA1483A, EPA1563A, EPA1556A, EPA1559A	
231.0732	$C_{10}H_{15}O_6$	EPA1563A	
231.0931	$C_{11}H_{15}O_5$	EPA1556A	
231.1087	$C_{14}H_{15}O_3$	EPA1483A	
233.0679	$C_9H_{13}O_7$	EPA1467A, EPA1483A, EPA1563A, EPA1559A	
233.0999	$C_{10}H_{17}O_6$	EPA1556A	
235.0041	$C_{12}H_{11}O_5$	EPA1467A, EPA1483A, EPA1559A	
235.1005	$C_9H_{15}O_7$	EPA1556A	
237.0649	$C_8H_{15}O_8$	EPA1467A, EPA1556A, EPA1559A	
239.0774	$C_8H_{15}O_8$	EPA1467A, EPA1556A	
239.1684	$C_{10}H_{23}O_6$	EPA1445A	
241.0643	$C_{11}H_{13}O_6$	EPA1467A, EPA1556A	
241.1234	$C_{16}H_{17}O_2$	EPA1483A	
243.0546	$C_{10}H_{11}O_7$	EPA1467A, EPA1559A	
243.0656	$C_{14}H_{11}O_8$	EPA1563A	
243.0834	$C_7H_{15}O_7$	EPA1483A, EPA1556A, EPA1566A	

245.0699	$C_{10}H_{13}O_7$	EPA1483A, EPA1563A, EPA1556A	(Nguyen, Bateman et al. 2010)
247.0792	$C_{10}H_{15}O_7$	EPA1467A, EPA1445A, EPA1483A, EPA1563A, EPA1556A	
249.0623	$C_9H_{13}O_8$	EPA1353A, EPA1467A, EPA1483A, EPA1563A, EPA1556A, EPA1559A	(Surratt, Chan et al. 2010; Sato, Nakao et al. 2011)
250.0763	$C_8H_{12}NO_8$		
251.0791	$C_9H_{15}O_8$	EPA1467A, EPA1556A	
252.0506	$C_7H_{10}NO_9$	EPA1559A	
253.0697	$C_{10}H_{15}O_8$	EPA1467A	(Lin, Zhang et al. 2012)
253.1052	$C_{10}H_{21}O_7$	EPA1556A	
255.0769	$C_{10}H_{21}O_7$	EPA1467A	
255.1033	$C_{12}H_{15}O_6$	EPA1556A	
257.0400	$C_{10}H_9O_8$	EPA1559A	
257.1033	$C_8H_{17}O_9$	EPA1556A	
257.1802	$C_{14}H_{25}O_4$	EPA1483A	
259.0576	$C_{10}H_{11}O_8$	EPA1559A	
259.0706	$C_7H_{15}O_9$	EPA1467A, EPA1556A	
259.0945	$C_{11}H_{15}O_7$	EPA1483A	
260.0286	$C_8H_6NO_9$	EPA1559A	
261.0078	$C_5H_9O_{12}$	EPA1563A	
261.0786	$C_{14}H_{13}O_5$	EPA1467A, EPA1483A	
263.0228	$C_{12}H_7O_7$	EPA1563A	
263.0755	$C_{10}H_{15}O_8$	EPA1353A, EPA1467A, EPA1483A, EPA1556A, EPA1559A	(Surratt, Chan et al. 2010; Sato, Nakao et al. 2011)
264.0893	$C_9H_{14}NO_8$		
265.0681	$C_{13}H_{13}O_6$	EPA1467A, EPA1556A	
266.0556	$C_8H_{12}NO_9$	EPA1353A, EPA1559A	(Surratt, Chan et al. 2010; Sato, Nakao et al. 2011)
267.0596	$C_{12}H_{11}O_7$	EPA1353A, EPA1467A, EPA1559A	
267.1122	$C_9H_{15}O_9$	EPA1556A	
269.0882	$C_9H_{17}O_9$	EPA1467A, EPA1556A	
271.0110	$C_{10}H_7O_9$	EPA1353A, EPA1559A	
271.0370	$C_{11}H_{11}O_8$	EPA1563A, EPA1566A	
271.1095	$C_{12}H_{15}O_7$	EPA1556A	
273.1136	$C_8H_{17}O_{10}$	EPA1556A	
275.0777	$C_{11}H_{15}O_8$	EPA1467A, EPA1483A	
277.0952	$C_{11}H_{17}O_7$	EPA1559A	
277.1113	$C_{15}H_{17}O_5$	EPA1467A	
279.0727	$C_{10}H_{15}O_9$	EPA1467A, EPA1483A	
280.0834	$C_9H_{14}NO_9$	EPA1559A	
281.0869	$C_{10}H_{17}O_9$	EPA1467A, EPA1556A	
282.0953	$C_{12}H_{12}NO_7$	EPA1559A	
283.0803	$C_{13}H_{15}O_7$	EPA1467A, EPA1556A	
285.0895	$C_{13}H_{17}O_7$	EPA1467A, EPA1556A	
286.0551	$C_7H_{12}NO_{11}$	EPA1382A	
287.1224	$C_{12}H_{15}O_8$	EPA1483A	
288.0359	$C_{10}H_{10}NO_9$	EPA1353A, EPA1559A	
289.0130	$C_{10}H_9O_{10}$	EPA1563A	
289.0542	$C_7H_{13}O_{12}$	EPA1559A	

289.0847	$C_{19}H_{13}O_3$	EPA1467A	
290.0527	$C_{13}H_8NO_7$	EPA1559A	
291.0765	$C_{11}H_{15}O_9$	EPA1353A, EPA1467A, EPA1559A	(Nguyen, Laskin et al. 2011)
293.0801	$C_{10}H_{13}O_{10}$	EPA1467A	(Nguyen, Bateman et al. 2010)
293.1069	$C_{11}H_{17}O_8$	EPA1483A	
296.0649	$C_9H_{14}N_1O_{10}$	EPA1353A	(Nguyen, Laskin et al. 2011)
297.1227	$C_{14}H_{17}O_7$	EPA1556A	
297.2479	$C_{17}H_{29}O_4$	EPA1445A	
298.0901	$C_9H_{16}NO_{10}$	EPA1559A	
299.1201	$C_{10}H_{29}O_{10}$	EPA1556A	
301.0857	$C_{12}H_{13}O_9$	EPA1556A	
301.1303	$C_{14}H_{21}O_7$	EPA1483A	
303.1205	$C_{13}H_{19}O_8$	EPA1483A	
304.0260	$C_{10}H_{10}NO_{10}$	EPA1353A, EPA1559A	(Nguyen, Laskin et al. 2011)
305.0867	$C_{12}H_{17}O_9$	EPA1353A, EPA1467A, EPA1559A	(Nguyen, Laskin et al. 2011)
307.0718	$C_{11}H_{15}O_{10}$	EPA1353A, EPA1467A, EPA1559A	(Nguyen, Laskin et al. 2011)
308.1061	$C_{10}H_{14}NO_{10}$	EPA1382A	
309.0910	$C_{11}H_{17}O_{10}$	EPA1467A	
311.2097	$C_{14}H_{31}O_7$	EPA1483A, EPA1563A	
312.0603	$C_9H_{14}NO_{11}$	EPA1353A, EPA1559A	
313.0488	$C_{13}H_{13}O_9$	EPA1563A, EPA1556A	
315.1410	$C_{10}H_{19}O_{11}$	EPA1556A	
315.1372	$C_{18}H_{19}O_5$	EPA1483A	
317.0411	$C_{12}H_{13}O_{10}$	EPA1563A	
317.1255	$C_{14}H_{17}O_{10}$	EPA1483A	
318.0381	$C_9H_{14}NO_{11}$	EPA1559A	
319.0997	$C_9H_{19}O_{12}$	EPA1467A, EPA1559A	
321.0861	$C_{12}H_{17}O_{10}$	EPA1353A, EPA1467A, EPA1559A	(Nguyen, Laskin et al. 2011)
322.1235	$C_8H_{20}NO_{12}$		
323.0976	$C_{12}H_{19}O_{10}$	EPA1353A, EPA1467A, EPA1559A	(Surratt, Chan et al. 2010; Sato, Nakao et al. 2011)
327.0699	$C_9H_{15}N_2O_{11}$	EPA1353A, EPA1559A	(Sato, Nakao et al. 2011)
328.0931	$C_{13}H_{14}NO_9$	EPA1559A	
329.1092	$C_{14}H_{17}O_9$	EPA1556A	
329.10710	$C_{10}H_{17}O_{12}$	EPA1563A	
331.1374	$C_{11}H_{23}O_{11}$	EPA1483A	
333.0097	$C_{11}H_9O_{12}$	EPA1563A	
333.0363	$C_{13}H_{17}O_{10}$	EPA1353A, EPA1467A, EPA1483A, EPA1556A, EPA1559A	(Nguyen, Laskin et al. 2011)
335.0973	$C_{13}H_{19}O_{10}$	EPA1353A, EPA1467A, EPA1556A, EPA1559A	(Nguyen, Laskin et al. 2011)
337.0958	$C_{12}H_{17}O_{11}$	EPA1467A	
337.1601	$C_{17}H_{21}O_7$	EPA1556A	
339.1387	$C_{12}H_{19}O_{11}$	EPA1353A, EPA1556A, EPA1559A	
349.0812	$C_{13}H_{17}O_{11}$	EPA1353A, EPA1467A, EPA1559A	
349.1545	$C_{14}H_{21}O_{10}$	EPA1556A	
350.1075	$C_{16}H_{14}NO_8$	EPA1559A	
351.0956	$C_{13}H_{19}O_{11}$	EPA1353A, EPA1467A, EPA1556A, EPA1559A	(Surratt, Chan et al. 2010; Sato, Nakao et al. 2011)
352.0969	$C_{12}H_{18}NO_{11}$	EPA1353A, EPA1559A	

353.1631	$C_{14}H_{25}O_{10}$	EPA1556A	
354.0724	$C_{11}H_{16}NO_{12}$	EPA1353A	
357.0986	$C_{11}H_{17}O_{13}$	EPA1559A	
363.0960	$C_{14}H_{19}O_{11}$	EPA1353A	
364.1384	$C_{16}H_{14}NO_9$	EPA1559A	
365.1100	$C_{14}H_{21}O_{11}$	EPA1353A, EPA1556A, EPA1559A	(Surratt, Chan et al. 2010; Sato, Nakao et al. 2011)
366.1010	$C_{13}H_{20}NO_{11}$	EPA1353A, EPA1559A	
367.1114	$C_{13}H_{19}O_{12}$		
367.1747	$C_{14}H_{23}O_{11}$	EPA1556A	
368.0856	$C_{12}H_{18}NO_{12}$	EPA1353A, EPA1559A	(Surratt, Chan et al. 2010; Sato, Nakao et al. 2011)
369.0887	$C_{16}H_{17}O_{10}$	EPA1353A, EPA1559A	
375.1139	$C_{15}H_{19}O_{11}$	EPA1559A	
377.1226	$C_{11}H_{21}O_{14}$	EPA1559A	
378.0847	$C_{13}H_{16}NO_{12}$	EPA1559A	
379.0950	$C_{13}H_{19}N_2O_{11}$	EPA1353A, EPA1559A	
380.1108	$C_{13}H_{18}NO_{12}$	EPA1559A	
382.1126	$C_{13}H_{20}NO_{12}$	EPA1559A	
384.1236	$C_{13}H_{22}NO_{12}$	EPA1559A	
391.1149	$C_{15}H_{19}O_{12}$	EPA1559A	
393.1063	$C_{15}H_{21}O_{12}$	EPA1353A, EPA1559A	(Nguyen, Laskin et al. 2011)
394.0930	$C_{13}H_{16}NO_{13}$	EPA1559A	
395.1062	$C_{11}H_{23}O_{15}$	EPA1353A	
400.1241	$C_{13}H_{22}NO_{13}$	EPA1559A	
401.1712	$C_{18}H_{25}O_{10}$	EPA1483A, EPA1556A	
406.1056	$C_{11}H_{20}NO_{15}$	EPA1559A	
407.1186	$C_{16}H_{23}O_{12}$	EPA1353A, EPA1559A	(Nguyen, Laskin et al. 2011)
408.1303	$C_{14}H_{18}NO_{13}$	EPA1559A	
409.1024	$C_{15}H_{21}O_{13}$	EPA1353A	
410.0975	$C_{14}H_{20}NO_{13}$	EPA1353A	
413.1982	$C_{16}H_{29}O_{12}$	EPA1445A	
415.1093	$C_{14}H_{23}O_{16}$	EPA1559A	
415.1833	$C_{18}H_{25}O_{10}$	EPA1483A	
417.1237	$C_{24}H_{17}O_7$	EPA1559A	
417.1850	$C_{17}H_{21}O_{12}$	EPA1483A	
420.1021	$C_{15}H_{18}NO_{13}$	EPA1559A	
422.1130	$C_{15}H_{20}NO_{13}$	EPA1559A	
423.1150	$C_{16}H_{23}O_{13}$	EPA1353A, EPA1559A	
425.1244	$C_{16}H_{25}O_{13}$	EPA1353A	(Surratt, Chan et al. 2010; Sato, Nakao et al. 2011)
427.2134	$C_{17}H_{31}O_{12}$	EPA1445A	
429.1011	$C_{13}H_{21}N_2O_{14}$	EPA1353A, EPA1559A	(Sato, Nakao et al. 2011)
429.1697	$C_{16}H_{29}O_{13}$	EPA1483A	
430.1284	$C_{14}H_{24}NO_{14}$	EPA1559A	
435.1182	$C_{17}H_{23}O_{13}$	EPA1353A	
437.1253	$C_{12}H_{25}N_2O_{15}$	EPA1353A	
444.1323	$C_{14}H_{22}NO_{15}$	EPA1559A	
445.1340	$C_{15}H_{25}O_{15}$	EPA1559A	
447.1638	$C_{30}H_{23}O_4$	EPA1483A	

451.1133	$C_{17}H_{23}O_{14}$	EPA1353A	
453.1250	$C_{17}H_{25}O_{14}$	EPA1353A, EPA1559A	(Surratt, Chan et al. 2010; Sato, Nakao et al. 2011)
454.1249	$C_{16}H_{24}NO_{14}$	EPA1353A	
457.2582	$C_{19}H_{37}O_{12}$	EPA1445A	
459.1415	$C_{14}H_{23}N_2O_{15}$	EPA1559A	
461.1603	$C_{27}H_{25}O_7$	EPA1483A	
465.1252	$C_{18}H_{25}O_{14}$	EPA1353A	
467.1386	$C_{18}H_{27}O_{14}$	EPA1353A, EPA1559A	(Surratt, Chan et al. 2010; Sato, Nakao et al. 2011)
468.1215	$C_{13}H_{26}NO_{17}$	EPA1353A, EPA1559A	
469.1214	$C_{17}H_{25}O_{15}$	EPA1353A	
470.1146	$C_{16}H_{24}NO_{15}$	EPA1353A, EPA1559A	(Surratt, Chan et al. 2010; Sato, Nakao et al. 2011)
471.1178	$C_{20}H_{23}O_{13}$	EPA1353A	
471.3020	$C_{20}H_{39}O_{12}$	EPA1445A	
472.1185	$C_{12}H_{26}NO_{18}$	EPA1353A	
481.1252	$C_{18}H_{25}O_{15}$	EPA1353A	
483.1321	$C_{13}H_{27}N_2O_{17}$	EPA1353A	
484.1449	$C_{17}H_{26}NO_{15}$	EPA1559A	
495.1360	$C_{19}H_{27}O_{15}$	EPA1353A	
496.1335	$C_{18}H_{26}NO_{15}$	EPA1353A	
498.1155	$C_{17}H_{24}NO_{16}$	EPA1353A	
500.1232	$C_{17}H_{26}NO_{16}$	EPA1353A	
509.1464	$C_{15}H_{29}N_2O_{17}$	EPA1353A	
511.1320	$C_{19}H_{27}O_{16}$	EPA1353A	
512.1274	$C_{18}H_{26}NO_{16}$	EPA1353A	(Ng, Kwan et al. 2008)
513.1380	$C_{14}H_{29}N_2O_{18}$	EPA1353A	
525.1438	$C_{20}H_{29}O_{16}$	EPA1353A	
527.1491	$C_{20}H_{31}O_{16}$	EPA1353A	(Surratt, Chan et al. 2010; Sato, Nakao et al. 2011)
531.1283	$C_{17}H_{27}N_2O_{17}$	EPA1353A, EPA1559A	(Sato, Nakao et al. 2011)
539.1519	$C_{17}H_{31}O_{19}$	EPA1353A	
553.1430	$C_{21}H_{29}O_{17}$	EPA1353A	
555.1539	$C_{21}H_{31}O_{17}$	EPA1353A	(Surratt, Chan et al. 2010; Sato, Nakao et al. 2011)
556.1522	$C_{20}H_{30}NO_{17}$	EPA1353A	
557.0560*	$C_{10}H_{16}N_5O_{18}$ + NO_3		(Ng, Kwan et al. 2008)
567.1535	$C_{22}H_{31}O_{17}$	EPA1353A	
569.1668	$C_{22}H_{33}O_{17}$	EPA1353A	
570.1480	$C_{17}H_{32}NO_{20}$	EPA1353A	
572.1445	$C_{20}H_{30}NO_{18}$	EPA1353A	(Surratt, Chan et al. 2010; Sato, Nakao et al. 2011)
573.1476	$C_{24}H_{29}O_{16}$	EPA1353A	
583.1538	$C_{22}H_{31}O_{18}$	EPA1353A	

597.1638	$C_{23}H_{33}O_{18}$	EPA1353A	
613.1606	$C_{23}H_{33}O_{19}$	EPA1353A	
614.1557	$C_{22}H_{32}NO_{19}$	EPA1353A	
627.1725	$C_{24}H_{35}O_{19}$	EPA1353A	
657.1823	$C_{25}H_{37}O_{20}$	EPA1353A	(Surratt, Chan et al. 2010; Sato, Nakao et al. 2011)
671.1933	$C_{26}H_{39}O_{20}$	EPA1353A	(Surratt, Chan et al. 2010; Sato, Nakao et al. 2011)
672.1750	$C_{17}H_{38}NO_{26}$	EPA1353A	
674.1723	$C_{24}H_{36}NO_{21}$	EPA1353A	(Surratt, Chan et al. 2010; Sato, Nakao et al. 2011)
675.1766	$C_{28}H_{35}O_{19}$	EPA1353A	
759.2090	$C_{29}H_{43}O_{23}$	EPA1353A	(Surratt, Chan et al. 2010; Sato, Nakao et al. 2011)
776.2022	$C_{28}H_{42}NO_{24}$	EPA1353A	(Surratt, Chan et al. 2010; Sato, Nakao et al. 2011)
878.2288	$C_{32}H_{48}NO_{27}$	EPA1353A	(Surratt, Chan et al. 2010; Sato, Nakao et al. 2011)

4.7 Figures

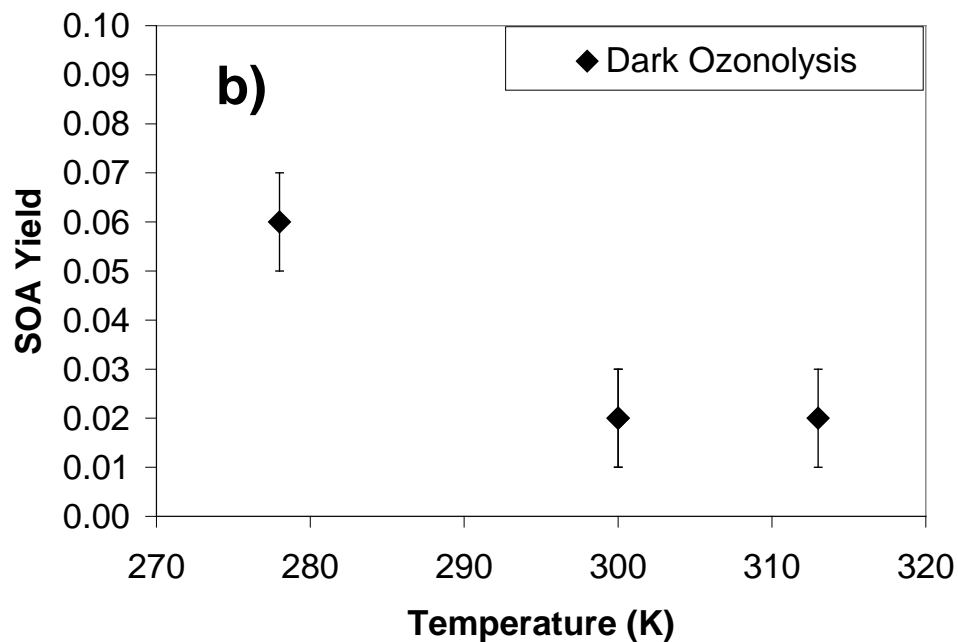
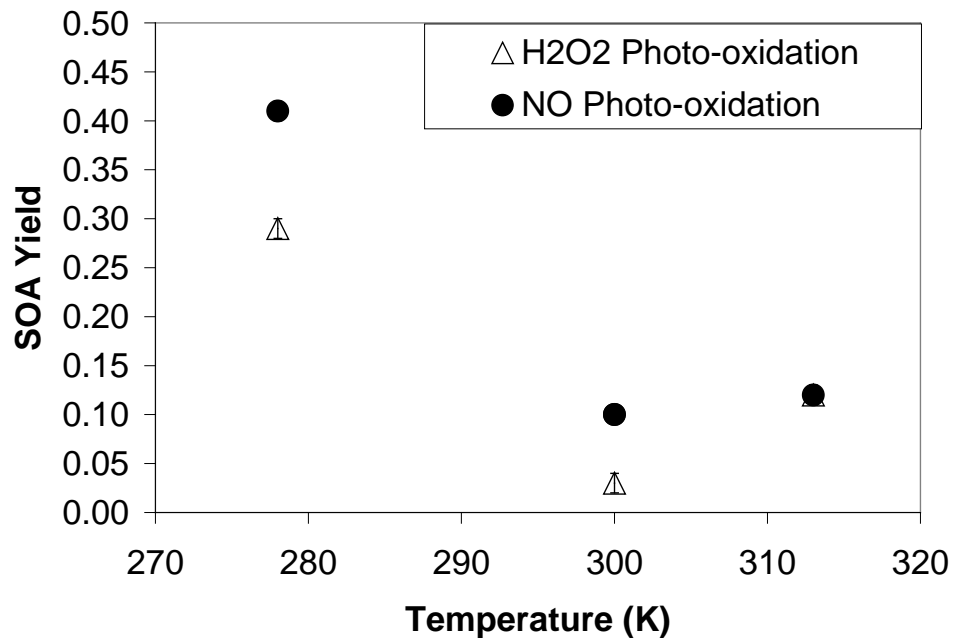


Figure 4.1: Experimental SOA yield as a function of environmental chamber reaction temperature for a) NO and H₂O₂ photo-oxidation experiments and b) dark ozonolysis experiments

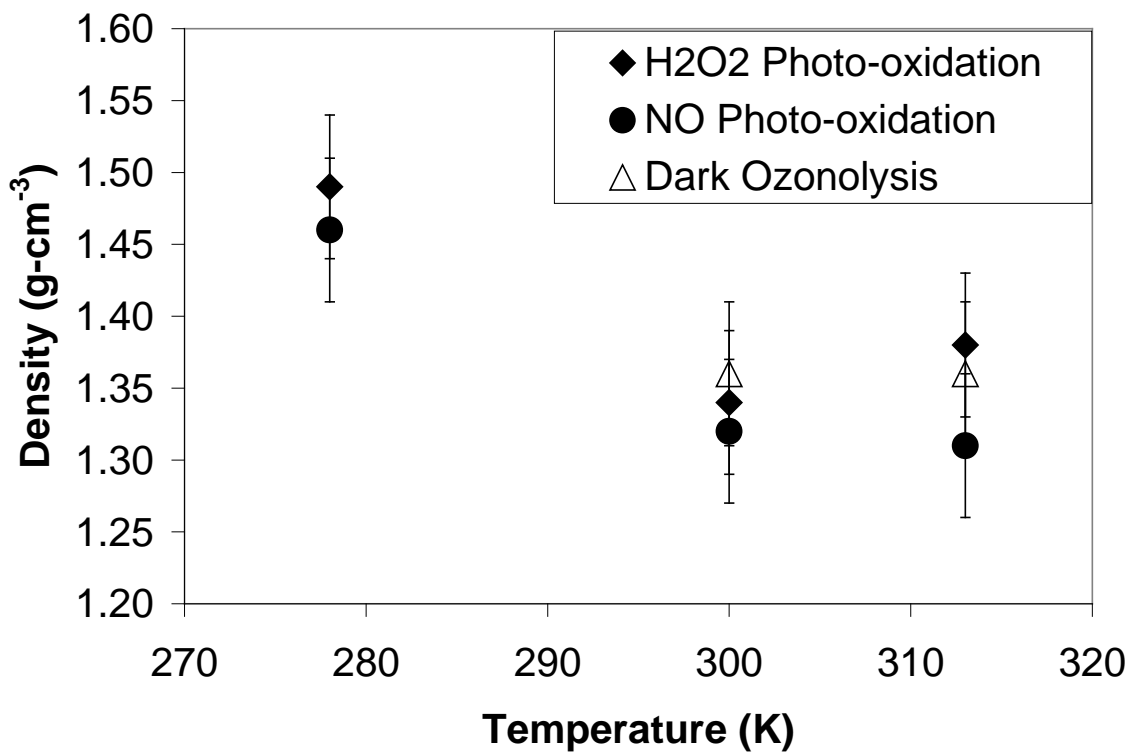


Figure 4.2: SOA density, as measured by APM-SMPS, as a function environmental chamber reaction temperature for isoprene H₂O₂ only photo-oxidation, NO + H₂O₂ photo-oxidation, and dark ozonolysis

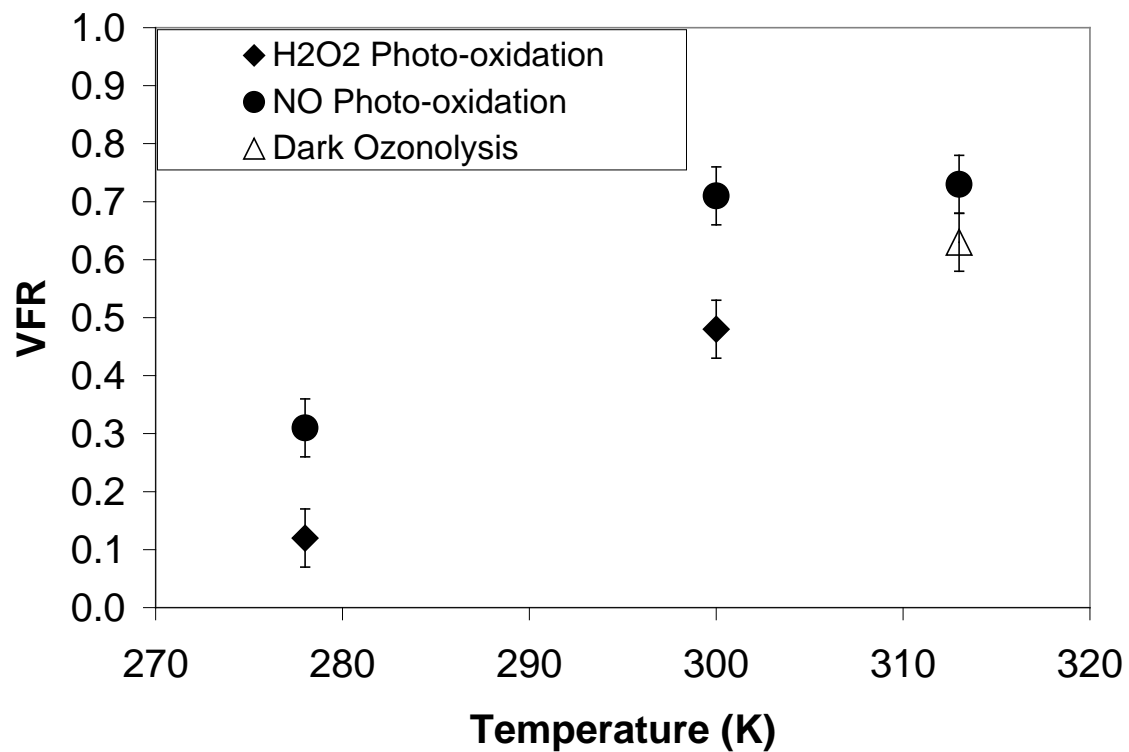


Figure 4.3: Volatile fraction remaining, as measured by VTDMA, as a function environmental chamber reaction temperature for isoprene H₂O₂ only photo-oxidation, NO + H₂O₂ photo-oxidation, and dark ozonolysis

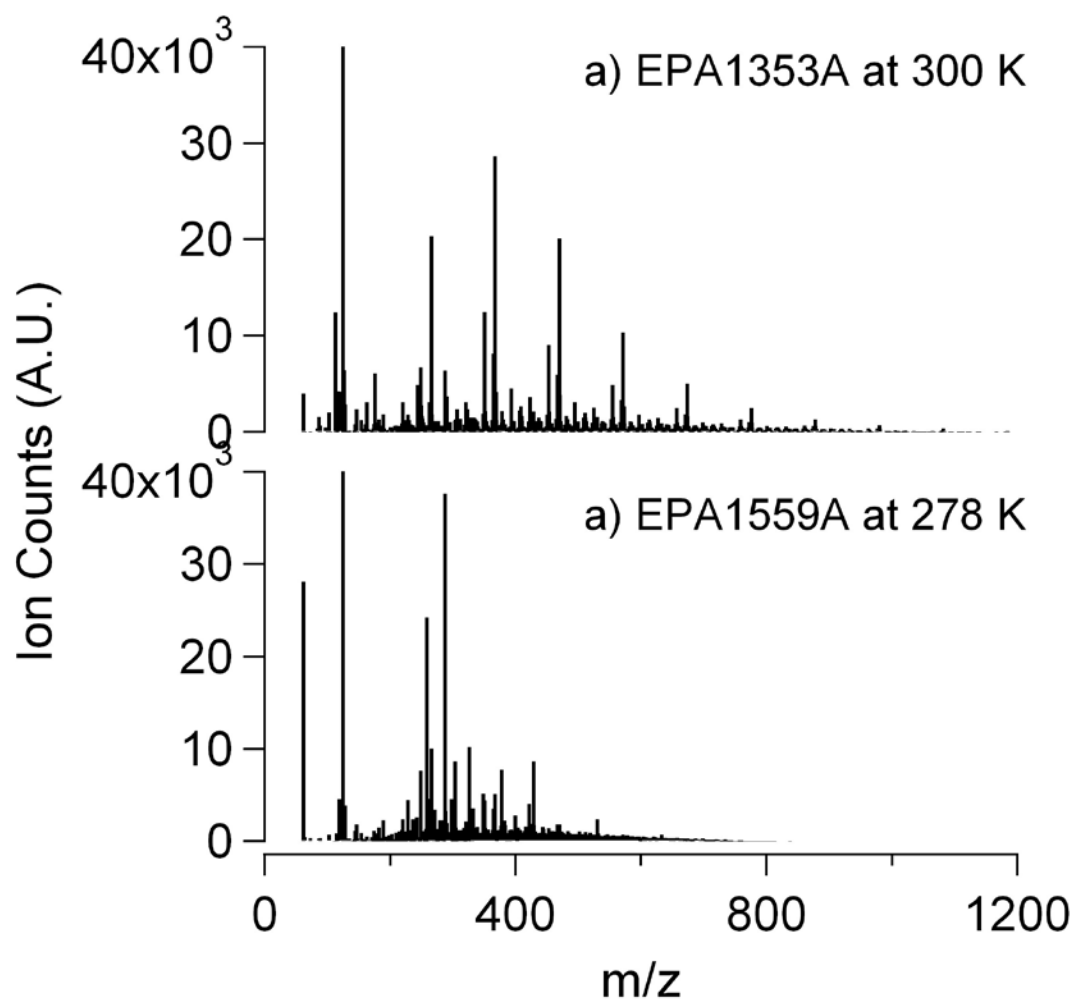


Figure 4.4: PILS-ToF mass spectra for isoprene NO photo-oxidation experiments (a) EPA1353A and (b) EPA1559A performed at environmental chamber temperatures of 300 K and 278 K respectively

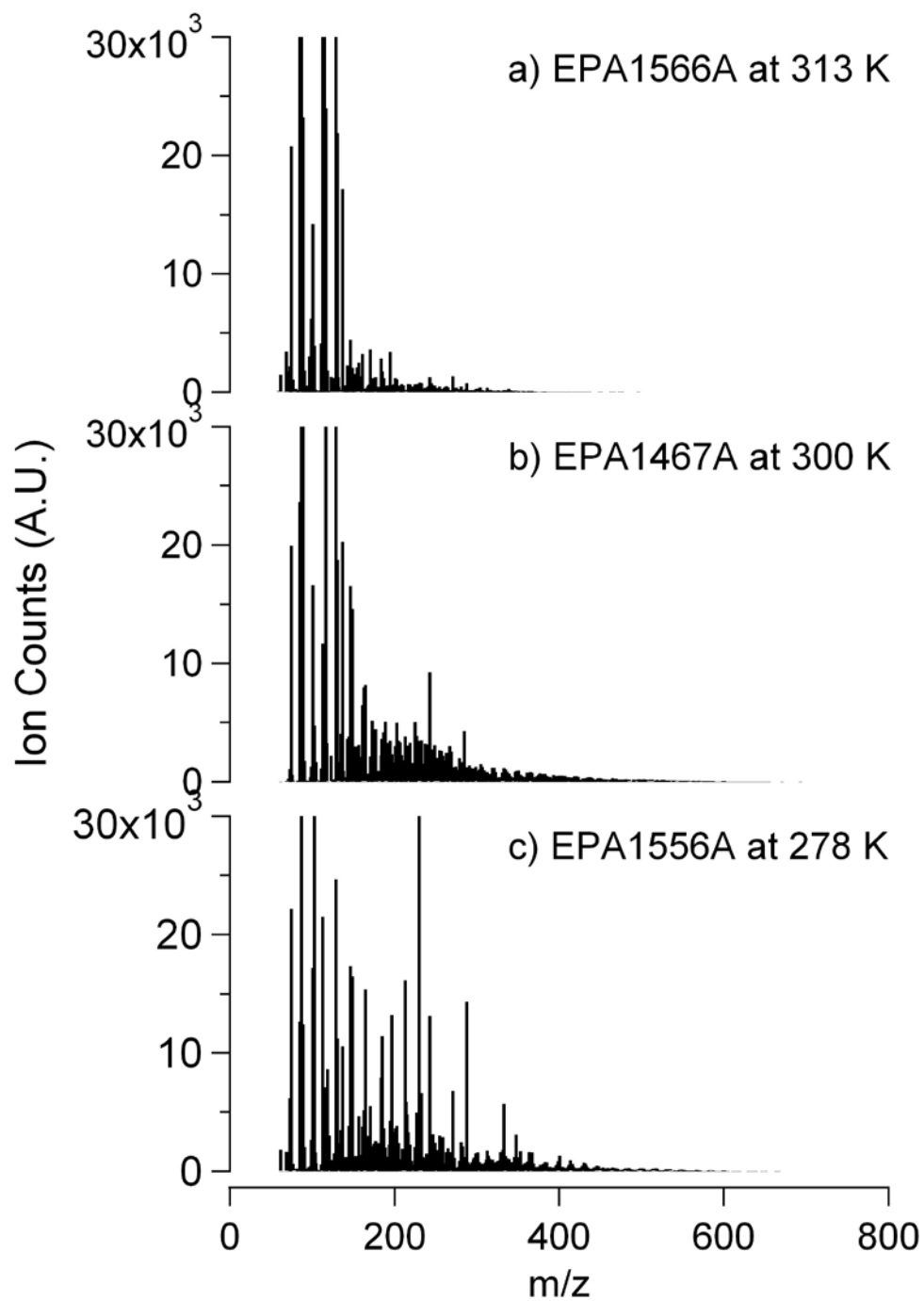


Figure 4.5: PILS-ToF mass spectra for isoprene H_2O_2 photo-oxidation experiments (a) EPA1566A, (b) EPA1467A, and (c) EPA1556A performed at environmental chamber temperatures of 313 K, 300 K, and 278 K respectively

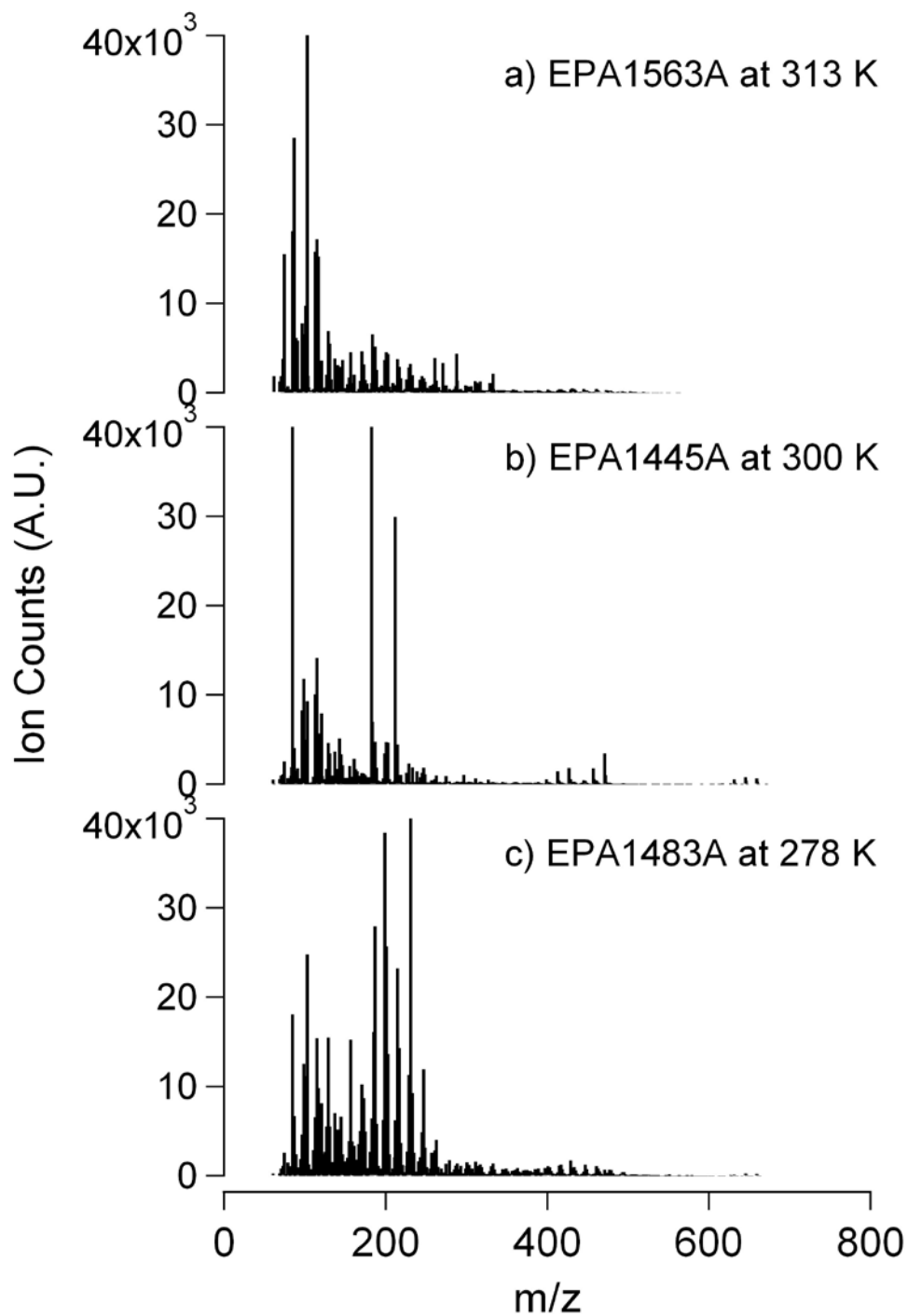


Figure 4.6: PILS-ToF mass spectra for isoprene dark ozonolysis experiments (a) EPA1563A, (b) EPA1445A, and (c) EPA1583A performed at environmental chamber temperatures of 313 K, 300 K, and 278 K respectively

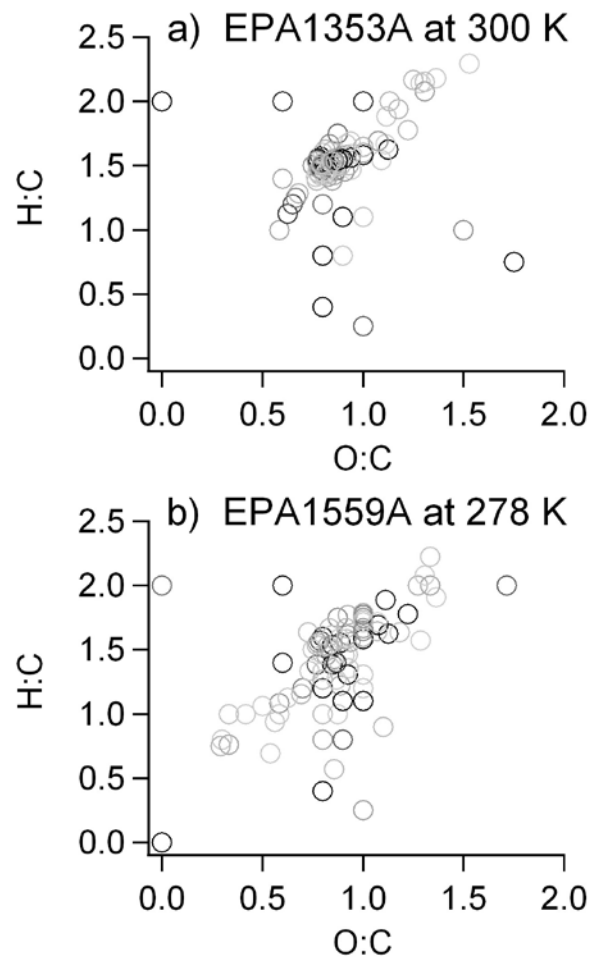


Figure 4.7: PILS-ToF ion matches presented as Van Krevelen Plots for isoprene NO photo-oxidation experiments (a) EPA1353A and (b) EPA1559A performed at environmental chamber temperatures of 300 K and 278 K respectively. *Note mass spectral intensity of an individual ion is presented through a gradient gray scale, where white represents no ion intensity, black represents an ion intensity of 5000 counts or above.

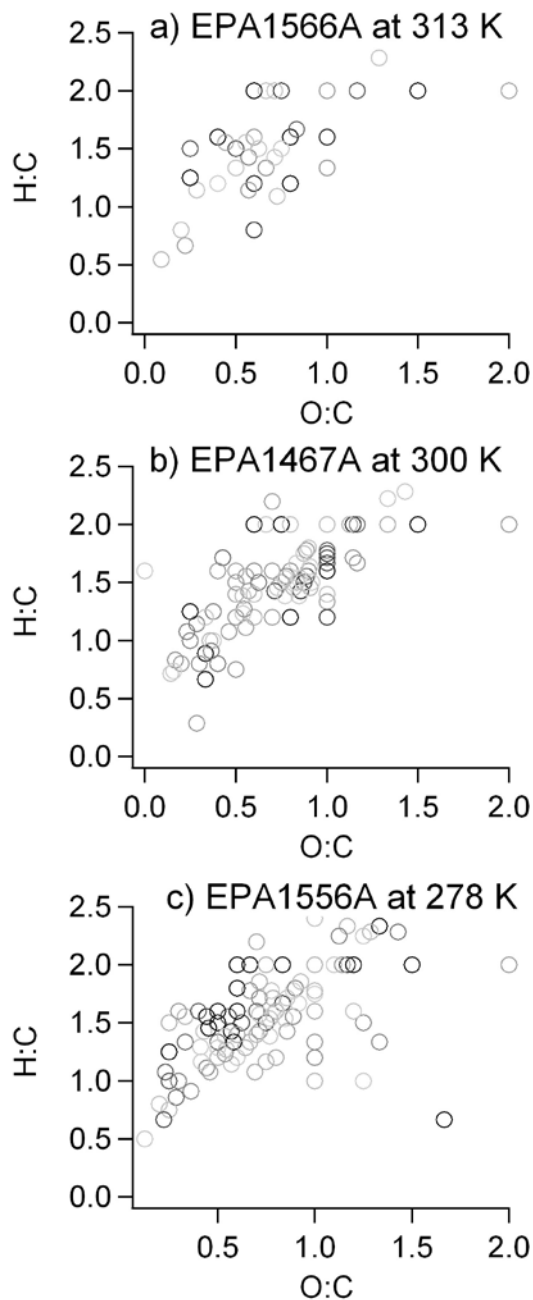


Figure 4.8: PILS-ToF ion matches presented as Van Krevelen for isoprene H₂O₂ photo-oxidation experiments (a) EPA1566A, (b) EPA1467A, and (c) EPA1556A performed at environmental chamber temperatures of 313 K, 300 K, and 278 K respectively. *Note mass spectral intensity of an individual ion is presented through a gradient gray scale, where white represents no ion intensity, black represents an ion intensity of 5000 counts or above.

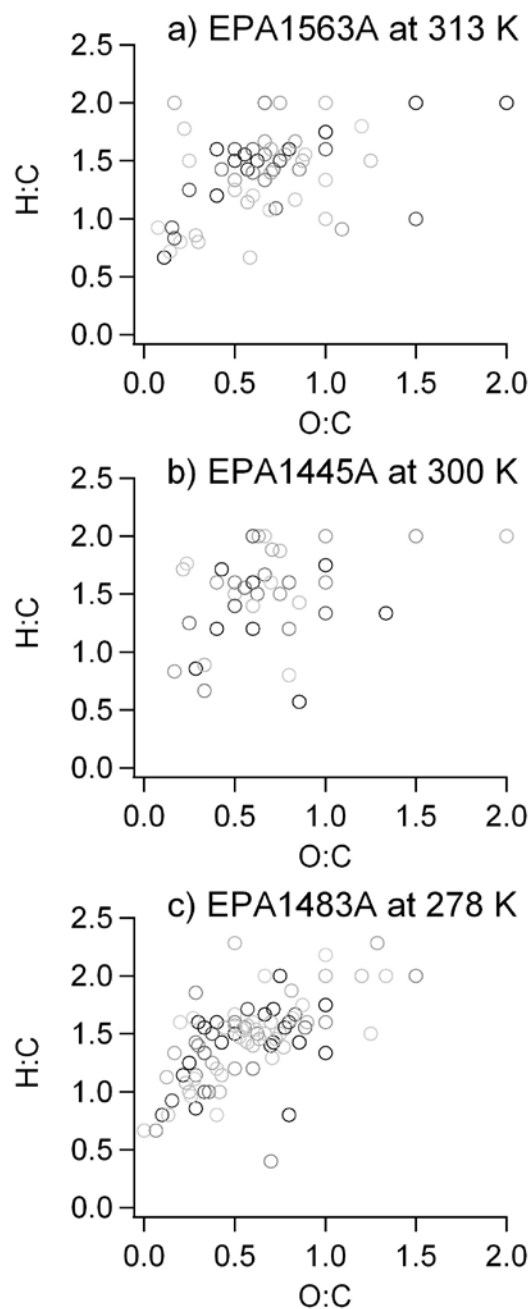


Figure 4.9: PILS-ToF ion matches presented as Van Krevelen for isoprene dark ozonolysis experiments (a) EPA1563A, (b) EPA1445A, and (c) EPA1583A performed at environmental chamber temperatures of 313 K, 300 K, and 278 K respectively. *Note mass spectral intensity of an individual ion is presented through a gradient gray scale, where white represents no ion intensity, black represents an ion intensity of 5000 counts or above.

Chapter 5: Characterization of secondary organic aerosol (SOA) formed during NO_x photo-oxidation and dark nitrate radical reactions of trimethyl amine and tributyl amine by particle into liquid sampling directly coupled to a time of flight mass spectrometry (PILS-ToF)

5.1 Introduction

Trimethylamine (TMA) and tributylamine (TBA) are significantly emitted into the atmosphere. TMA is emitted into the atmosphere by a myriad of sources such as: animal husbandry, industrial processes, landfill emission, biogenic emission, biomass burning, tobacco smoke, and transportation emission (Ge, Wexler et al. 2011). In contrast, TBA is reported only to be emitted by cattle (Ge, Wexler et al. 2011). These two amines serve as excellent experimental surrogates for understanding tertiary amines, as TMA is the simplest tertiary amine and TBA one of the larger, yet atmospherically relevant, tertiary amines. Preliminary experiments conducted in the CE-CERT environmental chambers have shown that both TMA and TBA have potential for SOA formation.

Recent unpublished work by Price and Tang et al. has characterized the particle formation, characterized the particle physical properties, and proposed a mechanism for SOA formation from TMA and TBA, among other primary, secondary, and tertiary amines (Price, Tang et al. 2012; Tang, Price et al. 2012). Here, in support of this larger body of work on amines, TMA and TBA SOA chamber experiments were conducted in

the CE-CERT mezzanine chamber with the focus being the characterization of the SOA by particle-into-liquid sampling coupled to time-of-flight mass spectrometry (PILS-ToF).

SOA formation from TMA and TBA was studied for low-NO_x photo-oxidation (where H₂O₂ alone was added to the chamber), high-NO_x photo-oxidation (where NO and H₂O₂ were added to the chamber), and dark nitrate radical reaction (where N₂O₅ was added to the chamber). Here particle formation data measured by a scanning mobility particle sizer (SMPS) and qualitative particle chemical characterization by PILS-ToF are used to validate the SOA formation mechanisms proposed by Price et al. for TMA and TBA (Price, Tang et al. 2012).

5.2 Materials and Methods

Experiments were conducted in UCR/CE-CERT mezzanine chamber described in detail elsewhere (Nakao, Shrivastava et al. 2011). In short, the mezzanine chamber is a 12 m³ FEP Teflon® film reactor enclosed in a 2.5 m x 3 m x 7.8 m room covered with reflective aluminum sheet, where the reactor is illuminated by 170 blacklights located on the walls of the enclosure. NO_x, CO, and O₃ concentrations were measured by Teledyne model 200E, 300E, and 400E analyzers respectively. Particle size distribution between 27 nm and 686 nm was monitored by a custom built Scanning Mobility Particle Sizer (SMPS) similar to that described by (Cocker, Flagan et al. 2001). A known volume of amine is injected through glass manifold system and flushed into the chamber with purified air. TMA used in chamber experiments is manufactured by Sigma-Aldrich as a

25% by weight solution in water. TBA used in experiments here is GC grade purum 99.0% grade manufactured by Sigma-Aldrich.

A Particle-Into-Liquid-Sampler (PILS) (Weber, Orsini et al. 2001; Orsini, Ma et al. 2003) was interfaced with an Agilent 6210 Time-of-Flight Mass Spectrometer (ToFMS), hereafter referred to as the PILS-ToF, equipped with a multimode ionization source for electrospray and atmospheric pressure chemical ionization (ESI/APCI) to provide an on-line accurate mass analysis of water soluble organic compounds (Bateman, Nizkorodov et al. 2010). In order to couple the PILS (Brechtel Manufacturing Inc.) to the ToFMS, the use of HPLC pumps in addition to a commonly used peristaltic pump was critical to overcome the backpressure of the ToFMS inlet and to supply steady flow of water (18.2M Ω , Milli-Q, Millipore) into the boiler. The PILS-ToF system is described in detail else where (Clark et al., 2012). For this study the ToFMS electrospray ionization sources (ESI) was operated in positive mode with a vaporizer temperature 200 °C, nebulizer pressure 40 psig, corona current 2 μ A, fragmentor voltage 100V. All ToFMS data reported here was acquired using only ESI in positive ion mode.

Occasionally higher mass errors (up to 100 ppm) were observed during sample analysis, which resulted in a consistent shift of mass throughout the mass range of the instrument. Since the extent of the shift can be inferred from repeatedly observed ions (e.g., pyruvic acid), formulas were carefully assigned based on tendency of shift and repeat experiments.

5.3 Results and Discussions

Wall-loss corrected aerosol mass concentration and PILS-ToF mass spectra were measured for three TMA and three TBA experiments, six experiments in total. Table 5.1 presents environmental chamber conditions for the experiments presented in this study. It should be noted that CE-CERT mezzanine chamber is without temperature control and experiments are conducted at room temperature, approximately 25°C. Additionally, amine concentration was not monitored during the experiments; initial amine concentration reported here is based on the volume of liquid injected into the chamber.

5.3.1 Trimethylamine (TMA)

SOA formation from TMA is observed in Table 5.1 to be highly dependent on the oxidant. The dark reaction of TMA with nitrate radical, added as N_2O_5 , is observed to have the highest particle mass formation reported here, $146 \mu\text{g m}^{-3}$, more than an order-of-magnitude greater than the SOA mass formed from TMA high NO_x photo-oxidation, $9 \mu\text{g m}^{-3}$. TMA photo-oxidation done in the absence of NO_x , with H_2O_2 as the only added hydroxyl radical source, is observed to form the median amount of aerosol mass for the three TMA experiments presented in Table 5.1, $41 \mu\text{g m}^{-3}$. Though gas phase amine concentration is not tracked for the TMA experiments here and SOA yield is not reported, it has been tracked in the gas phase by others (Tang, Price et al. 2012). In the gas-phase analysis by Tang et al., the concentration of TMA conversion is observed to scale with SOA formation. TMA's reaction with NO and H_2O_2 has the lowest conversion of TMA and the reaction with N_2O_5 has the highest conversion of TMA.

Figure 5.1 gives the mechanism proposed by Price et al. for oligomer formation from TMA under hydroxyl attack. In reaction group a) of Figure 5.1, hydroxyl radical first attacks a methyl group to form a methyl radical, O_2 then adds to the formed methyl radical to form a methyl peroxy radical, and finally through the formation of an ancillary hydrogen peroxide radical the formyl-amide C_3H_7NO is formed. In Figure 5.1 reaction group a) the peroxy radical could also reduce in a secondary reaction to a hydroxyl-amide. In reaction group b) of Figure 5.1 the hydroxyl attacks the second carbon yielding both a formyl radical and another peroxy radical, both on the number 2 carbon of the amide. The formyl radical and peroxy radical in Figure 5.1 reaction group b), which will be the monomer of an oligomerization process, react to form the dimer presented in reaction group c). This process of oligomerization can continue to add monomer to the initial diformyl-amide subunit until the reactants are completely consumed or the reaction is energetically unfavorable. It should be noted that the formyl groups formed in the mechanism in Figure 5.1 could easily further reduce to alcohols.

Presented in Figure 5.2 are the final state PILS-ToF mass spectra for the TMA experiments in Table 5.1. The mass spectra in Figure 5.2a for chamber experiment MEZ020312, the photo-oxidation of TMA in the presence of NO and H_2O_2 , has very little signal above 200 m/z. The overall PILS-ToF mass spectral signal for the chamber experiment MEZ020312 is the lowest, corresponding to the lowest particle mass formation among TMA chamber experiments. Mass spectral peaks with greater than 1000 ion-counts make up 88% of the total mass spectral signal in Figure 5.2a. These mass spectral peaks above 1000 ion-counts were also m/z chosen for molecular matching.

In Figure 5.2a 18% of the total ion intensity is from m/z 60.0809 corresponding to protonated ionic form of TMA. Although TMA is observed in significant quantities, the most abundant ion is m/z 74.0602 making up 30% of the ion counts observed in Figure 5.2a. The mass spectral peak at m/z 74.0602 matches the protonated ion form $[C_3H_7NO + H]^+$ correlating to a neutral product of reaction group a) of Figure 5.1. The final mechanistic match from Figure 5.1 observed in the PILS-ToF mass spectra is m/z 76.0757 which makes up 21% and corresponds to the protonated form of C_3H_9NO . In total, 69% of the PILS-ToF mass spectra in Figure 5.2a is accounted for by TMA and the products shown in Figure 5.1 reaction group a).

Figure 5.2b presents the PILS-ToF mass spectra of MEZ021012, the photo-oxidation TMA with H_2O_2 as the only added hydroxyl radical source. In Figure 5.2b significant mass spectral signal can be observed up to nearly 1000 amu with an apparent repeating pattern emerging in the mass spectra at 200 amu and continuing to above 600 amu. The mass spectral peaks making up this repeating pattern in Figure 5.2b, correspond to ion forms of the formed oligomer molecules in reaction groups c), d), and e) of Figure 5.1.

It should be noted that in the PILS-ToF mass spectra in Figure 5.2b, corresponding to experiment MEZ021012, a significant peak at m/z 186.2216 best matched to TBA is observed. In looking at the change in intensity of m/z 186.2216 it is found that it only appears as particle nucleation occurs, indicating that TBA is not in the gas-phase at the start of reaction and is a potential adsorbed contaminant in the chamber

during the MEZ021012 experiment. Once particle nucleation occurs, the intensity of m/z 186.2216 is not observed to change, indicating that TBA is not undergoing further processing. The particle phase is deemed a background contaminant and omitted from the calculation of total ion counts for experiment MEZ021012. Mass spectral peaks with greater than 1000 ion-counts in Figure 5.2b make up 81% of the total mass spectral signal in Figure 5.2b. This and all further mass spectral signal reports omit m/z 186.2216.

The ion form of TMA, observed at m/z 60.0815 in Figure 5.2b, makes up 23% of the total ion counts. Ions corresponding to all the molecular products of the reaction mechanism in Figure 5.1 are all matched to PILS-ToF spectral peaks observed in Figure 5.2b. In total, ion forms of the molecules corresponding to the mechanism in Figure 5.1 account for 43% of the total PILS-ToF ion counts observed in Figure 5.2b. Mass spectral peaks at m/z 74.0612, 76.0766, 88.0484, and 106.0513 correspond to the ion matches $[\text{C}_3\text{H}_7\text{NO} + \text{H}]^+$, $[\text{C}_3\text{H}_9\text{NO} + \text{H}]^+$, $[\text{C}_3\text{H}_5\text{NO}_2 + \text{H}]^+$, and $[\text{C}_3\text{H}_8\text{NO}_3 + \text{H}]^+$ which correlate to the neutral molecules in reaction groups a) and b) of Figure 5.1. These four ions account for 36% of the total PILS-ToF mass spectra in Figure 5.2b.

Oligomers shown in reaction groups c) through e) of Figure 5.1 correlate to the ion matches of the mass spectral peaks at m/z 191.0684, 294.0969, 312.1087, 397.1245, 500.1535, 603.1810, 706.2109, 809.2406 which correspond to the ion matches $[\text{C}_6\text{H}_{10}\text{N}_2\text{O}_5 + \text{H}]^+$, $[\text{C}_9\text{H}_{15}\text{N}_3\text{O}_8 + \text{H}]^+$, $[\text{C}_9\text{H}_{17}\text{N}_3\text{O}_9 + \text{H}]^+$, $[\text{C}_{12}\text{H}_{20}\text{N}_4\text{O}_{11} + \text{H}]^+$, $[\text{C}_{15}\text{H}_{25}\text{N}_5\text{O}_{14} + \text{H}]^+$, $[\text{C}_{18}\text{H}_{30}\text{N}_6\text{O}_{17} + \text{H}]^+$, $[\text{C}_{21}\text{H}_{35}\text{N}_7\text{O}_{20} + \text{H}]^+$, and $[\text{C}_{23}\text{H}_{40}\text{N}_8\text{O}_{23} + \text{H}]^+$. These oligomers are noted by 2-sided arrows in Figure 5.2b. Oligomer ions make

up only 8% of the PILS-ToF mass spectral intensity in Figure 5.2b. The presence of oligomers in experiment MEZ021012, TMA photo-oxidation done with H₂O₂ alone, is an explanation for the increased aerosol production over MEZ021012, TMA photo-oxidation done with NO and H₂O₂, where no significant oligomerization, as proposed in Figure 5.1, is observed by the PILS-ToF.

The PILS-ToF final state mass spectra of experiment MEZ021312, the dark reaction of TMA and N₂O₅, is provided in Figure 5.2c. PILS-ToF mass spectral signal is relatively insignificant above m/z 550 with only one peak at an m/z greater than 550 with an intensity of above 1000 ion counts at m/z 921.4633. The oligomers proposed in reaction group c) thru e) of Figure 5.1 are observed in Figure 5.2c for experiment MEZ021312, but they are not as readily apparent in the mass spectra as in Figure 5.2b for experiment MEZ021012. Regarding the mechanism in Figure 5.1, it is assumed that the nitrate radical attack, where N₂O₅ is the nitrate radical source, produces the same general result and mechanism as the hydroxyl radical attack; therefore generally following the mechanism in Figure 5.1.

Again it should be noted that as in the PILS-ToF mass spectra in Figure 5.2b, corresponding to experiment MEZ021012, in Figure 5.2c, corresponding to the PILS-ToF mass spectra for experiment MEZ021312, a significant peak at m/z 186.2216 best matched to TBA is observed. Ion matches of the PILS-ToF mass spectra for experiment MEZ021312, provided in Figure 5.2c, shown make up 82% of the total mass spectral

signal in Figure 5.2b, this and all further mass spectral signal reports for experiment MEZ021312 omit m/z 186.2095.

The PILS-ToF mass spectral ion in Figure 5.2c matched to TMA at m/z 60.0808 accounts for only 2.5% of the total observed ion counts. This is an order-of-magnitude lower signal intensity for TMA in the PILS-ToF mass spectra than observed for the TMA photo-oxidation experiments, MEZ020312 and MEZ021012. This lower PILS-ToF signal intensity for TMA observed in experiment 021312 indicates increased gas phase processing rate of TMA in its reactions with N₂O₅. Overall ions matching the molecular products proposed in the mechanism in Figure 5.1 account for only 29% of the total ion counts in Figure 5.2c, far less than that observed in Figures 5.2a and 5.2b for the photo-oxidation experiments. The mass spectral ions corresponding to oligomers reported in the Figure 5.1 reaction groups c) through e), and their corresponding reduced alcohols, account for 13% of the PILS-ToF ion counts observed in Figure 5.2c.

The observed mass spectral peaks in Figure 5.2c corresponding to the oligomers reaction groups c) thru e) of Figure 5.1, and their corresponding reduced alcohols, are m/z 191.0543, 193.0680, 209.0642, 280.1053, 294.0758, 312.0854, 397.0974, and 500.1292. These previously mentioned mass spectral peaks correspond to the ion matches [C₆H₁₀N₂O₅ + H]⁺, [C₆H₁₂N₂O₅ + H]⁺, [C₆H₁₂N₂O₆ + H]⁺, [C₉H₁₇N₃O₇ + H]⁺, [C₉H₁₅N₃O₈ + H]⁺, [C₉H₁₇N₃O₉ + H]⁺, [C₁₂H₂₀N₄O₁₁ + H]⁺, and [C₁₅H₂₅N₅O₁₄ + H]⁺ respectively. The ion corresponding to the dimer shown in Figure 5.1 reaction group c), observed at m/z 191.0662 corresponding to the protonated ion [C₆H₁₀N₂O₅ + H]⁺, is

the most intense ion in Figure 5.2c but only accounts for 12% of the total PILS-ToF ion counts. The two molecules in Figure 5.1 reaction group a) are observed in Figure 5.2c at m/z 74.0635 and 76.0696 and correspond to the ions $[\text{C}_3\text{H}_7\text{NO} + \text{H}]^+$ and $[\text{C}_3\text{H}_7\text{NO} + \text{H}]^+$ respectively, but only account for 11% of the total PILS-ToF ions counts.

Figure 5.3a-c give the Van Krevelen diagrams (Van Krevelen 1950; Nguyen, Bateman et al. 2010) of the neutral molecular matches for the PILS-ToF ions above 1000 ion counts for experiments MEZ020312, MEZ021012, and MEZ021312 respectively. Figure 5.3d-f gives modified Van Krevelen diagrams where molecule N:C ratios, opposed to O:C for a normal Van Krevelen diagram, is used on the x-axis. Additionally in Figure 5.3, all ion points in the Van Krevelen diagram have a gradient grey scale where white is zero ion counts and black is 5000 ion counts. In comparing Figures 5.3a, 5.3b, and 5.3c the patterns generally look similar, where nearly all molecules fall above the “1:1” line indicating relatively carbonaceous secondary aerosol. Figure 5.3c, 5.3d, and 5.3e all show an increasing N:C ratio indicating that other oligomerization mechanisms, beyond that presented in Figure 5.1, are occurring in all three chamber experiments.

5.3.2 Tributylamine (TBA)

SOA mass formation from TBA follows the same trend as observed above for TMA. With TBA dark nitrate reaction having the largest SOA mass formation, followed by photo-oxidation done in the absence of NO_x , and high NO_x photo-oxidation, the SOA mass formation for these experiments are 92, 40, and 13 $\mu\text{g m}^{-3}$ respectively. Like the

above results for TMA, high NO_x is observed to inhibit SOA formation. In the gas-phase analysis by Tang et al. and the PILS-ToF signal concentration of TBA is observed to scale with SOA formation, like above for TMA. Whereas, TBA's reaction with NO and H_2O_2 has the lowest conversion of TBA and the reaction with N_2O_5 has the highest conversion of TBA.

Figure 5.4 gives the mechanism proposed by Price et al. for TBA oxidation under hydroxyl attack (Price, Tang et al. 2012). The mechanistic process for initial hydrocarbon oxidation is the same for TBA as for TMA, but there are many more carbons to attack in TBA and therefore many more molecular permutations may form. It should be noted that oligomer formation is omitted from the mechanism in Figure 5.4 as oligomerization is not supported by high-resolution aerosol mass spectrometry (AMS) particle characterization presented by Price et al. (Price, Tang et al. 2012) and PILS-ToF data reported here. It is hypothesized that even first generation oxygenation products are SOA species as TBA already a relatively low-volatility semi-volatile compound with a vapor pressure of 0.0934 mm Hg at 25°C (Daubert and Danner 1989) and a Henry's Law Constant of 0.001 (Altschuh, Bruggemann et al. 1999).

Figure 5.5 gives the final state PILS-ToF mass spectra for the TBA experiments in Table 5.1. The mass spectra in Figure 5a for chamber experiment MEZ020612, the photo-oxidation of TBA in the presence of NO and H_2O_2 , has very little signal above 500 m/z. The overall PILS-ToF mass spectral signal for the chamber experiment MEZ020612 is the lowest, corresponding to the lowest particle mass formation among

TBA chamber experiments, a result consistent with those for TMA NO + H₂O₂ photo-oxidation reported above. TMA is observed to contaminate TBA experiment MEZ020612 as TBA is reported above to contaminate TMA experiments, though it is a trivial. The mass spectral signal for TMA protonated ion at m/z 60.0802 is therefore omitted from all further signal reports. Mass spectral peaks with greater than 1000 ion-counts in Figure 5.5a make up 92% of the total mass spectral signal in Figure 5.5a.

In Figure 5.5a, 15% of the total ion intensity is from m/z 186.2217 corresponding to protonated ionic form of TBA. Though TBA is observed in significant quantities, the most abundant ion is m/z 130.1611 making up 21% of the ion counts observed in Figure 5.5a. The mass spectral peak at m/z 130.1611 matches the protonated ion form [C₈H₁₉N + H]⁺ correlating to dibutylamine. In looking at the real time PILS-ToF ion trace of m/z 130.1611 it is observed that it follows the growth of the major initial proposed mechanistic products, discussed directly below, and does not follow exactly either time resolved aerosol mass growth of particles or the PILS-ToF time resolved trace of total ion counts. These results coupled with the many mass spectral peaks observed below the parent reactant TBA, recorded at m/z 186.2217, indicate that fragmentation reactions need to be taken into account in the mechanism of TBA NO +H₂O₂ photo-oxidation. The alcohols and ketones shown in Figure 5.4 correlate to the PILS-ToF mass spectral peaks in Figure 5.5a at m/z 200.2036, 202.2193, 214.1858, and 218.2143 which correspond to the ion matches [C₁₂H₂₅NO + H]⁺, [C₁₂H₂₇NO + H]⁺, [C₁₂H₂₃NO₂ + H]⁺, and [C₁₂H₂₇NO₂ + H]⁺. These mass spectral matches account for 6%, 5%, 0.5%, and 1%

of the PILS-ToF total ion counts respectively. In total 27% of the PILS-ToF mass spectra in Figure 5.5a is accounted for by TBA and the products of shown in Figure 5.4.

Figure 5.5b presents the PILS-ToF mass spectra of MEZ021112, the photo-oxidation TBA with H₂O₂ as the only added hydroxyl radical source. The broad mass spectral picture in Figure 5.5b is similar to that in Figure 5.5a with little mass spectral peaks above m/z 500, but significantly more mass spectral intensity observed between m/z 200 and 400 in Figure 5.5b compared to Figure 5.5a. TMA is observed to contaminate TBA experiment MEZ021112, as it did for MEZ020612, though it is a very minor component. The mass spectral signal for the TMA protonated ion at m/z 60.0802 is therefore omitted from all further signal reports. Mass spectral peaks with greater than 1000 ion-counts in Figure 5.5b make up 93% of the total mass spectral signal in Figure 5.5a.

The ion form of TBA, observed at m/z 186.2309 in Figure 5.5b, makes up 23% of the total ion counts and is the most intense mass spectral peak. Ions corresponding to all the molecular products of the reaction mechanism in Figure 5.4 are matched to PILS-ToF spectral peaks observed in Figure 5.5b. In total ion forms of the molecules corresponding to the mechanism in Figure 5.1 account for 48% of the total PILS-ToF ion counts observed in Figure 5.5b. Table 5.2 gives the observed m/z, percent contribution to the total ion counts, and the ion matches for those keto-amides, hydroxyl-amides, and keto-hydroxyl-amides that correlate to the proposed mechanism in Figure 5.4. These PILS-ToF mass spectral matches for experiment MEZ021112 the photo-oxidation of TBA with

H₂O₂ only, presented in Table 5.2, indicates that the mechanism in Figure 5.4 dominates fragmentation mechanisms.

The PILS-ToF final state mass spectra of experiment MEZ021512, the dark reaction of TBA and N₂O₅, is provided in Figure 5.5c. PILS-ToF mass spectral signal is relatively insignificant above m/z 500 with only one peak at an m/z greater than 500 with an intensity of above 1000 ion counts at m/z 516.437098. Mass spectral peaks with greater than 1000 ion-counts make up 92% of the total mass spectral signal in Figure 5.5c.

Again in Figure 5.5c, the protonated ion form of TBA, observed at m/z 186.2309, is the most intense mass spectral peak making up 43% of the total PILS-ToF ion counts. It should be noted that the protonated form of TMA was not observed in the PILS-ToF mass spectra for MEZ021512. The ions corresponding to products in mechanism provided in Figure 5.4 account for only 6% of the total PILS-ToF ions counts. Table 5.3 gives the observed m/z, percent contribution to the total ion counts, and the ion matches for those keto-amides, hydroxyl-amides, and keto-hydroxyl-amides that correlate to those molecules proposed mechanism in Figure 5.4.

Figure 5.6a-c give the Van Krevelen diagrams (Van Krevelen 1950; Nguyen, Bateman et al. 2010) of the neutral molecular matches for the PILS-ToF ions above 1000 ion counts for TBA experiments MEZ020612, MEZ021112, and MEZ021512 respectively. Figure 5.6d-f gives modified Van Krevelen diagrams where molecule N:C ratios (opposed to O:C for a normal Van Krevelen diagram) is used on the x-axis.

Additionally in Figure 5.6, all ion points in the Van Krevelen diagram have a gradient grey scale where white is zero ion counts and black is 5000 ion counts. In comparing Figures 5.6a, 5.6b, and 5.6c the patterns generally look similar where nearly all molecules fall above the “2:1” line indicating carbonaceous secondary aerosol. Figure 5.6c, 5.6d, and 5.6e molecules appear to form in extension of a focal point corresponding to molecule TBA at (0.083, 2.25) and generally reacting down and to the right.

Though the mechanism in Figure 5.4 does not include a path for addition of nitrogen, Figure 5.6a-c shows that nitrogens are being added to TBA. This nitrogen addition is potentially due to oligomerization as in all TBA experiments reported here. The expected products for an oligomerization occurring similar to that for TMA was assessed against the PILS-ToF matches in Figure 5.5 and no clear oligomerization trend could be determined. In comparing Figure 5.3 for TMA and Figure 5.6 for TBA, one can see that there are more ions with intensity over 1000 counts for all TBA experiments; SOA from TBA is far less oxidized, as it sets twice as close to the ordinate in Figure 5.6a-c. Furthermore, the grouping of the molecular matches is much closer to the ordinate in Figure 5.6d-f, showing that if oligomerization is occurring in the TBA it is occurring far less than for TMA. This leads one to speculate that the carbon number extending from then nitrogen in tertiary amine experiments does play a role in reaction products.

5.4 Conclusions

SOA particle mass formation and PILS-ToF characterization data was presented and analyzed for the $\text{NO} + \text{H}_2\text{O}_2$ photo-oxidation, H_2O_2 only photo-oxidation, and the dark reaction of N_2O_5 for both TMA and TBA. For both TMA and TBA the dark reaction of N_2O_5 formed the most aerosol mass, with H_2O_2 only photo-oxidation forming the median aerosol mass, and $\text{NO} + \text{H}_2\text{O}_2$ photo-oxidation forming the least amount of aerosol mass. A mechanism for reaction of TMA and TBA under radical attack proposed by Price et al. is presented (Price, Tang et al. 2012). The products of these mechanisms account for significant amounts of the PILS-ToF signal observed. For TMA, the PILS-ToF shows oligomerization is occurring for all TMA experiments reported here. The PILS-ToF indicates for TBA fragmentation reactions are relevant, though not proposed in the mechanisms. Though not reported here in the mechanistic description, a nitrogen addition reaction is also indicated in PILS-ToF characterization of all TBA experiments. Overall, PILS-ToF data supports the broad mechanistic interpretation of Price et al. (Price, Tang et al. 2012) for tertiary amines.

5.5 Reference

- Altschuh, J., R. Brüggemann, et al. (1999). "Henry's law constants for a diverse set of organic chemicals: Experimental determination and comparison of estimation methods." Chemosphere **39**(11): 1871-1887.
- Bateman, A. P., S. A. Nizkorodov, et al. (2010). "High-Resolution Electro-spray Ionization Mass Spectrometry Analysis of Water-Soluble Organic Aerosols Collected with a Particle into Liquid Sampler." Analytical Chemistry **82**(19): 8010-8016.
- Cocker, D. R., R. C. Flagan, et al. (2001). "State-of-the-Art Chamber Facility for Studying Atmospheric Chemistry." Environmental Science and Technology **35**: 2594-2601.
- Daubert, T. E. and R. P. Danner (1989). Physical and Thermodynamic Properties of Pure Chemicals Data Compilation. Washington, D.C., Taylor and Francis.
- Ge, X., A. S. Wexler, et al. (2011). "Atmospheric amines - Part I. A review." Atmos. Environ. **45**(3): 524-546.
- Nakao, S., M. Shrivastava, et al. (2011). "Interpretation of Secondary Organic Aerosol Formation from Diesel Exhaust Photooxidation in an Environmental Chamber." Aerosol Sci. Technol. **45**(8): 964-972.
- Nguyen, T. B., A. P. Bateman, et al. (2010). "High-resolution mass spectrometry analysis of secondary organic aerosol generated by ozonolysis of isoprene." Atmospheric Environment **44**: 1032-1042.
- Orsini, D. A., Y. Ma, et al. (2003). "Refinements to the particle-into-liquid sampler (PILS) for ground and airborne measurements of water soluble aerosol composition." Atmospheric Environment **37**: 1243-1259.
- Price, D., X. Tang, et al. (2012). "Mechanism of SOA formation from Amines." In Preparation.
- Tang, X., D. Price, et al. (2012). "Secondary Organic Aerosol (SOA) from amines." In Preparation.
- Van Krevelen, D. W. (1950). "Graphical-statistical method for the study of structure and reaction processes of coal." Fuel **29**: 269-284.

Weber, R. J., D. Orsini, et al. (2001). "A Particle-into-Liquid Collector for Rapid Measurement of Aerosol Bulk Chemical Composition." Aerosol Science and Technology **35**(3): 718-727.

5.6 Tables

Table 5.1. Experimental conditions and aerosol mass formation results

Run	Compound	[Amine] ₀ ^a ($\mu\text{g m}^{-3}$)	[NO] ₀ (ppb)	[H ₂ O ₂] ₀ ^b (ppb)	[N ₂ O ₅] ₀ ^c (ppb)	SOA ^d ($\mu\text{g m}^{-3}$)
MEZ020312	TMA	278	520	425	0	9
MEZ021012	TMA	278	0	425	0	41
MEZ021312	TMA	278	0	0	312	146
MEZ020612	TBA	939	520	425	0	13
MEZ021112	TBA	939	0	425	0	40
MEZ021512	TBA	939	0	0	312	92

^aInitial amine concentration is calculated using the injected volume.

^bInitial H₂O₂ is calculated using the injected volume.

^cInitial N₂O₅ concentration is calculated using the injected volume.

^dto calculate SOA mass concentration from SMPS data a density of 1 was assumed

Table 5.2. Ion matches corresponding to Figure 5.5b correlated to the mechanism in Figure 5.1 for experiment MEZ021112

PILS-ToF observed m/z	TOF-MS ion formula match	Percent of Total PILS-ToF Ion Counts
200.2109	[C ₁₂ H ₂₅ NO + H] ⁺	0.49%
202.2267	[C ₁₂ H ₂₇ NO + H] ⁺	2.35%
206.1158	[C ₁₂ H ₁₅ NO ₂ + H] ⁺	0.06%
208.1290	[C ₁₂ H ₁₇ NO ₂ + H] ⁺	0.17%
210.1588	[C ₁₂ H ₁₉ NO ₂ + H] ⁺	0.06%
212.1748	[C ₁₂ H ₂₁ NO ₂ + H] ⁺	0.46%
214.1912	[C ₁₂ H ₂₃ NO ₂ + H] ⁺	0.93%
216.2006	[C ₁₂ H ₂₅ NO ₂ + H] ⁺	0.05%
218.2212	[C ₁₂ H ₂₇ NO ₂ + H] ⁺	0.44%
224.1218	[C ₁₂ H ₁₇ NO ₃ + H] ⁺	0.03%
226.1412	[C ₁₂ H ₁₉ NO ₃ + H] ⁺	0.06%
228.1722	[C ₁₂ H ₂₁ NO ₃ + H] ⁺	0.45%
230.1865	[C ₁₂ H ₂₃ NO ₃ + H] ⁺	3.35%
234.2062	[C ₁₂ H ₂₇ NO ₃ + H] ⁺	0.06%
242.1492	[C ₁₂ H ₁₉ NO ₄ + H] ⁺	0.05%
244.1664	[C ₁₂ H ₂₁ NO ₄ + H] ⁺	0.37%
248.1971	[C ₁₂ H ₂₅ NO ₄ + H] ⁺	0.23%
262.1777	[C ₁₂ H ₂₃ NO ₅ + H] ⁺	6.76%
264.1933	[C ₁₂ H ₂₅ NO ₅ + H] ⁺	4.64%
266.1957	[C ₁₂ H ₂₇ NO ₅ + H] ⁺	0.09%
276.1582	[C ₁₂ H ₂₁ NO ₆ + H] ⁺	0.09%
278.1743	[C ₁₂ H ₂₃ NO ₆ + H] ⁺	0.45%
280.1894	[C ₁₂ H ₂₅ NO ₆ + H] ⁺	0.36%
294.1701	[C ₁₂ H ₂₃ NO ₇ + H] ⁺	0.13%
296.1851	[C ₁₂ H ₂₅ NO ₇ + H] ⁺	3.15%
298.1971	[C ₁₂ H ₂₇ NO ₇ + H] ⁺	0.08%

Table 5.3. Ion matches corresponding to Figure 5.5c correlated to the mechanism in Figure 5.1 for experiment MEZ021512

PILS-ToF observed m/z	TOF-MS ion formula match	Percent of Total PILS-ToF Ion Counts
200.2109	$[\text{C}_{12}\text{H}_{25}\text{NO} + \text{H}]^+$	2.48%
202.2267	$[\text{C}_{12}\text{H}_{27}\text{NO} + \text{H}]^+$	0.63%
210.1588	$[\text{C}_{12}\text{H}_{19}\text{NO}_2 + \text{H}]^+$	0.05%
212.1748	$[\text{C}_{12}\text{H}_{21}\text{NO}_2 + \text{H}]^+$	0.26%
214.1912	$[\text{C}_{12}\text{H}_{23}\text{NO}_2 + \text{H}]^+$	1.14%
216.2006	$[\text{C}_{12}\text{H}_{25}\text{NO}_2 + \text{H}]^+$	0.25%
218.2212	$[\text{C}_{12}\text{H}_{27}\text{NO}_2 + \text{H}]^+$	0.17%
226.1412	$[\text{C}_{12}\text{H}_{19}\text{NO}_3 + \text{H}]^+$	0.05%
228.1722	$[\text{C}_{12}\text{H}_{21}\text{NO}_3 + \text{H}]^+$	0.17%
230.1865	$[\text{C}_{12}\text{H}_{23}\text{NO}_3 + \text{H}]^+$	0.32%
232.1773	$[\text{C}_{12}\text{H}_{25}\text{NO}_3 + \text{H}]^+$	0.04%
242.1492	$[\text{C}_{12}\text{H}_{19}\text{NO}_4 + \text{H}]^+$	0.05%
244.1664	$[\text{C}_{12}\text{H}_{21}\text{NO}_4 + \text{H}]^+$	0.13%
246.1584	$[\text{C}_{12}\text{H}_{23}\text{NO}_4 + \text{H}]^+$	0.10%
260.1397	$[\text{C}_{12}\text{H}_{21}\text{NO}_5 + \text{H}]^+$	0.07%
262.1777	$[\text{C}_{12}\text{H}_{23}\text{NO}_5 + \text{H}]^+$	0.06%

5.7 Figures

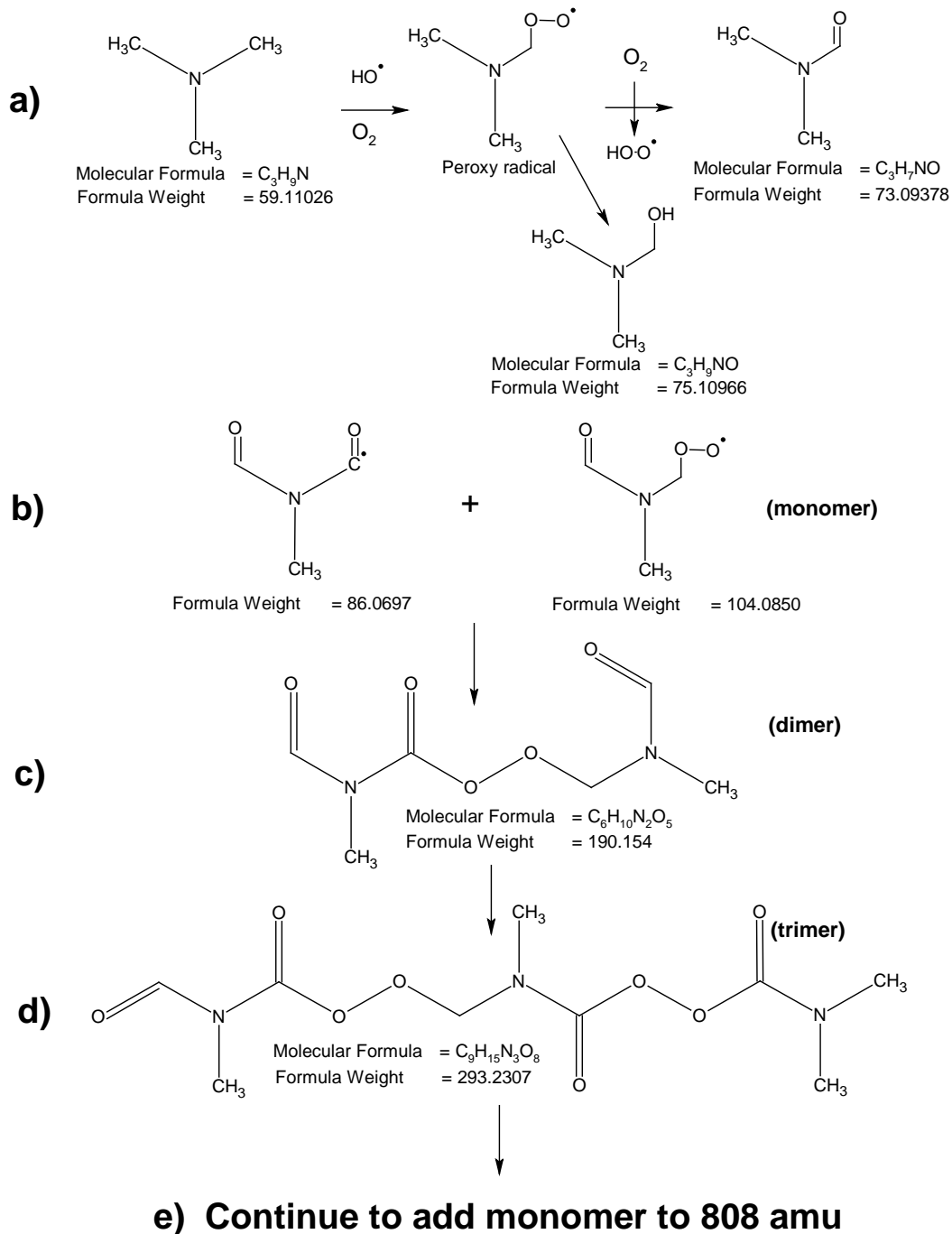


Figure 5.1: Proposed mechanism for oligomer formation from hydroxyl reaction with trimethylamine (TMA) reacting with hydroxyl radical (Price, Tang et al. 2012)

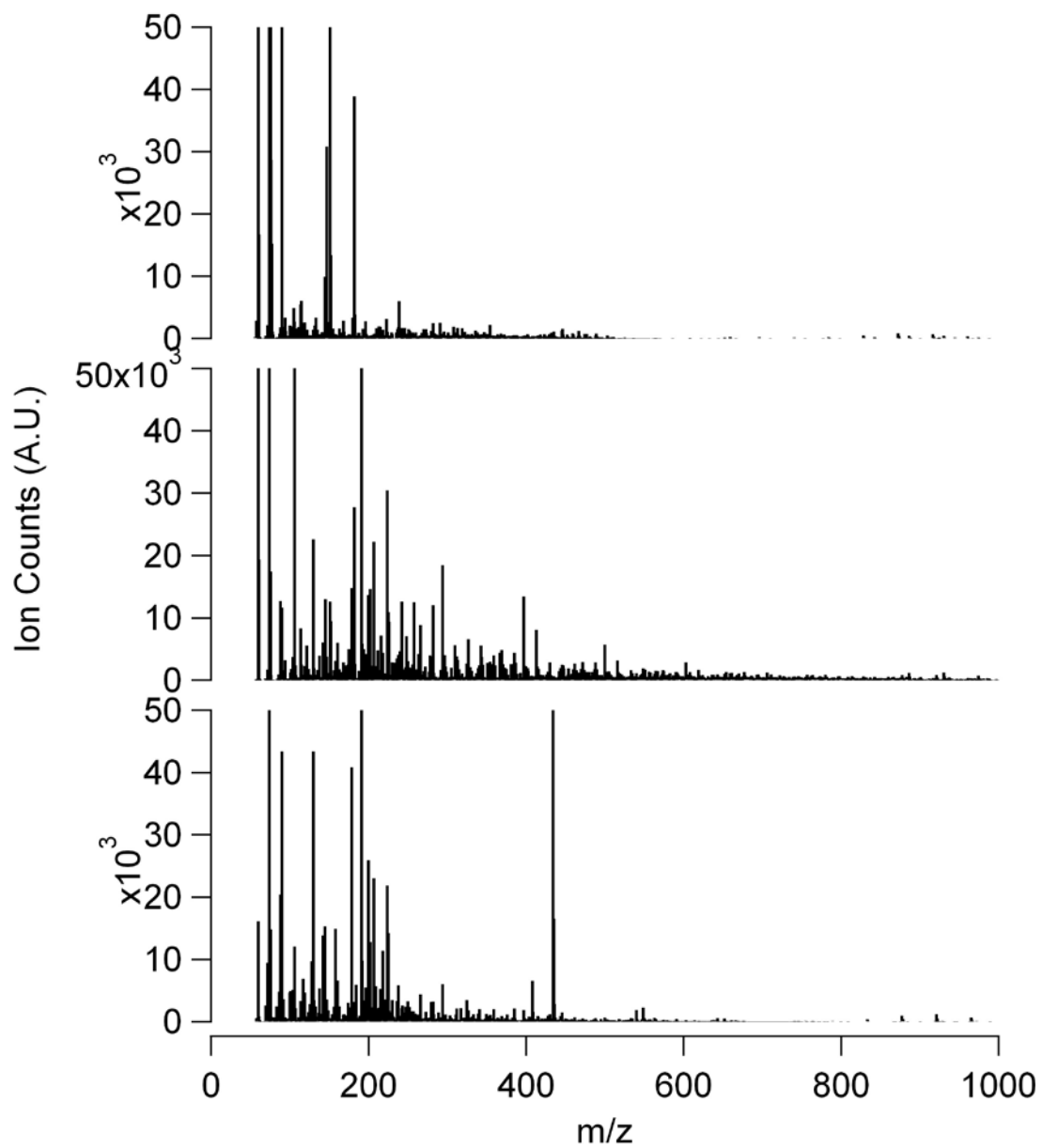


Figure 5.2: Trimethylamine (TMA) experimental end-state PILS-ToF mass spectra for a) MEZ020312, b) MEZ021012, and c) MEZ021312

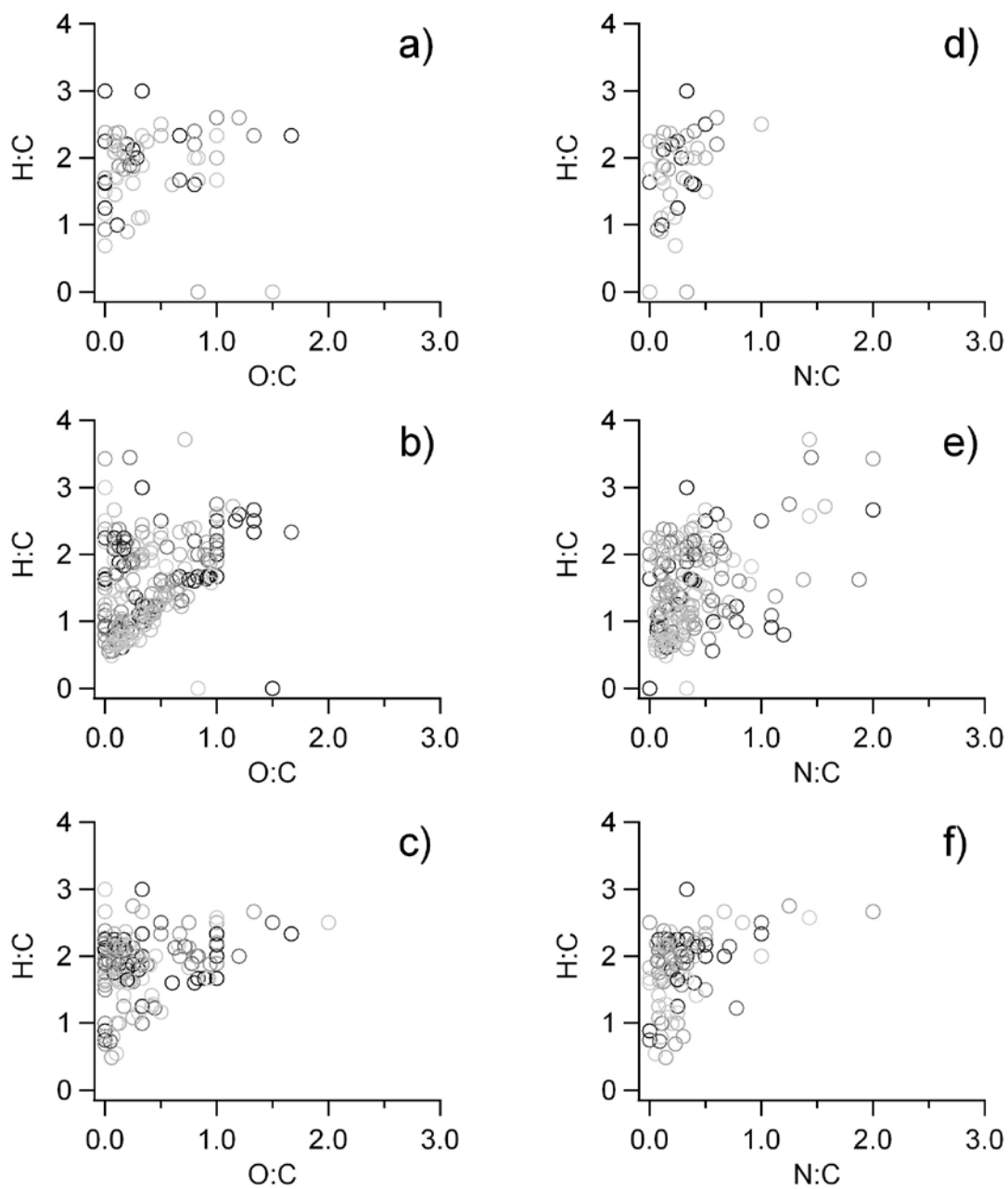


Figure 5.3: Van Krevelen plots (a-c) and modified-Van Krevelen plots (d-f), where N:C ratio is on the ordinate, for molecular matches of final state PILS-ToF mass spectra in trimethylamine (TMA) experiments a)MEZ020312, b)MEZ021012, c)MEZ021312, d)MEZ020312, e)MEZ021012, f)MEZ021312

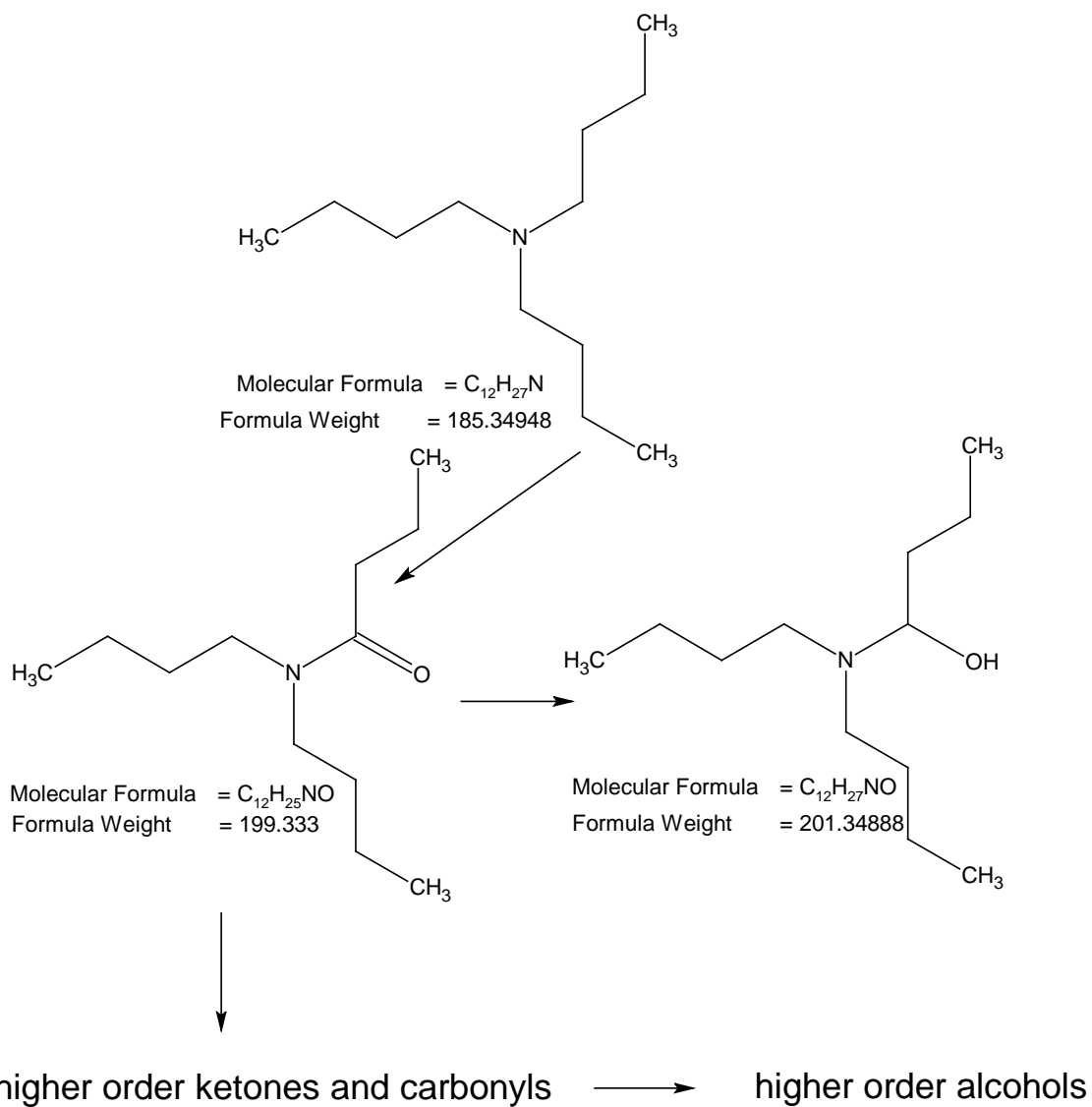


Figure 5.4: Proposed mechanism for formation of major PILS-ToF observed SOA species from tributylamine (TBA) (Price, Tang et al. 2012)

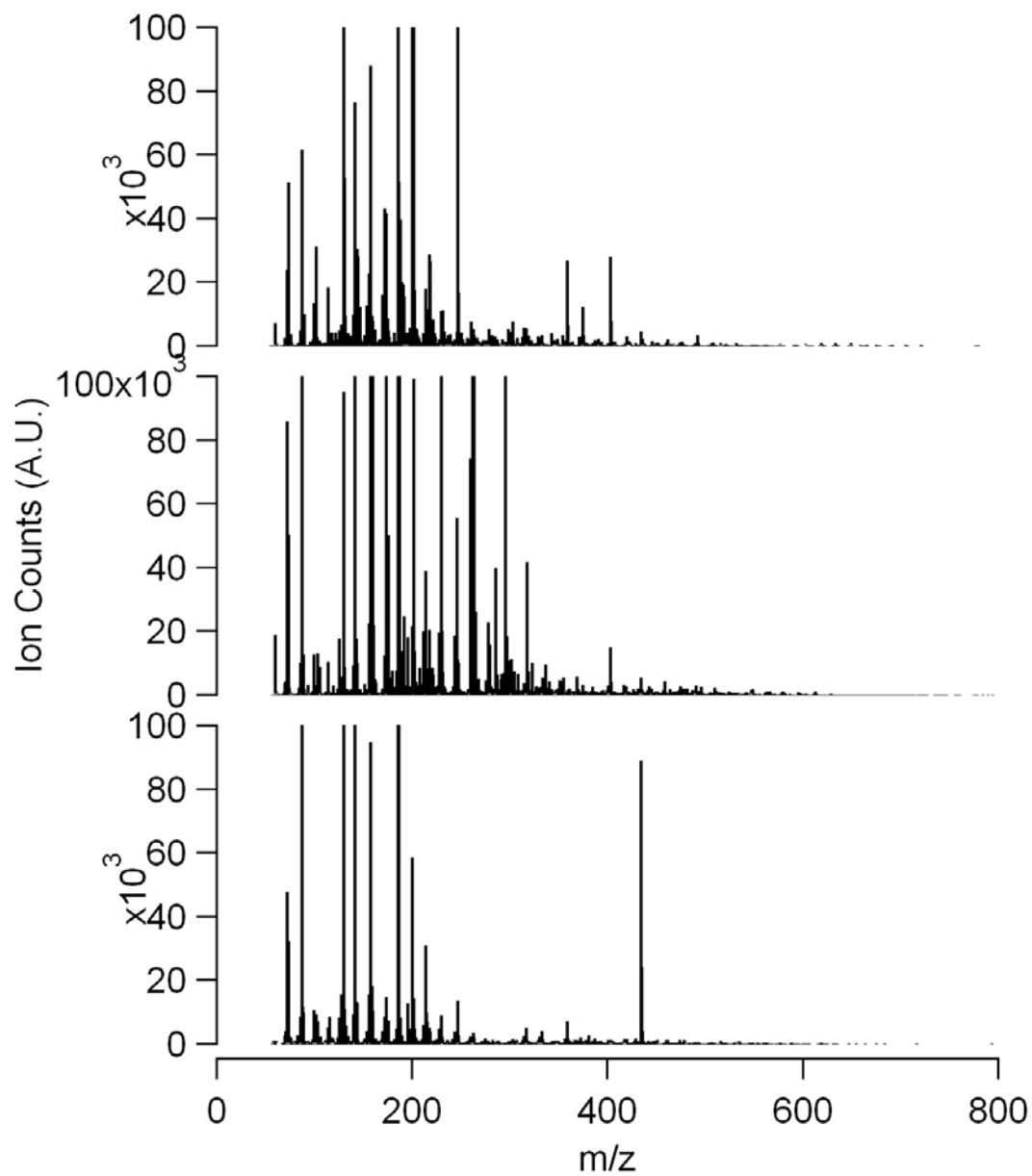


Figure 5.5: Tributylamine (TBA) experimental end-state PILS-ToF mass spectra for a) MEZ020612, b) MEZ021112, and c) MEZ021512

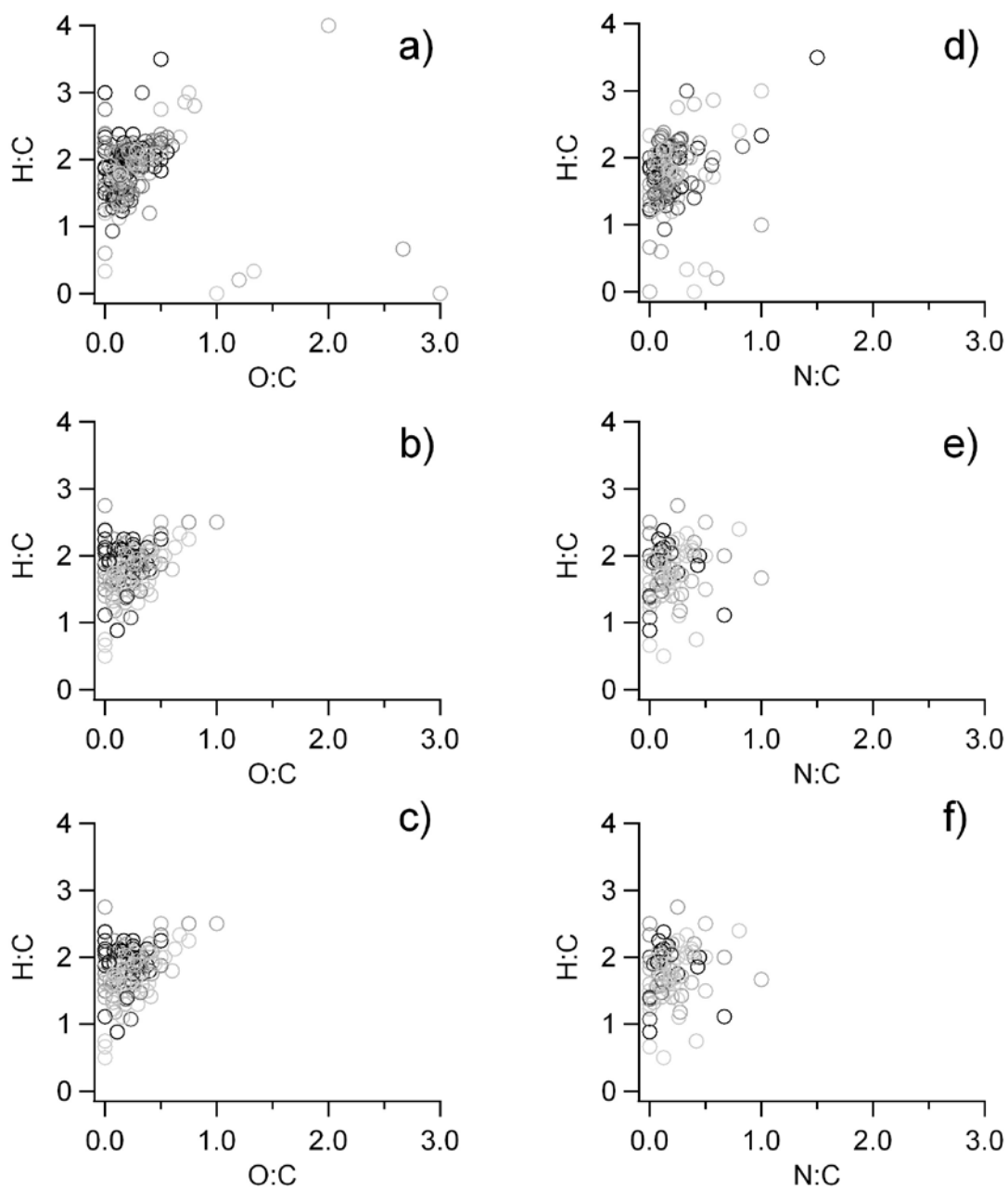


Figure 5.6: Van Krevelen plots (a-c) and modified-Van Krevelen plots (d-f), where N:C ratio is on the ordinate, for molecular matches of final state PILS-ToF mass spectra in tributylamine (TBA) experiments a)MEZ020612, b)MEZ021112, c)MEZ021512, d)MEZ020612, e)MEZ021112, f)MEZ021512

Chapter 6: Summary

In the introduction of the dissertation, Chapter 1, a research question was posited, “can a new mass spectral technique be developed that observes un-fragmented ions, provides near real-time data, and has an acceptable sensitivity be developed?” This dissertation successfully develops, characterizes, and makes use of the particle-into-liquid sampler coupled to a time-of-flight mass spectrometer (PILS-ToF) system toward answering this research question. The PILS-ToF is a new tool that provides simple unfragmented qualitative mass spectral chemical characterization of water-soluble aerosol. Development of the PILS-ToF instrument sought to improve upon drawbacks found in current state-of-the-art mass spectral chemical characterization methods to include lack of time resolution and ion fragmentation by electron impact ionization in the Aerodyne Aerosol Mass Spectrometer (AMS).

Chapter 2 introduces the PILS-ToF as a new time-resolved mass spectral method coupling the particle-into-liquid-sampler (PILS) to a “soft” ionization accurate mass time-of-flight mass spectrometer (ToF-MS). Data presented in Chapter 2 uses reactions of two different hydrocarbon systems known to form secondary organic aerosol (SOA) in chamber studies to validate the PILS-ToF. The PILS-ToF total ion counts are validated to the physical measurement of aerosol mass by SMPS, where the correlation is shown to be linear with an offset. The PILS-ToF is then validated chemically by comparing the chemical characterization results to those previously reported for dark α -pinene ozonolysis and the photooxidation of isoprene and NO using other mass spectral methods. Chapter 2 goes on to use the PILS-ToF to elucidate 5 new oligomeric path

ways in chamber studies of NO photo-oxidation of isoprene. Chapter 2 shows the PILS-ToF agrees with previously reported filter sampling results “soft-ionization” mass spectral results and Aerodyne aerosol mass spectral (AMS) results for dark α -pinene ozonolysis and the NO photo-oxidation of isoprene.

Chapter 3 makes use of the PILS-ToF as a key tool in characterizing SOA formed from oxidation of isoprene in the CE-CERT environmental chamber. It should be noted that the study of SOA from isoprene is deemed important as isoprene is globally the most abundant non-methane hydrocarbon in the ambient. Those SOA experiments discussed in Chapter 3 were performed with those oxidants pertinent to an atmospheric understanding of SOA from isoprene: NO, hydroxyl radical, ozone, and nitrate radical. For a representative subset of these isoprene experiments, the full suite of physical and chemical characterization techniques at CE-CERT were employed to provide insight into the SOA yield, mass formation, density, volatility, and chemical speciation. The study in Chapter 3 provides a complete and intercomparable set of SOA formation experiments from isoprene.

Chapter 3 shows that during NO photo-oxidation of isoprene in the presence of excess hydroxyl radical, added as H_2O_2 , not only was SOA yield and SOA mass formation increased compared to photo-oxidation experiments done in the absence of additional H_2O_2 , but chemical and physical differences in the SOA were observed. For the SOA photo-oxidation experiments there was a strong trend toward decreases in volatility as initial NO concentration was increased; attributable through correlation of

PILS-ToF chemical speciation and VFR measurements to increased nitro-oligomers concentrations. Furthermore, the optimum in SOA formation and yield for isoprene photo-oxidation experiments is observed not at the highest NO concentration but an intermediate NO concentration, corresponding approximately to a HC/NO_x ratio of 1. This optimum SOA formation is shown through PILS-ToF chemical speciation to be a balance between small oxygenated hydrocarbons formed in hydroxyl only photo-chemistry and the incorporation nitrogen into the SOA to form higher order nitro-oligomers.

Chapter 3 goes on to report SOA yields and mass formation from isoprene dark ozonolysis. Dark ozonolysis of isoprene was shown to form SOA with a higher volatility than that formed through isoprene photo-oxidation a result attributable to the prominence of small molecular weight less oxygenated chemical species observed by the PILS-ToF. Chemical composition of SOA formed through dark ozonolysis of isoprene, characterized by the PILS-ToF, done both with and without CO as a hydroxyl scavenger, broadly compares to the chemical composition of SOA formed from the photo-oxidation of isoprene with hydroxyl radical alone (photo-oxidation with H₂O₂ in the absence of NO).

Chapter 3 continues by making study SOA formation through the dark reaction of isoprene with nitrate radical, added to the environmental chamber as N₂O₅. Physical characterization, VFR and density, of the SOA formed through dark reaction of isoprene with N₂O₅ are observed to generally compare with that of high NO photo-oxidation experiments. PILS-ToF chemical characterization shows that chemical species making

up the SOA formed are largely highly nitrogenated compounds. The SOA from isoprene and nitrate radical is observed to contain much more nitrogen than isoprene NO photo-oxidation experiments and with no clear repeating nitro-oligomers. The physical and chemical characterization data for the dark reaction of N_2O_5 with isoprene generally supports the assertion that increased prevalence of nitrogenous species in the SOA leads to decreased SOA volatility in isoprene systems.

Chapter 4 extends the study of SOA from isoprene by probing the effect of reaction temperature. This study shows changes in SOA yield, density, volatility, and PILS-ToF chemical speciation as a function of reaction temperature for isoprene NO + H_2O_2 photo-oxidation, H_2O_2 photo-oxidation done in the absence of initial NO, and dark ozonolysis. Specifically in Chapter 3, SOA yield is observed to increase as reaction temperature is dropped from 300 K to 278K for all three isoprene oxidation systems. However, as reaction temperature is increased from 300 K to 313 K yield is observed to remain relatively unchanged for all three oxidant systems. SOA Density is observed to decrease as reaction temperature is increased from 278 K to 300 K, but is stable for further reaction temperature increase from 300 K to 313K for all isoprene oxidation systems. SOA volatility follows the trend expected from SOA yield and density results; where isoprene SOA volatility decreases in increasing reaction temperature from 278 K to 300 K, but appears to remain stable as reaction temperature is increased from 300 K to 313 K. PILS-ToF speciation, performed in Chapter 4, reveals that as temperature decreases mass spectral molecular matches correlating to lower H:C and O:C ratios are observed, a result consistent for all three isoprene oxidation systems reported here. In the

case of $\text{NO} + \text{H}_2\text{O}_2$ photo-oxidation oligomer production decreases as temperature decreases indicating a strong kinetic effect.

Chapter 5 uses the PILS-ToF to evaluate chemical mechanisms for SOA formation from trimethylamine and tributylamine, two atmospherically relevant tertiary amines emitted from industrial and animal husbandry processes. Chapter 5 presents SOA particle mass formation and PILS-ToF characterization data for the $\text{NO} + \text{H}_2\text{O}_2$ photo-oxidation, H_2O_2 only photo-oxidation, and the dark reaction of N_2O_5 for both trimethylamine and tributylamine. For both trimethylamine and tributylamine the dark reaction of N_2O_5 formed the most aerosol mass, with H_2O_2 only photo-oxidation forming the median aerosol mass, and $\text{NO} + \text{H}_2\text{O}_2$ photo-oxidation forming the least amount of aerosol mass. A mechanism for reaction of trimethylamine and tributylamine under radical attack proposed are presented in Chapter 5 with the products of these mechanisms accounting for large amounts of the PILS-ToF signal observed. For SOA from trimethyl amine the PILS-ToF shows that oligomerization is occurring for all trimethylamine experiments reported. The PILS-ToF indicates that for tributylamine experiments fragmentation and nitrogen addition reactions are relevant though not proposed in the mechanisms.

This dissertation illustrates the functionality and utility of the PILS-ToF system, but there seem obvious aerosol niches, outside the scope of this dissertation, for which the PILS-ToF can provide new and exciting characterization information. It is the hope of the author that future researchers will attempt to apply the PILS-ToF beyond the study

of SOA to other systems such as biological aerosol, primary anthropogenic aerosol, and ambient aerosol.

Appendix A: Secondary organic aerosol formation from the photooxidation of isoprene, 1,3-butadiene, and 2,3-dimethyl-1,3-butadiene under high NO_x conditions

A.1 Introduction

Isoprene is the most abundant nonmethane hydrocarbon emitted into the atmosphere, mainly originating from biogenic sources (Guenther et al., 2006). SOA formation during isoprene oxidation has been investigated via laboratory studies by many researchers (e.g., Pandis et al., 1991; Miyoshi et al., 1994; Jang et al., 2002; Edney et al., 2005; Kroll et al., 2005, 2006; Böge et al., 2006; Dommen et al., 2006; Surratt et al., 2006; Szmigielski et al., 2007; Sato, 2008; Kleindienst et al., 2009). The products formed from isoprene photooxidation (i.e., 2-methyltetrols, C₅-alkenetriols, and 2-methylglyceric acid) have been observed in ambient fine particles (Claeys et al., 2004a, 2004b, 2010; Wang et al., 2005; Xia and Hopke, 2006; Clements and Seinfeld, 2007; Fu et al., 2009, 2010a, 2010b). The atmospheric oxidation of isoprene is currently estimated to be the single largest source of SOA in the atmosphere (Henze and Seinfeld, 2006; Henze et al., 2008; Hallquist et al., 2009; Carlton et al., 2009).

Isoprene and other conjugated dienes are also emitted in urban environments from petrol and diesel engine exhaust or fuel vapor (Jemma et al., 1995; Shi and Harrison, 1997; Smith et al., 2002; Nelson et al., 2008; Agrawal et al., 2008), and measurements in the urban environment have been reported (Jeffries, 1995; Calvert et al., 2002; Liu et al., 2008). A representative conjugated diene emitted from anthropogenic sources is 1,3-butadiene, which is more volatile than isoprene. However, SOA can be produced from

1,3-butadiene if its oxidation products were to undergo particle-phase oligomerization. Three previous studies have investigated SOA formation from the photooxidation of 1,3-butadiene (Kroll et al., 2005; Angove et al., 2006; Sato, 2008), but the yield and the composition of SOA formed from this reaction remain poorly understood. In this study, we experimentally investigate the formation of SOA from the photooxidation of conjugated dienes in the presence of NO_x to improve our understanding of SOA formation from these reactions in urban air.

The major particle-phase products formed in the presence of NO_x from isoprene photooxidation are oligoesters; these oligoesters are produced by the aerosol-phase oligomerization of 2-methylglyceric acid (Surratt et al., 2006, 2010; Szmigielski et al., 2007; Chan et al., 2010). 2-Methyltetrols and C_5 -alkenetriols are formed as particle-phase products under low NO_x conditions (Surratt et al., 2006; Kleindienst et al., 2009; Paulot et al., 2009; Surratt et al., 2010) but are not produced under high NO_x conditions (Surratt et al., 2006). However, 2-methyltetrols are also found in ambient particles even under high NO_x conditions (Edney et al., 2005; Claeys et al., 2010). A possible source of 2-methyltetrols in the presence of NO_x is the decomposition of nitrooxypolyols (Sato, 2008; Szmigielski et al., 2010); however, experimental evidence of nitrooxypolyol formation during isoprene photooxidation under high NO_x conditions is still limited. Another likely source of 2-methyltetrols is the decomposition of organosulfates containing a nitrooxypolyol residue. These compounds are formed from isoprene in the presence of NO_x and sulfuric acid, and have been detected in ambient fine aerosol (Surratt et al., 2007, 2008; Gómez-González et al., 2008).

During oligoester formation from isoprene photooxidation, particle-phase oligomerization occurs following the gas-to-particle absorption of semi-volatile products. The gas-to-particle equilibrium shifts to the particle side with decreasing temperature (Odum et al., 1996; Takekawa et al., 2003). On the other hand, the rate of particle-phase oligomerization decreases with decreasing temperature if the oligomerization process has a substantial activation barrier. Measurement of the temperature dependence of SOA yield from the reaction of isoprene will provide a better understanding of SOA formation involving oligomerization in the particle phase. To our knowledge, the temperature dependence of aerosol yield or aerosol composition during isoprene photooxidation has never been investigated.

In this study, SOA formation from the photooxidation of isoprene (ISO), isoprene-1-¹³C (ISO-13C), 1,3-butadiene (BD), and 2,3-dimethyl-1,3-butadiene (DMB) was investigated under high NO_x conditions (Fig. 1). The aims of this study were to verify the known mechanism of SOA formation from isoprene/NO_x photooxidation and to elucidate the mechanism of SOA formation from the reactions of other conjugated dienes. We explored particle-phase products paying attention not only to known oligoester products but also to nitrooxypolyols and their derivatives. Furthermore, we studied the temperature dependence of SOA yield and SOA composition during isoprene photooxidation.

A.2 Experimental Section

A.2.1 materials

Isoprene (Aldrich, 99%), isoprene-1-¹³C (Aldrich, 99 atom % ¹³C, 97% (CP)), 1,3-butadiene (Aldrich, 99%), and 2,3-dimethyl-1,3-butadiene (Aldrich, 98%) were used as reactants. Hydrogen peroxide (Aldrich, 50% in H₂O) was used as an OH radical source without further concentration.

A.2.2 experimental procedure

Table A.1 shows the experimental conditions of this study. All experiments were conducted using the UCR CE-CERT 90-m³ environmental chamber (Carter et al., 2005; Malloy et al., 2009; Qi et al., 2010). Two Teflon 90-m³ reactors located in a 450-m³ enclosure were ventilated by dry purified air (dew point less than 233 K). Prior to an experiment, the reactors were filled with dry purified air. Nitrogen oxide (22–940 ppb), conjugated diene (20–965 ppb), and hydrogen peroxide (0–3 ppm) were injected into each reactor using nitrogen carrier gas. The gas mixture in each reactor was then stirred using a mixing fan for 1 min. Complete mixing was ensured by monitoring NO_x and diene concentration using a chemiluminescence NO/NO_x analyzer (Teco, Model 42C) and gas chromatography with flame ionization detection (GC-FID; Agilent, Model 6890N). The two reactors were then irradiated by black lights (Sylvania, 350BL, the light intensity is peaked at 350 nm with 40 nm FWHM). The NO₂ photolysis rates were 0.12 and 0.40 min⁻¹ when 80 and 276 black lights were used at 300 K, respectively. The pressure of each reactor was maintained at 5 Pa higher than the enclosure by pressing the

reactor wall in order to avoid any leakage of contaminants; thus, the reactor volume decreased with time. An experiment was finished when the volume of a chamber decreased to one-third the initial value. The experimental duration ranged from 6 to 9 h during the present experimental period. The H₂O₂ photolysis rate when 276 lights were used was evaluated to be $6.4 \times 10^{-4} \text{ min}^{-1}$ from the NO₂ photolysis rate, the black light spectrum, and the NO₂ and H₂O₂ absorption spectra (DeMore et al., 1997). No seed aerosol was used in all experiments.

The air temperature in the enclosure was controlled by an air handler with ~105 kW cooling power. Most experiments were conducted at room temperature ($300 \pm 1 \text{ K}$) while two experiments with isoprene were conducted at a low temperature ($278 \pm 1 \text{ K}$). In order to correct the change in light intensity caused by temperature decrease, the number of lights used at 278 K was adjusted to reproduce the NO₂ photolysis rate of experiments at 300 K (Qi et al., 2010).

Aerosol particles in the reactors were collected on a Teflon membrane disk filter (Pall, Teflo®, 2 µm pore, 47-mm diameter) for off-line analysis of particle-phase products. The samples were collected for 30 – 120 min at a flow rate of 25 L min⁻¹. Pretreatment of sample filters was conducted within 48 hrs of sampling. Sample filters were stored in a freezer until pretreatment. Each sample filter was extracted by sonication in 5 mL of methanol for 30 min. Each extract was concentrated under a gentle stream of dry nitrogen until dried. Each sample was reconstituted with 1-mL acetic

acid/methanol/water solution ($v/v/v = 0.1/49.95/49.95$) and was then used as an analytical sample.

A.2.3 instruments

The concentrations of gaseous compounds were measured by two GC-FID instruments, an NO/NO_x analyzer, and an ultraviolet absorption ozone analyzer (Dasibi, Model 1003-AH). Furthermore, reactant and product volatile organic compounds (VOCs) were measured by a high sensitivity proton transfer reaction – mass spectrometer (PTR-MS; Ionicon).

Particle-size distribution between 28 and 730 nm was measured using two custom-made scanning mobility particle sizer (SMPS) instruments similar in design to those described elsewhere (Cocker et al., 2001). Particle number and volume were wall-loss corrected using the method of Bowman et al. (1997). Particle-mass loading was calculated assuming a unit density. Note that the present yield would be higher if a higher aerosol density is used. The volatility of particles at 373 K was measured by a custom-made volatility tandem differential mobility analyzer (VTDMA) having a similar design as that described elsewhere (Qi et al., 2010). The volume fraction remaining (VFR) was monitored for 75, 100, and 125 nm particles, and the VFR was confirmed to be independent of the particle diameter within an experimental uncertainty. The residence time of the aerosol in the thermodenuder was 17 s, which is sufficiently long under present experimental conditions (An et al., 2007). The off-line analysis of SOA particles was conducted by high-pressure liquid chromatography/accurate mass (3 ppm) time-of-

flight mass spectrometry (LC-TOFMS; Agilent, Model 6210). A 10- μ L aliquot of analytical sample was injected into the LC-TOFMS instrument. The mobile phases used were 0.1% acetic acid aqueous solution (A) and 0.1% acetic acid methanolic solution (B). The total flow rate of mobile phases was set to 0.5 mL min⁻¹. The concentration of mobile phase B was set to 50% in the flow-injection analysis conducted without a column. On the other hand, in the column-injection analysis, the concentration of mobile phase B was set to 5% as an initial value and was linearly increased to 90% in 30 min. The column used was an octadecyl silica gel column (Agilent, 4.6 \times 150 mm Eclipse, XDB-C18); the temperature of the column was set to 298 K. Analytes were ionized by electrospray ionization (ESI) method in negative polarity mode; the temperature of the vaporizer was set to 448 K; nebulizer gas pressure was set to 276 kPa; and fragmentor voltage was set to 160 V. The ions formed were analyzed by a time-of-flight mass spectrometer.

The real-time mass spectrum of SOA was measured by a time-of-flight aerosol mass spectrometer (ToF-AMS; Aerodyne); details of the instrument are explained elsewhere (Drewnick et al., 2005). Particles collected through an aerodynamic lens were vaporized by a heater at 873 K. Vaporized compounds were ionized by electron ionization (EI) and analyzed by the time-of-flight mass spectrometer in V mode, which was selected to detect oligomers in a high sensitivity. The mass resolution in V mode was typically \sim 2700, and this enabled us to resolve the peaks of NO⁺ (m/z 29.997) and CH₂O⁺ (m/z 30.010). Data obtained was numerically analyzed by the ToF-AMS Analysis Toolkit program version 1.48 and ToF-AMS HR Analysis program version 1.07 (ToF-AMS Software Downloads, 2009).

A.3 SOA formation

A.3.1 Time profile

Figure A.2a shows the time profiles of gaseous reactants and products obtained from an isoprene photooxidation experiment (EPA1078W). The concentrations of isoprene and NO decreased with irradiation time. Figure A.2b shows a time profile of SOA mass concentration obtained in the same experiment. The plotted SOA concentrations are values obtained after wall-loss correction. The SOA mass concentration increased to above a detectable level after most of the initial NO was consumed. Similar results were observed under lower NO_x conditions (EPA1069W and EPA1070E; NO_x/HC = 0.06–0.08) as well as in this experiment (NO_x/HC = 2.23). The SOA concentration continued to increase after most of the isoprene was consumed. The SOA mass concentration had not leveled off by the end of the experiment. This was typical in experiments in which the NO₂ photolysis rate was 0.12 min⁻¹. Reported SOA yields in these experiments are probably underestimated by low extent of reaction.

Figure A.2c shows the time profiles of PTR-MS signals at *m/z* 69 and 71. Isoprene, having a molecular weight of 68, was detected by PTR-MS as protonated molecules at *m/z* 69. In the same figure, scaled GC-FID isoprene data is also plotted. The time profile at *m/z* 69 agreed with that of the relative isoprene concentration measured by GC-FID. Methacrolein and methyl vinyl ketone, produced as first-generation products during isoprene oxidation, were detected as protonated molecules at *m/z* 71. Signal intensity at *m/z* 71 increased and then decreased due to the formation and subsequent reactions of

these products. SOA concentration increased with decreasing signal intensity at m/z 71, suggesting that SOA particles are second- or higher-generation products of isoprene oxidation.

A.3.2 time-dependent growth curve

Time-dependent SOA growth curves (i.e., SOA concentrations plotted as a function of the concentration of hydrocarbon reacted) are used for the analysis of the SOA formation mechanism (Sato et al., 2004; Chan et al., 2007; Kroll and Seinfeld, 2008). Time-dependent growth curves of the reactions with isoprene, 1,3-butadiene, and DMB are shown in Fig. 3. Only experiments with NO_x ranging from 249–267 ppb were included in Fig. 3 since the yield and the product distribution of SOA during isoprene photooxidation depend strongly on the initial NO_x concentration (Kroll et al., 2005, 2006; Surratt et al., 2006), Experiment 1078W (Fig. 2) was conducted with a NO_2 photolysis rate of only 0.12 min^{-1} ; however, the signal at m/z 71, corresponding to methacrolein or methyl vinyl ketone, was still present when the experiment was finished. The NO_2 photolysis rate for all experiments in Fig. 3 was therefore raised in subsequent experiments to 0.40 min^{-1} to ensure complete consumption of m/z 71 within the limited duration of the experiments.

Figure A.3a shows the time-dependent SOA growth curves of the reaction with isoprene. All SOA formation curves were or nearly were vertical because the majority of SOA production occurred continued after most of the isoprene was consumed. Similar results were obtained in the range of 37–240 ppb of the initial isoprene concentration.

These results confirm that SOA is generated from a second- or higher-generation product. Vertically increasing growth curves are observed when the rate of precursor VOC oxidation is much higher than that following the oxidation of products leading to SOA formation (Kroll and Seinfeld, 2008). This is consistent with the OH reaction rate of isoprene being 3.2 and 5.5 times as high as that of methacrolein and methyl vinyl ketone, respectively (Atkinson, 1986). SOA yield, calculated using the maximum value of SOA concentration, was 0.077–0.103.

Similar results were obtained in an experiment with 1,3-butadiene (Fig. 3b). The measured SOA yield was 0.089–0.178 in the range of 41–269 ppb of diene concentration, close to or slightly higher than the results for isoprene. To our knowledge, this is the first study in which the SOA yield from the reaction of 1,3-butadiene was measured by changing the reactant concentration. Carter et al. (2005) reported a typical concentration of background particle matter formation of the present chamber is 0–1 $\mu\text{g m}^{-3}$. Detectable level SOA (4–7 $\mu\text{g m}^{-3}$) was produced in the experiments with DMB in the range of 250–291 ppb of diene concentration, but the measured SOA yield (0.005–0.007) was significantly lower than that of isoprene and 1,3-butadiene (Fig. 3c).

A.3.3 SOA yield

Table A.1 shows the SOA yield measured in all the present experiments. Typically, SOA concentrations of duplicate experiments agreed within 8% precision at the same reaction time. EPA1148W and EPA1148E are duplicate experiments. However, the SOA yields measured in these runs (0.152 and 0.105) are inconsistent; this is because,

the experimental duration of EPA1148E was shorter than EPA1148W due to the difference in chamber leakage.

The SOA yield measured in all the present isoprene/NO_x/H₂O₂ experiments at 300 K was 0.015–0.103. Some of these results were higher than the previous results reported by Kroll et al. (2006) for isoprene/NO_x/H₂O₂ system (0.014–0.055). One major difference between the two studies is the aerosol loadings which are known to affect SOA yields (Odum et al, 1996). The aerosol loadings of the present experiments (in which the SOA yield was higher than 0.055) were 8–63 μg m⁻³; these were higher than the previous experiments (1.7–6.7 μg m⁻³). Surratt et al. (2006) examined the isoprene/NO_x/H₂O₂ system under similar aerosol loading conditions as this study. The SOA yield reported by Surratt et al. (2006) is 0.049–0.080 and is close to the present result.

Among present yield data of the isoprene/NO_x/H₂O₂ system, there are data lower than 0.055 in a region > 6.7 μg m⁻³; these cannot be explained by the difference in the aerosol loading. For example, the yield was 0.051 at 136 μg m⁻³ in EPA1070W in which the NO_x level was very high. The difference in the NO_x level is known to affect SOA yields (Carlton et al., 2009) The difference in the NO_x level as well as the extent of the reaction is a possible reason of these low-yield data.

The SOA yield measured in the absence of H₂O₂ was 0.006 (EPA1087W). Literature value of SOA yield in isoprene/NO_x system was 0.002–0.049 (Dommen et al., 2006). The SOA yield measured in the absence of H₂O₂ was lower than that in the presence of H₂O₂. The PTR-MS signal of *m/z* 71 maintained 69% of its highest level at

the end of the experiment in the absence of H₂O₂ (EPA1087W), whereas that decreased to 18 % in the presence of H₂O₂ (Fig. 2c). The extent of the reaction in the absence of H₂O₂ is lower than that in the presence of H₂O₂. Further, the OH concentration and the rate of semi-volatile compound formation increase in the presence of an OH radical source; these will also affect SOA yields (Carlton et al., 2009). The SOA formation from the heterogeneous reactions with H₂O₂ (e.g., Carlton et al., 2006) will be less significant under present dry conditions.

A.4 Chemical Composition of SOA

A.4.1 LC-ToF mass spectrum

Flow-injection analysis of SOA off-line samples was conducted by LC-TOFMS (Fig. 4). The results obtained in experiment with isoprene at 300 K (EPA1108W) are shown in Fig. 4a. A series of oligomer signals with regular mass difference of 102 amu was found at m/z 119, 221, and 323 (series 1A). Similar oligomer signals were found at m/z 266, 368, 470, 572, 674, 776 (series 2A); m/z 249, 351, 453, 555, 657, 759 (series 3A); and m/z 263, 365, 467, 569, 671, 773 (series 4A). The mass numbers of these oligomer signals agreed with those measured in previous studies (Surratt et al., 2006; Chan et al., 2010). In this study, a new series of oligomer signals with a regular mass difference of 102 amu was observed at m/z 327, 429, 531, 633, and 735 (series 5A). Mass signals of all 1A–5A oligomers were also detected in an experiment without using hydrogen peroxide as an additional OH radical source (EPA1087W). Very low or no signals of 1A–5A

oligomers were observed in experiments conducted under lower NO_x conditions (EPA1069W and EPA1070E).

The results of an experiment with isoprene at 278 K (EPA1148W) are shown in Fig. 4b. Mass signals were found at the same mass numbers as those found in experiments at 300 K. The ratio of the total signals of 5A oligomers to the total signals of other 1A–4A oligomers measured at 278 K increased compared with that at 300 K.

Figure A.4c shows the results of an experiment with isoprene-1-¹³C (EPA1082W). All mass signals corresponding to 1A–5A oligomers found in the experiments with isoprene were observed; however, all mass peaks had shifted due to the substitution by ¹³C atoms. For example, mass signals corresponding to series 2A were detected at *m/z* 268, 371, and 474. Mass numbers 268, 371, and 474 were 2, 3, and 4 amu larger than those of the corresponding mass signals measured in the experiments with isoprene; these mass signals were identified as a dimer, a trimer, and a tetramer, respectively. The regular mass difference of all 1A–5A oligomers was 103 amu in the experiment with isoprene-1-¹³C.

The results of an experiment with 1,3-butadiene (EPA1094W) are shown in Fig. 4d. A series of oligomer signals with regular mass difference of 88 amu was found at *m/z* 105, 193, 281, 369, 457, and 545 (series 1B). Another series of oligomer signals with a regular mass difference of 88 amu was also observed at *m/z* 387, 475, 563, 651, and 739 (series 5B). In an experiment with DMB (EPA1104W), four series of oligomer signals were observed and identified as series 1A–4A observed in the experiments with isoprene (Fig. 4e).

From data of Fig. 4, the signal ratios of the oligomers identified to the total products observed were determined to be 0.33 (isoprene at 300 K), 0.28 (isoprene at 278 K), 0.20 (isoprene-¹³C), 0.10 (1,3-butadiene), and 0.14 (2,3-dimethyl-1,3-butadiene). The signals of the oligomers identified comprise a major fraction of the signals of the SOA products observed from all dienes investigated.

A.4.2 LC-TOFMS base peak chromatogram

To confirm the presence of oligomers in the off-line sample solution, column injection analysis was conducted (Fig. 5). The base peak chromatogram measured in the experiment with isoprene (EPA1058E) is shown in Fig. 5a. Mass numbers illustrated with black, red, green, blue, and orange ink correspond to oligomer series 1A, 2A, 3A, 4A, and 5A, respectively. Chromatographic peaks of each oligomer series with different mass numbers were successfully separated in the column-injection analysis; signals with different mass numbers were obtained from molecules with different degrees of oligomerization. These results confirm that the observed mass signals with high mass numbers were not produced during the ionization process, and oligomers were originally present in the off-line sample solution. The sample solution obtained in EPA1058E and its 1/5, 1/25, and 1/125 diluted samples were analyzed to measure chromatographic peak areas as a function of relative concentration. Linear relationships were observed between chromatographic peak area and relative concentration for all observed oligomers ($r > 0.998$, $p < 0.002$).

Figure A.5b shows the results of the experiment with isoprene at 278 K (EPA1148W). The ratio of the total peak area of 5A oligomers to the total peak area of other 1A–4A oligomers measured at 278 K increased compared with that at 300 K. The results of the experiment with 1,3-butadiene (EPA1132W) are shown in Fig. 5c. Chromatographic peaks of 1B and 5B oligomers measured in experiments with 1,3-butadiene were also successfully separated.

A.4.3 identification of products

Accurate masses were measured for ions resulting from column-separated oligomers. Measured accurate mass, suggested ion formula, and identified product molecular structure are shown in Table A.2. Generally, analyte molecules are deprotonated to form $[M - H]^-$ ions during the negative-mode ESI process. For product identification, all detected ions in this study were assumed to be deprotonated molecules. All ion formulae suggested for oligomer series 1A–4A in the present study agreed with those suggested in a recent study by Chan et al. (2010). The products of series 1A, 2A, 3A, and 4A were identified as 2-methylglyceric acid oligoesters and their mononitrates, monoformates, and monoacetates, respectively. The products of series 5A were identified as oligomers produced by the dehydration reaction between nitrooxypolyol and 2-methylglyceric acid monomer or its oligomer. It is believed that the 2-methyltetrols found in ambient fine particles under high NO_x conditions are produced by the decomposition of nitrooxypolyols or organosulfates containing nitrooxypolyol residues (Claeys et al., 2010). Nitrooxypolyols are directly produced by the gas phase isoprene oxidation and/or the particle phase hydrolysis of 5A oligomers under ambient humid conditions.

Organosulfates are more commonly detected in ambient particles than are nitrooxypolyols; this is probably because tertiary organonitrates undergo rapid substitution reactions in which nitrate is substituted by water or sulfate (Darer et al., 2011).

The products of series 1B formed from 1,3-butadiene oxidation were tentatively identified as glyceric acid monomer and its oligomers. Products of series 5B were tentatively identified as oligoesters produced by the dehydration reaction between nitrooxypolyol and glyceric acid monomer or its oligomer.

A.4.4 AMS mass spectrum

To determine if oligomers are present in suspended SOA particles, particles were directly measured by ToF-AMS. Raw mass spectra, obtained by averaging the data collected for 3-h measurements, are shown in Fig. 6. The results obtained in the experiment with isoprene (EPA1170W) are shown in Fig. 6a. Strong mass signals were observed at m/z 103, 131, 145, 205, 233, and 247. The mass difference between m/z 103 and 205, between m/z 131 and 233, and between m/z 145 and 247 was 102 amu. Chan et al. (2010) reported that positive fragment ions formed from the dehydroxylation of 1A, 3A, and 4A oligomers ($[M - OH]^+$) were observed by ToF-AMS. Mass signals at m/z 103, 131, and 145 were identified as dehydroxylated ions of 1A, 3A, and 4A monomers, whereas mass signals at m/z 205, 233, and 247 were identified as dehydroxylated ions of 1A, 3A, and 4A dimers (Table A.2). The results of the experiment with isoprene-1- ^{13}C (EPA1082W) are shown in Fig. 6b. In the experiment with the isotopomer, the mass

numbers of the monomer and dimer peaks shifted by 1 and 2 amu, respectively. These ToF-AMS results confirm that oligomers detected by LC-TOFMS off-line analysis are present in SOA particles.

If dehydroxylated fragment ions of 1B oligomers formed from 1,3-butadiene oxidation can be detected by ToF-AMS, mass signals with a regular mass difference of 88 amu would be expected to appear at m/z 89, 177, and 265 (Table A.2). The results of the experiment with 1,3-butadiene (EPA1094W) are shown in Fig. 6c. Mass signals were detected at these predicted mass numbers, but the peaks are not as strong when compared with the oligoester mass signals observed in the experiments with isoprene. Values of m/z measured for oligomers by ToF-AMS in V mode were compared with those calculated assuming chemical formulae shown in Table A.2. An each measured m/z value agreed with a calculated value within m/z of 0.04.

A.5 Reaction Mechanism

A.5.1 isoprene and 1,3-butadiene

The proposed mechanism of oligomer formation from the reactions of isoprene and 1,3-butadiene is shown in Fig. 7. In the figure, R_1 represents a methyl group or a hydrogen atom for the reaction of isoprene or 1,3-butadiene, respectively. The atmospheric oxidation of isoprene proceeds through the reaction with OH radicals, NO_3 radicals, and O_3 although the major daytime oxidant is the OH radical (Yokouchi, 1994). Hydroxyperoxy radicals formed from the OH + isoprene reaction react with NO to form methacrolein (e.g., Miyoshi et al., 1994) and unsaturated nitroxyalcohols (Chen et al.,

1998; Lockwood et al., 2010). The subsequent oxidation of methacrolein produces peroxyacetyl nitrate (MPAN); it is suggested that this product undergoes subsequent oxidation to form 2-methylglyceric acid and 2-methylglyceric acid mononitrate in the particle phase (Surratt et al., 2010; Chan et al., 2010). Subsequent oxidation of nitroxyalcohols leads to the formation of nitrooxypolyols, which are then absorbed into the particle phase (Sato, 2008).

2-Methylglyceric acid contains both a hydroxyl and a carboxyl group. The dehydration reaction between the hydroxyl group of one molecule and the carboxyl group of another molecule produces ester dimers. Successive condensation reactions result in the formation of oligomers of series 1A (Surratt et al., 2006). Oligomers of series 2A are produced when one of these monomers is 2-methylglyceric acid mononitrate. The condensation reactions between oligomers of series 1A and formic acid (or acetic acid) form oligomers of series 3A (or those of series 4A). Oligomers of series 5A are produced by the condensation reaction between nitrooxypolyols and 2-methylglyceric acid monomer or its oligomer.

Oligomers of series 1B and 5B, found during the reaction of 1,3-butadiene, are produced through similar reactions to those resulting in the formation of 1A and 5A oligomers, respectively. Oligomers corresponding to series 2A, 3A, and 4A were not detected in the reaction of 1,3-butadiene.

A.5.2 isoprene-1-¹³C and DMB

The photooxidation of isoprene-1-¹³C produces ¹³C atom labeled methacrolein and non ¹³C labeled methyl vinyl ketone (Fig. 8a). According to the proposed mechanism, 2-methylglyceric acid monomer is produced by the reaction of methacrolein. If this is the case, then the ¹³C atom is involved in the production of every C₄ monomer. Actually, the regular mass difference of all 1A–5A oligomers found in the experiment with isoprene-¹³C was 103 amu, which is 1 amu larger than that observed in the reaction of isoprene (Fig. 4a and 4c). In addition, mass differences between monomer and dimer observed by ToF-AMS were also 103 amu (Fig. 6b). These results support the proposed mechanism in which the gaseous intermediate of oligoester formation is assumed to be methacrolein.

The unsaturated ketone (2-methyl-1-butene-3-one) is produced as a primary product of DMB oxidation; however, no unsaturated aldehyde is produced from DMB oxidation. Oligomers of series 1A–4A were found to be present in SOA particles from DMB (Fig. 4e). These oligomers would be produced by the oxidation of 2-methyl-1-butene-3-one or the oxidation of isoprene impurity. If we assume that 2-methylglyceric acid is produced by the reaction of 2-methyl-1-butene-3-one, a ketone group needs to be converted to a carboxyl group. However, the oxidation of a ketone group is very slow. This is congruent with the small yield of SOA from photooxidation of DMB since unsaturated aldehydes are not produced as primary products. The present result of DMB is consistent with the prior observation that the methacrolein gas-phase oxidation forms SOA but that of methyl vinyl ketone does not (Kroll et al., 2005; Surratt et al., 2006).

A.6 Check of Proposed Mechanism

A.6.1 low mass loading experiment

Oligoesters are produced through gas/particle absorption of semi-volatile compounds followed by particle-phase oligomerization. Since the equilibrium of gas/particle partitioning is determined by existing particle mass concentration, the concentration of oligoesters produced will depend on the SOA mass loading in the reactor. Most previous studies have detected the presence of oligomers in SOA particles under higher mass loading conditions than ambient levels (e.g., Dommen et al., 2006; Surratt et al., 2006). However, the AMS identification of oligomers in isoprene + OH SOA under low aerosol loadings ($1.7\text{--}9.3 \mu\text{g m}^{-3}$) was also carried out by Kroll et al. (2006). In this study, we investigate whether or not oligomers can be detected at ambient particle levels using our environmental chamber designed for low-concentration experiments. SOA mass loading was controlled by changing the initial isoprene concentration between 20 and 573 ppb, while maintaining the initial isoprene/ NO_x ratio within the range 0.6–0.9 (EPA1058W, EPA1058E, EPA1060W, EPA1060E, EPA1061W, and EPA1061E). Figure A.9 shows the oligomer distribution for series 1A, 2A, and 5A determined by LC-TOFMS analysis at mass loadings of 26, 19, and $3 \mu\text{g m}^{-3}$. Signals of 1A–5A oligomers were detected even at the lowest SOA mass loading of all six experiments. These results confirm that semi-volatile compounds resulting in oligoester formation are sufficiently absorbed into the particle phase even at $3 \mu\text{g m}^{-3}$ of SOA mass loading.

A.6.2 Time profiles of oligomers

According to the proposed mechanism, oligoesters are produced by successive condensation reactions of 2-methylglyceric acid in the particle phase. In a previous study, concentrations of oligomers at different degrees of oligomerization were monitored by AMS to examine particle-phase oligomerization (Surratt et al., 2006). Time profiles of oligoesters were also monitored by ToF-AMS in this study. Figure A.10a shows the time profiles of m/z 103 and 205 signals measured by ToF-AMS in the experiment with isoprene (EPA1070W). The monitored signals correspond to monomers and dimers of series 1A. No clear difference was observed between the time profiles of monomers and dimers after 150 min. Trimer or higher oligomers were not detected, probably because these oligomers undergo dissociative ionization during the EI process of ToF-AMS in this study. Therefore, monomer and dimer signals measured by ToF-AMS are significantly affected by fragment ions formed from the ionization of higher oligomers.

Time profiles of particle-phase products have also been studied by analyzing multiple off-line samples collected at different reaction times (e.g., Hatakeyama et al., 1985; Jang and Kamens, 2001). We collected hourly filter samples (6 total) to study the time profiles of oligomers in an isoprene experiment (EPA1078E). The concentrations of 2-methylglyceric acid monomer and its oligomers, determined by LC-TOFMS analysis, are plotted as a function of time (Fig. 10b); the vertical axis is the relative concentration on a linear scale. Each determined concentration value involves about 15% of uncertainty, mainly resulting from the uncertainty of recovery during sample extraction. The concentrations of monomer (m/z 119) and dimer (m/z 221) increased above

detectable levels at 60–120 min, and continued to increase until 180–240 min. After that, these concentrations maintained a constant level or decreased slightly. In contrast, the concentrations of trimer or higher oligomers increased monotonically with time. These results indicate that the production of trimer or higher oligomers is competitive with monomer and dimer formation after 180–240 min. In other words, oligoesters are produced by particle-phase successive reactions as assumed in the proposed mechanism.

A.6.3 Lights-off experiment

According to the proposed mechanism, 2-methylglyceric acid is produced by reactions initiated by the gas-phase OH + methacrolein reaction. If this is the case, no 2-methylglyceric acid monomer is produced in the absence of irradiation. In order to study the lights-off effect, we conducted experiments with isoprene in which black lights were turned off after 178 min of irradiation time (EPA1090W and EPA1090E). The results of EPA1090W are shown in Fig. 11. When the lights were turned off, PTR-MS results showed that most of the isoprene (m/z 69) was consumed by the reaction, whereas a substantial amount of methacrolein and methyl vinyl ketone (m/z 71) was still present in the reaction system (Fig. 11a). The slope of m/z 71 does not greatly change when the lights are turned off. The loss of m/z 71 in the dark will be caused by the reactions with O_3 and NO_3 . The O_3 level when the lights were turned off was about 300 ppb. This O_3 concentration was confirmed to be high enough to explain the loss rate of m/z 71 in the dark; the loss rate of methyl vinyl ketone was $3.2 \times 10^{-5} \text{ s}^{-1}$; the loss rate of methacrolein was $8.2 \times 10^{-6} \text{ s}^{-1}$; where the rate constants measured by Treacy et al. (1992) were used.

When the lights are turned off, SOA particles had already been produced (Fig. 11b). The SOA concentration increased even after the lights were turned off, suggesting that SOA is formed from the reactions of gaseous oxidation products with NO_3 radicals or O_3 during this period. The filter was changed every 60 min, and five SOA filter samples in total were collected during this experiment (Fig. 11c). Again, the concentration data involved about 15% uncertainty. Monomer and all detected oligomers (i.e., dimer, trimer, and tetramer) increased until the lights were turned off. After the lights were turned off, the concentrations of monomer and oligomers were maintained at constant values or decreased slightly with time; these results are slightly different from those of the irradiated experiments in which trimer and tetramer concentrations increased monotonically with time. Pentamer was not detected in the lights-off experiment. Oligoester formation was suppressed when the lights were turned off, which is consistent with the proposed mechanism.

If oligomer formation in the particle phase involves successive reactions, the concentration of the monomer might decrease more rapidly than that of a higher oligomer immediately after the lights were turned off. However, no such result was obtained. After the lights are turned off, the reactions of isoprene oxidation products with O_3 and NO_3 occur to form SOA. Particulate 2-methylglyceric acid is known to be produced by the O_3 + isoprene reaction (Kleindienst et al., 2007). Formation of the 2-methylglyceric acid monomer by the reaction with O_3 would affect the oligomer time profiles in the dark.

A new product signal was found at m/z 509 by LC-TOFMS analysis in samples collected after the lights were turned off. The accurate mass of these ions was 509.0859 amu; the suggested ion formula is $C_{12}H_{21}N_4O_{18}^-$. The same product was observed in SOA formed from the $NO_3 +$ isoprene reaction (Ng et al., 2008). This product is therefore likely produced by the reaction of an isoprene oxidation product with NO_3 radical.

A.7 Temperature Dependence

In this study, experiments with isoprene were conducted at 300 K (EPA1078W and EPA1078E) and 278 K under similar reactant concentration conditions (EPA1148W and EPA1148E). NO_2 photolysis rates in experiments at 300 and 278 K were set to 0.12 min^{-1} . Initial isoprene concentrations of experiments at 300 K (EPA1078W) and 278 K (EPA1048W) were 115 and 132 ppb, respectively (Fig. 12a). The SOA yield measured at 278 K (0.105–0.152) was about 2–3 times as high as that measured at 300 K (0.047–0.053), as shown in Fig. 12b. Even though oligomerization occurs in the particle phase, the temperature dependence of SOA yield is largely explained by the gas/particle partitioning of semi-volatile compounds.

We measured the 373 K VFR in the experiments at 300 and 278 K, and confirmed the VFR was independent of the particle diameter. If the temperature dependence of SOA yield (Y) is purely determined by the gas/particle partitioning of semi-volatile compounds, the $VFR(300 \text{ K})/VFR(278 \text{ K})$ ratio would be the same as the $Y(278 \text{ K})/Y(300 \text{ K})$ ratio. Thus, a comparison of the temperature dependence of Y with

that of VFR will provide us information on the chemical conversion of aerosol constituents in the particle phase. In the present study, the VFR(300 K) was 0.45–0.56, whereas the VFR(278 K) was 0.26–0.43 (Fig. 12c). The change in SOA yield cannot be solely explained by changes in the VFR (SOA yield increased 2–3 times while the VFR changes by less than a factor of 2). Although the temperature dependence of SOA yield is largely explained by gas/particle partitioning of semi-volatile compounds, the VFR results support the present findings that oligoesters are formed in the particle phase.

The ratio of total peak area of nitrooxypolyol-involving oligoesters (series 5A) to the total peak area of other oligoesters (series 1A–4A) measured at 278 K increased compared with that at 300 K. From GC-FID data, the methacrolein yields at 278 and 300 K were estimated, and the gaseous product yield was confirmed to be basically constant between 278 and 300 K. This indicates that the observed temperature dependence of particulate chemical composition is mainly determined by the changes in gas/particle partitioning of semi-volatile compounds. The lower temperature will result in higher condensation of 2-methylglyceric acid precursors and much higher condensation of nitrooxypolyols.

Series 2A and 5A oligomers involving nitrooxy groups are expected to be detected as nitrates by high-resolution ToF-AMS. Therefore, the ratio of nitrates to organics ($\text{HRNO}_3/\text{HROrg}$) measured by ToF-AMS at 278 K would be expected to be higher than 300 K. This is confirmed as $\text{HRNO}_3/\text{HROrg}$ ratio measured at 278 K (0.07–0.14) was higher than 300 K (0.03–0.05). The lower temperature could result in higher

condensation of HNO₃. Despite the low relative humidity, organic acids can retain water and provide a medium for HNO₃ to condense. We checked HNO₃ condensation by the ToF-AMS signal ratio of *m/z* 30 to *m/z* 46. This ratio is 3–5 for organic nitrates and < 3 for inorganic nitrates (Rollins et al., 2009; Sato et al., 2010). The *m/z* 30 to *m/z* 46 ratio at 300 K (EPA1078W) was 4.7 ± 1.2 , whereas that at 278 K (EPA1148W) was 4.7 ± 0.6 , indicating HNO₃ is a minor particulate component both at 278 and 300 K.

A.8 Atmospheric Implications

The present results confirm that SOA is produced from the diene/NO_x photooxidation in which unsaturated aldehyde is formed as a gaseous intermediate; that is, 1,3-butadiene as well as isoprene is a possible SOA precursor in urban air. The present results also show that the yield of isoprene SOA increases with decreasing the temperature; that is, in ambient air the yield of isoprene SOA depends on the altitude, the latitude, the season, and etc. This finding will have a large impact when we evaluate a total amount of global SOA formation.

A.9 Conclusions

In this study, SOA formation from the photooxidation of isoprene, isoprene-1-¹³C, 1,3-butadiene, and DMB was investigated under high NO_x conditions. The SOA yield measured for the reaction of 1,3-butadiene was close to or slightly higher than that measured for the reaction of isoprene, suggesting that the photooxidation of 1,3-butadiene is a potential source of SOA in urban air. On the other hand, only a very small amount of SOA was produced during the photooxidation of DMB.

Off-line LC-TOFMS analysis revealed that the signals of the oligoesters identified comprise a major fraction (0.10–0.33) of the signals of the SOA products observed from all dienes investigated. During the photooxidation of conjugated dienes under high NO_x conditions, oligoesters are produced by a reaction of unsaturated aldehyde, which is a gas-phase oxidation product. The results of an experiment with isoprene-1-¹³C confirmed the proposed mechanism in which methacrolein is assumed to be a key intermediate of oligoester formation. This mechanism was also confirmed by the reaction of DMB: only a very small amount of SOA was produced during DMB photooxidation, in which no unsaturated aldehyde is formed.

Oligoesters produced by the dehydration reaction between nitrooxypolyol and 2-methylglyceric acid monomer or its oligomer (oligomer series 5A) were characterized in the experiments with isoprene. These oligomers are possible sources of 2-methyltetrols found in ambient aerosol samples collected under high NO_x conditions.

The proposed mechanism was also checked by measurements of oligomer signals as functions of SOA mass loading and irradiation time. Oligoester formation was confirmed to occur even under low SOA mass loading conditions (> 3 μg m⁻³). Time profiles of oligomers, measured by off-line analysis, suggested that oligomerization involves successive reactions as assumed in the proposed mechanism. Oligoester formation was suppressed when the lights were turned off. This result was consistent with the proposed mechanism although the result would be interfered by reactions with O₃ in the dark.

This is the first study to investigate the temperature dependence of SOA formation from isoprene photooxidation. The ratio of total chromatographic peak area of nitrooxypolyol-involving oligoesters (series 5A) to total peak area of other oligoesters measured at 278 K increased compared to that at 300 K. The SOA yield measured at 278 K was higher than that measured at 300 K; the temperature dependence of SOA yield is largely explained by gas/particle partitioning of semi-volatile compounds even though oligomerization occurs in the particle phase.

A.10 Reference

- Agrawal, H., Welch, W. A., Miller, J. W., and Cocker, D. R.: Emission measurements from a crude oil tanker at sea, *Environ. Sci. Technol.*, 42, 7098-7103, 2008.
- An, W. J., Pathak, R. K., Lee, B.-H., Pandis, S. N.: Aerosol volatility measurement using an improved thermodenuder: Application to secondary organic aerosol, *J. Aerosol Sci.*, 38, 305-314, 2007.
- Angove, D. E., Fookes, C. J. R., Hynes, R. G., Walters, C. K., and Azzi, M.: The characterization of secondary organic aerosol formed during the photodecomposition of 1,3-butadiene in air containing nitric oxide, *Atmos. Environ.*, 40, 4597-4607, 2006.
- Atkinson, R.: Kinetics and mechanisms of gas-phase reactions of the hydroxyl radical with organic compounds under atmospheric conditions, *Chem. Rev.*, 86, 69-201, 1986.
- Böge, O., Miao, Y., Plewka, A., and Herrmann, H.: Formation of secondary organic particle phase compounds from isoprene gas-phase oxidation products: An aerosol chamber and field study, *Atmos. Environ.*, 40, 2501-2509, 2006.
- Bowman, F. M., Odum, J. R., Seinfeld, J. H., and Pandis, S. N.: Mathematical model for gas-particle partitioning of secondary organic aerosols, *Atmos. Environ.*, 31, 3921-3931, 1997.
- Calvert, J. G., Atkinson, R., Becker, K. H., Kamens, R. M., Seinfeld, J. H., Wallington, T. J., and Yarwood, G.: Importance of aromatic hydrocarbons in the chemistry of ozone generation in the urban atmosphere, in: *The Mechanisms of Atmospheric Oxidation of Aromatic Hydrocarbons*, Oxford University Press, New York, USA, 3-35, 2002.
- Carlton, A. G., Lim, H.-J., Altieri, K., Seiting, S., and Turpin, B. J.: Link between isoprene and SOA: fate of pyruvic acid in dilute aqueous solution, *Geophys. Res. Lett.*, 33, L06822, doi:10.1029/2005GL025374, 2006.
- Carlton, A. G., Wiedinmyer, C., Kroll, J. H., A review of secondary organic aerosol (SOA) formation from isoprene, *Atmos. Chem. Phys.*, 9, 4987-5005, 2009.
- Carter, W. P. L., Cocker, D. R., III, Fitz, D. R., Malkina, I. L., Bumiller, K., Sauer, C. G., Pisano, J. T., Bufalino, C., and Song, C.: A new environmental chamber for

- evaluation of gas-phase chemical mechanisms and secondary organic aerosol formation, *Atmos. Environ.*, 39, 7768-7788, 2005.
- Chan, A. W. H., Kroll, J. H., Ng, N. L., and Seinfeld, J. H.: Kinetic modeling of secondary organic aerosol formation: effects of particle- and gas-phase reactions of semi-volatile products, *Atmos. Chem. Phys.*, 7, 4135-4147, 2007.
- Chan, A. W. H., Chan, M. N., Surratt, J. D., Chhabra, P. S., Loza, C. L., Crouse, J. D., Yee, L. D., Flagan, R. C., Wennberg, P. O., and Seinfeld, J. H.: Role of aldehyde chemistry and NO_x concentrations in secondary organic aerosol formation, *Atmos. Chem. Phys.* 10, 7169-7188, 2010.
- Chen, X. H., Hulbert, D., and Shepson, P. B.: Measurement of the organic nitrate yield from OH reaction with isoprene, *J. Geophys. Res.*, 103, 25563-25568, 1998.
- Claeys, M., Graham, B., Vas, G., Wang, W., Vermeylen, R., Pashynska, V., Cafmeyer, J., Guyon, P., Andreae, M. O., Artaxo, and P., Maenhaut, W.: Formation of secondary organic aerosols through photooxidation of isoprene, *Science*, 303, 1173-1176, 2004a.
- Claeys, M., Wang, W., Ion, A. C., Kourtchev, I., Gelencsér, A., and Maenhaut, W.: Formation of secondary organic aerosols from isoprene and its gas-phase oxidation products through reaction with hydrogen peroxide, *Atmos. Environ.*, 38, 4093-4098, 2004b.
- Claeys, M., Kourtchev, I., Pashynska, V., Vas, G., Vermeylen, R., Wang, W., Cafmeyer, J., Chi, X., Artaxo, P., Andreae, M. O., and Maenhaut, W.: Polar organic marker compounds in atmospheric aerosols during the LBA-SMOCC 2002 biomass burning experiment in Rondônia, Brazil: sources and source processes, time series, diel variations and size distributions, *Atmos. Chem. Phys.*, 10, 9319-9331, 2010.
- Clements, A. and Seinfeld, J. H.: Detection and quantification of 2-methyltetrols in ambient aerosol in the southeastern United States, *Atmos. Environ.*, 41, 1825-1830, 2007.
- Cocker, D. R., III, Flagan, R. C., and Seinfeld, J. H.: State-of-the-art chamber facility for studying atmospheric aerosol chemistry, *Environ. Sci. Technol.*, 35, 2594-2601, 2001.
- Darer, A. I., Cole-Filipiak, N. C., O'Connor, A. E., and Elrod, M. J.: Formation and stability of atmospherically relevant isoprene-derived organosulfates and organonitrates, *Environ. Sci. Technol.*, 45, 1895-1902, 2011.

- DeMore, W. B., Sander, S. P., Golden, D. M., Hampson, R. F., Kurylo, M. J., Howerd, C. J., Ravishankara, A. R., Kolb, C. E., and Molina, M. J.: Chemical Kinetics and Photochemical Data for Use in Stratospheric Modeling, JPL Publication 97-4, NASA Jet Propulsion Laboratory, Pasadena, USA, 1997.
- Dommen, J., Metzger, A., Duplissy, J., Kalberer, M., Alfarra, M. R., Gascho, A., Weingartner, E., Prevot, A. S. H., Verheggen, B., and Baltensperger, U.: Laboratory observation of oligomers in the aerosol from isoprene/NO_x photooxidation, *Geophys. Res. Lett.*, 33, L13805, doi:10.1029/2006GL026523, 2006.
- Drewnick, F., Hings, S. S., DeCarlo, P. F., Jayne, J. T., Gonin, M., Fuhrer, K., Weimer, S., Jimenez, J. L., Demerjian, K. L., Borrmann, S., and Worsnop, D. R.: A new time-of-flight aerosol mass spectrometer (ToF-AMS)—instrument description and first field deployment. *Aeros. Sci. Tech.*, 39, 637-658, 2005.
- Edney, E. O., Kleindienst, T. E., Jaoui, M., Lewandowski, M., Offenberg, J. H., Wang, W., and Claeys, M.: Formation of 2-methyl tetrols and 2-methylglyceric acid in secondary organic aerosol from laboratory irradiated isoprene/NO_x/SO₂/air mixtures and their detection in ambient PM_{2.5} samples collected in the eastern United States, *Atmos. Environ.*, 39, 5281-5289, 2005.
- Fu, P. Q., Kawamura, K., Chen, J., and Barrie, L. A.: Isoprene, monoterpene, and sesquiterpene oxidation products in the high arctic aerosols during late winter to early summer, *Environ. Sci. Technol.*, 43, 4022-4028, 2009.
- Fu, P. Q., Kawamura, K., Kanaya, Y., and Wang, Z.: Contributions of biogenic volatile organic compounds to the formation of secondary organic aerosols over Mt. Tai, Central East China, *Atmos. Environ.*, 44, 4817-4826, 2010a.
- Fu, P. Q., Kawamura, K., Pavoluri, C. M., Swaminathan, T., and Chen, J.: Molecular characterization of urban organic aerosol in tropical India: contributions of primary emissions and secondary photooxidation, *Atmos. Chem. Phys.*, 10, 2663-2689, 2010b.
- Gómez-González, Y., Surratt, J. D., Cuyckens, F., Szmigielski, R., Vermeylen, R., Jaoui, M., Lewandowski, M., Offenberg, J. H., Kleindienst, T. E., Edney, E. O., Blockhuys, F., Van Alsenoy, C., Maenhaut, W., and Claeys, M.: Characterization of organosulfates from the photooxidation of isoprene and unsaturated fatty acids in ambient aerosol using liquid chromatography/(-)electrospray ionization mass spectrometry, *J. Mass Spectrom.*, 43, 371-382, 2008.

- Guenther, A., Karl, T., Harley, P., Wiedinmyer, C., Palmer, P. I., and Geron, C.: Estimation of global terrestrial isoprene emissions using MEGAN (model of emissions of gases and aerosols from nature), *Atmos. Chem. Phys.*, 6, 3181-3210, 2006.
- Hatakeyama, S., Tanonaka, T., Weng, J. H., Bandow, H., Takagi, H., and Akimoto, H.: Ozone cyclohexene reaction in air-quantitative analysis of particulate products and the reaction mechanism, *Environ. Sci. Technol.*, 19, 935-942, 1985.
- Hallquist, M., Wenger, J. C., Baltensperger, U., Rudich, Y., Simpson, D., Clayes, M., Dommen, J., Donahue, N. M., George, C., Goldstein, A. H., Hamilton, J. F., Herrmann, H., Hoffmann, T., Iinuma, Y., Jang, M., Jenkin, M. E., Jimenez, J. L., Kiendler-Scharr, A., Maenhaut, W., McFiggans, G., Mentel, Th. F., Monod, A., Prevot, A. S. H., Seinfeld, J. H., Surratt, J. D., Szmigielski, R., and Wildt, J.: The formation, properties and impact of secondary organic aerosol: current and emerging issues, *Atmos. Chem. Phys.*, 9, 5155-5236, 2009.
- Henze, D. K. and Seinfeld, J. H.: Global secondary organic aerosol from isoprene oxidation, *Geophys. Res. Lett.*, 33, L09812, doi:10.1029/2006GL025976, 2006.
- Henze, D. K., Seinfeld, J. H., Ng, N. L., Kroll, J. H., Fu, T.-M., Jacob, D. J., and Heald, C. L.: Global modeling of secondary organic aerosol formation from aromatic hydrocarbons: high- vs. low-yield pathways, *Atmos. Chem. Phys.*, 8, 2405-2421, 2008.
- Jang, M. and Kamens, R. M.: Characterization of secondary aerosol from the photooxidation of toluene in the presence of NO_x and 1-propene, *Environ. Sci. Technol.*, 35, 3626-3639, 2001.
- Jang, M., Czoschke, N. M., Lee, S., and Kamens, R. M.: Heterogeneous atmospheric aerosol production by acid-catalyzed particle-phase reactions, *Science*, 298, 814-817, 2002.
- Jeffries, H. E.: Photochemical air pollution, in: *Composition, Chemistry, and Climate of the Atmosphere*, Van Nostrand Reinhold, New York, USA, 308-348, 1995.
- Jemma, C. A., Shore, P. R., and Widdicombe, K. A.: Analysis of C₁-C₁₆ hydrocarbons using dual-column capillary GC: Application to exhaust emissions from passenger car and motorcycle engines, *J. Chromatogr. Sci.*, 33, 34-48, 1995.

- Kleindienst, T. E., Lewandowski, M. L., Offenberg, J. H., Jaoui, M., and Edney, E. O.: Ozone-isoprene reaction: Re-examination of the formation of secondary organic aerosol, *Geophys. Res. Lett.*, 34, L01805, doi:10.1029/2006GL027485, 2007.
- Kleindienst, T. E., Lewandowski, M., Offenberg, J. H., Jaoui, M., and Edney, E. O.: The formation of secondary organic aerosol from the isoprene + OH reaction in the absence of NO_x, *Atmos. Chem. Phys.*, 9, 6541-6558, 2009.
- Kroll, J. H. and Seinfeld, J. H.: Chemistry of secondary organic aerosol: formation and evolution of low-volatility organics in the atmosphere, *Atmos. Environ.*, 42, 3593-3624, 2008.
- Kroll, J. H., Ng, N. L., Murphy, S. M., Flagan, R. C., and Seinfeld, J. H.: Secondary organic aerosol formation from isoprene photooxidation under high-NO_x conditions, *Geophys. Res. Lett.*, 32, L18808, doi:10.1029/2005GL023637, 2005.
- Kroll, J. H., Ng, N. L., Murphy, S. M., Flagan, R. C., and Seinfeld, J. H.: Secondary organic aerosol formation from isoprene photooxidation, *Environ. Sci. Technol.*, 40, 1869-1877, 2006.
- Liu, Y., Shao, M., Fu, L., Lu, S., Zeng, L., and Tang, D.: Source profiles of volatile organic compounds (VOCs) measured in China: Part I, *Atmos. Environ.*, 42, 6247-6260, 2008.
- Lockwood, A. L., Shepson, P. B., Fiddler, M. N., and Alaghmand, M.: Isoprene nitrates: preparation, separation, identification, yields, and atmospheric chemistry, *Atmos. Chem. Phys.*, 10, 6169-6178, 2010.
- Malloy, Q. G. J., Qi, L., Warren, B., Cocker, D. R., III, Erupe, M. E., and Silva, P. J.: Secondary organic aerosol formation from primary aliphatic amines with NO₃ radical, *Atmos. Chem. Phys.*, 9, 2051-2060, 2009.
- Miyoshi, A., Hatakeyama, S., and Washida, N.: OH radical-initiated photooxidation of isoprene: an estimate of global CO production, *J. Geophys. Res.*, 99, 18779-18787, 1994.
- Nelson, P. F., Tibbett, A. R., and Day, S. J.: Effects of vehicle type and fuel quality on real world toxic emissions from diesel vehicles, *Atmos. Environ.*, 42, 5291-5303, 2008.
- Ng, N. L., Kwan, A. J., Surratt, J. D., Chan, A. W. H., Chhabra, P. S., Sorooshian, A., Pye, H. O. T., Crounse, J. D., Wennberg, P. O., Flagan, R. C., and Seinfeld, J. H.:

- Secondary organic aerosol (SOA) formation from reaction of isoprene with nitrate radicals (NO_3), *Atmos. Chem. Phys.*, 8, 4117-4140, 2008.
- Odum, J. R., Hoffmann, T., Bowman, F., Collins, D., Flagan, R. C., and Seinfeld, J. H.: Gas/particle partitioning and secondary organic aerosol yields, *Environ. Sci. Technol.*, 30, 2580-2585, 1996.
- Pandis, S. N., Paulson, S. E., Seinfeld, J. H., and Flagan, R. C.: Aerosol formation in the photooxidation of isoprene and β -pinene, *Atmos. Environ.*, 25A, 997-1008, 1991.
- Paulot, F., Crouse, J. D., Kjaergaard, H. G., Kürten, A., St. Clair, J. M., Seinfeld, J. H., and Wennberg, P. O.: Unexpected epoxide formation in the gas-phase photooxidation of isoprene, *Science*, 325, 730-733, 2009.
- Qi, L., Nakao, S., Tang, P., and Cocker, D. R., III: Temperature effect on physical and chemical properties of secondary organic aerosol from *m*-xylene photooxidation, *Atmos. Chem. Phys.*, 10, 3847-3854, 2010.
- Rollins, A. W., Kiendler-Scharr, A., Fry, J. L., Brauers, T., Brown, S. S., Dorn, H.-P., Dubé, W. P., Fuchs, H., Mensah, A., Mentel, T. F., Rohrer, F., Tillmann, R., Wegener, R., Wooldridge, and P. J., Cohen, R. C.: Isoprene oxidation by nitrate radical: alkyl nitrate and secondary organic aerosol yields, *Atmos. Chem. Phys.*, 9, 6685-6703, 2009.
- Sato, K.: Detection of nitrooxypolyols in secondary organic aerosol formed from the photooxidation of conjugated dienes under high- NO_x conditions, *Atmos. Environ.*, 42, 6851-6861, 2008.
- Sato, K., Klotz, B., Hatakeyama, S., Imamura, T., Washizu, Y., Matsumi, Y., and Washida, N.: Secondary organic aerosol formation during the photo-oxidation of toluene: dependence on initial hydrocarbon concentration, *Bull. Chem. Soc. Jpn.*, 77, 667-671, 2004.
- Sato, K., Takami, A., Isozaki, T., Hikida, T., Shimono, A., and Imamura, T.: Mass spectrometric study of secondary organic aerosol formed from the photo-oxidation of aromatic hydrocarbons, *Atmos. Environ.*, 44, 1080-1087, 2010.
- Shi, J. P. and Harrison, R. M.: Rapid NO_2 formation in diluted petrol-fuelled engine exhaust—A source of NO_2 in winter smog episodes, *Atmos. Environ.*, 31, 3857-3866, 1997.

- Smith, D., Cheng, P., and Spanel, P.: Analysis of petrol and diesel vapour and vehicle engine exhaust gases using selected ion flow tube mass spectrometry, *Rapid Commun. Mass Sp.*, 16, 1124-1134, 2002.
- Surratt, J. D., Murphy, S. M., Kroll, J. H., Ng, N. L., Hildebrandt, L., Sorooshian, A., Szmigielski, R., Vermeylen, R., Maenhaut, W., Claeys, M., Flagan, R. C., and Seinfeld, J. H.: Chemical composition of secondary organic aerosol formed from the photooxidation of isoprene, *J. Phys. Chem. A*, 110, 9665-9690, 2006.
- Surratt, J. D., Lewandowski, M., Offenberg, J. H., Jaoui, M., Kleindienst, T. E., Edney, E. O., and Seinfeld, J. H.: Effect of acidity on secondary organic aerosol formation from isoprene, *Environ. Sci. Technol.*, 41, 5363-5369, 2007.
- Surratt, J. D., Gómez-González, Y., Chan, A. W. H., Vermeylen, R., Shahgholi, M., Kleindienst, T. E., Edney, E. O., Offenberg, J. H., Lewandowski, M., Jaoui, M., Maenhaut, W., Claeys, M., Flagan, R. C., and Seinfeld, J. H.: Organosulfate formation in biogenic secondary organic aerosol, *J. Phys. Chem. A*, 112, 8345-8378, 2008.
- Surratt, J. D., Chan, A. W. H., Eddingsaas, N. C., Chan, M. N., Loza, C. L., Kwan, A. J., Hersey, S. P., Flagan, R. C., Wennberg, P. O., and Seinfeld, J. H.: Reactive intermediates revealed in secondary organic aerosol formation from isoprene, *Proc. Natl. Acad. Sci. USA*, 107, 6640-6645, 2010.
- Szmigielski, R., Surratt, J. D., Vermeylen, R., Szmigielska, K., Kroll, J. H., Ng, N. L., Murphy, S. M., Sorooshian, A., Seinfeld, J. H., and Claeys, M.: Characterization of 2-methylglyceric acid oligomers in secondary organic aerosol formed from the photooxidation of isoprene using trimethylsilylation and gas chromatography/ion trap mass spectrometry, *J. Mass. Spectrom.*, 42, 101-116, 2007.
- Szmigielski, R., Dommen, J., Metzger, A., Maenhaut, W., Baltensperger, U., and Claeys, M.: The acid effect in the formation of 2-methyltetrols from the photooxidation of isoprene in the presence of NO_x, *Atmos. Res.*, 98, 183-189, 2010.
- Takekawa, H., Minoura, H., and Yamazaki, S.: Temperature dependence of secondary organic aerosol formation by photo-oxidation of hydrocarbons, *Atmos. Environ.*, 37, 3413-3424, 2003.
- ToF-AMS Software Downloads: <http://cires.colorado.edu/jimenez-group/ToFAMSResources/>, access: 12 January 2010.

- Treacy, J., El Hag, M., O'Farrell, D., and Sidebottom, H.: Reactions of ozone with unsaturated organic compounds, *Ber. Bunsenges. Phys. Chem.*, 96, 422-427, 1992.
- Wang, W., Kourtchev, I., Graham, B., Cafmeyer, J., Maenhaut, W., and Claeys, M.: Characterization of oxygenated derivatives of isoprene related to 2-methyltetrols in Amazonian aerosols using trimethylsilylation and gas chromatography/ion trap mass spectrometry, *Rapid Commun. Mass Spectrom.*, 19, 1343-1351, 2005.
- Xia, X. and Hopke, P. K.: Seasonal variation of 2-methyltetrols in ambient air samples, *Environ. Sci. Technol.*, 40, 6934-6937, 2006.
- Yokouchi, Y.: Seasonal and diurnal-variation of isoprene and its reaction-products in a semirural area, *Atmos. Environ.*, 28, 2651-2658, 1994

A.11 Tables

Table A.1. Experimental conditions and results.

Run ^a	Compound	[Diene] ₀ (ppb)	[NO _x] ₀ ^b (ppb)	Diene reacted (μg m ⁻³)	SOA ^c (μg m ⁻³)	SOA Yield	Note
EPA1058W	ISO	573	940	1595	24	0.015	d
EPA1070E	ISO	965	56	1734	32	0.018	d
EPA1069W	ISO	552	43	1350	25	0.019	d
EPA1069E	ISO	247	42	688	16	0.023	d
EPA1058E	ISO	255	398	710	26	0.037	d
EPA1068W	ISO	115	44	320	12	0.038	d
EPA1082E	ISO	376	273	1046	46	0.044	d
EPA1078W	ISO	115	257	320	15	0.047	d
EPA1070W	ISO	957	907	2663	136	0.051	d
EPA1068E	ISO	49	42	136	7	0.052	d
EPA1078E	ISO	115	257	320	17	0.053	d
EPA1087E	ISO	244	250	678	36	0.053	d
EPA1061E	ISO	20	22	55	3	0.055	d
EPA1060W	ISO	145	240	403	28	0.069	d
EPA1061W	ISO	42	50	116	9	0.077	d
EPA1060E	ISO	66	103	184	19	0.103	d
EPA1115E	ISO	37	268	103	8	0.077	e
EPA1108W	ISO	240	256	668	63	0.094	e
EPA1108E	ISO	115	256	320	33	0.103	e
EPA1087W	ISO	338	315	939	6	0.006	d,f
EPA1090E	ISO	197	339	548	6	0.011	d,g
EPA1090W	ISO	199	343	555	9	0.016	d,g
EPA1148E	ISO	133	300	371	39	0.105	d,h
EPA1148W	ISO	132	297	368	56	0.152	d,h
EPA1082W	ISO-13C	317	275	881	50	0.057	d
EPA1072W	BD	106	333	234	5	0.021	d
EPA1072E	BD	51	146	112	4	0.036	d
EPA1094E	BD	112	267	247	22	0.089	e
EPA1094W	BD	269	267	594	66	0.111	e
EPA1132E	BD	41	250	91	11	0.121	e
EPA1132W	BD	214	249	473	84	0.178	e
EPA1137W	BD	227	275	501	22	0.044	e,f
EPA1137E	BD	228	276	504	30	0.060	e,f
EPA1104E	DMB	115	259	386	1	0.003	e

^a Typical experiments were conducted in the presence of ~3 ppm H₂O₂ at 300±1 K, unless otherwise specified. ^b NO_x used in all experiments was pure NO. ^c SOA mass was converted from SMPS volume assuming 1 g cm⁻³ density. ^d NO₂ photolysis rate was set to 0.12 min⁻¹. ^e NO₂ photolysis rate was set to 0.40 min⁻¹. ^f No hydroxyl radical source (H₂O₂) was used. ^g Lights-off experiment. ^h Low-temperature experiment at 278 K.

Table A.2. Oligoesters detected by LC-TOFMS and AMS.

<i>n</i>	LC-TOFMS measured [M-H] ⁻	LC-TOFMS suggested formula	Error (ppm)	AMS measured [M-OH] ⁺	AMS suggested formula	Structure	
Products of ISO or DMB							
Series 1A	1	119.0349	C ₄ H ₇ O ₄ ⁻	8.5	103	C ₄ H ₇ O ₃ ⁺	
	2	221.0665	C ₈ H ₁₃ O ₇ ⁻	4.2	205	C ₈ H ₁₃ O ₆ ⁺	
	3	323.0978	C ₁₂ H ₁₉ O ₁₀ ⁻	1.6			
	4	425.1281	C ₁₆ H ₂₅ O ₁₃ ⁻	-2.0			
	5	527.1582	C ₂₀ H ₃₁ O ₁₆ ⁻	-4.7			
Series 2A	1	ND					
	2	266.0515	C ₈ H ₁₂ NO ₉ ⁻	3.2			
	3	368.0832	C ₁₂ H ₁₈ NO ₁₂ ⁻	2.3			
	4	470.1149	C ₁₆ H ₂₄ NO ₁₅ ⁻	1.8			
	5	572.1464	C ₂₀ H ₃₀ NO ₁₈ ⁻	1.2			
Series 3A _a	1	ND		131		C ₅ H ₇ O ₄ ⁺	
	2	249.0615	C ₉ H ₁₃ O ₈ ⁻	4.0	233	C ₉ H ₁₃ O ₇ ⁺	
	3	351.0928	C ₁₃ H ₁₉ O ₁₁ ⁻	1.7			
	4	453.1245	C ₁₇ H ₂₅ O ₁₄ ⁻	1.4			
	5	555.1560	C ₂₁ H ₃₁ O ₁₇ ⁻	0.8			
Series 4A _b	1	ND		145		C ₆ H ₉ O ₄ ⁺	
	2	263.0768	C ₁₀ H ₁₅ O ₈ ⁻	2.5	247	C ₁₀ H ₁₅ O ₇ ⁺	
	3	365.1080	C ₁₄ H ₂₁ O ₁₁ ⁻	0.4			
	4	467.1394	C ₁₈ H ₂₇ O ₁₄ ⁻	-0.3			
	5	569.1706	C ₂₂ H ₃₃ O ₁₇ ⁻	-1.1			

n	LC-TOFMS measured [M-H] ⁻	LC-TOFMS suggested formula	Error (ppm)	AMS measured [M-OH] ⁺	AMS suggested formula	Structure
Series 5A ^c	1	ND				
	2	327.0683	C ₉ H ₁₅ N ₂ O ₁₁ ⁻	3.9		
(Newly found)	3	429.0989	C ₁₃ H ₂₁ N ₂ O ₁₄ ⁻	0.4		
	4	531.1302	C ₁₇ H ₂₇ N ₂ O ₁₇ ⁻	-0.4		
Products of BD						
	1	105.0181	C ₃ H ₅ O ₄ ⁻	-1.3	89	C ₃ H ₅ O ₃ ⁺
	2	193.0336	C ₆ H ₉ O ₇ ⁻	-3.5	177	C ₆ H ₉ O ₆ ⁺
Series 1B	3	281.0491	C ₉ H ₁₃ O ₁₀ ⁻	-4.4	265	C ₉ H ₁₃ O ₉ ⁺
	4	369.0650	C ₁₂ H ₁₇ O ₁₃ ⁻	-3.7		
	5	457.0819	C ₁₅ H ₂₁ O ₁₆ ⁻	-1.1		
Series 5B	1	ND				
(Newly found)	2	299.0364	C ₇ H ₁₁ N ₂ O ₁₁ ⁻	2.2		
	3	387.0516	C ₁₀ H ₁₅ N ₂ O ₁₄ ⁻	-0.2		
	4	475.0681	C ₁₃ H ₁₉ N ₂ O ₁₇ ⁻	0.6		
	5	563.0844	C ₁₆ H ₂₃ N ₂ O ₂₀ ⁻	0.9		

^aThis oligoester series involves esterification with formic acid. ^bThis oligoester series involves esterification with acetic acid. ^cThis series was only produced by the reaction of isoprene and was not produced by the reaction of DMB.

A.12 Figures

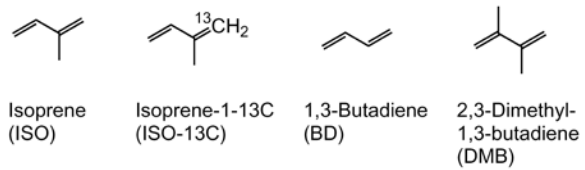


Figure A.1: Conjugated dienes used in this study.

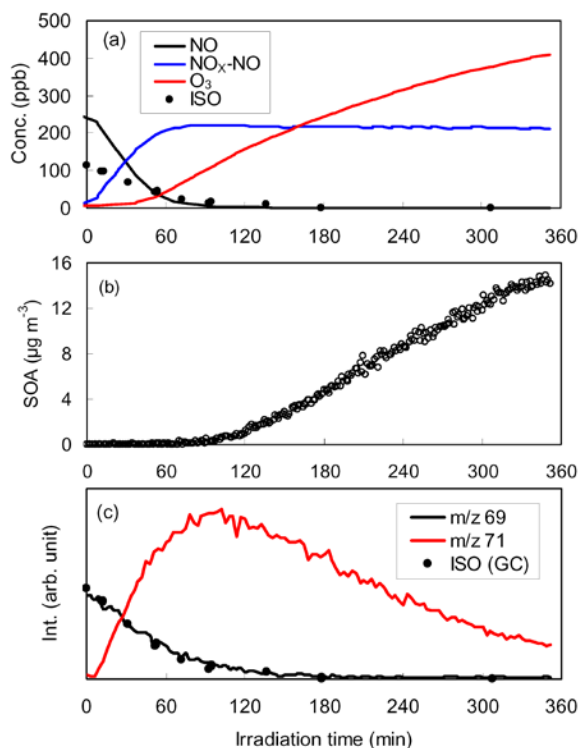


Figure A.2: Time profiles of (a) gas concentration, (b) SOA mass concentration, and (c) PTR-MS signals during isoprene/NO_x/H₂O₂ experiment at 300 K (EPA1078W). The NO₂ photolysis rate for this run was 0.12 min⁻¹. The NO_x analyzer used was a chemiluminescence type; NO_x signals of this instrument include not only the signals of NO and NO₂ but also the signals of NO_y species (e.g., nitric acid).

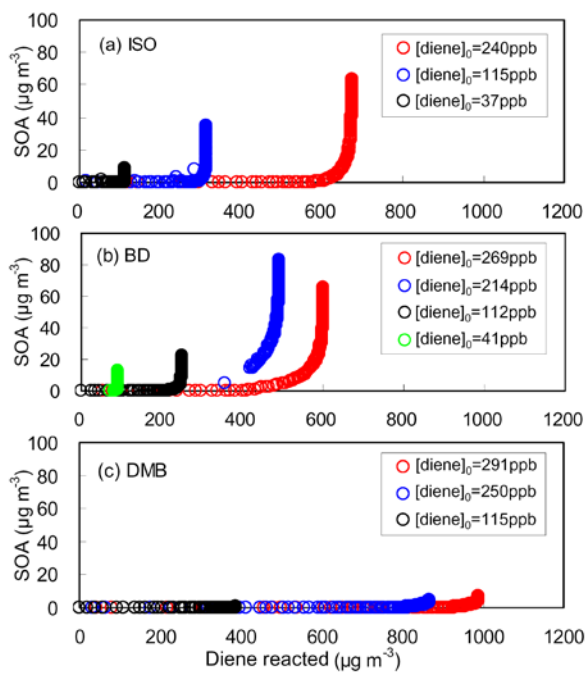


Figure A.3: Time-dependent SOA growth curves measured in diene/NO_x/H₂O₂ experiments with (a) isoprene (EPA1108W, EPA1108E, EPA1115E), (b) 1,3-butadiene (EPA1094W, EPA1094E, EPA1132W, EPA1132E), and (c) DMB (EPA1104W, EPA1104E, EPA1115W). All results plotted were obtained at initial NO_x concentrations of 249–267 ppb and at an NO₂ photolysis rate of 0.40 min⁻¹.

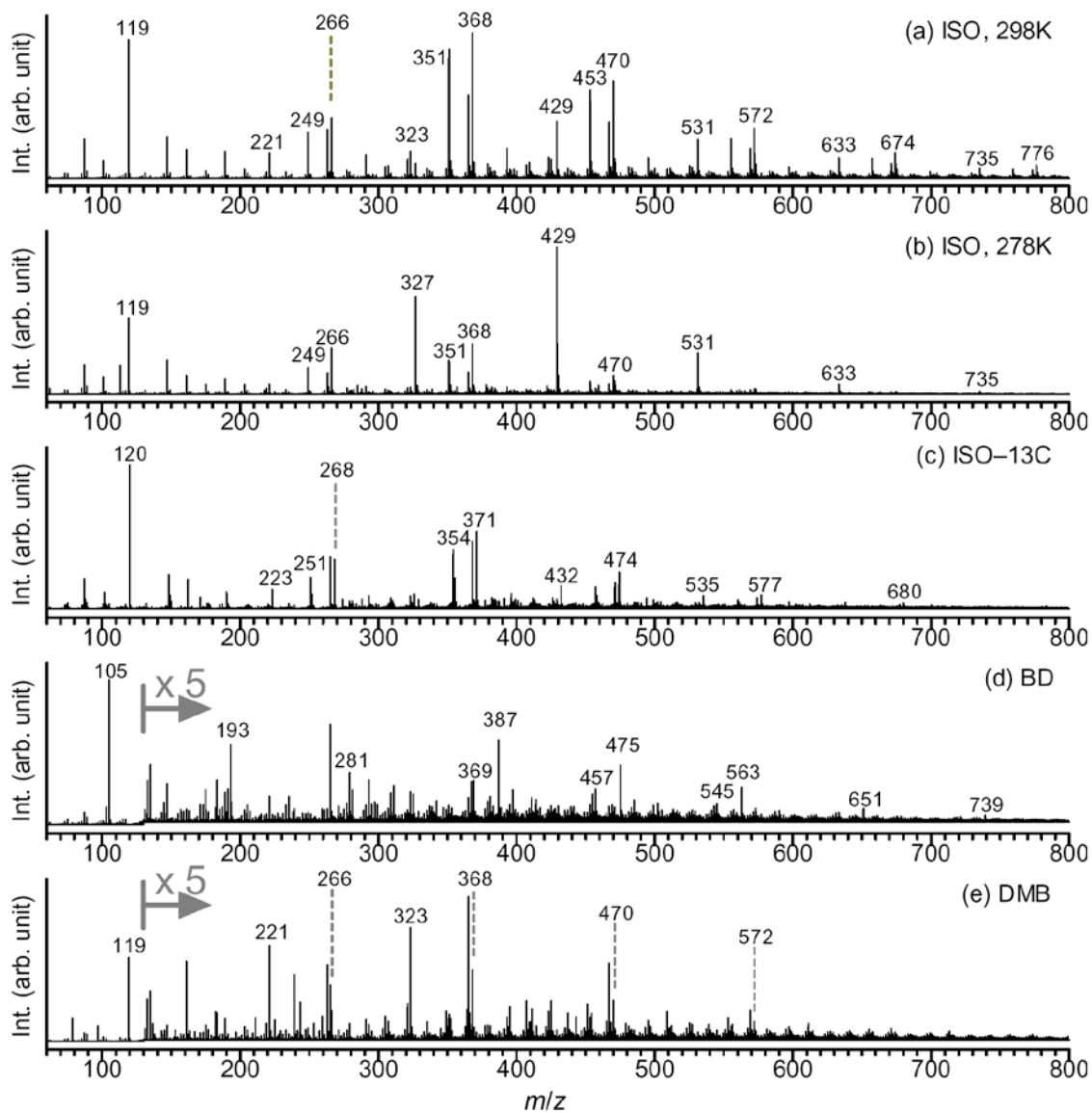


Figure A.4: Flow-injection LC-TOF mass spectra of off-line SOA samples obtained during the photooxidation of (a) isoprene at 300 K (EPA1108W), (b) isoprene at 278 K (EPA1148W), (c) isoprene-1- ^{13}C (EPA1082W), (d) 1,3-butadiene (EPA1094W), and (e) DMB (EPA1104W).

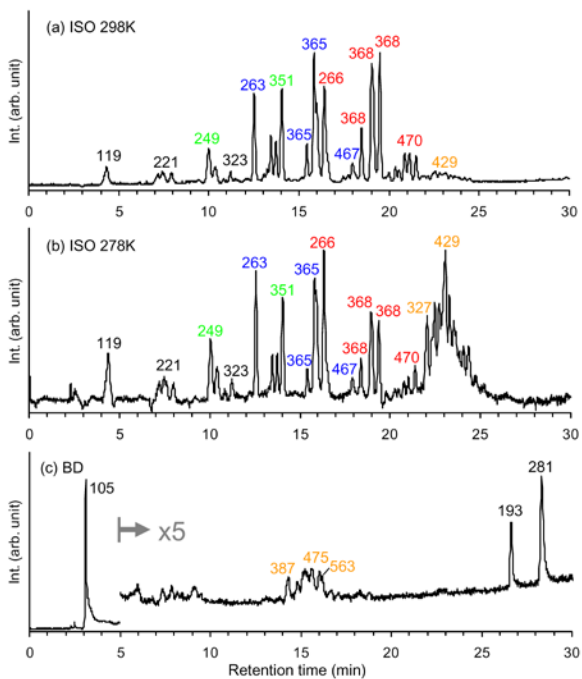


Figure A.5: Typical LC-TOFMS base peak chromatograms of SOA formed from the photooxidation of (a) isoprene at 300 K (EPA1058E), (b) isoprene at 278 K (EPA1148W), and (c) 1,3-butadiene (EPA1132W).

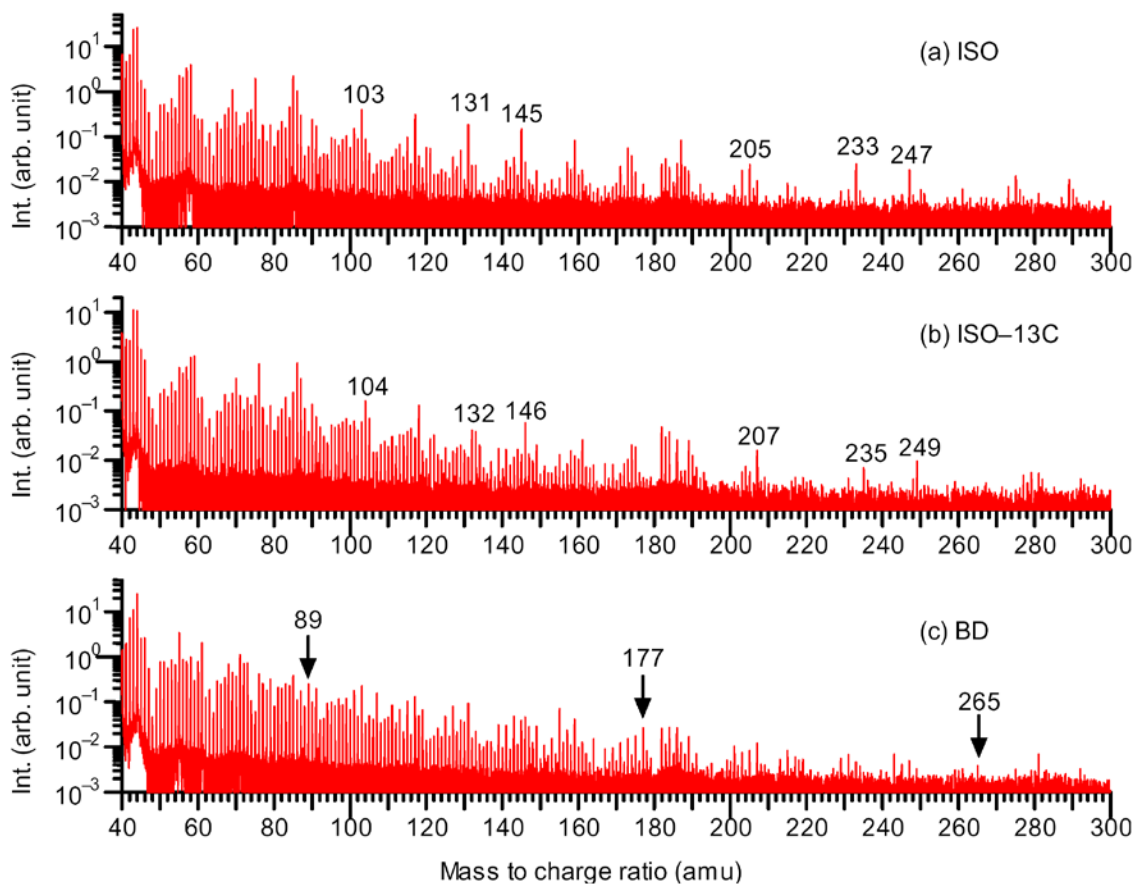


Figure A.6: Typical TOF-AMS raw mass spectra of SOA formed from the photooxidation of (a) isoprene (EPA1170W), (b) isoprene-1-13C (EPA1082W), and (c) 1,3-butadiene (EPA1094W).

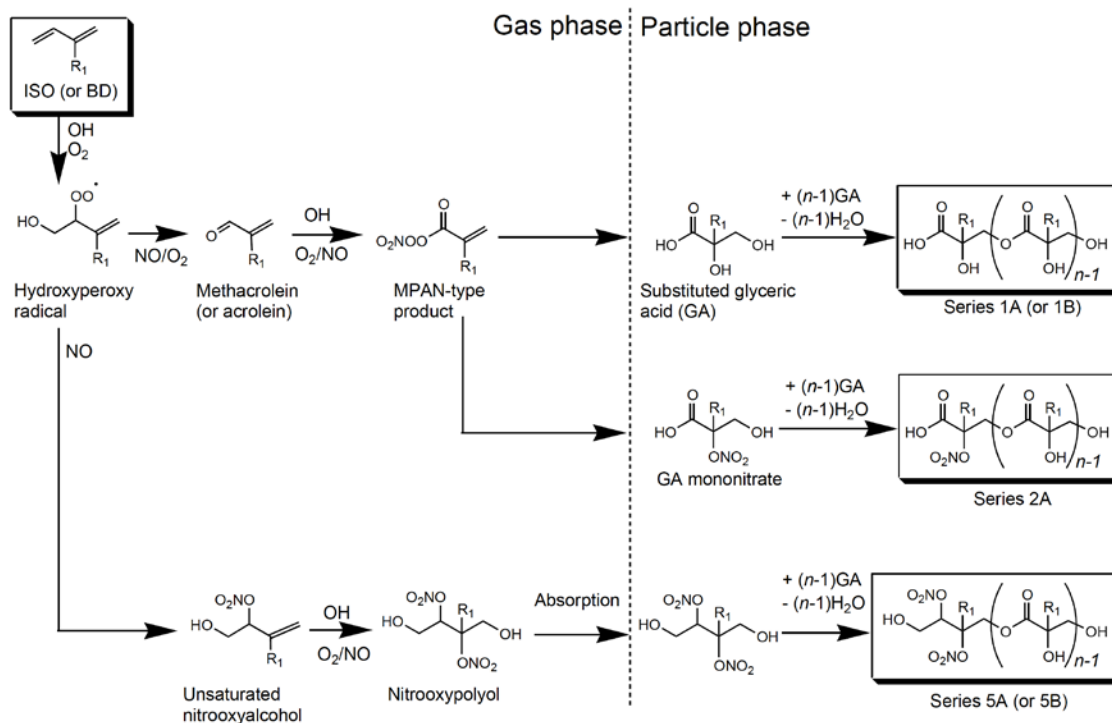


Figure A.7: Proposed mechanism of particle-phase product formation from the photooxidation of isoprene and 1,3-butadiene in the presence of NO_x. R₁ is a methyl group (isoprene) or a hydrogen atom (1,3-butadiene).

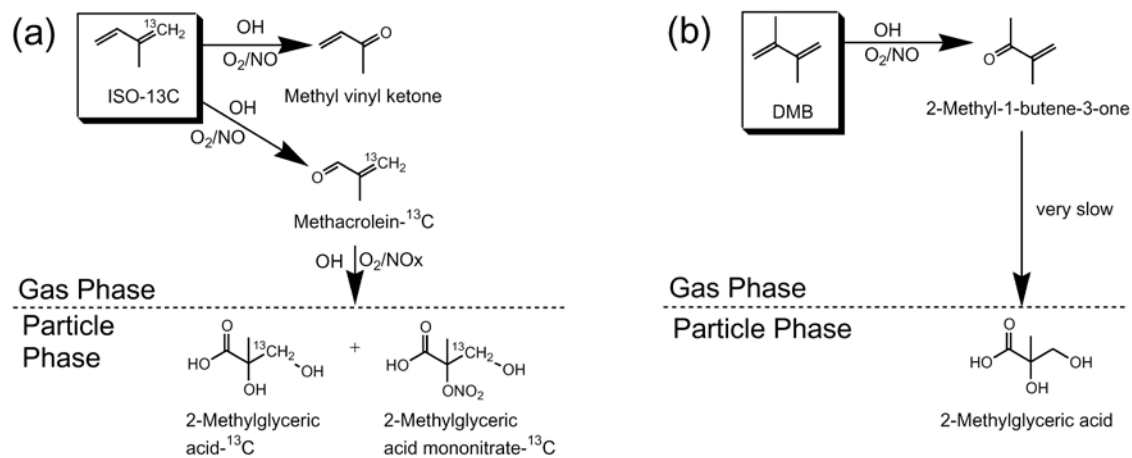


Figure A.8: Proposed mechanism of (a) isoprene-1-¹³C and (b) DMB photooxidation in the presence of NO_x.

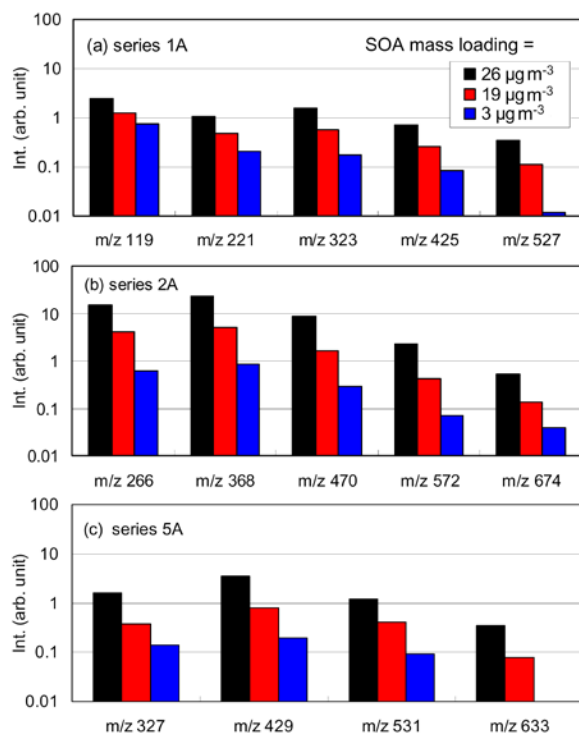


Figure A.9: Oligomer distribution measured in experiments with isoprene (EPA1058E, EPA1060E, and EPA1061E). SOA mass loading was changed between 3 and 26 $\mu\text{g m}^{-3}$ by changing the initial reactant concentrations, maintaining the isoprene/ NO_x ratio within the range 0.6–0.9.

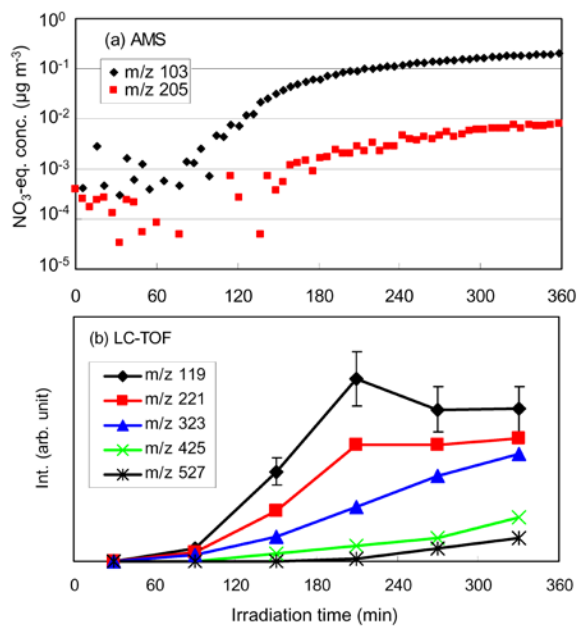


Figure A.10: Time profiles of particulate product mass signals measured by (a) ToF-AMS during an experiment with isoprene (EPA1070W) and (b) LC-TOFMS during an experiment with isoprene (EPA1078E).

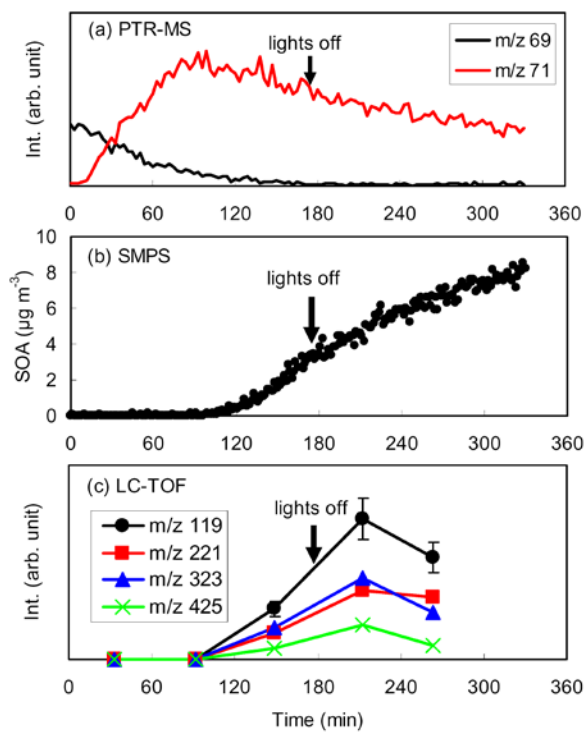


Figure A.11: Time profiles of (a) PTR-MS signals, (b) SOA mass concentration, and (c) LC-TOFMS oligomer mass signals measured in a lights-off experiment with isoprene (EPA1090W).

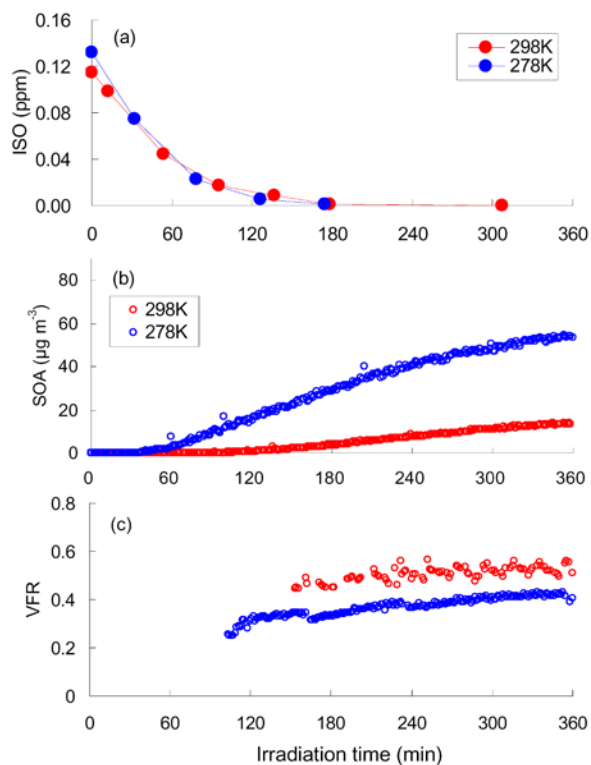


Figure A.12: Time profiles of (a) isoprene concentration, (b) SOA concentration, and (c) volume fraction remaining (VFR) measured during experiments with isoprene at 278 K (EPA1148W) and 300 K (EPA1078W). The NO_2 photolysis rate for both experiments was set to 0.12 min^{-1} .

Appendix B: Secondary Organic Aerosol Formation from Phenolic Compounds in the Absence of NO_x

B.1 Introduction

Secondary organic aerosol (SOA) is formed from oxidative processing of volatile organic compounds in the atmosphere. SOA has been suggested to contribute to climate change (IPCC, 2007; Kanakidou et al., 2005), adverse human health effects (Davidson et al., 2005; Pope and Dockery, 2006), and a reduction in visibility (Eldering and Cass, 1996). Previous researchers have estimated approximately 70% of organic aerosols are secondary in nature (Hallquist et al., 2009 and references therein). Aromatic hydrocarbons comprise ~20% of nonmethane hydrocarbons in the urban atmosphere and are considered to be one of the major precursors to urban SOA (Calvert et al., 2002).

A number of studies have investigated gas-phase photooxidation of aromatic hydrocarbons (e.g., Arey et al., 2009; Calvert et al., 2002; Coeur-Tourneur et al., 2006; Johnson et al., 2004; Johnson et al., 2005; Olariu et al., 2002; Takekawa et al., 2003; Volkamer et al., 2002). Previously identified first generation products of aromatic compound photooxidation explain approximately 50% of carbon balance (Calvert et al., 2002). Although multigenerational reactions have been suggested to contribute to aromatic SOA formation (Hurley et al., 2001; Ng et al., 2007; Sato et al., 2007), the extent of the contribution from the second or further reaction products to SOA is poorly understood.

Phenolic compounds are one of the major first generation products of OH reaction with aromatic hydrocarbons (Calvert et al., 2002). Previous studies suggested the major gas-phase reaction products from OH reaction of phenolics are dihydroxy compounds (e.g., 80% catechol formation from phenol, Olariu et al. (2002)). However, the mechanisms of SOA formation from phenolic compounds are highly uncertain. In addition, since phenolic compounds are significant products in wood smoke (Hawthorne et al., 1989; Hawthorne et al., 1992; Schauer et al., 2001; Simoneit, 1999), the reaction mechanism of phenolic compounds leading to SOA formation is of a great interest (Chang and Thompson, 2010; Coeur-Tourneur et al., 2010a; Coeur-Tourneur et al., 2010b; Grosjean, 1984; Henry et al., 2008; Iinuma et al., 2010; Sun et al., 2010).

SOA formation from individual aromatic and phenolic compounds were investigated using an environmental chamber under low NO_x (and high HO₂) conditions to evaluate the role of phenolic species in SOA formation from aromatic hydrocarbons. Chemical analysis was performed using on-line and off-line mass spectrometry to infer the structure of aromatic and phenolic SOA.

B.2 Experimental

B.2.1 environmental chamber

Most of the experiments were conducted in the UC Riverside/CE-CERT environmental chamber described in detail in Carter et al. (2005). In short, this facility consists of dual 90m³ Teflon® reactors suspended by rigid frames in a temperature controlled enclosure (27 ± 1 °C) continuously flushed with dry (a dew point below -40

°C) purified air generated by an Aadco 737 series (Cleves, Ohio) air purification system. The top frames are slowly lowered during the experiments to maintain a slight positive differential pressure (0.03”H₂O) between the reactors and enclosure to minimize dilution and possible contamination of the reactors. 272 115W Sylvania 350 black lights are used as the light source for all the experiments reported herein.

Some of the results of dimethylphenols (DMPs) were acquired in the UCR/CE-CERT mezzanine chamber (Nakao et al., 2011). The UCR/CE-CERT mezzanine chamber is within a 2.5 m x 3 m x 7.8 m enclosure covered with reflective aluminum sheets and is illuminated with 170, 40W blacklights with peak intensity at 350 nm (SYLVANIA, 350 BL) with the NO₂ photolysis rate of 0.6 min⁻¹. Within this enclosure is a 12 m³ volume 2 mil FEP Teflon[®] film reactor. A minimum of 1 m space between the reactor surface and blacklights avoids excessive heating at the surface of the film. Additionally, six fans are used to mix the air inside the enclosure with room air to minimize heating in the enclosure. Prior to each experiment, the bag is flushed overnight with purified air. Background particle concentration is below the detection limit of 0.2 cm⁻³.

B.2.2 gas and particle analysis

The Agilent 6890 Gas Chromatograph – Flame Ionization Detector was used to measure concentrations of reactants and products. All phenolic compounds were analyzed by a GC equipped with a thermal desorption system (CDS analytical, ACEM9305, Sorbent Tube MX062171 packed with Tenax-TA/Carbopack/Carbosieve S111) except for dimethylphenols for mezzanine chamber experiments. Aromatic

hydrocarbon measurements were calibrated using a dilute gas cylinder (SCOTT-MARIN, Inc) or by introducing known amount of liquid hydrocarbons into the reactor. Calibration for phenolic compounds was performed by impregnation of the glass cartridges with known quantities of phenolic compounds in acetonitrile. The Ionicon Proton Transfer Reaction – Quadrupole Mass Spectrometer (PTR-MS) was used to measure dimethylphenol decay for mezzanine chamber experiments.

Particle size distribution between 27 nm and 686 nm was monitored by a custom built Scanning Mobility Particle Sizer (SMPS) similar to that described by Cocker et al. (2001). Particle effective density was measured with an Aerosol Particle Mass Analyzer (APM, Kanomax) (Ehara et al., 1996) and SMPS in series. The APM is located upstream of the SMPS for improved time resolution and sensitivity (S/N) over the more common configuration of Differential Mobility Analyzer (DMA) – APM (Khalizov et al., 2009; McMurry et al., 2002; Xue et al., 2009). A detailed description of the APM-SMPS system and data algorithms are described elsewhere (Malloy et al., 2009).

The high resolution time-of-flight aerosol mass spectrometer (HR-ToF-AMS) (DeCarlo et al., 2006) was operated in high resolution W mode. Elemental analysis (EA) was used to determine the atomic ratio (O/C) of non-refractory organic aerosols (Aiken et al., 2008).

The Agilent 6210 Accurate-Mass Time-of-Flight Mass Spectrometer equipped with multimode ionization source for electrospray and atmospheric pressure chemical ionization (ESI/APCI-TOFMS) is used to obtain accurate mass of analytes. Soft ionization by ESI and APCI provides lower fragmentation of the analytes compared to

electron impact (EI) used for the HR-ToF-AMS or other conventional GC-MS techniques. Mass accuracy is routinely calibrated by standard compounds (Agilent low concentration MMI tuning mix, G1969-85020) before analysis and in most cases mass accuracy of less than 5ppm is achieved. Occasionally higher mass errors (~30ppm) were observed during sample analysis, which resulted in a consistent shift of mass throughout the mass range of the instrument. Since the extent of the shift can be inferred from repeatedly observed ions (e.g., pyruvic acid), formulas were carefully assigned based on tendency of shift and repeat experiments. Filter samples were collected onto Teflo® filters (2µm, 47mm, PALL Life Sciences) at 25 L/min for 1~4 hours. After collection, filters were stored in a freezer until extraction. Extractions were achieved by sonicating the filter in 5mL of acetonitrile. The extract volume was reduced under a gentle stream of N₂ until near dryness and reconstituted by 300 µL of acetonitrile/water/acetic acid (50/50/0.1v). Samples were directly infused to the TOFMS. A: Water (0.1v% acetic acid) and B: acetonitrile were used as eluents (B 50%, 0.5mL/min). Acetonitrile was chosen as the organic solvent to reduce the solvent-analyte reaction compared to methanol (Bateman et al., 2008). Mixed mode ionization (simultaneous APCI and ESI) was used with vaporizer temperature 200°C, nebulizer pressure 40 psig, corona current 2 µA, fragmentor voltage 100V. Although the mixed mode is used to survey a wide range of products, the resulting major signals were the same as in ESI only. APCI yielded lower sensitivity in this study. All Agilent TOFMS data was acquired in negative ion mode.

A Particle-Into-Liquid-Sampler (PILS) (Orsini et al., 2003; Weber et al., 2001) was interfaced with the TOFMS to provide an on-line accurate mass analysis of water

soluble organic compounds (Bateman et al., 2010). In order to couple the PILS (Brechtel Manufacturing Inc.) to the TOFMS, the use of HPLC pumps in addition to a commonly used peristaltic pump was critical to overcome the backpressure of the TOFMS inlet and to supply steady flow of water (18.2 M Ω , Milli-Q, Millipore) into the boiler. The PILS-TOFMS system will be described in more detail in an upcoming publication (Clark et al., 2011). The negative ESI was used as the ionization method with similar conditions as the filter analysis without the corona current.

B.2.2 chamber experiments

The experimental test matrix is summarized in Table B.1. A known volume of high purity liquid aromatic hydrocarbon (All purchased from Sigma-Aldrich: $\geq 99\%$ or $\geq 99.5\%$, except 2,4-DMP $\geq 98\%$) was injected through a heated glass injection manifold system and flushed into the chamber with pure N₂. Since phenolic compounds are less volatile than hydrocarbons typically used for chamber experiments, injection into the chambers were carefully performed using a heated oven (50~80°C) through a heated transfer line maintained at a temperature higher than the oven. The glass manifold inside the oven was packed with glass wool to increase the mass transfer surface area. Since reasonable agreement between the calculated concentration of phenolics (based on injected amount) and observed concentrations were confirmed, loss of phenolics in the transfer line and to the wall was assumed to be negligible. H₂O₂ was used as an OH (and HO₂) radical source. H₂O₂ 50wt% solution was injected through the same oven system. Since the H₂O₂ solution did not spread through glass wool, the glass wool was processed with an acid/base bath and cleaned by water and acetone which enabled the H₂O₂

solution to spread. Initial H₂O₂ concentration was not measured, but is estimated to be 1~5ppm based on amount injected and hydrocarbon decay rate. No seed particles were used in this study. Exponential decay rates of particle number is used to calculate particle volume wall loss (Carter et al., 2005). To investigate the role of organic peroxides, additional high NO experiments were also performed and the chemical composition of SOA was compared to low NO_x condition. Initial ratio of approximately 50/50/500 ppb for phenolic/methyl nitrite/NO was used to ensure that excess NO was present to suppress RO₂ + HO₂ reaction.

B.3 Results and Discussions

B.3.1 SOA formation

SOA yield (Y) is defined as the mass of aerosol formed (wall-loss-corrected) (M_o) divided by mass of hydrocarbon reacted (ΔHC)

$$Y = \frac{M_o}{\Delta HC} \quad \text{Equation 1}$$

Its dependence on aerosol mass loading has been traditionally parameterized by as shown below: (Odum et al., 1996)

$$Y = \sum Y_i = M_o \sum_i \frac{\alpha_i K_i}{1 + M_o K_i} \quad \text{Equation 2}$$

where α_i is the mass-based stoichiometric coefficient for the reaction generating product i , K_i is the partitioning coefficient of product i . Equation 1 and 2 were applied for the SOA yields obtained (Figure B.1). Particle density of 1.4 g/cm³ was used. 2,4-DMP

had the highest SOA formation potential of the three DMP isomers, with a SOA yield approximately twice as high as the other DMP isomers. SOA yield from phenol was higher than benzene.

SOA from aromatic hydrocarbons formed under low NO_x conditions was previously reported to be effectively non-volatile (Ng et al., 2007), in which case SOA yield would be independent of particle mass concentration (flat SOA yield curves). However, for benzene, *o*-/*m*-cresol, and possibly DMPs, the SOA yield was observed to be slightly dependent on particle concentration. Therefore, in this study, constant SOA yield was not assumed and a one product model fit was applied to perform calculation of the contribution of phenolic route in the following section of the contribution of phenolic route.

B.3.2 contribution of phenolic route

The formation yields of phenolics from aromatics were obtained. An example for *o*-cresol and *m/p*-cresol formation from toluene is shown in Figure B.2. The cresol formation yields from toluene were calculated from measured cresol by correcting for the further reaction of cresols with OH. Equations in Atkinson et al. (1982) and rate constants from Calvert et al. (2002) were used for the correction. Phenol, cresols, and DMPs formation yields are in reasonable agreement with previous studies (Table B.3) (Atkinson, 1989; Atkinson et al., 1991; Berndt and Böge, 2006; Klotz et al., 1998; Smith et al., 1999; Smith et al., 1998; Volkamer et al., 2002).

Contributions of the phenolic route to aromatic SOA formation in the low NO_x system were estimated by combining SOA yield measurement (Figure B.1), phenolic

yields, and consumption of phenolics (e.g., Figure B.2). The amount of phenolics (as products) reacted is calculated as the gap between the observed concentration of phenolic compounds and the concentration corrected for the secondary reaction. Phenolic route SOA is calculated by multiplying reacted phenolics and their SOA yield at appropriate mass loading using the phenolic SOA yield curves in Figure B.1. SOA yields from cresol isomers (*o*-, *m*-, and *p*-) were assumed to be the same (Henry et al., 2008). The ratio of 2,4-DMP and 2,6-DMP produced from OH reaction of *m*-xylene was assumed to be the same as that reported by Smith et al. (1999). Formation of 3,5-DMP is assumed to be insignificant (Smith et al., 1999). Contribution of the phenolic route in the no NO_x system is summarized in Table B.1. The contribution was approximately 20% for benzene, toluene, and *m*-xylene in low NO_x conditions.

B.3.3 particle chemical composition

B.3.3.1 SOA elemental ratio and density

The results of elemental analysis of HR-ToF-AMS data (O/C ratio) are shown in Figure B.3. The O/C ratios during the experiments were nearly constant with only a small increase in O/C observed over time. The O/C ratio decreased as the number of methyl substituents on the parent aromatic ring increased; ~0.6 for C₆ species (benzene, phenol, and catechol), ~0.5 for C₇ species (toluene and cresols), and ~0.4 for C₈ species (*m*-xylene and dimethylphenols). The decrease in O/C is approximately consistent with the increasing number of carbons in the parent aromatics, indicating that the methyl substituents did not play a major role in the SOA formation mechanism. Therefore the H-

abstraction from methyl substituents is not likely to be an important route to aromatic SOA formation under low NO_x conditions. The O/C ratios of SOA between aromatic hydrocarbons and corresponding phenolics were similar, suggesting the significance of multi-generational reactions.

Real-time SOA density measured by the APM-SMPS is shown in Figure B.4. The SOA densities were observed to be initially high (~1.8 g/cm³), which could be due to high density of nucleating species. The final SOA densities were in the range of 1.3-1.4 g/cm³, in reasonable agreement with previous studies (Ng et al., 2007; Sato et al., 2010). Although Bahreini et al. (2005) observed weak correlation between effective density and relative contribution of m/z 44 signal to total organic signal of AMS, the final SOA densities were found to be independent of elemental composition of SOA from aromatics tested in this study (Figure B.5). Therefore a constant SOA density (1.4 g/cm³) is applied to all the experiments in this study.

B.3.3.2 Filter analysis

Chemical The results of elemental analysis of HR-ToF-AMS data (O/C ratio) are shown in Figure B.3. The O/C ratios during the experiments were nearly constant with only a small increase in O/C observed over time. The O/C ratio decreased as the number of methyl substituents on the parent aromatic ring increased; ~0.6 for C₆ species (benzene, phenol, and catechol), ~0.5 for C₇ species (toluene and cresols), and ~0.4 for C₈ species (*m*-xylene and dimethylphenols). The decrease in O/C is approximately consistent with the increasing number of carbons in the parent aromatics, indicating that the methyl substituents did not play a major role in the SOA formation mechanism.

Therefore the H-abstraction from methyl substituents is not likely to be an important route to aromatic SOA formation under low NO_x conditions. The O/C ratios of SOA between aromatic hydrocarbons and corresponding phenolics were similar, suggesting the significance of multi-generational reactions.

Real-time SOA density measured by the APM-SMPS is shown in Figure B.4. The SOA densities were observed to be initially high (~1.8 g/cm³), which could be due to high density of nucleating species. The final SOA densities were in the range of 1.3-1.4 g/cm³, in reasonable agreement with previous studies (Ng et al., 2007; Sato et al., 2010). Although Bahreini et al. (2005) observed weak correlation between effective density and relative contribution of m/z 44 signal to total organic signal of AMS, the final SOA densities were found to be independent of elemental composition of SOA from aromatics tested in this study (Figure 2.5). Therefore a constant SOA density (1.4 g/cm³) is applied to all the experiments in this study.

Composition of SOA was analyzed by off-line filter analysis. Samples were directly infused to the ESI/APCI-TOFMS. Although direct infusion of SOA extract into ESI-MS is often done (e.g., Altieri et al., 2006; Camredon et al., 2010; De Haan et al., 2009; Heaton et al., 2009), caution must be taken in interpreting the mass spectrums due to possible formation of adducts or analyte-solvent reaction products (Bateman et al., 2008; Pratt and Prather, 2011). Mass spectra obtained by ESI/APCI-TOFMS are shown in Figure B.6. High mass accuracy measurements enabled determination of empirical formula typically within 5 ppm mass error. Inclusion of nitrogen or halogens in the formula calculation did not yield reasonable formulae. Major ions in each spectrum

contained the same number of carbon as reactants (e.g., $C_6H_8O_6$ from phenol, $C_7H_{10}O_6$ from *o*-cresol, and $C_8H_{12}O_6$ from 2,4-DMP).

The possibility of adduct formation between acetic acid mobile phase modifier and analytes was investigated by changing acetic acid to formic acid; however, the major signals were still the same, indicating that the observed products are not adducts of the acid modifier. Acetonitrile was used in this study instead of methanol to reduce the risk of analyte-solvent reactions (particularly reactions of methanol and carbonyls or carboxylic acids) (Bateman et al., 2008). Tests substituting methanol as an organic solvent did not alter the major MS signal distribution indicating those MS signals did not result from analyte-solvent reaction. The agreement of carbon number and apparent CH_2 shift with increasing number of methyl substituents on the aromatic precursor suggests that these major signals are not likely to be adducts formed during ionization.

Since only formulae were determined and no structural information is available in this study, there are a number of possible structures such as unsaturated multi-functional ring-opening products (e.g., diacids, polyols). Although column separation using different types of reverse-phase column was attempted, most of the major signals appeared in the non-retained peak, indicating that these species were too polar to be retained by conventional reversed-phase columns.

Another possible reaction products consistent with these formulae of the major signals are the bicyclic hydroperoxides formed from the reaction of HO_2 and bicyclic peroxy radicals (Figure B.7). The formation of bicyclic peroxy radicals intermediate from OH-initiated reaction of aromatic hydrocarbons in gas-phase has been reported

experimentally and theoretically (Andino et al., 1996; Birdsall et al., 2010; Birdsall and Elrod, 2011; Glowacki et al., 2009; Huang et al., 2008; Wyche et al., 2009). Johnson et al. (2004; 2005) predicted bicyclic hydroperoxides as one of the predominant aerosol species from aromatic hydrocarbons. Currently, organic peroxides such as hydroperoxides and peroxyhemiacetals have been suggested to be important component of SOA (e.g., monoterpene ozonolysis (Docherty et al., 2005), isoprene photooxidation (Surratt et al., 2006), naphthalene photooxidation (Kautzman et al., 2010), and toluene photooxidation (Sato et al., 2007)). Reinnig et al. (2008) reported that the parent ion from two hydroperoxide surrogates, cumene hydroperoxide and tert-butylhydroperoxide were not seen by either negative or positive mode ESI and APCI. Further, only fragments for cumene hydroperoxide were observed for ESI and APCI operating only in the positive mode and for tert-butylhydroperoxide only in the positive APCI mode. This poses an uncertainty in our detection of bicyclic hydroperoxide in this study; however, since the tentatively proposed bicyclic hydroperoxide are highly oxidized and multi-functional (with an oxygen-bridge), other functional groups may enable the ionization.

The presence of peroxides was investigated by conducting phenol photooxidation experiments under excess NO. In excess NO condition, the (bicyclic) peroxy radicals rapidly react with NO to form the alkoxy radical, which is suggested to undergo decomposition (Atkinson, 2000; Calvert et al., 2002). The resulting mass spectrum (after separating nitrophenolic species by a reverse phase column; not shown) indicated $C_6H_8O_6$ and $C_6H_8O_7$ were still present, suggesting that at least some fraction of $C_6H_8O_6$ and $C_6H_8O_7$ are formed via a non-peroxy radical route. Although uncertainty remains, it

is still interesting that major signals in ESI/APCI-TOFMS matched the widely recognized bicyclic hydroperoxides. Additional analytical techniques, such as column separation of the highly polar species, derivatization, MS/MS or NMR, are necessary for unambiguous identification of the products.

B.3.3.3 PILS-TOFMS

Mass spectra obtained by PILS-ESI-TOFMS of SOA formed from OH reaction with phenol, catechol, and *o*-cresol are shown in Figure B.8. Major signals observed from off-line filter analysis were also observed by the on-line PILS-TOFMS such as m/z 175 and 191 from the phenol SOA mass spectrum (Figure B.8 (a)). Since the PILS-TOFMS was operated without a denuder upstream, water soluble gas-phase compounds can potentially be collected by the PILS system. The highest signal in Figure B.8 (a) (mass spectrum when SOA was highest), m/z 109 is catechol ($C_6H_6O_2$), which is consistent with previous gas-phase studies (80.4% yield from phenol, Olariu et al. (2002)). From *o*-cresol, methylcatechol (m/z 123) was observed. Although further reaction mechanisms of catechol species is highly uncertain, a series of signals consistent with $-OH$ addition to catechol was observed ($C_6H_6O_2$, $C_6H_6O_3$, $C_6H_6O_4$, $C_6H_6O_5$), which could imply successive addition of $-OH$ group to the aromatic ring. Although the absence of column separation before TOFMS may introduce adduct formation, the agreement between carbon number of major products and reactants is obvious, and hence the major signals are unlikely to be artifacts. Additionally, the agreement between off-line filter samples and on-line PILS indicates that the major signals from off-line filter analysis are not likely to be artifacts formed during filter collection.

B.4 Conclusions

The significance of phenolic compounds as intermediate species of aromatic SOA and possible SOA formation mechanism in the absence of NO_x was investigated using the UCR/CE-CERT Environmental Chamber. SOA formation yield measurements coupled to gas-phase yield measurements indicate that approximately 20% of the SOA of benzene, toluene, and *m*-xylene could be ascribed to the phenolic route. Initial SOA densities were as high as approximately 1.8 g/cm^3 and eventually reached the range of $1.3\text{-}1.4 \text{ g/cm}^3$, independent of elemental ratio (O/C) of SOA tested in this study. The major products observed by ESI/APCI-TOFMS contained the same number of carbons as parent aromatics. Major signals from on-line PILS-TOFMS and off-line filter analysis agreed, with some additional possible water soluble gas phase products observed by PILS-TOFMS such as catechol.

B.5 Reference

- Aiken, A. C., DeCarlo, P. F., Kroll, J. H., Worsnop, D. R., Huffman, J. A., Docherty, K., Ulbrich, I., Mohr, C., Kimmenl, J. R., Sun, Y., Zhang, Q., Trimborn, A. M., Northway, M., Ziemann, P. J., Canagaratna, M. R., Onasch, T. B., Alfarra, M. R., Prevot, A. S., Dommen, J., Duplissy, J., Metzger, A., Baltensperger, U., Jimenez, J. L.: O/C and OM/OC ratios of primary, secondary, and ambient organic aerosols with High-Resolution Time-of-Flight Aerosol Mass Spectrometry, *Environmental Science & Technology*, 42, 4487-4485, 2008
- Altieri, K. E., Carlton, A. G., Lim, H.-H., Turpin, B. J., Seitzinger, S. P.: Evidence for oligomer formation in clouds: Reactions of isoprene oxidation products, *Environmental Science & Technology*, 40, 4956-4960, 2006
- Andino, J. M., Smith, J. N., Flagan, R. C., Goddard, W. A., Seinfeld, J. H.: Mechanism of atmospheric photooxidation of aromatics: A theoretical study, *J. Phys. Chem.*, 100, 10967-10980, 1996
- Arey, J., Obermeyer, G., Aschmann, S. M., Chattopadhyay, S., Cusick, R. D., Atkinson, R.: Dicarbonyl products of the OH radical-initiated reaction of a series of aromatics hydrocarbons, *Environmental Science & Technology*, 43, 683-689, 2009
- Atkinson, R.: Kinetics and mechanisms of the gas-phase reactions of the hydroxyl radical with organic compounds, *J. Phys. Chem. Ref. Data, Monograph 1*, 1-246, 1989
- Atkinson, R.: Atmospheric chemistry of VOCs and NO_x, *Atmospheric Environment*, 34, 2063-2101, 2000
- Atkinson, R., Aschmann, S. M., Arey, J.: Formation of ring-retaining products from the OH radical-initiated reactions of o-, m-, and p-xylene, *International Journal of Chemical Kinetics*, 23, 77-97, 1991
- Atkinson, R., Aschmann, S. M., Carter, W. P. L., Winer, A. M., Pitts, J. N.: Alkyl nitrate formation from the NO_x - air photooxidations of C₂-C₈ n-alkanes, *J. Phys. Chem.*, 86, 4563-4569, 1982
- Bahreini, R., Keywood, M. D., Ng, N. L., Varutbangkul, V., Gao, H., Flagan, R. C., Seinfeld, J. H., Worsnop, D. R., Jimenez, J. L.: Measurements of secondary organic aerosol from oxidation of cycloalkenes, terpenes, and m-xylene using an

- Aerodyne Aerosol Mass Spectrometer, *Environmental Science & Technology*, 39(15), 5674-5688, 2005
- Bateman, A. P., Nizkorodov, S. A., Laskin, J., Laskin, A.: High-resolution electrospray ionization mass spectrometry analysis of water-soluble organic aerosol collected with a particle into liquid sampler, *Anal. Chem.*, 82, 8010-8016, 2010
- Bateman, A. P., Walser, M. L., Desyaterik, Y., Laskin, J., Laskin, A., Nizkorodov, S. A.: The effect of solvent on the analysis of secondary organic aerosol using electrospray ionization mass spectrometry, *Environmental Science & Technology*, 42, 7341-7346, 2008
- Berndt, T., Böge, O.: Formation of phenol and carbonyls from the atmospheric reaction of OH radicals with benzene, *Phys. Chem. Chem. Phys.*, 8, 1205-1214, 2006
- Birdsall, A. W., Andreoni, J. F., Elrod, M. J.: Investigation of the role of bicyclic peroxy radicals in the oxidation mechanism of toluene, *J. Phys. Chem.*, 114, 10655-10663, 2010
- Birdsall, A. W., Elrod, M. J.: Comprehensive NO-Dependent Study of the Products of the Oxidation of Atmospherically Relevant Aromatic Compounds, *The Journal of Physical Chemistry A*, 115(21), 5397-5407, 2011
- Calvert, J. G., Atkinson, R., Becker, K. H., Kamens, R. M., Seinfeld, J. H., Wallington, T. J., Yarwood, G.: *The mechanism of atmospheric oxidation of aromatics hydrocarbons*. New York, Oxford University Prss. 2002.
- Camredon, M., Hamilton, J. F., Alam, M. S., Wyche, K. P., Carr, T., White, I. R., Monks, P. S., Rickard, A. R., Bloss, W. J.: Distribution of gaseous and particulate organic composition during dark α -pinene ozonolysis, *Atmospheric Chemistry and Physics*, 10, 2893-2917, 2010
- Carter, W. P. L., Cocker, D. R., Fitz, D. R., Malkina, I. L., Bumiller, K., Sauer, C. G., Pisano, J. T., Bufalino, C., Song, C.: A new environmental chamber for evaluation of gas-phase chemical mechanisms and secondary aerosol formation, *Atmospheric Environment*, 39, 7768-7788, 2005
- Chang, J. L., Thompson, A. E.: Characterization of colored products formed during irradiation of aqueous solutions containing H₂O₂ and phenolic compounds, *Atmospheric Environment*, 44, 541-551, 2010

- Clark, C. C., Nakao, S., Sato, K., Qi, L., Asa-Awuku, A., Cocker, D. R., III: Chemical Characterization by Particle into Liquid Sampling Directly Coupled to an Accurate Mass Time-of-Flight Mass Spectrometer (PILS-ToFMS) of Secondary Organic Aerosol (SOA), in preparation 2011
- Cocker, D. R., Flagan, R. C., Seinfeld, J. H.: State-of the art chamber facility for studying atmospheric aerosol chemistry, *Environmental Science & Technology*, 35(12), 2594-2601, 2001
- Coeur-Tourneur, C., Cassez, A., Wenger, J. C.: Rate coefficients for the gas-phase reaction of hydroxyl radicals with 2-methoxyphenol (Guaiacol) and related compounds, *J. Phys. Chem.*, 114, 11645-11650, 2010a
- Coeur-Tourneur, C., Foulon, V., Lareal, M.: Determination of aerosol yields from 3-methylcatechol and 4-methylcatechol ozonolysis in a simulation chamber, *Atmospheric Environment*, 44, 853-857, 2010b
- Coeur-Tourneur, C., Henry, F., Janquin, M.-A., Brutier, L.: Gas-phase reaction of hydroxyl radicals with m-, o- and p-cresol, *International Journal of Chemical Kinetics*, 38(9), 553-562, 2006
- Davidson, C. I., Phalen, R. F., Solomon, S.: Airborne particulate matter and human health: A review, *Aerosol Science and Technology*, 39, 737-749, 2005
- De Haan, D. O., Corrigan, A. L., Smith, K. W., Stroik, D. R., Turley, J. J., Lee, F. E., Tolbert, M. A., Jimenez, J. L., Cordova, K. E., Ferrell, G. R.: Secondary Organic Aerosol-Forming Reactions of Glyoxal with Amino Acids, *Environmental Science & Technology*, 43(8), 2818-2824, 2009
- DeCarlo, P. F., Kimmel, J. R., Trimborn, A. M., Northway, M., Jayne, J. T., Aiken, A. C., Gonin, M., Fuhrer, K., Horvath, T., Docherty, K., Worsnop, D. R., Jimenez, J. L.: Field-deployable, high-resolution, Time-of-Flight Aerosol Mass Spectrometer, *Anal. Chem.*, 78, 8281-8289, 2006
- Docherty, K. S., Wu, W., Lim, Y. B., Ziemann, P. J.: Contributions of organic peroxides to secondary aerosol formed from reactions of monoterpenes with O₃, *Environmental Science & Technology*, 39, 4049-4059, 2005
- Ehara, K., Hagwood, C., Coakley, K. J.: Novel method to classify aerosol particles according to their mass-to-charge ratio-Aerosol particle mass analyzer, *Journal of Aerosol Science*, 27(2), 217-234, 1996

- Eldering, A., Cass, G. R.: Source-oriented model for air pollutant effects on visibility, *Journal of Geophysical Research*, 101(D14), 19343-19369, 1996
- Glowacki, D. R., Wang, L., Pilling, M. J.: Evidence of formation of bicyclic species in the early stages of atmospheric benzene oxidation, *J. Phys. Chem. A*, 113, 5385-5396, 2009
- Grosjean, D.: Atmospheric reactions of ortho cresol: Gas phase and aerosol products, *Atmospheric Environment*, 18(8), 1641-1652, 1984
- Hallquist, M., Wenger, J. C., Baltensperger, U., Rudich, Y., Simpson, D., Claeys, M., Dommen, J., Donahue, N. M., George, C., Goldstein, A. H., Hamilton, J. F., Herrmann, H., Hoffmann, T., Iinuma, Y., Jang, M., Jenkin, M., Jimenes, J. L., Kiendler-Scharr, A., Maenhaut, W., McFiggans, G., Mentel, T. F., Monod, A., Prevot, A. S., Seinfeld, J. H., Surratt, J. D., Szmigielski, R., Willdt, J.: The formation, properties and impact of secondary organic aerosol: current and emerging issues, *Atmospheric Chemistry and Physics*, 9, 5155-5236, 2009
- Hawthorne, S. B., Krieger, M. S., Miller, D. J., Mathiason, M. B.: Collection and quantitation of methoxylated phenol tracers for atmospheric pollution from residential wood stoves, *Environmental Science & Technology*, 23(4), 470-475, 1989
- Hawthorne, S. B., Miller, D. J., Langenfeld, J. J., Krieger, M. S.: PM-10 high-volume collection and quantitation of semi- and nonvolatile phenols, methoxylated phenols, alkanes, and polycyclic aromatic hydrocarbons from winter urban air and their relationship to wood smoke emissions, *Environmental Science & Technology*, 26, 2251-2262, 1992
- Heaton, K. J., Sleighter, R. L., Hatcher, P. G., Hall, W. A., Johnston, M. V.: Composition domains in monoterpene secondary organic aerosol, *Environmental Science & Technology*, 43, 7797-7802, 2009
- Henry, F., Coeur-Tourneur, C., Ledoux, F., Tomas, A., Menu, D.: Secondary organic aerosol formation from the gas phase reaction of hydroxyl radicals with m-, o- and p-cresol, *Atmospheric Environment*, 42, 3035-3045, 2008
- Huang, M., Zhang, W., Wang, Z., Hao, L., Zhao, W., Liu, X., Long, B., Fang, L.: Theoretical investigation on the detailed mechanism of the OH-initiated atmospheric photooxidation of o-xylene, *International Journal of Quantum Chemistry*, 108, 954-966, 2008

- Hurley, M. D., Sokolov, O., Wallington, T. J., Takekawa, H., Karasawa, M., Klotz, B.: Organic aerosol formation during the atmospheric degradation of toluene, *Environmental Science & Technology*, 35(7), 1358-1366, 2001
- Iinuma, Y., Boge, O., Grafe, R., Herrmann, F.: Methyl-nitrocatechols: Atmospheric tracer compounds for biomass burning secondary organic aerosols, *Environmental Science & Technology*, 44, 8453-8459, 2010
- IPCC (2007). Intergovernmental Panel on Climate Change: Climate Change 2007: The Physical Science Basis, Cambridge University Press, UK.
- Johnson, D., Jenkin, M., Wirtz, K., Martin-Reviejo, M.: Simulating the formation of secondary organic aerosol from the photooxidation of toluene, *Environ. Chem.*, 1, 150-165, 2004
- Johnson, D., Jenkin, M. E., Wirtz, K., Martin-Reviejo, M.: Simulating the formation of secondary organic aerosol from the photooxidation of aromatics hydrocarbons, *Environ. Chem.*, 2, 35-48, 2005
- Kanakidou, M., Seinfeld, J. H., Pandis, S. N., Barnes, I., Dentener, F. J., Facchini, M. C., Van Dingenen, R., Ervens, B., Nenes, A., Nielsen, C. J., Swietlicki, E., Putaud, J. P., Balkanski, Y., Wilson, J.: Organic aerosol and global climate modelling: a review, *Atmospheric Chemistry and Physics*, 5, 1053-1123, 2005
- Kautzman, K. E., Surratt, J. D., Chan, M. N., Chan, A. W. H., Hersey, S. P., Chhabra, P. S., Dalleska, N. F., Wennberg, P. O., Flagan, R. C., Seinfeld, J. H.: Chemical composition of gas- and aerosol-phase products from the photooxidation of naphthalene, *J. Phys. Chem.*, 114, 913-934, 2010
- Khalizov, A. F., Zhang, R., Zhang, D., Xue, H., Pagels, J., McMurry, P. H.: Formation of highly hygroscopic soot aerosols upon internal mixing with sulfuric acid vapor, *Journal of Geophysical Research*, 114, D05208, doi: 10.1029/2008JD010595, 2009
- Klotz, B., Sorensen, S., Barnes, I., Becker, K. H., Etkorn, T., Volkamer, R., Platt, U., Wirtz, K., Martin-Reviejo, M.: Atmospheric oxidation of toluene in a large-volume outdoor photoreactor: In situ determination of ring-retaining product yields, *J. Phys. Chem. A*, 102, 10289-10299, 1998
- Malloy, Q., Nakao, S., Qi, L., Austin, R. L., Stothers, C., Hagino, H., Cocker, D. R.: Real-time aerosol density determination utilizing a modified Scanning Mobility

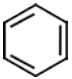
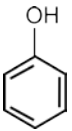
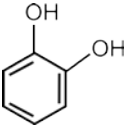
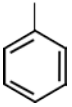
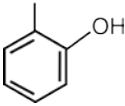
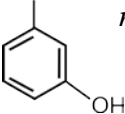
- Particle Sizer - Aerosol Particle Mass Analyzer system, *Aerosol Science and Technology*, 43, 673-678, 2009
- McMurry, P. H., Wang, X. W., Park, K., Ehara, K.: The relationship between mass and mobility for atmospheric particles: A new technique for measuring particle density, *Aerosol Science and Technology*, 36, 227-238, 2002
- Nakao, S., Shrivastava, M., Nguyen, A., Jung, H., Cocker, D.: Interpretation of Secondary Organic Aerosol Formation from Diesel Exhaust Photooxidation in an Environmental Chamber, *Aerosol Science and Technology*, 45(8), 954-962, 2011
- Ng, N. L., Kroll, J. H., Chan, A. W. H., Chhabra, P., Flagan, R. C., Seinfeld, J. H.: Secondary organic aerosol formation from m-xylene, toluene, and benzene, *Atmospheric Chemistry and Physics*, 7, 3909-3922, 2007
- Odum, J. R., Hoffman, T., Bowman, F., Collins, D., Flagan, R. C., Seinfeld, J. H.: Gas/particle partitioning and secondary organic aerosol yields, *Environmental Science & Technology*, 30(8), 2580-2585, 1996
- Olariu, R. I., Klotz, B., Barnes, I., Becker, K. H., Mocanu, R.: FT-IR study of the ring-retaining products from the reaction of OH radicals with phenol, o-, m-, and p-cresol, *Atmospheric Environment*, 36, 3685-3697, 2002
- Orsini, D. A., Ma, Y., Sullivan, A., Sierau, B., Baumann, K., Weber, R. J.: Refinements to the particle-into-liquid sampler (PILS) for ground and airborne measurements of water soluble aerosol composition, *Atmospheric Environment*, 37, 1243-1259, 2003
- Pope, C. A., Dockery, D. W.: Health effects of fine particulate air pollution: Lines that connect, *J. Air & Waste Manage. Assoc.*, 56, 709-742, 2006
- Pratt, K. A., Prather, K. A.: Mass spectrometry of atmospheric aerosols—recent developments and applications. Part I: Off-line mass spectrometry techniques, *Mass Spectrometry Reviews*, DOI 10.1002/mas.20322 2011
- Reinmig, M.-C., Müller, L., Warnke, J., Hoffmann, T.: Characterization of selected organic compound classes in secondary organic aerosol from biogenic VOCs by HPLC/MSn, *Analytical and Bioanalytical Chemistry*, 391(1), 171-182-182, 2008
- Sato, K., Hatakeyama, S., Imamura, T.: Secondary organic aerosol formation during the photooxidation of toluene: NO_x dependence of chemical composition, *J. Phys. Chem. A*, 111, 9796-9808, 2007

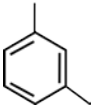
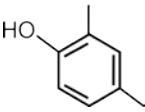
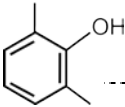
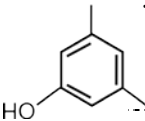
- Sato, K., Takami, A., Isozaki, T., Hikida, T., Shimono, A., Imamura, T.: Mass spectrometric study of secondary organic aerosol formed from the photo-oxidation of aromatic hydrocarbons, *Atmospheric Environment*, 44, 1080-1087, 2010
- Schauer, J. J., Kleeman, M. J., Cass, G. R., Simoneit, B. R. T.: Measurement of emissions from air pollution sources. 3. C1-C29 organic compounds from fireplace combustion of wood, *Environmental Science & Technology*, 35, 1716-1728, 2001
- Simoneit, B. R. T.: A review of biomarker compounds as source indicators and tracers for air pollution, *Environ. Sci. & Pollut. Res.*, 6(3), 159-169, 1999
- Smith, D. F., Kleindienst, T. E., McIver, C. D.: Primary product distributions from the reaction of OH with m-, p-xylene, 1,2,4- and 1,3,5-trimethylbenzene, *Journal of Atmospheric Chemistry*, 34, 339-364, 1999
- Smith, D. F., McIver, C. D., Kleindienst, T. E.: Primary product distribution from the reaction of hydroxyl radicals with toluene at ppb NO_x mixing ratios, *Journal of Atmospheric Chemistry*, 30, 209-228, 1998
- Sun, Y. L., Zhang, Q., Anastasio, C., Sun, J.: Insights into secondary organic aerosol formed via aqueous-phase reactions of phenolic compounds based on high resolution mass spectrometry, *Atmospheric Chemistry and Physics*, 10, 4809-4822, 2010
- Surratt, J. D., Murphy, S. M., Kroll, J. H., Ng, N. L., Hildebrandt, L., Sorooshian, A., Szmigielski, R., Vermeylen, R., Maenhaut, W., Claeys, M., Flagan, R. C., Seinfeld, J. H.: Chemical composition of secondary organic aerosol formed from the photooxidation of isoprene, *J. Phys. Chem. A*, 110, 9665-9690, 2006
- Takekawa, H., Minoura, H., Yamazaki, S.: Temperature dependence of secondary organic aerosol formation by photo-oxidation of hydrocarbons, *Atmospheric Environment*, 37, 3413-3424, 2003
- Volkamer, R., Klotz, B., Barnes, I., Imamura, T., Washida, N.: OH-initiated oxidation of benzene Part 1. Phenol formation under atmospheric conditions, *Phys. Chem. Chem. Phys.*, 4, 1598-1610, 2002
- Weber, R. J., Orsini, D. A., Daun, Y., Lee, Y.-N., Klotz, P. J., Brechtel, F.: A particle-into-liquid collector for rapid measurement of aerosol bulk chemical composition, *Aerosol Science and Technology*, 35, 718-727, 2001

- Wyche, K. P., Monks, P. S., Ellis, A. M., Cordell, R. L., Parker, A. E., Whyte, C., Metzger, A., Dommen, J., Duplissy, J., Prevot, A. S., Baltensperger, U., Rickard, A. R., Wulfert, F.: Gas phase precursors to anthropogenic secondary organic aerosol: detailed observations of 1,3,5-trimethylbenzene photooxidation, *Atmospheric Chemistry and Physics*, 9, 635-665, 2009
- Xue, H., Khalizov, A. F., Wang, L., Zheng, J., Zhang, R.: Effects of coating of dicarboxylic acids on the mass-mobility relationship of soot particles, *Environmental Science & Technology*, 43, 2787-2792, 2009

B.6 Tables

Table B.1. Experimental test matrix (low NO_x)

	Run ID	HC _i (ppb)	HC _f (ppb)	ΔHC (μg/m ³)	Mo (μm ³ /cm ³)	SOA yield ^c
<i>benzene + H₂O₂</i>						
	EPA1141A	491	434	182	25	0.19
	EPA1149A	490	429	195	26	0.18
	EPA1161A	1031	929	326	64	0.28
	EPA1161B	528	478	160	21	0.19
	EPA1225A	953	833	383	73	0.27
	EPA1225B	959	882	246	36	0.20
<i>phenol + H₂O₂</i>						
	EPA1206A	51	21	115	35	0.43
	EPA1206B	52	20	122	40	0.45
	EPA1217A	138	49	338	96	0.40
	EPA1217B	76	28	184	51	0.38
<i>catechol + H₂O₂</i>						
	EPA1293A	71 ^a	0	318	89	0.39
<i>toluene + H₂O₂</i>						
	EPA1266A	104	77	100	12	0.17
	EPA1251B	84	59	93	12	0.19
	EPA1141B	85	57	108	15	0.20
	EPA1290B	432	326	397	65	0.23
<i>o-cresol + H₂O₂</i>						
	EPA1251A	75	27	210	74	0.49
	EPA1252A	54	12	184	52	0.39
	EPA1252B	45	8	166	41	0.35
	EPA1266B	101	41	263	87	0.46
	EPA1427A	105	29	333	101	0.43
<i>m-cresol + H₂O₂</i>						
						

	EPA1255A	67	18	212	41	0.27
	EPA1255B	55	16	174	38	0.31
<hr/>						
<i>m</i> -xylene + H ₂ O ₂						
	EPA1244A	124	47	333	57	0.24
	EPA1180B	234	90	621	134	0.30
	EPA1209A	229	77	656	126	0.27
	EPA1209B	177	59	509	95	0.26
	EPA1212A	114	21	401	91	0.32
	EPA1212B	52	6	197	45	0.32
	EPA1248A	315	262	229	16	0.10
	EPA1248B	121	48	318	48	0.21
<hr/>						
<i>2,4</i> -DMP + H ₂ O ₂						
	EPA1238A	83	6	381	199	0.73
	EPA1238B	62	2	293	140	0.67
	EPA1412A	184	41	710	340	0.67
<hr style="border-top: 1px dashed black;"/>						
mezzanine chamber runs ^b						
	mez100809	68	2.2	327	222	0.95
	mez100909	131	4.9	628	331	0.74
	mez101009	48	1	234	108	0.65
	mez101109	72	2	349	155	0.62
	mez101309	77	1.9	373	197	0.74
	mez102109	66	1	322	162	0.70
<hr/>						
<i>2,6</i> -DMP + H ₂ O ₂						
	EPA1240A	98	6	457	134	0.41
	EPA1240B	58	2	278	75	0.38
<hr style="border-top: 1px dashed black;"/>						
mezzanine chamber runs ^b						
	mez081409	64	0	319	79	0.35
	mez081609	66	0	327	86	0.37
	mez081809	67	16	255	24	0.13
	mez100609	64	2.8	305	95	0.44
	mez100709	130	2.7	632	196	0.43
	mez120309	125	0	621	149	0.34
	mez120409	96	0	478	124	0.36
<hr/>						
<i>3,5</i> -DMP + H ₂ O ₂						
	EPA1243A	90	9	400	83	0.29
	EPA1243B	60	7	262	33	0.17
<hr style="border-top: 1px dashed black;"/>						
mezzanine chamber runs ^b						
	mez051910	72.24	0	359	61	0.24
	mez052010	85.09	0	422	75	0.25
	mez052310	154.1	0	765	148	0.27

mez060210 160.5 0 797 174 0.31

- a) Initial concentration calculated by amount injected. Injection done with oven temperature ~ 120°C.
- b) Initial DMPs concentrations calculated based on injection. Final concentration obtained by the PTR-MS.
- c) yields calculated using SOA density 1.4g/cm³

Table B.2. Phenolic formation yield from OH reaction with benzene, toluene, and *m*-xylene

	Phenolic formation yield (%)		NO _x (ppm)
	Phenol		
This study	41.3		0
Berndt and Böge (2006)	61 ± 6		0
Volkamer et al. (2002)	53.1 ± 6		0.002-2
	<i>o</i> -Cresol	<i>(m+p)</i> -Cresol	
This study	15.8	7.3	0
Atkinson et al. (1989)	20.4 ± 2.7	4.8 ± 0.9	0-10
Klotz et al. (1998)	12.0 ± 1.4	5.9 ± 0.9	0.003-0.3
Smith et al. (1998)	12.3 ± 0.6	5.6 ± 0.4	0.10-0.42
	(2,4 + 2,6 + 3,5)-DMP		
This study*	8.2 ± 1.3		0
Smith et al. (1999)	10.9 ± 0.5		0.157-1.081
Atkinson et al. (1991)	21.0 ± 5.6		0-10
Noda et al. (2009)	14.1 ± 2.6		0.01-0.1

*acquired in mezzanine chamber using PTR-MS

Table B.3. Estimated contribution of phenolic route to benzene, toluene, and *m*-xylene SOA.

	Benzene	Toluene	<i>m</i> -Xylene
Phenolic route (%)	23.5 ± 4.7*	15.8 ± 3.8*	16.9 ± 3.4 (n=4)

*Error estimated based on repeated *m*-xylene experiments and phenolic route calculations

B.7 Figures

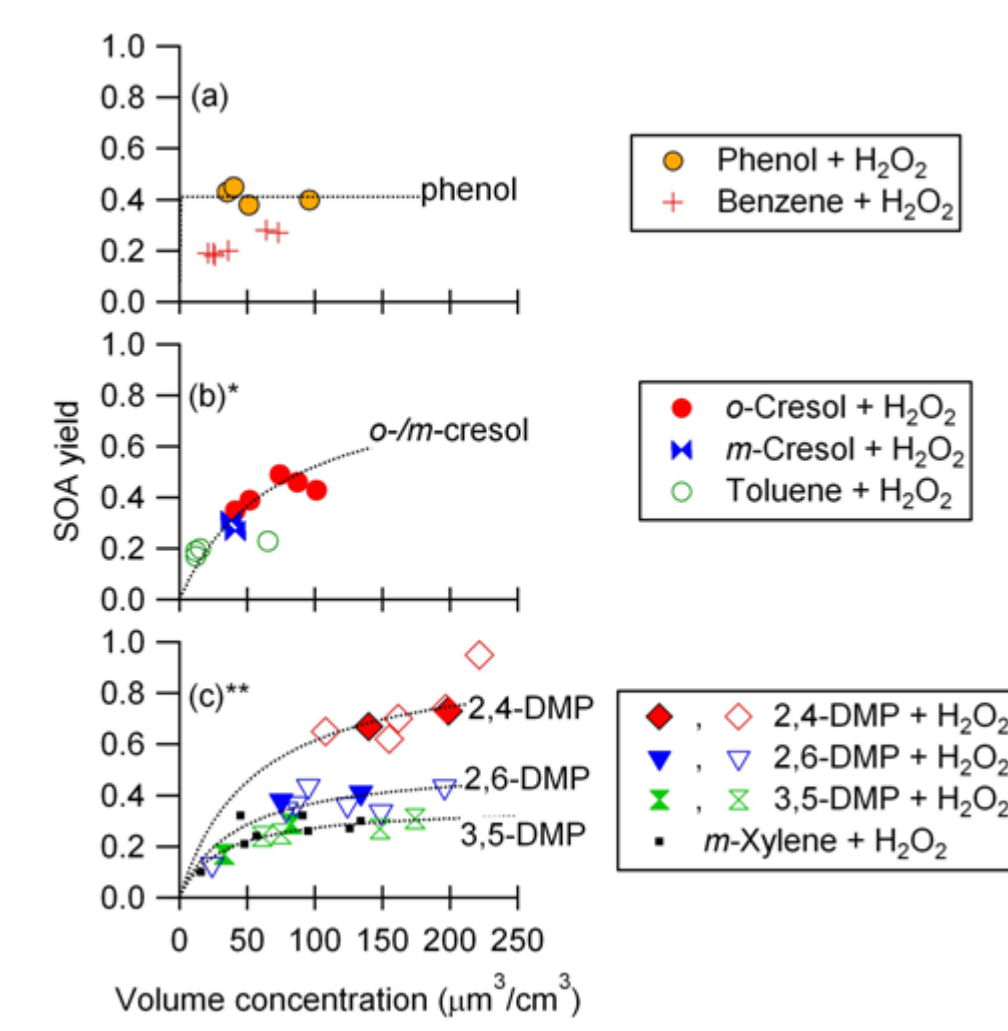


Figure B.1: SOA yield of benzene, toluene, m-xylene, and their phenolic compounds in the absence of NO_x (Dotted lines are one product model fit for phenolic compounds).

*** SOA yields from cresols isomers are combined.**

**** Open symbols are data acquired in CE-CERT mezzanine chamber**

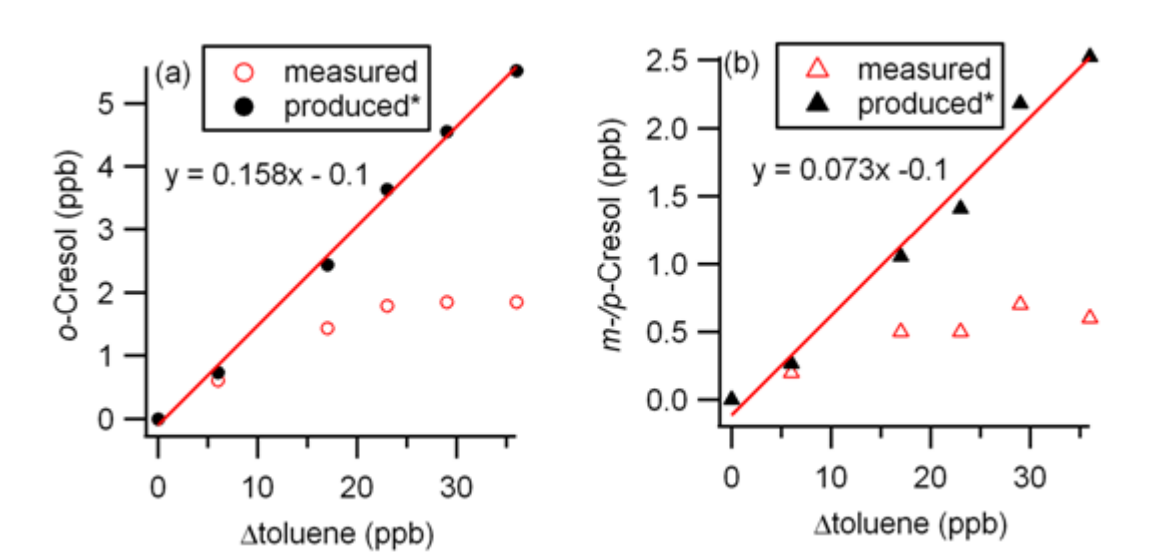


Figure B.2: Formation of cresols from OH reaction with toluene.
 *measured cresol concentrations were corrected for secondary reaction

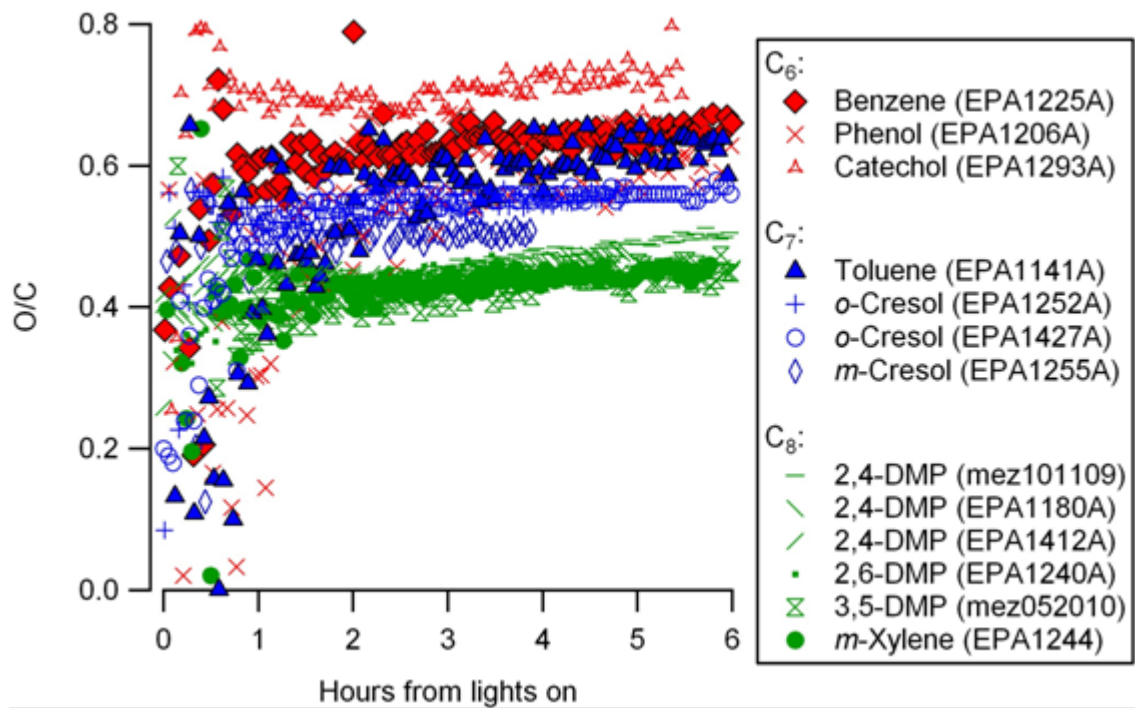


Figure B.3: Time series of the O/C ratio of SOA formed from aromatic hydrocarbons and phenolic compounds

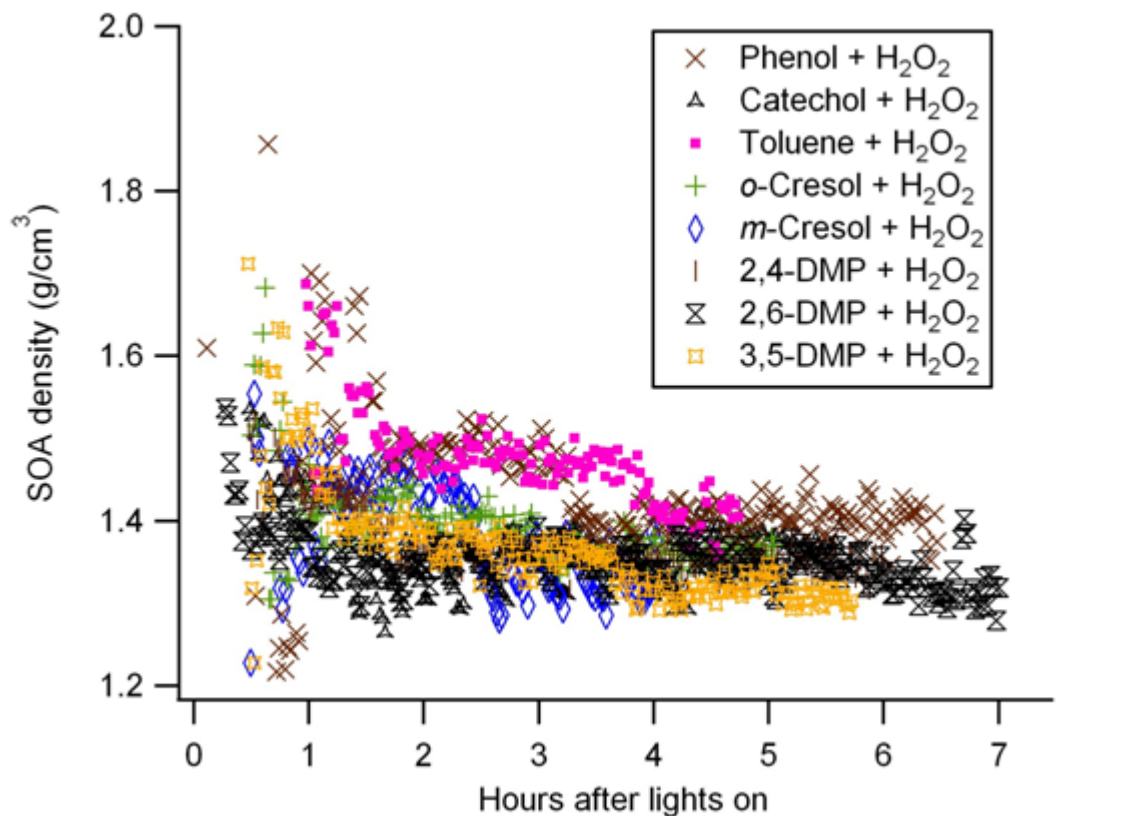


Figure B.4: Time series of the density of SOA formed from aromatic hydrocarbons and phenolic compounds

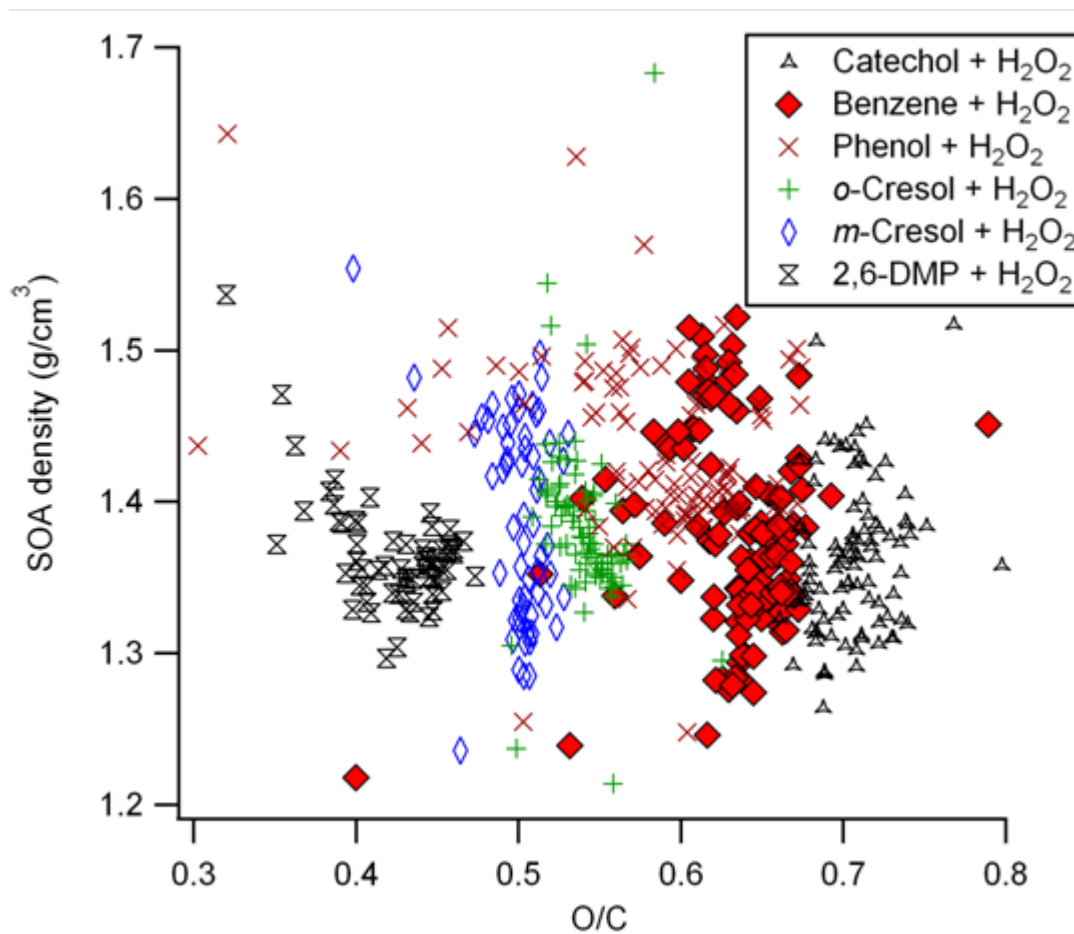


Figure B.5: The relationship between density and elemental compositions of SOA formed from aromatic hydrocarbons and phenolic compounds

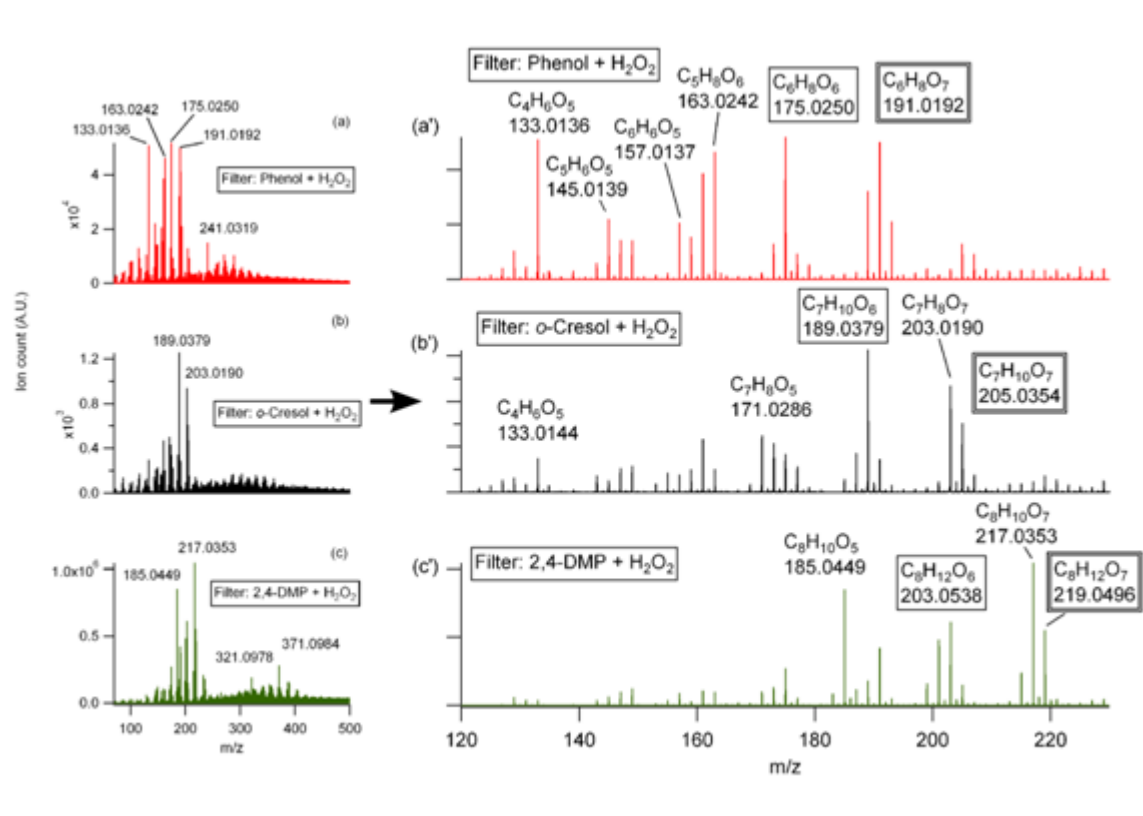


Figure B.6: ESI/APCI-ToF mass spectrums of SOA formed by OH reaction with phenolic compounds

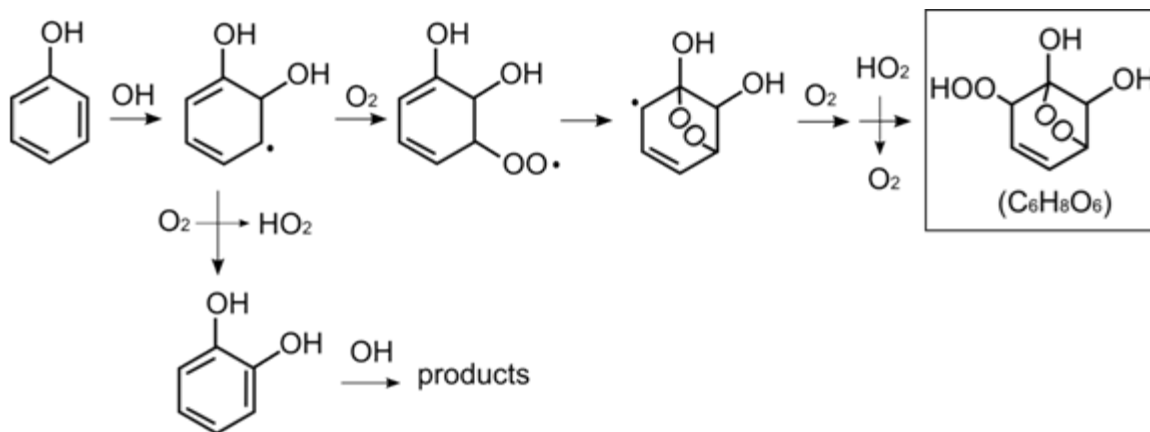


Figure B.7: Possible formation pathway of a bicyclic hydroperoxide (C₆H₈O₆) from OH reaction with phenol in the absence of NO_x inferred from aromatics oxidation mechanisms (e.g., Calvert et al., 2002; Johnson et al., 2005). Catechol formation from phenol is reported to be approximately 80% (Olariu et al., 2002).

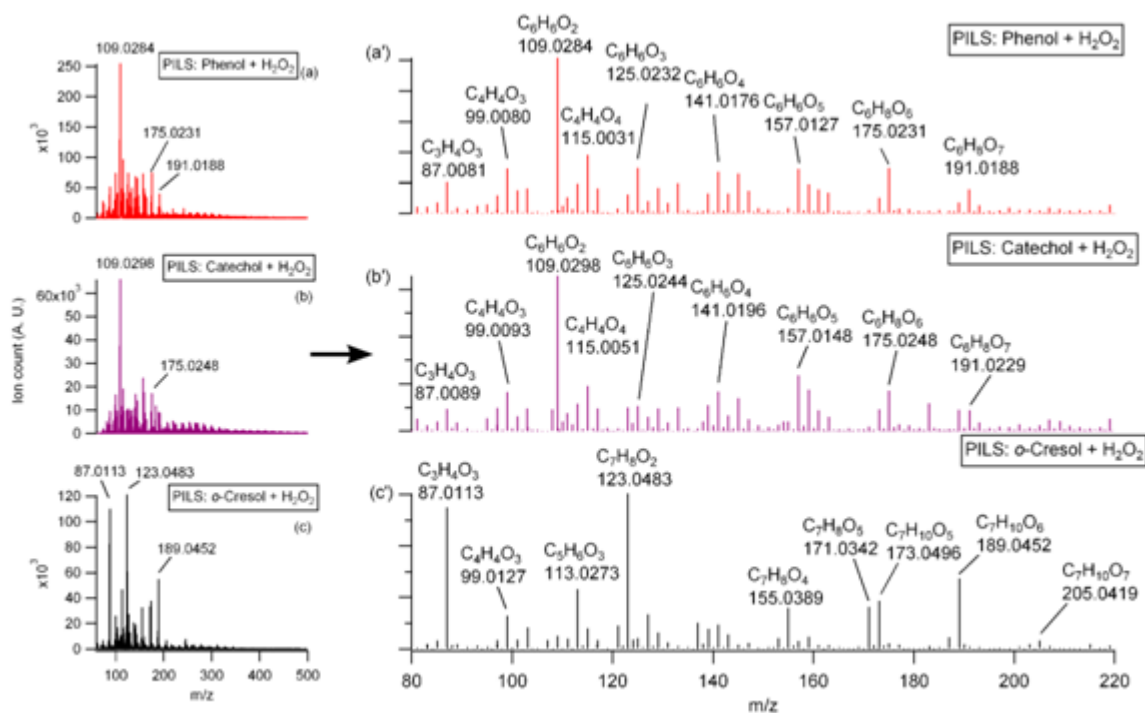


Figure B.8: PILS-ESI-ToF mass spectrometry of SOA formed by OH reaction with phenolic compounds

(The spectrum for phenol (a) and catechol (b) is taken when SOA concentration was highest. For *o*-cresol (c), spectrum at highest C₇H₈O₂ is shown.)